CONTENTS

Research on Fatigue Driving System Based on OpenCV

LIN Si-yu[1]; SHI Shu-tong[2]; ZHAO Hong-wei[3,4]; CHEN Chang-zheng[4]

(1. College of Instrumentation and Electrical Engineering ,Jilin University； 2. College of Communication Engineering,Jilin University；3.Department of computer science and technology ,Jilin University；4.Department of computer science and technology ,Jilin University, Changchun, China)

***Abstract*—This paper proposes a human eye recognition algorithm based on Haar-like feature and adaboost classifier to solve the problem that traditional human eye detection technology have in low recognition rate and long training time. The first thing to do is to position the face. After the face is positioned successfully, we use the upper half part of the face image to further locate the human eye. Then the haar features are extracted and the human eye classifier is trained by using adaboost algorithm.This experiment shows that method used in the paper has higher recognition rate than the traditional adaboost algorithm and effectively reduces the interference effect of light in the recognition process.**

***Key words*—Haar feature Adaboost eye Detection**

I. INTRODUCTION

STATISTICS show that there are thousands of traffic accidents caused by fatigue driving each year. How to prevent fatigue driving by using corresponding technical means is of crucial importance. With the development of machine vision and the traditional contact fatigue detection technology have many disturbances on the driver's normal driving, the current detection technology tends to be non-contact fatigue early warning system, in which judgment of the human eye state is fatigue detection important part. Opencv platform is developed by Intel Corporation, digital image processing and computer vision software, small-scale, high efficiency, widely used in researchers for secondary development. The contents of this paper are based on the Opencv platform, through the use of adaboost algorithm to achieve rapid eye positioning, and then to facilitate subsequent fatigue state determination.

II. FACE DETECTION

A. Adaboost Algorithm

Adaboost algorithm is proposed by Freund and Schapire according to the online distribution algorithm, which is based on an improved iterative algorithm of Boosting, overcoming the requirement of prior knowledge of weak learning by Boosting algorithm [1], The adaboost algorithm can be detected in real time and accuracy higher, less disturbed by the external environment. The basic idea of adaboost algorithm is to give each classifier different weights by comparing the error rates of a large number of weak classifiers whose classification ability is not strong, and then to construct a strong classifier by a certain method. Based on this method, the target location can be identified with high accuracy and quickness. In this paper, face detection based on Haar-like features of face detection method [2].

B. Image processing

Grayscale processing and grayscale stretching: The color of each pixel in a color image is determined by the three components of R, G and B. Each pixel has 255 values and the pixel color conversion range is large. When R = G = B, a special color image-grayscale image is formed. The variation range of one pixel is 255 kinds. Because the color image has no obvious visual effect for face recognition [3] , the image can be converted into a gray image to reduce the amount of computation. Grayscale stretching Stretch the grayscale image so that it can cover a large range of values, increase the contrast of the image, brighten the area of light, weaken the area of weak light, making the edge of the image more obvious. Through the grayscale stretching we can reduce the impact of light on the recognition process. Next the integral graph is used to process the image for the subsequent adaboost algorithm.

C. Classifier Training

The current research on face detection can be roughly divided into three categories.The first type is based on face features such as skin color features, face edge features, but the above method is susceptible to external noise. The second type is the template matching method. The third type is based on statistical detection methods such as neural network and support vector machines, which need to collect a large amount of sample data and take a long time ,although the recognition rate is not high. In this paper, we choose the adaboost program training classifier that comes with the Opencv platform to cascade the weak classifiers formed by the face samples extracted from the haar features into a strong classifier, which makes the program run conveniently and efficiently.

To use Opencv to train Haar feature classifier,corresponding positive sample image and counterexample sample picture are needed [4]. The positive sample is mainly collected by drivers who are photographed in different angles, different faces and different body inclining degrees. The number of positive pictures which need to unify the size taken from multiple angle faces is about 200. Then we use

about twice the number of non-face photos as a negative sample, where the negative sample contains as much as possible the background of the positive sample part in order to quickly separate the non-target part of the positive sample. The next step is to load the positive and negative samples and having the iterative judgment continuously until the required strong classifier is constructed.

III .HUMAN EYE LOCATION

A. Haar feature

Haar features ,that is,the gray-scale rectangular features. The calculation method is to grayscale the image first and then divide them into two parts black and white. In the calculation process, the integral graph method is used. The integral graph can be traversed only once to obtain the characteristic value, which greatly improves the calculation speed. The difference between the white rectangle and the black rectangle is the Haar eigenvalue. The feature classification using the Haar feature for human judgment has high accuracy .Meanwhile it has the advantages of low sample requirement and fast training speed. Common haar feature maps [5] are as follows.

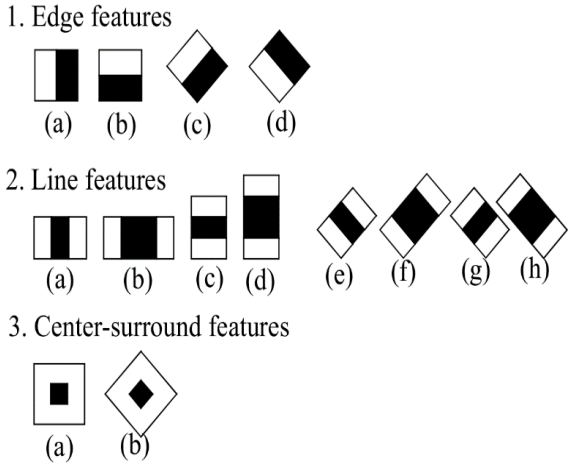

Fig.1. Feature prototypes of haar-like

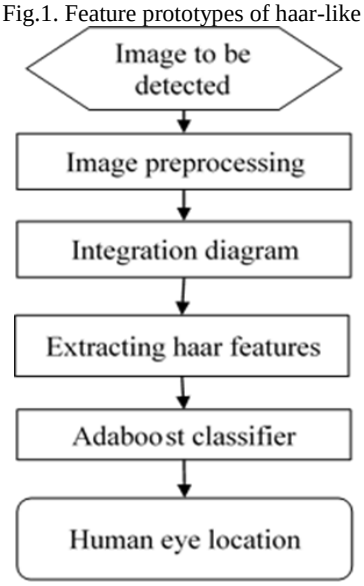

Fig. 2. Human eye training flow chart

B. Haar-like features improved

Human eye detection currently has integral projection, gray template, hough transform and template matching. Eye target is smaller than the face, if we detect the human eyes directly, the impact of external interference will be relatively large. In this paper, the human eye orientation is based on face detection . At the same time ,in order to facilitate rapid positioning, we take face recognition images from the top half, so that the target are narrowed after the treatment, eliminating the mouth and other interference in the identification process. The haar-like feature is a simple rectangular feature introduced by Viola et al. in face detection systems. Lienhart et al. [6] proposed an extended Haar-like feature based on Viola's algorithm, which can effectively improve the system's recognition without affecting the recognition speed greatly. Based on the distribution of facial features and the grayscale features of different organs, five new types of rectangular features are used [7,8] to extract the features of human eyes and to construct human classifier classifier, finally through the Adaboost cascade into a strong classifier to detect the human eye. During the detection,there will produce a detection window as the same size as the detection object sliding on the input image, if detected the target feature to meet the set of extended rectangular features during the detection of, can be identified as the target position.

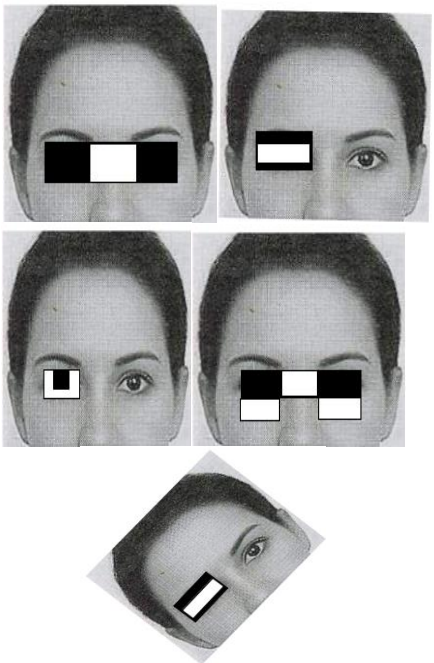

Fig. 3. Improved haar-like features
Results of experimental operation

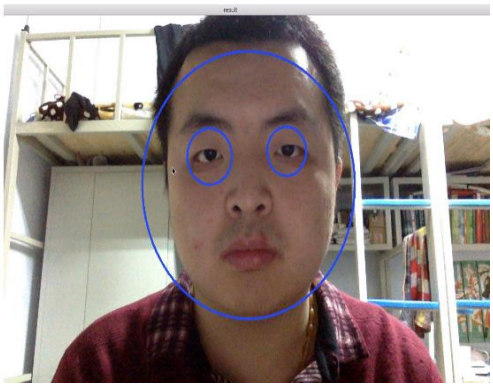

Fig. 4. positioning human face and eye results with strong light

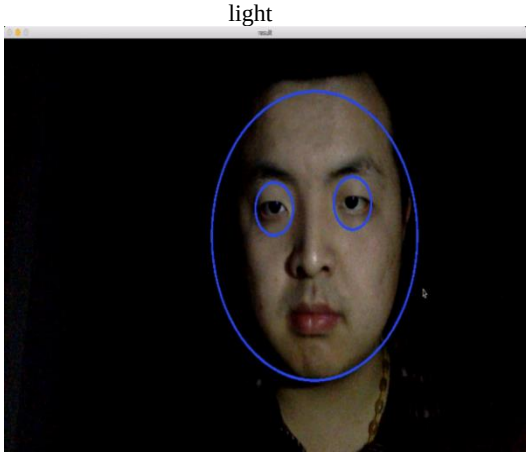

Fig. 5. positioning human face and eye results with weak light

C. Detection results

The detection results show that the experimental method can quickly locate the human face and the human eye under the conditions that the human body has a small deflection angle.The experiment has higher recognition accuracy under strong light or low light,and effectively overcomes light interference factors.The stability of detection is also good. But, when the human body is greatly deflected, the detection of the human eye is prone to error detection.

IV. CONCLUSION

This paper focuses on fast eye positioning in a fatigue driving environment. Considering the cab environment [9], the system should meet the requirements of not disturbing the driver's operation, correcting light and other environmental factors. Therefore, this paper first uses Adaboost algorithm to classify the face to detect the face, and the corresponding gray-scale processing of the image effectively eliminates the interference of environmental factors such as light and greatly improves the stability and usability of the system. By locating the human face first and then locating the human eye, the calculation time for positioning the human eye is further reduced, thereby enhancing the real-time performance of the system. Experiments show that the new Haar feature proposed in this experiment has higher accuracy than the traditional Haar feature, and the algorithm is simple and has high practicability. However, there are still some shortcomings in this experiment, such as the human eye can not be accurately detected when the driver's body deflect. At the same time for the study of fatigue driving test, we also the need for further precise positioning of the pupil. So there are still many improvement needed. What we need to do think next is how to further pinpoint the pupil and confirm the fatigue status.

References

[1] LI Yang, CAO Zhu-ming.Face Detection Based on Skin Color and AdaBoost Algorithm [J] .Modern Computer: Professional Edition, 2017 (55): 77-80

[2] Dong Choi Chao. Expression Recognition and Timeliness Analysis Based on Haar-like Features [D]. Tianjin: Tianjin University, 2012.

[3] Zhang Yanmei. Research and Implementation of Fatigue Driving Test Based on Human Eye Tracking [D]. Shenyang: Northeastern University, 2014.

[4] Chen Shengyong, Liu Sheng. Implementation of Computer Vision Based on OpenCV [M]. Beijing: Science Press, 2008: 65-68

[5] Viola and Jones, "Rapid object detection using a boosted cascade of simple features", Computer Vision and Pattern Recognition, 2001

[6] Lienhart R,Maydt J.An extended set of Haar-like features forrapid object detection[A] .The IEEE International Conferenceon Image Processing[C] .New York , USA , 2002 , 1 :900 -903

[7] Yao Yao. Vision-based fatigue driving warning system [D]. Hefei: Hefei University of Technology, 2015.

[8] Long Min Min. Face detection method based on Adaboost and eye location algorithm [D]. Chengdu: University of Electronic Science and Technology, 2008.

[9] Thomas S M,Chan Y T.A simple approach for the estimation ofcircular arc centre and its adius[J].Computer Vision,Graph-ics,and Image Processing,45(3):362-370

Development and Analysis of Five-Axis Robot and Its System

ZHANG Hang-ming; HUANG Yu-yao
(College of Instrumentation and Electrical Engineering ,Jilin University, Changchun, China)

***Abstract*—The five-axis robot is the symbol of China's scientific and technological innovation. Based on the current development of China's social economy and technology, combined with the application characteristics of five-axis robots in recent years, it understands the advantages and disadvantages of its application in practical applications. Its innovative direction analyzes the development of five-axis robot systems.**

***Key words*—five-axis robot; system development; characteristics**

I. INTRODUCTION

IN the past forty years, industrial robots have been used to carry out grinding, polishing, etc., while welding, assembly, auxiliary and other process technologies are also the direction of enterprise application, but only Three to four percent of industrial robots used in the processing technology. The comparison and analysis of industrial robots and machine tool systems has lower cost, more sensitive operation and a very large development space. This is also the main reason why people are willing to use robots instead of machine tools to implement some multi-axis milling processes. In order to improve the effective application of robots in the processing area, it is of vital importance to fully implement the research work of five-axis robots.

II. RESEARCH ON FIVE-AXIS ROBOT

The joint robot, also known as the joint arm robot, or the joint robot arm, is one of the forms of industrial robots that are often used in the industrial field at the present stage, and meets the various demands put forward by various industrial fields. A five-axis joint robot is a robot that has five rotating axes and is similar to a human arm. The practical application range includes loading, painting, surface treatment, and measurement, spot welding, assembly, chip cutting, forging, fixing, etc. In practical applications, it can be divided into various types according to the difference of construction.

In the application process, the advantages exhibited by the five-axis robot are divided into the following points: First, a very high degree of freedom. The five-axis robot works almost all the trajectories or angles; the second is that it can be programmed autonomously to complete the automation work; the third is to improve the efficiency of production and effectively control the error probability of the operation; fourth, the replacement is not suitable for human completion. Harmful work that is harmful to health. Such as bright spot welding outside the car. The shortcomings exhibited by the five-axis robot are divided into the following points: First, the price is high, and the initial investment in the industry is large; secondly, a lot of preparation work before production, such as programming and computer simulation, takes too long[1].

In the industrial scope, the five-axis robot technology is very familiar at home and abroad, but in the scope of teaching, the teaching development and training facilities for the five-axis robot are very few, because it is a classic training equipment. And the system, in order to ensure that the industrial talents in the new era can do their jobs better, they need to provide theoretical knowledge and operation time in the learning phase, so that they can lay the foundation and provide guarantee for the future job requirements.

III.THE DEVELOPMENT SIGNIFICANCE OF THE FIVE-AXIS ROBOT SYSTEM

Design requirements: through the five-axis robot teaching and development demonstration system as the key goal of teaching work, pay attention to the design process, simple show the control scheme. According to the simple form to show the control method, the development thought, the difficulty and the solution, it can let the specialized science talented person to better understand and the research in their study process, and satisfies the electronic and the automation basic personnel to self-study and apply. The following takes the development process of five-axis drilling robot as an example, citing the case-based teaching method, from simple to complex to show the robot operation steps and work links, so that autodidact can easily keep up with the design process in layers of progressive.

The five-axis punching robot proposes a set of automated flexible drilling systems for industrial robots based on PC control. This system is based on analysis and is a CNC system that integrates the robot controller. Based on the research of the frequently used PC numerical control system framework structure, and comparing the advantages and disadvantages of various architecture types, PC plus CNC mode can be applied as the system control method. Through this program, the hardware platform of the system is built to complete the system architecture. The following is a system analysis using a five-axis punching robot as an example.

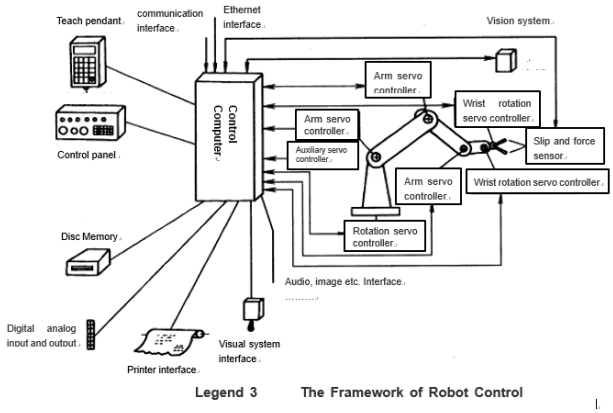

Legend 3 The Framework of Robot Control

IV. SYSTEM DESIGN

A.Research ideas and methods

The overall design, motion simulation, hardware construction and operation debugging of the five-axis robot include the selection of the motion joint motor, the transmission mechanism and the sensor, the three-dimensional modeling of the mechanical arm and the components, and the drawing of the engineering drawing, motion simulation and dynamic simulation. And so on[2].

B.Implementation plan

An effective solution is proposed for the design of the manipulator, the selection of the sensor type, the definition of the drive structure, the proposed control scheme, and the smoothness of the robotic arm during the drilling process, and the deep exploration of the five-axis robot from simple to complex. the study.

C.Technical route

On the one hand, the overall hardware structure is driven by the control system for both the drive system and the position detection. The former includes the actuator and the machined workpiece; the latter will eventually process the workpiece.

On the other hand, the main controller in the embedded hardware of the electronic control system and the touch screen, FLASH, 24C02, USB interface are mutually influential, and the one-way influence relationship with the reset circuit, the startup mode interface, the button, the stroke switch and the power supply circuit In actual operation, the main controller contains two contents, one is the servo motor driver, and the other is the system indicator light, wherein the servo motor driver includes five servo motors [3].

D.*Software Design*

First, the software control of the touch screen. In the system UC, a liquid crystal display template is constructed. In the system, it is determined whether there is an action of pressing the touch screen by a person. To achieve this requirement, the system needs to continuously scan for acquisition. If the system is in the test and is touched again, it is necessary to determine which part is the system and to design the corresponding value. In conjunction with the associated values, a second scan is performed, and at this stage it is necessary to determine which part of the touch screen is touched, each part being opposite its function. Design the corresponding value, the MCU will reserve in the flash memory and protect the information.

Second, the working principle of the RESET program is to make the RESET program in the system multiple scans, clear that the RESET button is touched, the first step of the system will clear the flag bit, after the flag bit is cleared, the system The plurality of servo motors in the control will return to the original position, so that the overall operation of the RESET program is completed.

Third, the robot is driven by the servo motor, and the management of the servo motor is performed by the position. The drive pulse of the system-controlled servo motor can better manage the five servo motors selected for the application. The working principle of the servo motor is to invert the control input and output ports to generate pulses for the servo motor. The working efficiency of the pulse affects the running speed of the servo motor, and the data of the pulse is affected by the static variable of the interrupt function.

Fourth, the teaching control part is a combination of high-quality features of flash memory. This feature is a power outage problem in the flash memory process. The information stored in the flash memory will not disappear at will, and can be started directly after the robot is re-run [4]. The actual running process is as follows: Start → Clear flash flag bit storage area → Whether the program is running for the first time, if it is “Yes”, then the FLASH parameter will be loaded, and vice versa will be clear whether the program is in the first running state. After that, the change of the parameter is clarified. If it is "Yes", it will be written to FLASH. If it is "No", it will be clear again whether the parameter has changed.

V. DESIGN OUTPUT

AS is shown in legend 2, the design of a five-axis teaching robot is finally completed. The virtual industrial robot is controlled by a real hand-held teacher and a robot control system to complete the field teaching programming. By replacing the hand-held teaching device and the industrial robot model, the industrial robot can be trained in real teaching and programming, and the robot drilling application scene and programming process package can be provided, and the control system is a decentralized control system. The system has eight relatively independent microprocessor chips (I. E. CPU): SYS-CPU,M-CPU,ARITH-CPU,AXIS1-CPU,AXIS2-CPU,SL-CPU,I/O-CPU,PP-CPU,) as follows:

1. SYS-CPU System-CPU is the system CPU, responsible for the management of the entire system and coordination;
2. M-CPU Motioncutroc-CPU, is responsible for motion control, coordinate transformation trajectory planning, etc.
3. ARITH-CPU Arithmetic-CPU is a mathematical operation coprocessor, responsible for floating-point operation, so that the system operation speed is greatly improved;
4. AXIS1-CPU Axis-CPU (Servo Control CPU,) is responsible for the servo control function of the first, second and third axes. The CPU chip has high operation speed.
5. AXIS2-CPU function and AXIS1-CPU control

object for the third, fourth, fifth axis;

6. I/O-CPU is responsible for processing parallel I / O port signals and decentralized I / O serial ports and I / O analog input / output signals; SL-CPU is responsible for processing the sudden external I / O signal, which can quickly allow the detection of the signal to be effective, and make the corresponding response processing quickly.

7. PP-CPU teaching box CPU (Program Pendant CPU) is responsible for teaching box function management and operation;

8. The hardware structure of the control system is shown in legend 1.

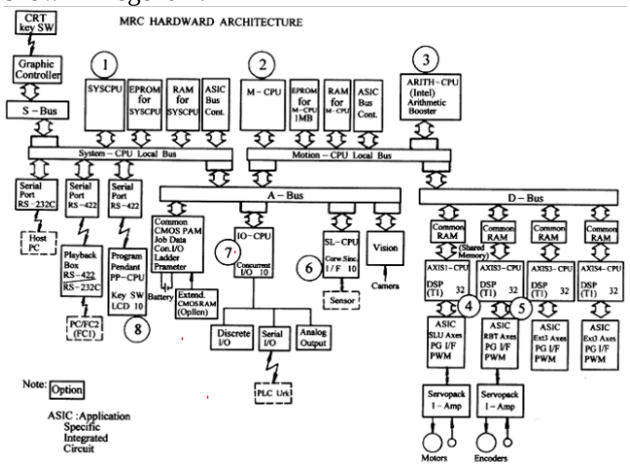

Legend 1 hardware architecture of MRC control system

VI. CONCLUSION

All in all, through the above dynamic demonstration and simulation, all the design requirements of the five-axis robot system have been realized, the design scheme is feasible and has certain stability. It can be integrated and studied according to actual demand in practical application, and analyze the role of five-axis robot in machining, manufacturing and other work from various aspects. As the foreign technology is now mature and used in the market, the domestic technology research and application work has just started, which requires the major manufacturing enterprises and universities to carry out effective research work.

References

[1] Jiang Wei. Design of control system for five-axis painting robot based on PLC[J]. Hangzhou University of Electronic Science and Technology, 2014.

[2] Xia Boxiong, Du Jun. Modeling and experiment of reconfigurable robot based on five-axis machining system of complex parts[J]. China Mechanical Engineering, 2014, 25(9): 1208-1213.

[3] Wang Jintao. Research on intelligent measurement, modeling and processing integrated robot system[J]. China Mechanical Engineering, 2017, 9(04): 1207-1209

[4] Xia Yifei. Development of small five-axis robots [J]. Xihua University, 2015.

Development and Application of Control System for New Intelligent Robot

ZHANG Hang-ming
(College of Instrumentation and Electrical Engineering ,Jilin University, Changchun, China)

***Abstract*— Intelligent robot control systems generally consist of multiple subsystems which have both division of labor and cooperation, both coordination and competition. The use of traditional centralized or hierarchical control methods to design the entire system encounters a series of insurmountable difficulties. In view of the above situation, the article aims at designing a robot control system based on 32-bit embedded system for a series of problems in the traditional closed control system. This system is equipped with an open hardware structure, detailing the components of the control system hardware and the specific design conditions, including: motion control, sensors and other modules. The software system is designed based on the hybrid architecture. The modules are designed based on the principle of top-down layering on the Linux platform, and the Python script is used to effectively and flexibly solve the problem of task strategy transformation. On this basis, select the example to verify the performance of the intelligent robot control system. The research results show that the designed control system has good openness and can provide a reliable platform for system expansion functions and human-machine hybrid control.**

***Keywords*—intelligent robot; control system; hardware design; validity test**

I. INTRODUCTION

SINCE the birth of the first industrial robot (in the early 1960s), the development and application of robots should take half a century. Throughout the history of robotics in the world, robotics has also grown tremendously. As a highly automated equipment that integrates advanced technologies in various subjects (such as automatic control, mechanical engineering, artificial intelligence, etc.), with the rapid development of science and technology, intelligent robots have also developed more rapidly, the range of their application is continuously expanding. Mainly used in automation factories, deep sea operations, space operations, etc., and some complex tasks need to be achieved through multiple robots. Compared with a single robot, multi-robot cooperative mission will have better accuracy and bearing capacity flexibility and other requirements. Through more than 20 years of research, development and use, the research on multi-robot collaboration system has gained certain recognition in both theoretical and practical fields. This is also a hot issue for most scholars in the field of robotics. Multi-intelligent robots need to cooperate with each other to complete corresponding tasks, not simply to combine multiple robots together. Simply stacking multiple robots is not only difficult to accomplish tasks with high performance, but also causes conflicts or confrontation between multiple robots, thus reducing the performance of the robot. Relatively speaking, multi-robot collaboration can also smoothly achieve work that is difficult or impossible for a single robot. Distributed control is called the most promising framework for robot collaboration. If the number of robots increases, it will show a series of advantages, such as: strong flexibility.

The main goal of the design of intelligent robot control system is to develop a distributed control system and smoothly realize the transition from simple control of individual to control of complex group behavior. The overall system needs to bring out the corresponding problems through the interaction between the robots, especially the research on the coordination of the multi-intelligent robot system level. ： This also requires intelligent robots to be equipped with control platforms which have good scalability, portability and openness. Based on the intelligent robot as the research object, this paper proposes a control platform based on Linux operating system and 32-bit embedded processor. This control platform has high reliability, strong scalability and small size,which can meet the need of multi-intelligent robot cooperation to complete the task.

II. SYSTEM STRUCTURE AND FUNCTION DIVISION

Intelligent robots are robots developed by using equipment and technology such as computers and sensors. Compared with traditional robots, the new intelligent robots have higher requirements on intelligence, and can collect information about the external language and natural environment, reasonably control the hands and feet, and complete various activities independently without the need for staff to control them[1]. In order to facilitate the expansion operation and meet the needs of heterogeneous design, the control system is designed by hardware modularization and software layering. The hardware part is divided into main control module, power supply module, sensing module, etc. according to functions, wherein the main control module is used as the brain of the whole intelligent robot mainly plays the functions of collecting various data, transmitting data to the remote control platform, and accepting remote control commands. The main function of the sensor module is to sense the corresponding information, including: collecting temperature, infrared, gas and other data information. The power module can provide the required energy for the motion of the intelligent robot and is designed to provide the power for the main control and motion control modules. The main function of the wireless communication module is to receive the data transmitted by the main control module to the remote end in real time, and receive the instructions sent by the remote end to the main control module to realize communication between the modules. As the motion execution part of the designed intelligent robot, the motion control module is designed to accept the commands issued by the main control module and

smoothly realize the travel, turn and other operations through the DC motor drive. In this case, each module can independently complete its own tasks, and can also complete tasks with other functions according to actual task requirements.

The intelligent robot control system software is mainly composed of the task layer, the information sensing layer, the decision layer, etc. The main control program only needs to insert the corresponding script which can be flexibly applied to various tasks without re-implementing the compiling process and achieve the control needs of the above task operation. The overall design framework of the system is shown below.

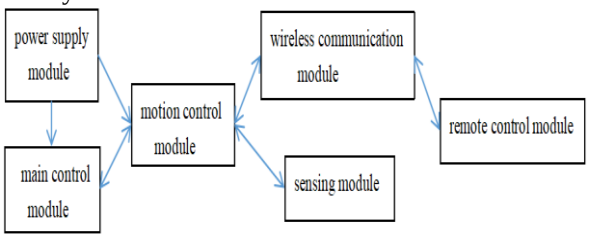

Figure 1 Overall framework of the intelligent robot control system

III. DESIGN THE HARDWARE PLATFORM OF THE SYSTEM

The hardware of the robot control system designed is mainly composed of the main control module, the sensor module, the wireless communication module, etc., as shown in Figure 2. Among them, the control system selects the ARMP core S3C2410 as the core control chip, which is based on the 32-bit processor core $ARM920T$, It shows the advantages of high performance, high integration, rich interface, strong configurability and so on [2]. In addition, the $S3C2410$ chip has integrated most of the functional unit channels, USB interfaces, LCD controllers and other general-purpose devices, which not only can effectively reduce the board area, but also support TCP/TP protocol and porting UC/OS operations, and achieve remote and real-time control.

The sensor module mainly includes two aspects of image and non-image acquisition. The image acquisition mainly uses the USB camera to smoothly complete the image transmission with the main control module through the interface. Sensors for non-image acquisition applications typically include temperature sensors, light sensors, and so on This research uses infrared obstacle avoidance ($E18-D80NK-N$) and temperature sensor ($PT100$), which is a photoelectric sensor that integrates emission and reception, which can help the robot to avoid obstacles smoothly; non-image sensor relies on AHB bus and main control module implements data transmission [3].

As a more important part of the robot hardware, the motion control module is also the basis of the entire robot construction, which directly affects the layout and volume of the intelligent robot. In addition, this module is the core of the control system and is closely linked to the highest level of intelligent motion that can be performed by intelligent robots. If the designed motion control module does not have good performance, it is useless to have the best control software. Therefore, the motion control module has a non-negligible influence on the designed intelligent robot. The motor can provide the required power for the motion control module, and the quality of the motor determines the performance of the module, the selection of the power battery, and so on. Since the target of the intelligent robot designed is: fast speed, small size, etc., therefore, it is selected to meet the requirements of this aspect and take into account the influence of cost factors. Through the comparison of various types of motors, the $L293D$ motor drive chip is finally selected. Because of its integrated bipolar $H-$bridge circuit, both DC motors can be controlled by one L293D chip. The data transmitted by the $H-$bridge circuit can set the forward or reverse rotation of the motor, causing the signal to be applied to the pulse width modulation (PWM), PWM acts on the two DC motors, enabling them to control the speed and steering of the robot at different speeds [4].

The power module mainly consists of the direct motor power supply, the motor drive, and the processor. Among them, the direct power supply part of the motor uses the lithium ion battery to provide the required power for the motor. The rated voltage of the motor is 9V. Considering the fluctuation of the battery voltage, it is necessary to set aside a certain amount for the battery. It is more appropriate to choose a 12V battery for a certain amount of battery. The 12V battery is not easy to buy on the market. After the comprehensive consideration and analysis, three series of 3.7V lithium batteries are selected as the power source of the motor. In addition, the battery capacity must be properly measured. The main power-consuming equipment of the intelligent robot lies in the motor. If the motor is in normal working state, the current required is about 120 mA. A certain amount of time and current is set aside in the actual operation of the robot. Combining the analysis of multiple factors, the battery of 250mA/h was finally selected. It must be noted that the battery voltage will be greatly reduced due to the power consumption, which will affect the control effect of the motor. Therefore, the voltage detection circuit will be designed later, and adjust the voltage at both ends of the motor reasonably based on the timely detection of voltage drop.

Wireless communication module application the $Nordic$ company's single-chip wireless transceiver chip ($nRF2401$) , $nRF2401$ integrates most of the built-in modules, using only a small number of peripheral components. In addition, this design data transmission rate is high, low power consumption, to meet the actual needs of each module communication.

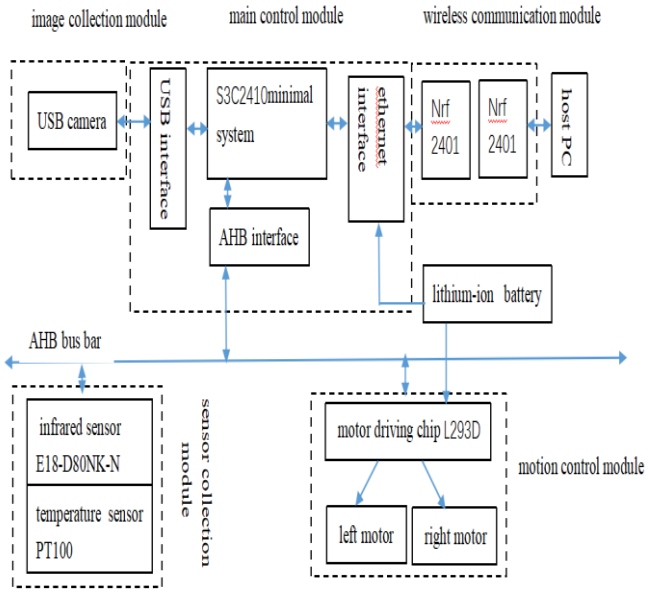

Figure 2 Intelligent robot control system hardware composition

IV.SOFTWARE PLATFORM DESIGN

The software platform designed in this paper can integrate the functions of perception, transmission of information and decision-making, and play a good control effect. According to the requirement of RCS system design theory, the system is divided into different layers by top-down software development. The task layer aims to provide operation functions such as setting tasks and input external control information. Decision-making layer is composed of decision-making control procedures and other parts, which can smoothly realize the functions of avoiding road barriers and making reasonable paths, and can also give appropriate treatment to the unexpected time [5]. The information perception layer can acquire and process the information from outside and its own state in time, while the executive layer mainly performs the control commands issued by the decision-making layer.

In order to achieve the stability and high efficiency of the control system, we select embedded operating system embedded with strong real-time property in the main control chip, which can not only meet the specific development needs of the software platform, but also provide development tools with open source characteristics, which can be better used in the development environment and system design. In addition, the selected embedded operating system *Linus* belongs to the open source system, it has multi-user characteristics, the system resources can be used by multiple users at the same time, each user has the corresponding access limit for their own resources [6]. At the same time, it can also realize multi-task or multi-thread management, and can execute multiple programs at the same time, and each program runs independently.

In the task layer and decision-making layer, ***Python*** scripting technology is used to write the tasks to be set and the initial operation of the system into script files ***Python***. Strategy layer can obtain various strategy scripts by encapsulation processing [7]-[8]. On this basis, we rely on embedded code ***Python*** to configure the required calling interface for the underlying layer. This design scheme can not only meet the actual needs of changing real-time adjustment strategy according to the task or environment, but also meet the requirements of modular design of software system, and enhance the flexibility and practicality of the whole system. Wireless communication requires communication between robots and workstations or between different robots via Ethernet or conventional ***TCP/IP*** protocol stacks. In addition, the system can also use blackboard and point-to-point mode to communicate. Among them, the blackboard of the former mode belongs to shared storage space, and each intelligent agent writes corresponding information to the blackboard. The above information can be provided to other intelligent agents of the system. Different intelligent agents can also access the blackboard at any time and check the information needed to carry out various tasks. The latter is a communication mode used for cooperative tasks between intelligent agents. With the support of various protocols, the data packets can be transmitted stably and reliably. It must be noted that when communication between points is carried out, the intelligent agent will obtain the information of other agents through the blackboard, such as operation state and so on.

V.SYSTEM EFFECTIVENESS TEST

In the specific research and development project, the communication, formation and control tests are carried out on the designed multi-agent robot control platform to evaluate the performance of the system. When the wireless communication function of a single robot is tested, 5000 message packets (***128bytes***) in the queue are selected as the feedback time for a series of tests. Based on the same wireless communication network, the average round trip time is 3ms, and the packet loss rate is controlled within the range of $0.08-0.1\%$. But in the PC processing platform, the test results show that the average time of round-trip operation is $1ms$, while the packet loss rate is $0.08-0.09\%$. According to the issued command packages and status packages, the robot can execute various instructions and process the information returned to the status.

Based on the $5\times16m$ platform, a multi-agent robot team experiment is carried out. Multiple robots are randomly placed at each starting point and 12 sets of departure directions are selected randomly. After continuing the experiment, the robot adopts the *leader-following* formation control method to form a formation, which is based on the closed-loop control of the formation algorithm, according to the distance (I)and angle（ φ ） between the robots to achieve formation and formation change.In specific experiment, the time is defined as $t1$、$t2$ in turn, which represent time needed till forming stable queue and stable 1-shaped queue respectively. After more than 200 experiments to carry out statistical analysis, which are randomly placed in the scattered area $500\times300cm$, two robots for formation, the average time of $t1$、$t2$ used is 1.38s, 2.15s respectively; with four groups for formation, the average time $t1$、$t2$ in turn are $2.44s$、$3.86s$, the formation and the formation effect as shown in Figure 3.

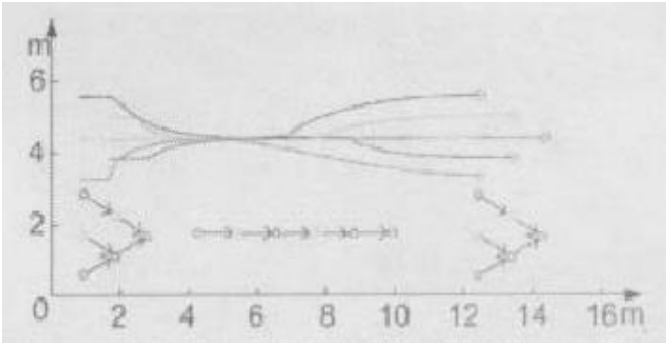

Figure 3 Five robot formation change and trajectory map

Through the above experiments, it can be seen that the intelligent robot control system designed in this paper has high processing efficiency, good stability and reliability,and meets the actual operation requirements.

VI.CONCLUSION

In summary, robot technology has gradually entered people's lives, and has been applied in the fields of military, disaster relief and other fields. In the future, robots will develop towards the direction of intelligence, flexibility and miniaturization. Control system is the core of the whole robot, and its design has an important impact on the operation of the robot. This research takes Linux operating system as the design platform, develops the corresponding control system for the intelligent robot, aims at changing the shortcomings of the former robot, such as being huge, bulky, and poor control ability, and meets the requirements of intelligent, flexible and miniaturized robots in the new era, so as to make the intelligent robot control system get a qualitative change. It is believed that with the rapid development of science and technology, the application prospect of intelligent robots will be more extensive.

References

[1] Shen Weijia. Design and research of control system for multi-sensor trolley [D]. Nanjing University of Science and Technology, 2015.

[2] Xu Chaoli, Lin Ke, Yang Chen et al. Intelligent robot cooperative control method based on calf surface electromyography[J]. Chinese Journal of Biomedical Engineering, 2016, 35(4): 385-393.

[3] Chang Zhoulin, Yuan Ting. Application of Artificial Intelligence in Intelligent Robot System[J]. Science & Technology Innovation Review, 2016, 13(23): 10, 12.

[4] Zhang Wanxu, Zhang Xianglan, Li Ying et al. Path planning of intelligent robot based on improved particle swarm optimization algorithm[J]. Journal of Computer Applications, 2014, 34(2): 510-513.

[5] Ma Xiaoyu.Design of laser range finder for intelligent robot obstacle avoidance in cloud computing environment[J].Bulletin of Science and Technology,2017,33(8):110-113.

[6] Wan Xinyu. Design and Implementation of Intelligent Robot Based on Visual Servo Control [D]. Hunan University, 2016.

[7] Zhou Lei. Development of intelligent robot cooperative assembly system based on vision/force perception [D]. Xi'an University of Technology, 2014.

[8] Lu Guoce. Research on the Application of Control System of Single Chip Microcomputer in Intelligent Robot[J]. Electronics Production, 2015, (4): 56-56.

Surface plasmon resonance marine oil spill warning device simulation

Shi Chenyang; Gan Yang; Zhang Xuebin
（*jilin university instrument science and engineering institute,changchun,130021*）

***Abstract*—Surface plasmon resonance（SPR）technique is one of the most effective methods to monitor oil spill. As it is sensitive to subtle changes in the refractive index of the external medium, it can monitor inchoate and miniature oil spill. Use software MATLAB simulate the parameters when the refractivity of oil is between 1.4 to 1.55, use software C++ manipulate data and make alert. The experiment results show that surface plasmon resonance technique can monitor oil spill reliably and software can make effective alert.**

***Keywords*—oil spill, SPR, simulation, MATLAB**

0 PREFACE

OFFSHORE oil exploitation has become one of the main ways to obtain oil resources. The offshore oil pollution caused by insufficient advanced mining technology and natural disasters has seriously affected the environment. In order to deal with marine oil pollution in a timely manner, it is necessary to detect and warn the oil spill at sea. At present, the main technical means of marine oil spill detection are SAR satellite remote sensing monitoring [1-2], aerial remote sensing monitoring [3], ship remote sensing monitoring, fixed point monitoring and buoy tracking [4], but they are not able to monitor small area oil spills around the clock. The surface plasma resonance (SPR) technique was first discovered by Wood[5], which is caused by the excitation light and the metal free electron resonance. SPR technology has outstanding advantages such as fast detection speed, high sensitivity, mark-free, real-time detection, etc. Therefore, SPR sensing technology is widely used in life science, drug development, medical diagnosis, public safety, environmental pollution and other fields. In view of the defects and deficiencies of the existing marine oil spill detection methods, surface plasmon resonance (SPR) technology is used to detect and predict the oil spill on the sea by detecting the refractive index of the liquid on the surface of the ocean, with high measurement accuracy and accurate detection. Features. The surface plasma resonance sensor designed and used by this technology is small in size and convenient for instrument deployment, and it is easy to realize real-time, networked and intelligent monitoring of marine oil spill.

1 PRINCIPLE OF SPR-BASED MARINE OIL SPILL DETECTION

1.1Principle of SPR sensing technology

SPR sensing technology is mainly based on Surface Plasmon Resonance (SPR) principle, which is a physical optical phenomenon. When a bundle of monochromatic light is incident on the light-diffusing medium (refractive index is n1) by the optically dense medium (refractive index n0) (where n0 > n1), when the incident angle θ0 is greater than the critical angle θ1, it will be generated at the intersection of the medium. Total reflection. When the surface of the medium is plated with a metal film (generally a gold film or a silver film with a refractive index of n2), part of the energy of the incident light is reflected back to the prism during the total reflection, and the other part of the incident light is P-polarized component of incident light with evanescent wave (Evanescent Wave) propagates to the interface between the metal medium and the light-diffusing medium and passes through the metal film. In this process, the evanescent wave decreases with increasing depth [6], and finally causes the metal surface to generate regular oscillation. Surface plasmon wave (SPW) is generated. When the surface plasmon wave and the evanescent wave have the same wave vector and frequency, the surface plasmon wave and the evanescent wave will undergo affinity resonance, resulting in a large amount of light energy transfer to the electrons in the metal. The energy of the light is rapidly reduced, and this process is reflected in the spectrum of the reflected light, and a strong resonance absorption peak appears. The SPR sensor is sensitive to the refractive index change of the medium. When the refractive index of the sample to be tested changes, the absorption peak generated by the SPR resonance will also change accordingly. With this change, accurate detection of the refractive index change of the sample can be realized [7] , the schematic diagram is shown in Figure 1.1.

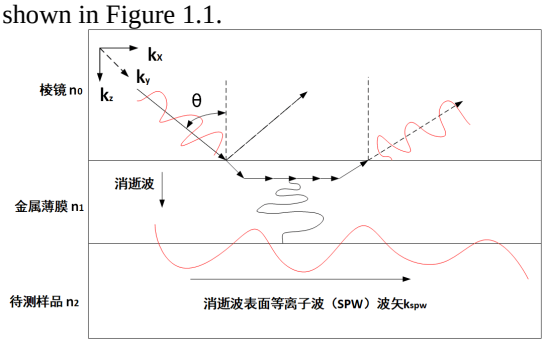

Figure 1.1 - Schematic diagram of surface plasmon resonance

1.2 SPR sensor design principle

Surface plasmon resonance sensors mainly have the following two classification methods, one is classified according to the coupling structure, mainly prism type, grating type, optical waveguide type and fiber type surface plasmon sensor; the other type is classified according to modulation mode, mainly There are four modulation type surface plasmon sensors with phase, angle, intensity and wavelength. Among them, Krestchmann prism type SPR sensor has the characteristics of high detection precision and relatively simple structure and easy to implement [8]. At the same time, to further simplify the structure and ensure higher

resolution, an angle modulation type surface plasmon resonance sensor is selected, in this type of SPR sensor. Most of them use the poor coherence near-infrared LED as the light source, which does not require complicated rotating devices, and can avoid the influence of the interference effect generated by the laser on the measurement results. The receiving end uses the linear array CCD to collect the reflected light intensity at different incident angles [9].

The Krestchmann prism coupling structure is mainly such that a metal film layer having a thickness of one tenth (about several tens of nm) of the light wavelength λ is attached to the prism surface without a gap, and the sample to be tested is attached to the surface of the metal film, when the color is monochromatically polarized.

When the light is refracted by the prism to the interface between the prism and the metal film, the surface plasmon resonance effect is excited by changing the incident angle or the wavelength of the incident light, and the generated resonance light is emitted, and the resonance absorption peak is detected by a photosensitive element such as a linear CCD. A schematic diagram of the Krestchmann prism coupling is shown in Figure 1.2.

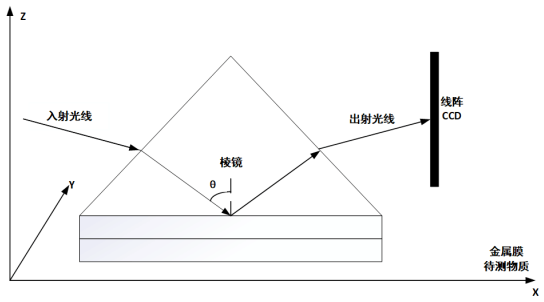

Figure 1.2 - Schematic diagram of the Krestchmann prism coupling device

The main description of surface plasmon resonance detection is as follows: Combining Fresnel's theorem and Maxwell's equation, it is known that when P-polarized light is totally reflected at the interface between the metal film and the prism and generates a horizontal wave vector, the free electrons on the surface of the gold film are excited. The surface plasmon is generated, and the horizontal wave vector of the incident light wave and the wave vector of the surface plasmon are:

$$k_s = \frac{2\pi}{\lambda}\varepsilon_0 sin\theta \quad \cdots\cdots (1)$$

$$k_{sp} = \frac{2\pi}{\lambda}\sqrt{\frac{\varepsilon_2\varepsilon_3}{\varepsilon_2+\varepsilon_3}} \quad \cdots\cdots (2)$$

When the incident angle of the light wave satisfies certain conditions, the surface plasma wave is equal to the frequency of the horizontal component of the incident light, and the two will resonate

Use the reflection formula:

$$r_{p12} = \frac{E_{1P}}{E_{1P}} = \frac{n_2 cos\theta_1 - n_1 cos\theta_2}{n_2 cos\theta_1 + n_1 cos\theta_2} \quad \cdots\cdots (3)$$

$$= \frac{\varepsilon_2 k_{pz1} - \varepsilon_1 k_{pz2}}{\varepsilon_2 k_{pz1} + \varepsilon_1 k_{pz2}} \quad \cdots\cdots (4)$$

$$r_{p23} = \frac{E_{2P}}{E_{2P}} = \frac{n_3 cos\theta_2 - n_2 cos\theta_3}{n_3 cos\theta_2 + cos\theta_3} \quad \cdots\cdots (5)$$

$$= \frac{\varepsilon_3 k_{pz2} - \varepsilon_2 k_{pz3}}{\varepsilon_3 k_{pz2} + \varepsilon_2 k_{pz3}} \quad \cdots\cdots (6)$$

The wave vector of the incident light in the z direction is:

$$k_{pzi} = \sqrt{\frac{\omega^2}{c^2}\varepsilon_i - k_s^2} \quad \cdots\cdots (7)$$

$$= \sqrt{\frac{\omega^2(\varepsilon_m - n^2 sin^2\theta)}{c^2}} \quad \cdots\cdots (8)$$

The total reflectance formula is:

$$R = |r_{13}|^2 = \left|\frac{r_{12} + r_{23}e^{i2k_{pz2}d}}{1 + r_{12}r_{23}e^{i2k_{pz2}d}}\right|^2 \quad \cdots\cdots (9)$$

Where: λ is the incident light wavelength, θ is the incident angle of the light wave, ε0, ε1, ε2, ε3 are the dielectric constants of the prism, the sensor slide, the gold film, and the oil, respectively, and the light wave is on the sensing slide, The wave vectors along the z direction in the gold-sensing film and the medium to be tested are kpz1, kpz2, and kpz3, respectively, and d is the thickness of the gold film.

When the oil adheres to the surface of the gold film, the change in the refractive index of the oil (1.41-1.55) due to the change in the oil composition causes a corresponding change in the total reflectance, and the change is used to monitor the oil spill. The linear reflectance is detected by a linear array CCD and transmitted to the control terminal for data processing and early warning using satellite communication. The overall design of the surface plasmon resonance marine oil spill warning device is shown in Figure 1.3.

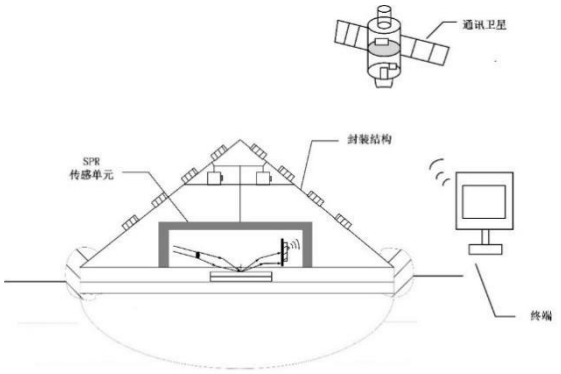

Figure 1.3 - Schematic diagram of the overall design of the surface plasmon resonance marine oil spill warning device

2 SOFTWARE DESIGN OF PARAMETER SIMULATION SYSTEM FOR SURFACE PLASMON RESONANCE MARINE OIL SPILL WARNING DEVICE

MATLAB is a powerful mathematical software from Mathworks. It combines numerical analysis, matrix calculation, signal processing and graphic display. It contains a large number of highly integrated functions for calling,powerful command statements for scientific research and engineering. Design and a wide range of subject areas provide a simple and efficient programming tool, and is widely used in image processing, control design, signal detection, financial modeling design, etc. [10-11]. Using the GUI designer in MATLAB, design the

parameters of the SPR oil spill monitoring device, including the incident light wavelength λ, the incident angle θ of the light wave, the thickness of the metal film d, the prism dielectric constant ε0, the dielectric constant of the sensor slide ε1, gold The dielectric constant of the film ε2 and the dielectric constant ε3 of the oil. Using the above quantities as input, design the data input box and input the value of the value to the corresponding value of the formula in 1.2. At the same time, according to the total reflectance formula in 1.2, in order to solve the relationship between a plurality of variables, the three wavelengths of the incident light wavelength λ, the incident angle θ of the light wave, and the thickness d of the metal film are required to be adjustable, so the design range is At the data input frame interface, only one of the refractive index n of the sample to be tested, the thickness d of the gold film, the incident angle θ of the light wave, or the wavelength λ of the incident light is a variable. When the rest is a constant, a relationship between the single variable and the reflectance can be plotted. The lowest point of reflectivity, which is the value corresponding to the strongest resonance effect of the plasma, is the optimal value for the single variable selection. This value can be obtained by solving the minimum value method.

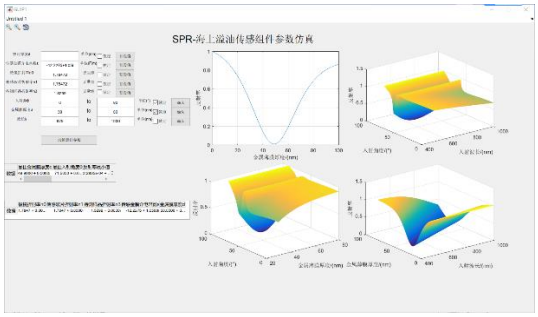

Figure 2.1 - GUI interface diagram of the parameter simulation system for surface plasmon resonance marine oil spill warning device

3 MATLAB DATA SIMULATION

3.1 Prism

Using the total reflectance formula of 1 , the dielectric constant ε2 of the gold film is -12.2275+1.05i [12], and the prism and the sensing slide are made of ZF13 heavy flint glass of the same material, and the dielectric constant ε0 = ε1 is 1.78472 [8].

3.2 Light source

The light source is the excitation source that generates the surface plasmon resonance effect. According to the formula in 1.2, the parameters related to the light source that affect the surface plasmon resonance effect are mainly the wavelength of the light source, the convergence angle, and the line width. When the thickness of the gold film is set to d=50 nm [13] and the incident angle θ of the light wave is in the range of 0 to 90 °, the incident wavelength value is changed, and the image superposition can be used to determine the corresponding incident wavelengths in the range of 0 to 90 ° incident angle. A comparison of reflectances, as shown in Figure 3.1. At the same time, the three-dimensional relationship between incident wavelength and reflectivity at incident angle can be established, and the relationship diagram is shown in Figure 3.2. It can be clearly seen from Fig. 3.2 that the absorption peak with an incident wavelength of about 650 nm and an incident angle of about 70 ° is the best. In this range, the optimal parameters can be further accurately solved. Calculate the spatial point corresponding to the lowest reflectance value in the three-dimensional relation diagram in Figure 3.1, and obtain the optimum angle of incidence angle θ=71.85° under the condition of gold film thickness d=50nm, and the optimal wavelength of incident wavelength λ=650mm . The fixed incident angle θ=71.85° and the gold film thickness d=50 nm can also be used to extract the optimum parameters of the incident wavelength. The schematic diagram is shown in Figure 3.3.

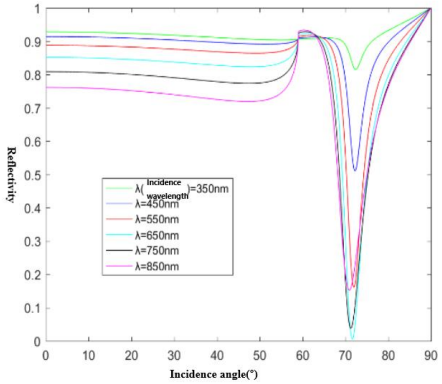

Figure 3.1 - Schematic diagram of the corresponding SPR reflectance curve at incident wavelengths λ = 350 nm, 450 nm, 550 nm, 650 nm, 750 nm, 850 nm

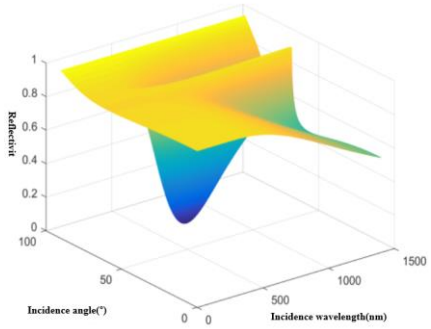

Figure 3.2 - The relationship between the wavelength λ of the incident light, the incident angle θ of the light wave and the refractive index

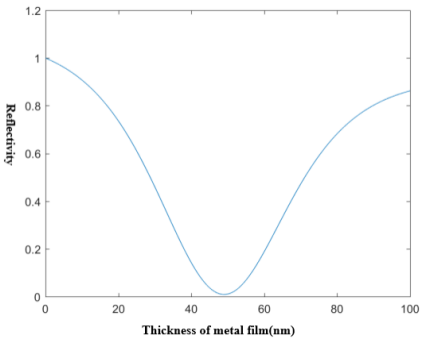

Figure 3.3 - Relationship between gold film thickness d and refractive index at incident angle θ = 71.85 ° and incident wavelength λ = 650 nm

3.3 Metal film thickness

According to the principle of surface plasmon resonance, the penetration depth dp of the evanescent wave is related to the thickness of the metal film. Therefore, it is necessary to determine a suitable thickness of the gold film to ensure that the evanescent wave can penetrate the metal film to generate plasmon resonance. The angle of incidence is 0~90 °, the thickness of the metal film is 0~100nm, and the selected incident wavelength is 650nm. The three-dimensional relationship between incident angle, incident wavelength and reflectivity is obtained, as shown in Figure 3.4. Under the same conditions, the relationship between the thickness of the gold film, the incident wavelength and the reflectivity can be obtained when the thickness of the metal film is in the range of 0-100 nm and the incident wavelength is in the range of 0-1500 nm for a given incident angle θ=71.85°. 3.5 is shown. According to Fig. 3.5, when the incident angle is around 70 °and the thickness of the metal film is about 50 nm, the lowest value of the reflectance value appears, that is, the strongest peak of the absorption peak. At the same time, the contrast between the reflectances of different gold film thicknesses in the range of 0~90 °incident angle can be obtained by using the graphic superposition, as shown in Figure 3.6. The optimal parameters of the gold film thickness can be solved by the same reason in 3.2, d=48.98nm, and the optimal angle of incidence angle θ=71.85°. Similarly, the fixed incident angle θ = 71.85 ° and the incident wavelength λ = 650 nm can also be used to extract the best parameters for the long thickness of the gold film. The schematic diagram is shown in Figure 3.7.

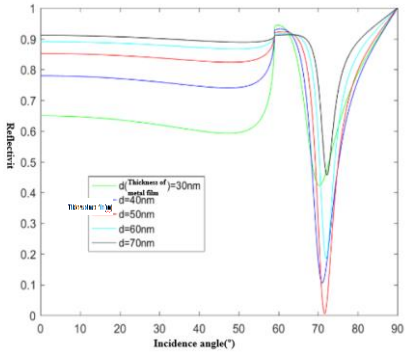

Figure 3.4 - Correlation range gold film thickness d, light wave incident angle and refractive index

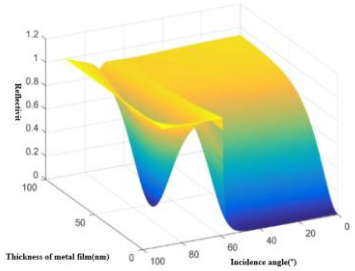

Figure 3.5 - Thickness of gold film in a given range d, wavelength λ of incident light and refractive index

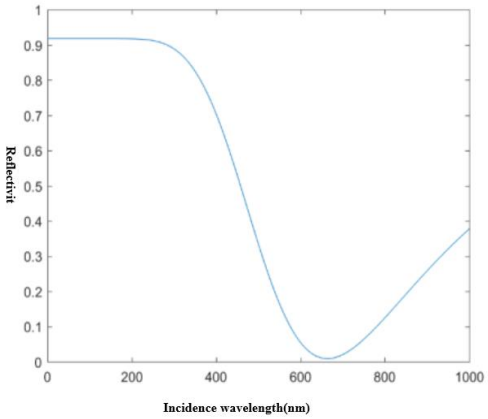

Figure 3.6 - Gold film thickness d=30nm, 40nm, 50nm, 60nm, 70nm corresponding SPR reflectance curve

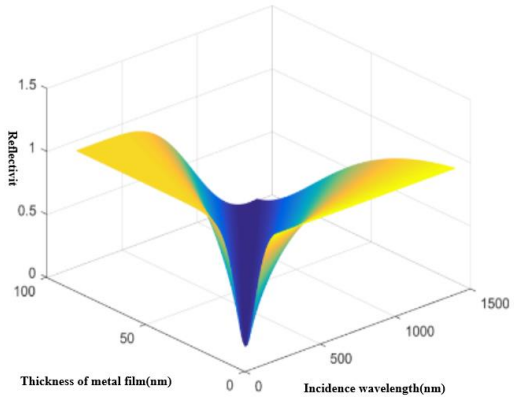

Figure 3.7 - Relationship between incident light wavelength λ and refractive index (incident angle 71.85 °, gold film thickness 50 nm)

4 BASED ON C++ DATA PROCESSING AND EARLY WARNING SOFTWARE DESIGN

The C/C++ language is one of the most popular high-level programming languages, and it can directly operate on operating systems, applications, and hardware. The C/C++ language is superior to other interpreted high-level languages[13]. Combined with the advantages of C++ language for user graphical interface design, C++ is chosen as the computer language for data processing and early warning interface design of surface plasmon resonance marine oil spill warning device.

4.1 Data Acquisition Module

Data acquisition card is used for data acquisition. Firstly, the data acquisition card is self-tested. After the self-test, the program function function is called to set the relevant parameters and start collecting. The collected data is stored in the storage device and the satellite communication and other means are used. The machine communicates. The data collection flow chart is shown in Figure 4.1.

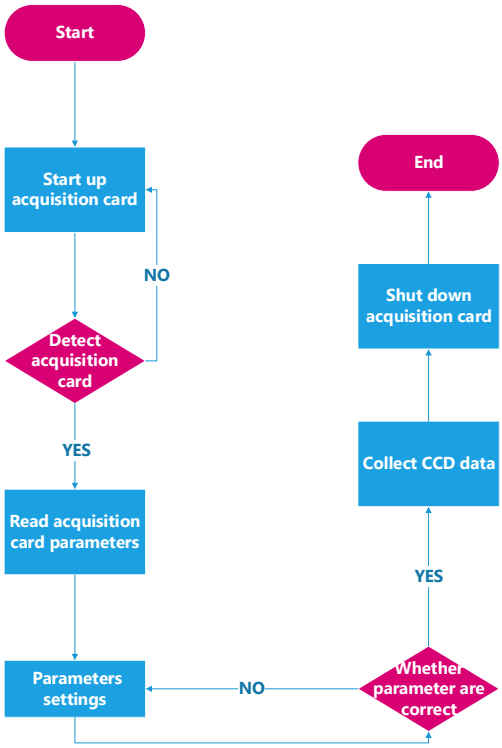

Figure 4.1 - Data Collection Flowchart

4.2 Data Storage and Processing Module

When no oil spill occurs, the light intensity signal received by the linear array CCD changes stably within a certain range. When the oil spill occurs, surface plasmon resonance occurs, and the discrete data collected by the acquisition system will be displayed on the client interface. A gradual absorption peak. Due to the interference of noise signals (natural fluctuation of seawater, natural environmental noise, power frequency noise), the actual collected signal will deviate from the simulated signal. After the data is denoised and normalized by the filtering algorithm, the terminal interface will display A smoother curve that automatically analyzes the data and generates an alert when it detects a rapidly changing absorption peak. The oil spill detection process is shown in Figure 4.2. The data processing and storage flow chart is shown in Figure 4.3.

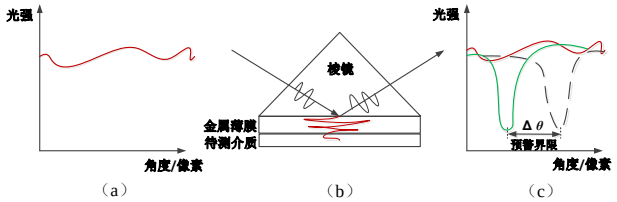

Figure 4.2 - Schematic diagram of the marine oil spill detection process

Figure (a) is the data collected in the background of sea water or air, which approximates a straight line; Figure (b) shows the approximate process of SPR; the warning boundary in Figure (c) is in the laboratory. Using the difference in refractive index of the test object, an early warning limit obtained by doing multiple experiments

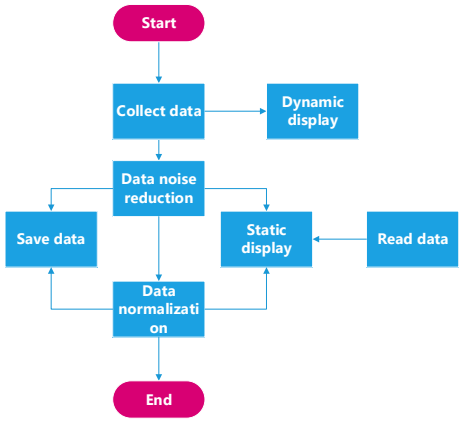

Figure 4.3 - Data Processing Flow Chart

4.3 Data Display Module

Different types of display of the processed data, allowing users to see the experiment in a more intuitive way As a result, understand the meaning of the experimental data. The client display interface is shown in Figure 4.4.

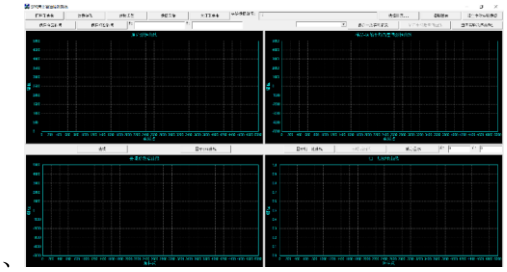

Figure 4.4 - Client Display Interface

5 SUMMARY

This paper introduces the method of simulating the marine oil spill warning device based on the principle of surface plasmon resonance. It introduces the principle of SPR technology and the classification of SPR sensor. The design principle and method of Krestchmann prism SPR sensor are introduced in detail. Software design flow and simulation results of sensor parameter simulation of MATLAB software and data processing and early warning software design based on C++. The experimental data is compared with the simulation results. The experimental results show that the surface plasma resonance sensing technology can reliably detect marine oil spills, and the software can make effective warning.

References

[1] Song Shasha, Zhao Yupeng, Su Tengfei, Ma Youjun, An Wei, Meng Junmin, Zhao Chaofang.Research and development of satellite remote sensing monitoring system for marine oil spill SAR[J].Remote Sensing Technology and Application,2013,28(05):928-933 .

[2] Jiang Qiufu. Research on satellite multi-spectral remote sensing data oil spill detection method [D]. Ocean University of China, 2011.

[3] An Jubai, Zhang Yongning. Analysis of the Status Quo of Remote Sensing Monitoring of Marine Oil Spill in Developed Countries[J].Communication and environmental protection,2002(03):27-29.

[4] Pan Honglei, Wang Zugang. Analysis of emergency response and treatment technology for offshore oil spills[J]. China Safety Production Science and Technology, 2010(S1): 65-67.

[5] RW Wood, XLII. On a remarkable case of uneven distribution of light in a diffraction grating spectrum [J]. The London, Edinburgh, and Dublin Philosophical Magazine and Journal of Science, 1902, 4(21): 396-402 .

[6] Lu Lansong. Research on sensor principle and characteristics based on surface plasmon [D]. University of Electronic Science and Technology, 2018.

[7] Wei Pengqi. Optical fiber sensor based on surface plasmon resonance principle [D]. East China Normal University, 2014.

[8] Zheng Zheng. Research on miniaturization device based on surface plasmon resonance marine oil spill detection [D]. Jilin University, 2016. [9]] Zheng Rongsheng, Lu Yonghua, Lin Kaiqun, Xie Zhiguo, Wang Pei, Luo Zhaofeng, Ming Hai. New Progress in Surface Plasmon Resonance Sensors[J]. Chinese Journal of Quantum Electronics, 2008(06): 657-664.

[9] Zong Jiebao, Duan Liuyun, Wang Ying, Duan Liuyu, Li Wei. Research and implementation of software based on MATLAB GUI software[J]. Electronic Design Engineering, 2010, 18(07): 54-56.

[10] Hu Xinyan, Huo Wenxiao, Li Aitao. Application of MATLAB in the Teaching of Signal and System Course[J].Science and Technology Information,2009(27):136-137.

[11] Raether H. Surface Plasmons on Smooth and Rough Surfaces and on Gratings [M]. Berlin Heidelberg: Springer-Verlag, 1988.

[12] Fan Zhi-bo, Gong Xiao-qing, Lu Dang-feng, et al. Surface plasmon resonance imaging sensor based on hue algorithm[J]. Chinese Journal of Liquid Crystals and Displays, 2017,32(5):402 -209.

[13] Pan Dafu, Wang Wei, Zhou Zhiqiang. Research on Mixed Programming Technology of Matlab and C/C++[J]. Computer Engineering and Design, 2009, 30(02): 465-468+521.

Detection and Analysis of Epileptic Seizure Based on Wavelet Transform and Modulus Maximum Approach

LIU Guangda; WANG Yimeng; HU Qiuyue; MA Mengze; CAI Jing
（jilin university instrument science and engineering institute,changchun,130021）

***Abstract*—Epilepsy is a chronic disorder of brain dysfunction caused by sudden abnormal discharge of brain neurons. The detection of epileptic seizure can be achieved by the detection and analysis of spike waves. In this paper, a method of detection based on wavelet transform and modulus maximum is proposed. First, it uses the continuous wavelet transform of epileptic eeg signals in a certain scale to divide the frequency bands. Second, it applys the modulus algorithm and refining algorithm to detect singular points of eeg signals, which are taken as the suspect points of spike waves. Finally, through screening based on power spectral density analysis and space surface fitting, the final characteristic spike waves are detected to determine whether the epileptic seizure occurres. The verification experimental results indicate the efficiency and reliability of the proposed method with a diagnostic accuracy as high as 92.5%. It provides a valuable reference method for epileptic seizure detection.**

***keywords*—epileptic seizure, eeg signal, wavelet transform, modulus maximum method**

I. INTRODUCTION

EPILEPSY is a chronic disease in which sudden abnormal discharge of brain neurons leads to transient brain dysfunction. Seizures are complex and variable due to the difference in the initial location and mode of transmission of abnormal brain discharge caused by epilepsy. They often manifest as paroxysmal movement, sensation, autonomic nerve, consciousness and mental disorder. The types of seizures can be divided into: comprehensive Attack, partial seizure, secondary generality. Seizure; clinical subdivision: comprehensive tonic - clonic seizures, absence seizures, tonic seizures, myoclonic seizures and other symptoms, often accompanied by varying degrees of disturbance of consciousness, muscle spasm, etc. as a chronic disease, long-term Frequent seizures lead to the physical and mental health of the patient, and the intelligence is seriously affected. Due to the sudden onset of epilepsy, the patient is prone to falls, burns, drowning, traffic accidents, etc. Epilepsy is a type of brain dysfunction, and patients with epilepsy may have memory disorders. Serious cognitive impairments such as decreased intelligence, personality changes, and finally gradual loss of ability to work and even life. In addition, the harm of epilepsy is also reflected in mental harm. People with epilepsy are often discriminated against by society, in employment, marriage, family life, etc. All aspects encountered difficulties, the patient was depressed, and physical and mental health was greatly affected in view of epilepsy. The prevalence and harmfulness of the disease, the pathogenesis of epilepsy, clinical detection and focal location have become the focus and difficulty of research.If your paper is intended for a *conference*, please contact your conference editor concerning acceptable word processor formats for your particular conference.

The diagnosis of epilepsy is mainly through clinical history and electroencephalography, and the spike is used as a characteristic wave of epilepsy. Its detection is decisive for judging whether it has epilepsy. In recent years, with the rapid development of signal analysis processing and computer-aided intelligent diagnosis technology in the medical field, research related to epilepsy has been promoted. (1) Using signal analysis to directly analyze EEG and find differences in certain parameters of EEG signals for prediction. For example, Manish N. Tibdewal [1] et al. based on variance and multiple entropy on epilepsy/non-epileptic brain The electrical signal is statistically analyzed to complete the detection and identification of epileptic EEG signals. Zhu Dongsheng [2] obtained the developed EEG features by performing nuclear magnetic resonance scanning on the patient's head and performing power spectrum analysis based on Fourier transform to compare with normal EEG signals. Xu Yaning [3] used the fast Fourier transform to compare the EEG signals of normal people and seizures, and identified the epileptic signals in the frequency domain. Wang Pengxiang [4] et al. used wavelet transform-based epilepsy EEG feature wave recognition algorithm to achieve signal analysis. Because EEG signals belong to multi-component non-stationary pseudo-random signals, Fourier transform has poor adaptability, so its The prediction accuracy is not high; (2) Using a signal analysis method and the machine Morteza Behnam [5] designed a seizure-specific wavelet based on the epileptic mode maxima model, which models the captured EEG signals. Through the past processing of AdaBoost classifier to detect and classify seizures. Shivnarayan Patidar and Trilochan Panigrahi [6] using TQWT-based Kraskov entropy analysis method for single feature detection of epileptic EEG signals, and using least squares support vector machine (LS-SVM) The classifier classifies epileptic and non-epileptic EEG signals. Zhao Jianlin [7] classifies normal EEG and epileptic EEG by wavelet analysis and support vector machine SVM classifier. Han Min [8] through the comparative analysis of EEG signals in the episodes of normal people and epilepsy patients, using

SVM method to classify to determine whether seizures occur. Li Muzhen [9] applied a method based on sample entropy and limit learning. After multi-layer wavelet decomposition of EEG signals, the required EEG signals were extracted and their sample entropy was used as the feature vector, and then the extreme learning machine algorithm was used. Classification identification. In the case of no fitting, the higher the dimension of the feature vector, the higher the classification accuracy of the algorithm, but the above method uses only one feature parameter. At the same time, the SVM and Extreme Learning Machine classification algorithms do not have a universal solution for nonlinear classification, so the accuracy is not very high.

Based on the above problems, this paper proposes a method based on wavelet transform and modulus maxima for epilepsy detection. Compared with classical algorithms such as SVM, the wavelet transform modulus maxima algorithm has higher accuracy and better detection results. The epilepsy EEG experimental data used in this study was derived from the CHB epilepsy database of the Massachusetts Institute of Technology.

II. EPILEPTIC FEATURE WAVE EXTRACTION

A. Epileptic characteristic wave of EEG signal

The human brain electrical signal is the overall reflection of the electrophysiological activity of the brain nerve cells on the surface of the cerebral cortex or scalp. EEG signals contain a large amount of physiological and disease information. In clinical practice, EEG signals are mainly divided into four frequency bands according to different frequencies, which are slow wave, alpha wave, fast wave and medium fast wave. Spikes and spikes are classified according to their waveforms that are significantly sharper than other parts of the signal. Spikes and spikes protrude from the background activity and are distinct from the waves and rhythms that form other background activities.

Typical epileptic waves consist of spikes, spikes, and slow waves. Common spikes, spikes, spine-slow complexes, and slow-slow complexes (see Figure 1).

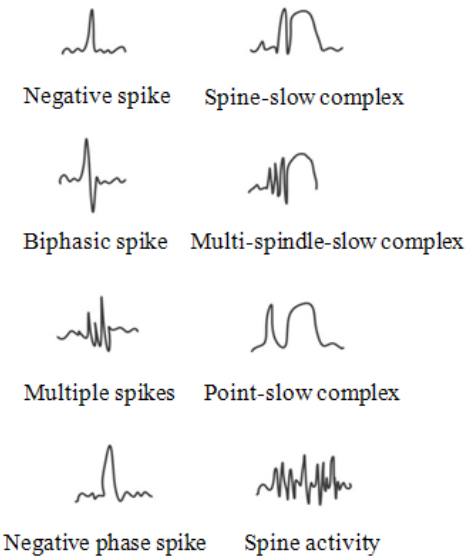

Fig. 1. Typical epilepsy EEG characteristic wave

B. Feature extraction

Wavelet analysis is a very effective signal time-frequency analysis method. It transforms the one-dimensional signal in the time domain into the two-dimensional space of time/scale, which has unique advantages for processing time-varying signals.

The continuous wavelet transform process (CWT) [11] can be expressed by:

$$W(a,b)=\frac{1}{\sqrt{a}}\cdot\int_0^T\left(\Psi\left(\frac{t-b}{a}\right)\cdot s(t)\right)dt \quad (1\text{-}1)$$

Where a is the transformation scale parameter, b is the time shift parameter, s is the original signal, t is the recording time, T is the length of the original signal, and Ψ(a, b, t) is the mother wavelet function. The matrix form Wa,b of the wavelet transform coefficients can be obtained by the following equation, where amax is the maximum transform scale:

$$W_{a,b}=W(a,b)|(a,b\in N)\wedge(a\in[1,a_{max}])\wedge(b\in[1,T]) \quad (1\text{-}2)$$

When the transformation scale a is small [3], the center frequency is higher, the bandwidth is wider, and the high frequency components in Wa and b are more; on the contrary, when a is larger, the center frequency is lower, the bandwidth is narrower, and the low frequency components in Wa and b are More. The spike is a relatively high-frequency component of brain waves, and its information is more likely to appear at a small scale.

The modulus maximal algorithm is an algorithm based on wavelet analysis. Based on wavelet analysis, the signal is singularly judged and analyzed. In this paper, the refinement algorithm is used to calculate the modulus maxima column [11]. The expression of the refinement algorithm function is:

$$LcMx_{a,b}=\begin{cases}1 \mid \frac{\partial(W(a,b))^2}{\partial b}=0\\ 0 \mid \neg(\frac{\partial(W(a,b))^2}{\partial b}=0)\end{cases} \quad (1\text{-}3)$$

a,b∈N^(a∈[1,amax])^(b∈[1,T]);

Ignore the local maximum of the "LcMx(a,b) | (T-a≤b)∨(b≤a)" gap and the corner, which has the following formula:

$$LcMx_{a,b}=\begin{cases}1 \mid (\frac{\partial(W(a,b))^2}{\partial b}=0)\wedge(a<b<T-a)\\ 0 \mid \neg(\frac{\partial(W(a,b))^2}{\partial b}=0)\vee(T-a\le b)\vee(b\le a)\end{cases} \quad (1\text{-}4)$$

a,b∈N^(a∈[1,amax])^(b∈[1,T]);

Finally, the wavelet modulus maximum coefficient can be obtained by the following formula, where Wabs is a matrix of absolute wavelet coefficients:

WTMMa,b=Wabsa,b*LcMxa,b (1-5)

a,b∈N^(a∈[1,amax])^(b∈[1,T]);

Combining the wavelet transform and the modulus maxima method, the small-scale wavelet modulus maximum coefficient WTMMai, b is selected as the characteristic wave. And because the scale a decreases, the wavelet window becomes narrower, the low-frequency component energy will gradually decrease, and the high-frequency component energy will not decrease. Therefore, by analyzing the variation of the wavelet modulus maximum value coefficients WTMMa,b at each scale, the suspected points of the spikes in the characteristic waves can be screened out, and the spikes and high-frequency components are separated.

II. EXPERIMENT ANALYSIS

To verify the validity of the algorithm, the epileptic EEG data used in this experiment was derived from the US authoritative CHB-MIT Scalp EEG Database (https://www.physionet.org/pn6/chbmit/) [12,13]. The database records EEG during epileptic seizures and records a total of 23 files from 22 subjects (5 males, 3-22 years old; 17 females, aged 1.5-19 years). All signals are sampled at a 256 Hz sampling rate with 16-bit resolution. Most files contain 23 EEG signals (in a few cases 24 or 26). In addition, the data record has been initially processed to remove noise such as environmental interference and eye-track interference, and the time node of the attack period has been marked and can be directly applied to epilepsy data analysis.

According to the statistics, the location of epileptic lesions is most common in the frontal and anterior, middle, and posterior regions of the electrode network. The corresponding electrodes are Fp1, Fp2, F7, F8, T3, T4, T5, T6 (using international The EEG electrode position of the 10-20 system has a total of 8 electrodes, so the data in the 8 electrodes is used for characteristic wave extraction in the experiment. The following experiment uses the Fp1 channel as an example.

First, the original EEG signal in the database is segmented into segments with a data length of 1024 data points. Wavelet analysis is performed on one of the sections, the decomposition order is 10, the sampling rate is 256, and the number of iterations is 6. The wavelet is based on db4 wavelet, and its mother wavelet function is shown in Figure 2.

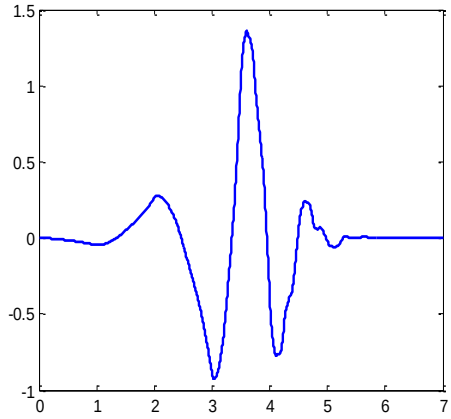

Fig. 2. Db4 mother wavelet function

After wavelet analysis, the channel Fp1 is taken as an example, and the results of the partial hierarchy are shown in Fig. 3.

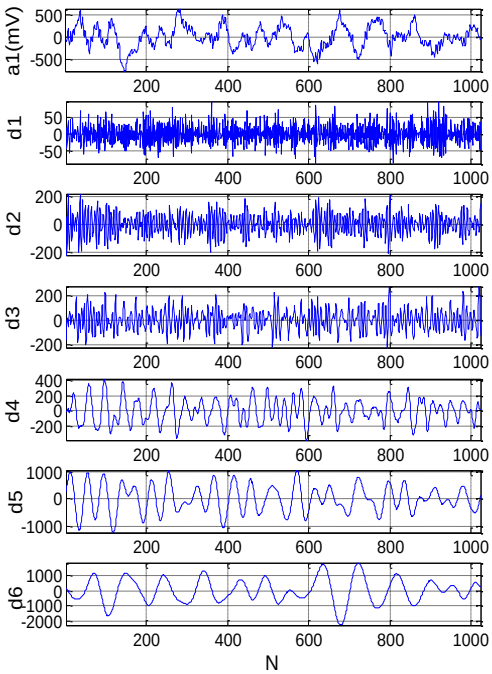

Fig. 3. Waveform analysis of partial levels after wavelet nalysis

Then, for each wavelet detail level in the wavelet transform result matrix, the modulus maximum value is calculated according to the steps of 2, and the singular point is tested by the formula (1-5) to obtain the modulus maximum wave train result as shown in Fig. 4.

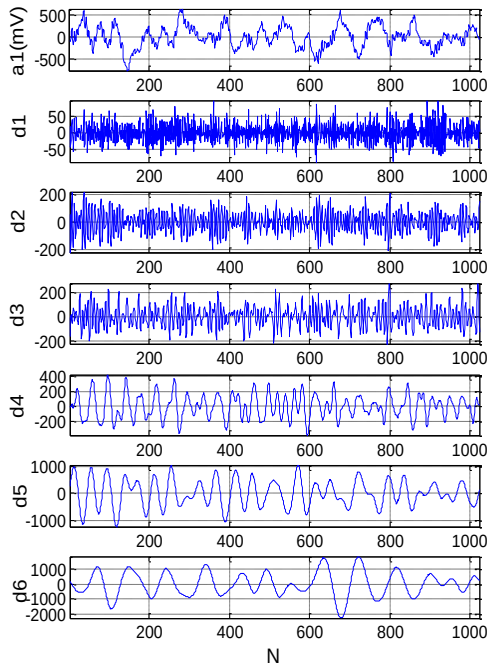

Fig. 4. Modulus maxima wave train waveform

Furthermore, the statistical analysis of the variation trend between the singular point mode maximum wave train bands is carried out to screen out the suspected spike value points. The recognition algorithm is as follows:

(1) Set a threshold ε>0, for 1≤a≤6, any point 1≤x≤1024, if |WTMM(a,x)|<ε, let WTMM(a,x)=0;

(2) For 1 ≤ a ≤ 6, let WTMM(a, 1) = WTMM(a, 1024) = 0, reduce the error rate of misjudgment caused by the inclusion of incomplete characteristic waves at the edge of the segment;

(3) Since the duration of the spike is mostly between 20 and 80 ms, combined with the sampling rate of the database, a large amount of information about the suspected point of the spike is more likely to appear on the three levels of d1, d2, and d3, so the characteristic wave is taken as :

D(x)=p1*WTMM(1,x)+p2*WTMM(2,x)+p3*WTMM(3,x), where p1, p2, p3 are distribution weights;

(4) Calculate the power spectral density column using the correlation method, and the autocorrelation function sequence of the (2Φ-1) point:

$$\hat{R}_D(\varphi) = \frac{1}{1024}\sum_{x=0}^{1023} D_N(x)D_N(x+\varphi)$$

(5) Power spectral density:

$$\hat{S}_D(e^{jw}) = \sum_{\varphi=-(\Phi-1)}^{\Phi-1} \hat{R}_x(\varphi)e^{-jw\varphi}$$

(6) Spatially fitting the composite wave train D(x) and the power spectral density column S^_D (e^jw) by moving least squares method;

(7) The curvature Hx and the curvature differential dHx of the fitting surface of the x-point are used to determine the contribution M(x) of the point to the high-frequency component in the interval [-θ, θ]. Set a threshold ω>0, if M(x)<ω, let D(x)=0;

(8) According to the waveform characteristics near the position of the suspected epileptic spike point obtained by the above detection: width, maximum slope, further determine whether it is a spike point, and finally select the spike value column Df (x).

The result of the fitted surface is shown in the figure below. Figure 5 shows the fitted surface of the suspected point of the spike, and Figure 6 shows the fitted surface of the suspected point.

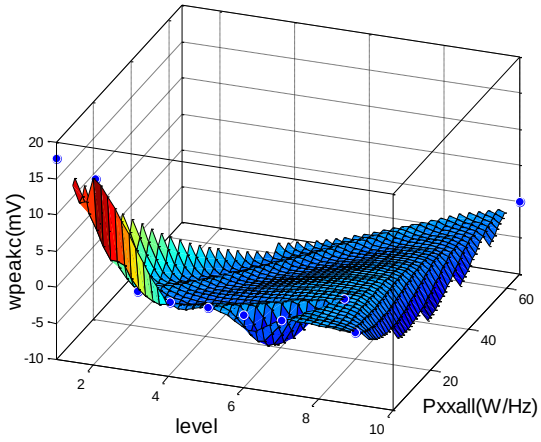

Fig. 5. Spike wave suspect point fitting surface

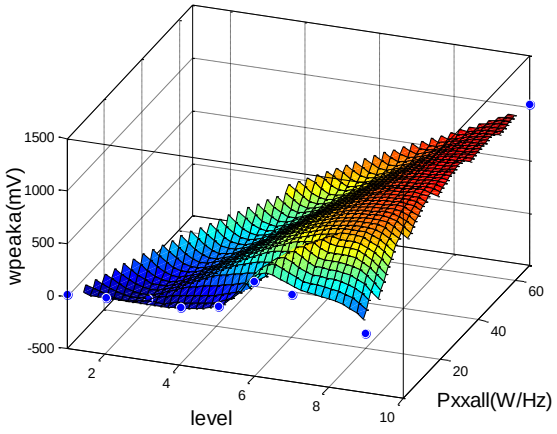

Fig. 6. Non-spike suspect point fitting surface

Finally, through the above part, the eigenvalue wave train is screened to obtain the detected spike value column, and the extracted spike value column is compared with the original EEG signal as shown in Fig. 7. The original EEG signal is derived from the 0.5p to 4.5s of the Fp1 channel in the Chb01/, 001 signal, and a total of 1024 samples. A is the spike value column extracted by the detection algorithm, and B is the original brain electrical signal.

The detection of brain electric spikes in 19 patients with epilepsy was divided into two data sets, the attack period and the interictal period, according to the state of the patient at the time of the test, and the high spike recognition rate was obtained. The results are shown in

Table 1.

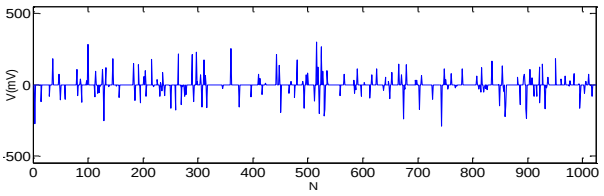

(A) Extracted spike value column

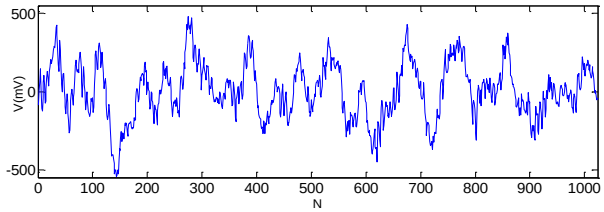

(B) Original EEG signal

Fig. 6. Comparison of the extracted spike value column with the original EEG signal

TABLE I
FALSE DETECTION RATIO OF 19 PATIENTS WITH EPILEPSY

Case	Status	Number of spikes	False Positive	Miss	False	False ratio (%)
01	attack	103	0	0	0	0
02	attack	106	6	2	8	7.5
03	attack	98	4	1	5	5.1
04	interval	0	0	0	0	0
05	attack	87	3	3	6	7.0
06	interval	0	0	0	0	0
07	attack	101	3	2	5	4.9
08	attack	91	3	1	4	4.3
09	attack	82	2	0	2	2.4
10	attack	94	1	3	4	4.2
11	attack	104	2	5	7	6.7
12	interval	1	0	0	0	0
13	attack	79	2	1	3	3.7
14	attack	103	4	2	6	5.8
15	interval	0	0	0	0	0
16	attack	95	0	1	1	1.0
17	attack	88	0	0	0	0
18	attack	102	2	1	3	2.9
19	interval	4	0	0	0	0

It can be seen from the above results that the wavelet transform-modular maximum value detection method can effectively detect the number of spike waves. For different EEG signals, the accuracy rate is different due to individual differences, interference and other factors. Compared with the number of spikes detected by experts, the accuracy rate is as low as 92.5% among the 19 samples. It can be seen that the system has strong ability to identify the position and number of spikes. The distribution of the number of spikes detected in the two datasets during the onset and interictal phases is shown in Figure 8. The statistical principle is used to analyze the variance data of the spikes. The results are shown in Fig. 9.

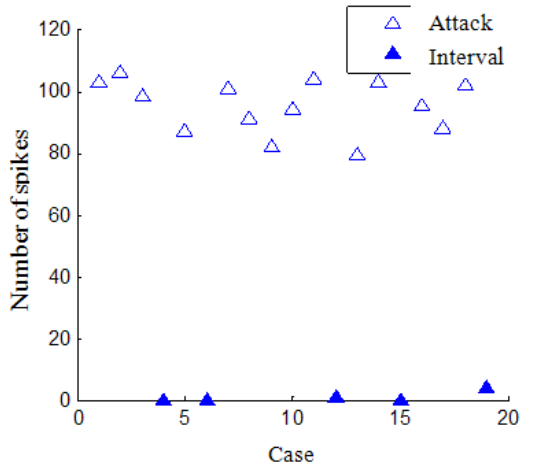

Fig. 8. The number of spikes measured during the attack period and the interictal interval

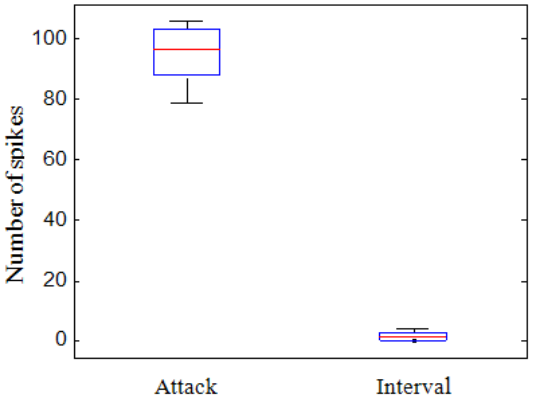

Fig. 9. Spiral number box line graph measured during the attack period and the interictal interval

By observing the spike number distribution map and the one-way variance analysis graph, the following conclusions can be drawn: for the fixed-length original signal, the number of spikes in the electroencephalogram signal detected by the system during seizure and interictal period is obvious. difference. The proportion of spikes in the epileptic seizures is significantly higher than that in the interictal period. The episodes and episodes can be separated. This confirms that the number of spikes detected by the system can be used as a basis for judging whether seizures occur.

II. CONCLUSION

In this study, the wavelet transform and the modulus maxima algorithm are combined to adapt to the non-stationary and multi-component characteristics of EEG signals.

The influence of parameters on EEG epilepsy signal, and in the modulus maxima method, the simple, efficient and high-precision algorithm of refinement function is used. Through analysis and experimental

verification, when the EEG signal is analyzed by wavelet analysis combined with the modulus maxima algorithm, the diagnostic accuracy is above 92.5%, and the effect is ideal.

This study can help doctors to better diagnose patients with epilepsy in clinical practice, and can help people with high risk of epilepsy to receive timely treatment from professional medical staff and reduce mortality. The next step is to locate the epileptic foci and to predict epileptic seizures as much as possible.

References

[1] Manish N. Tibdewal, Himanshu R. Dey, Manjunatha Mahadevappa, AjoyKumar Ray, Monika Malokar. Multiple entropies performance measure for detection and localization of multi-channel epileptic EEG [J]. Biomedical Signal Processing and Control, 2017, 38: 158-167.

[2] Zhu Dongsheng. Analysis of epilepsy signal and lesion location [D]. Yanshan University, 2016.

[3] Xu Yaning. EEG signal epileptic spike detection based on wavelet transform[J]. Journal of Guilin University of Electronic Technology, 2008, 28(03): 197-199.

[4] WANG Pengxiang,ZHANG Zhaoji.Study on EEG Echo Feature Wave Recognition Algorithm Based on Wavelet Transform[J].Information and Computer (Theoretical Edition),2017,17:63-65.

[5] Morteza Behnam, Hossein Pourghassem. Seizure-specific wavelet (Seizlet) design for epileptic seizure detection using CorrEntropy ellipse features based on seizure modulus maximas patterns [J]. Journal of Neuroscience Methods, 2017, 267: 84-107.

[6] Shivnarayan Patidar, Trilochan Panigrahi. Detection of epileptic seizure using Kraskov entropy applied on tunable-Q wavelet transform of EEG signals [J]. Biomedical Signal Processing and Control, 2017, 34: 74-80.

[7] ZHAO Jianlin, ZHOU Weidong, LIU Kai, CAI Dongmei.A classification method of EEG signals based on SVM and wavelet analysis[J].Computer Applications and Software,2011,28(05):114-116.

[8] HAN Min, SUN Zhuo-ran. Classification of epileptic EEG signals based on wavelet transform and AdaBoost extreme learning machine[J]. Journal of Computer Applications, 2015, 35(09): 2701-2705+2709.

[9] Li Muzhen. Study on automatic detection of epileptic EEG signals [D]. Zhengzhou University, 2014.

[10] Wang Chunmei. Research on feature extraction and automatic detection of epilepsy EEG signals [D]. East China University of Science and Technology, 2011.

[11] Andrejs Puckovs, Andrejs Matvejevs. Wavelet Transform Modulus Maxima Approach for World Stock Index Multifractal Analysis [J]. Information Technology and Management Science, 2012, 15: 76-86.

[12] Goldberger AL, Amaral LAN, Glass L, Hausdorff JM, et al. PhysioBank, PhysioToolkit, and PhysioNet: Components of a New Research Resource for Complex Physiologic Signals. Circulation .2018,101(23):e215-e220.

[13] Shoeb, Ali Hossam. Application of Machine Learning to Epileptic Seizure Onset Detection and Treatment [D]. PhD Thesis, Massachusetts Institute of Technology, September 2009

Research on five-axis teaching robot based on STM32

Yuyao Huang; Hangming Zhang
（*instrument science and engineering institute, Jilin university*）

***Abstract*-With the rapid development of industrialization, various types of robots have become a mainstream research direction in the world.At present, there are mostly large manipulator in market, and small five-axis drilling robot has not been popularized.The development of small five-axis teaching robot can better help students to learn the knowledge of mechanical and electrical control and improve people's understanding of robots.**

***Keywords*-Five-axis, manipulator, drill hole, control,mechanical**

INTRODUCTION

THE main purpose of this paper is to develop a small five-axis drilling robot, which can carry out some simple automatic drilling procedures, so as to facilitate simple operation and debugging[1].Combined with the existing small robot and the traditional robot structure design, we proposed the five-axis robot overall structure design scheme.In this paper, the kinematics analysis of the robot is carried out, so that the trajectory can be designed by adjusting relevant parameters and finally a fixed coordinate can be punched.

I.HARDWARE STRUCTURE DESIGN

The manipulator system consists of drive part, actuator, control system and power supply.The whole body is controlled by the control system for the motion of each joint, and the motion state of each joint is perceived through sensors to adjust and control the entire motion trajectory.The actuator---the terminal actuator, completes the corresponding tasks directly, and the actuator is driven by the power supply to provide the power for high-speed rotation of the borehole to achieve the purpose of drilling[2-3].The drive part completes the drive to each joint, that is, to provide the power to each joint and to complete the specified rotation Angle.The power supply provides energy input to the whole system.The overall structural framework of the five-axis robot is shown in figure 1.

The manipulator consists of five parts: waist, big arm, small arm, wrist and hand. It can complete five degrees of freedom.Between each joints respectively are connected by a TBS2701 steering gear, steering servo system can be made of variable pulse width to regulate driving moment rotation. Internal sensor reads the position of the motor driven rotational torque,and return the information to the motor control system. Internal servo motor control system connect to the STM32 motherboard, receiving the pulse input to control the movement and control servo motion state.

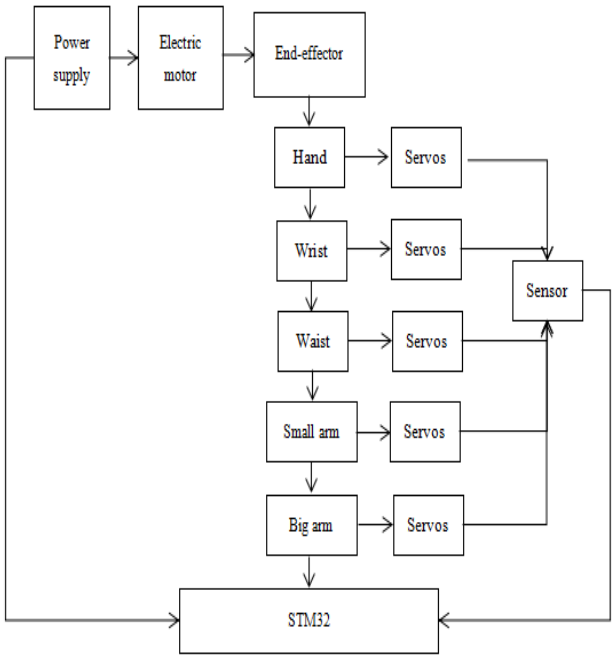

Fig. 1. Frame of mechanical hand structure.

II. THE DESIGN OF DRIVE MECHANISM

The rotation Angle of the steering gear is determined by the pulse length provided by the control line. This control method is pulse modulation. The period of most reference signals of steering engine is 20ms, and the width is 1.5ms.The rotation Angle and the position reached by the reference signal are taken as the middle position, and the specific Angle is set as the pulse of corresponding time according to the reference signal and the middle position[4].The control line is connected with STM32's multi-channel PMW to realize the signal output of the multi-channel steering gear controller.Combined with the communication control of the upper computer and the lower computer, the mechanical arm can be debugged.Upper computer communicates with stm32 through USB bus.Stm32 controls the output of the five road PWM steering gear.In addition, a certain action group can be stored in flash to control the robot arm to complete a certain motion trajectory so as to achieve the goal of positioning the end-effector to punch holes.Communications setting between the upper computer and the lower computer can directly complete set of mechanical arm movements and the

adjustment of the relevant parameters. And through the pulse modulation of STM32, it can complete relatively accurate drive control of the end of the actuator .

III.ROBOT KINEMATICS ANALYSIS

A. Robot kinematics

Kinematics consists in solving the motion trail of mechanical arm, and it consists of forward kinematics and reverse kinematics. Forward kinematics is the study of how robots judge oneself's position in space by using some own states [5]. The inverse kinematics is the study of how the robots move to change some of the state to achieve the specified location.

The relative position of each adjacent link in the D-H coordinate can be represented by the matrix:

$$H_{\mathrm{i}} = \begin{matrix} A_i & -B_i A_{\alpha i} & B_i B_{\alpha i} & a_i A_i \\ B_i & A_i A_{\alpha i} & -A_i B_{\alpha i} & a_i B_i \\ 0 & B_i & A_i & d_i \\ 0 & 0 & 0 & 1 \end{matrix} .$$

H_{i} Is the relative position of each adjacent connecting rod, and $A_{\mathrm{i}} = \cos\theta_i; B_i = \sin\theta_i; A_{\alpha_i} = \cos_{\alpha i}; B_{\alpha i} = \sin_{\alpha i}$. And θ is the joint variable.αi is the joint torque.ai is the length of the rod.di is the distance between two links. According to the position matrix of each adjacent link, the position matrix of the end-effector relative to the base can be obtained-- $H = H_1 \bullet H_2 \bullet H_3 \bullet H_4 \bullet H_5$. According to different robot systems, the relevant parameters can be obtained by measuring and viewing respectively.In the end, only θ is a variable, that is, different robot trajectories can be obtained by changing each joint variable, that is, different spatial positions of end-effector[6].Inverse kinematics is to obtain the corresponding joint variables according to the given spatial position, and then complete the process by driving control.According to inverse kinematics, there are given spatial coordinates

$$H_{\mathrm{g}} = \begin{matrix} n_x & o_x & a_x & p_x \\ n_y & o_y & a_y & p_y \\ n_z & o_z & a_z & p_z \\ 0 & 0 & 0 & 1 \end{matrix}$$

,then there is the formula H= H_{g} and five joint variables --θ can be obtained. The pulses were modulated according to the obtained joint variables and output the corresponding length of the pulses . The coordinate position can be determined by the communication between the upper computer software and the lower computer.

B.Simulation verification based on simulink

The five-degree-of-freedom manipulator is basically connected according to the hardware structure diagram in the Simlink, and the resolution between the five joints is connected by five rods. Each joint is driven by the Actuator joint, represented by Actuator in Simulink, and input signals are added to control the joint variables of each joint to control the trajectory of the manipulator arm.In order for each joint to display its spatial position and some parameters, it is necessary to add joint sensors at the joint and connect Scope module so that it can open a workspace in matlab to observe its data[5]. The final output connecting to Scope and the x-y waveform are displayed to observe the final waveform of the end-effector.Figure 2 shows the simulation diagram.

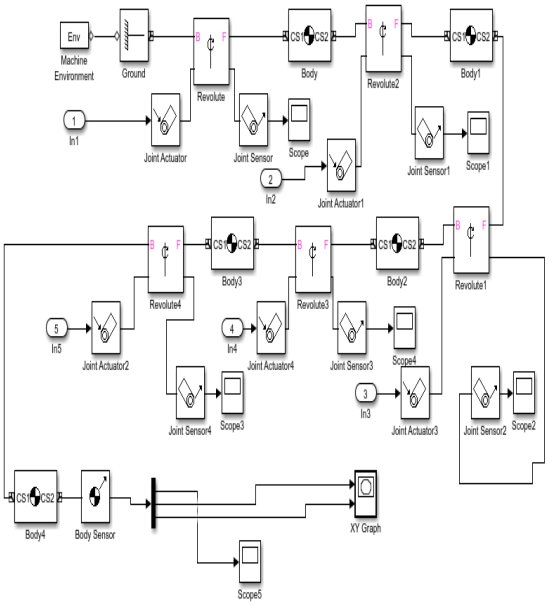

Fig. 2. the simulation diagram.

According to the established simulation model of the robot, the kinematics simulation analysis of the robot can be realized by setting analysis types in the simulation environment. After setting the distance between the connecting rods of the robot, we can set the joint rotation Angle 1 and 2 to be 90 degrees, and other angles to be 0 degrees, and solve the problem according to the inverse kinematics of the robot.The expected effect is a straight line in the x, y plane.By setting the input initial parameters and using simulink, the movement track of the end-effector is shown in the figure.The results are basically consistent with the calculation results.Therefore, according to the inverse kinematics solution, the joint Angle can be set to make the end-effector move to a fixed position.

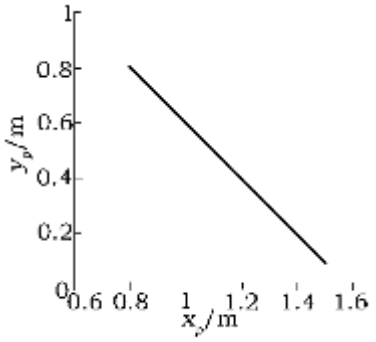

Fig.3 The movement track of the end-effector

IV.THE CONCLUSION

On the basis of STM32, a simple five-axis drilling manipulator is designed and controlled briefly.Based on the communication between PC upper computer and PC lower computer, the control of manipulator is completed based on pulse modulation.The precise positioning of the manipulator refers to the kinematics of the robot and Simulink is used to simulate its spatial position.The study completes simple control and positioning of the manipulator, and it can find a certain position and punch holes under the set procedure.

References

[1] Liu Shichuan, Deng Jihao, Zhan Yinyu, ye yong. Design and control method of small manipulator based on STM32 [J]. Journal of detection and control,2017,39(02):19-23.

[2] Xia Yifei. Development of small five-axis robot [D]. Xihua university,2015.

[3] Mao Li. Design and simulation of stacking and transporting robot mechanism [D]. Nanjing forestry university,2014.

[4] Pang Shujuan, Ni Shoudong. Kinematics analysis and simulation of 5-dof teaching robot [J]. Modern manufacturing engineering,2007,(06):126-128.

[5] Zhang Xiaochao, DongYuhong. Robot kinematics simulation based on MATLAB/Simulink [J]. Modern manufacturing engineering,2005,(S1):61-62.

[6] Wang Lumin, Li Yanwen. Simulation of space motion trajectory of teaching robot based on Matlab [J]. Mechanics and electronics,2005,(09):55-57.

Three – component magnetic measurement apparatus on water surface based on magnetoresistive sensor

TANG hui; XIAO rui; ZHANG zai-yi
(College of Instrumentation and Electrical Engineering, Jilin University, Changchun 130021, China)

***Abstract*—Electronic system of water surface three-component magnetometer based on magnetoresistive sensor, gyroscope, high-precision ADC, GPS module, WIFI module, STM32 microprocessor was designed. The sensor module, the attitude measurement module, the signal acquisition module and the software were given. The three-component magnetic measurement apparatus can detect the magnetic anomaly of the underwater ferromagnetic material through the dragging work on the water surface, and has the advantages of small volume, low power consumption and high precision.**

***Key words*—Magnetoresistive sensor; Three-components; Gesture correction; LabVIEW**

0 INTRODUCTION

MAGNETIC exploration is an important branch of geophysical exploration. It can utilize the magnetic differences of underground rock ore to detect underground geological structures, find mineral resources and solve hydrological, engineering geological problems and environmental monitoring[1]. In recent years, the exploration of oceans and the detection of the seabed environment have received more and more attention. The application of magnetic exploration to water can achieve the purpose of searching for underwater abandoned munitions, locating aircraft wreckage, finding underwater vessels, purifying waters and so on.

Magnetic field measurements are broadly divided into total field measurements and vector measurements. With the increasing requirements of geological prospecting and geological engineering problems, the traditional single field magnetic survey can no longer meet the geological exploration requirements, vector measurement can obtain more abundant geomagnetic information, and effectively reduce the multi-solution in inversion. It can help quantitative interpretation of magnetic bodies, improve the detection resolution and positioning accuracy of underground ore bodies, and become one of the main development directions of geophysical magnetic exploration.

At present, the magnetic measuring device is mainly divided into two basic types: proton precession type and optical pump type, but only the total field measurement can be performed and is greatly affected by the magnetic field gradient[2].The three-component water surface magnetic measuring device designed in this paper uses the magnetoresistive sensor as the magnetic probe to measure the magnetic field vector. Compared with the proton precession type and the optical pump type magnetic measuring device, it can obtain rich magnetic field parameters, and has the advantages of small volume and low cost. The device is capable of wireless data transmission and has the advantages of high efficiency, high speed and large data volume.

1 HOW THE SYSTEM WORKS

The system uses an anisotropic magnetoresistive sensor HMC1001/1002 to form a three-axis magnetoresistive sensor as a magnetic probe of a magnetic measuring device for magnetic field signal detection; using a high-precision and high-sensitivity AD7799 for signal acquisition and processing;using STM32 as a microprocessor to process and analyze signals At the same time, the gyro MPU6050 is used as the attitude measurement module to correct the deflection angle during the magnetic probe travel, so that the magnetic probe is continuously measured in the correct direction; the GPS module is used to read the geographical position of the magnetic probe; finally, all the measurements are performed by using the WIFI module. The data is transmitted to the host computer to complete the measurement of the three-component magnetic field strength of the underwater ferromagnetic material. The measurement results are stored and comprehensively analyzed by the host computer software. The block diagram of the three-component water surface magnetic measuring device designed in this paper is shown in Figure 1.

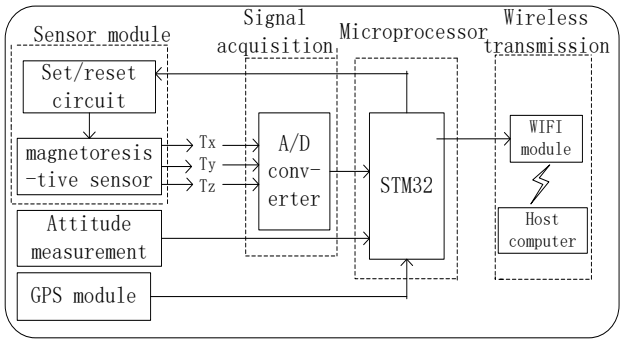

Fig. 1.System block diagram

2 HARDWARE CIRCUIT DESIGN

2.1 Sensor module design

The sensor module consists of a magnetoresistive sensor and a set/reset circuit. The HMC1001 and the

HMC1002 are perpendicular to each other to form a three-axis magnetoresistive sensor. The magnetic field measurement of the underwater ferromagnetic material is completed by measuring the magnetic field strength of the x, y, and z axes in the carrier. The magnetic field measurement range is ±2 Gs. In order for the HMC1001/1002 to achieve higher resolution of the magnetic field in the 2 Gauss range, a set reset (S/R pulse) circuit is designed to eliminate magnetic domain interference in order to achieve high sensitivity and repeated reading requirements. The sensor probe structure is shown in Figure 2.

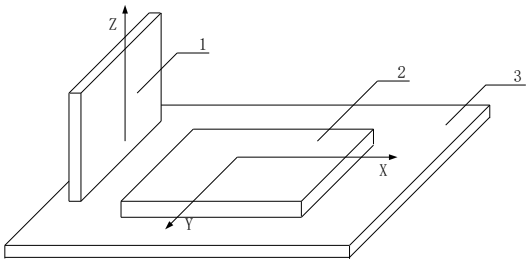

Fig. 2.Sensor probe structure

In the figure, 1 - HMC1001; 2 - HMC1002; 3 - carrier.

2.2 Attitude measurement module design

The attitude measurement module of the device mainly uses the MPU-6050 as a magnetic probe terminal to record the change of the attitude angle of the magnetic probe during the movement of the water surface, and transmits the data to the microprocessor for analysis and subsequent algorithm processing, thereby completing the three-axis operation. Angle measurement and attitude correction of the attitude ensure that the magnetic measuring device obtains more accurate magnetic measurement data. The principle circuit of the attitude measurement module is shown in Figure 3.

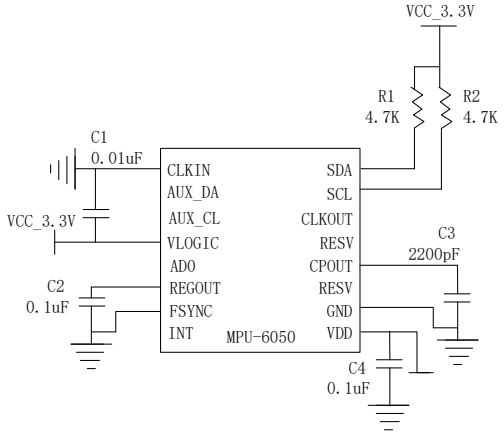

Fig. 3.Schematic circuit diagram of attitude measurement module

2.3 Signal acquisition module design

In order to ensure the high-precision and high-sensitivity characteristics of the three-component magnetometer, a high-precision AD chip should be selected. In this paper, the 24-bit high-precision Σ-Δ AD7799 is used as the signal acquisition. The low-noise instrumentation amplifier is integrated inside, so the measured signal does not need to be sent to the amplifier circuit again. The three differential analog inputs contained in the internal are matched. The three-channel signal output of the HMC1001/1002 enables simultaneous data acquisition, while its self-calibration function eliminates the effects of zero error and temperature drift. The A/D conversion circuit diagram is shown in Figure4.

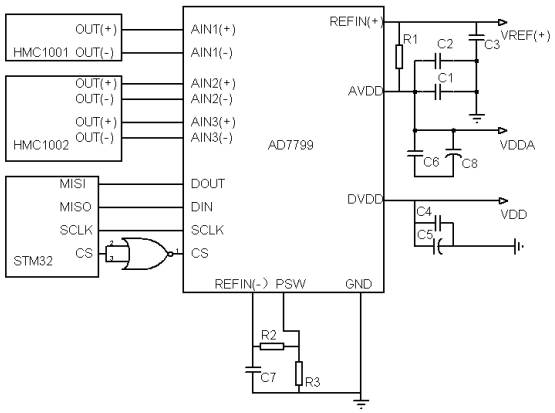

Fig. 4.A / D conversion circuit diagram

The three-axis magnetoresistive sensor and the AD analog power supply are powered by a +3.3V power supply. The external reference power supply Vref is divided by two precision resistors to form a proportional sampling circuit. To reduce the interference of the digital part to the analog part, the digital power supply of the AD can be used + 5V power supply.

2.4 Attitude correction algorithm design

Since the towed surface magnetic probe travels on the water surface, deflection due to changes in water flow and wind direction may occur. To ensure the accuracy of the magnetic field measurement, attitude measurement and attitude correction must be performed in time. The main methods for solving common attitudes are: Euler method, direction cosine method and quaternion method. Compared with the other two methods, the quaternion method is more suitable for the three-axis input, and its calculation accuracy is high, the real-time performance is good, and the theory is perfect. Therefore, the device uses the quaternion method for attitude measurement and correction [3].

The system uses the quaternion-based attitude solution to obtain the attitude angle of the carrier. The basic idea of the quaternion is: The multiple rotation of a coordinate system around the coordinate axis can be equivalent to rotating a certain angle around a certain rotation axis. You can use a quaternion q to indicate the direction of the shaft and the size of the corner.

$$q = q_0 + q_1 i + q_2 j + q_3 k \quad (1)$$

(1) Quaternion initialization

The initial angle of the carrier can be calculated from a high-precision compass, and the initial attitude angle pitch angle θ0 and the yaw angle ψ0 roll angle γ0 of the carrier relative to the geographic coordinate

system are obtained.

$$\begin{bmatrix} q_0 \\ q_1 \\ q_2 \\ q_3 \end{bmatrix} = \begin{bmatrix} \cos\frac{\psi_0}{2}\cos\frac{\theta_0}{2}\cos\frac{\gamma_0}{2}+\sin\frac{\psi_0}{2}\sin\frac{\theta_0}{2}\sin\frac{\gamma_0}{2} \\ \cos\frac{\psi_0}{2}\cos\frac{\theta_0}{2}\sin\frac{\gamma_0}{2}-\sin\frac{\psi_0}{2}\sin\frac{\theta_0}{2}\cos\frac{\gamma_0}{2} \\ \cos\frac{\psi_0}{2}\sin\frac{\theta_0}{2}\cos\frac{\gamma_0}{2}+\sin\frac{\psi_0}{2}\cos\frac{\theta_0}{2}\sin\frac{\gamma_0}{2} \\ \sin\frac{\psi_0}{2}\cos\frac{\theta_0}{2}\cos\frac{\gamma_0}{2}-\cos\frac{\psi_0}{2}\sin\frac{\theta_0}{2}\sin\frac{\gamma_0}{2} \end{bmatrix} \quad (2)$$

(2) Quaternion update

The essence of updating quaternions is to solve quaternion differential equations.

$$\frac{dQ(t)}{dt} = \frac{1}{2}Q(t)w(t) \quad (3)$$

Where $\omega = 0 + \omega_x\vec{i} + \omega_y\vec{j} + \omega_z\vec{k}$, ωx, ωy, and ωz are the original triaxial angular velocity data output by the MPU6050. Write the above formula into a matrix form, you can get:

$$\begin{bmatrix} q_0' \\ q_1' \\ q_2' \\ q_3' \end{bmatrix} = \frac{1}{2}\begin{bmatrix} 0 & -w_x & -w_y & -w_z \\ w_x & 0 & w_z & -w_y \\ w_y & -w_z & 0 & w_x \\ w_z & w_y & -w_x & 0 \end{bmatrix}\begin{bmatrix} q_0 \\ q_1 \\ q_2 \\ q_3 \end{bmatrix} \quad (4)$$

There are many solutions to the quaternion differential equations, such as the Runge-Kutta algorithm, the Newton method, and the Pika algorithm[4]. According to the accuracy requirements of the Microcontrollers, the second-order Runge-Kutta method has higher precision and less calculation.

$$\begin{cases} K_1 = \frac{1}{2}w(t)q(t) \\ K_2 = \frac{1}{2}w(t+\Delta t)[q(t)+\Delta t\cdot K_1] \\ q(t+\Delta t) = q(t)+\frac{\Delta t(K_1+K_2)}{2} \end{cases} \quad (5)$$

(3) Substituting the second-order Runge-Kutta equation into the quaternion differential equation is:

$$\begin{bmatrix} q_0(t+\Delta t) \\ q_1(t+\Delta t) \\ q_2(t+\Delta t) \\ q_3(t+\Delta t) \end{bmatrix} = \begin{bmatrix} 1 & -\frac{w_x}{2}\Delta t & -\frac{w_y}{2}\Delta t & -\frac{w_z}{2}\Delta t \\ \frac{w_x}{2}\Delta t & 1 & \frac{w_z}{2}\Delta t & -\frac{w_y}{2}\Delta t \\ \frac{w_y}{2}\Delta t & -\frac{w_z}{2}\Delta t & 1 & \frac{w_x}{2}\Delta t \\ \frac{w_z}{2}\Delta t & \frac{w_y}{2}\Delta t & -\frac{w_x}{2}\Delta t & 1 \end{bmatrix}\begin{bmatrix} q_0 \\ q_1 \\ q_2 \\ q_3 \end{bmatrix} \quad (6)$$

Then normalize the differential equation:

$$q_i = \frac{q_i}{\sqrt{\hat{q}_0^{\,2}+\hat{q}_1^{\,2}+\hat{q}_2^{\,2}+\hat{q}_3^{\,2}}} \quad (7)$$

Where $\hat{q}_0\ \hat{q}_1\ \hat{q}_2\ \hat{q}_3$ is the updated quaternion.

(4) Transformation of quaternion and Euler angle:

The pitch angle θ、 yaw angle ψ and roll angle γ can be obtained by the inverse function of Equation 1.

$$\begin{cases} \theta = -\arcsin\left(2(p_1p_3 - p_0p_2)\right) \\ \psi = \arctan\left(\frac{2(p_1p_2 - p_0p_3)}{p_0^{\,2}+p_1^{\,2}-p_2^{\,2}-p_3^{\,2}}\right) \\ \gamma = \arctan\left(\frac{2(p_2p_3 - p_0p_1)}{p_0^{\,2}+p_3^{\,2}-p_1^{\,2}-p_2^{\,2}}\right) \end{cases} \quad (8)$$

Correction matrix C: pitch angle θ、yaw angle ψ and roll angle γ.

$$C = [T_1 \quad T_2 \quad T_3] \quad (9)$$

$$T_1 = \begin{bmatrix} \cos\psi\cos\theta \\ \cos\psi\sin\theta\sin\gamma - \sin\psi\cos\gamma \\ \cos\psi\sin\theta\cos\gamma + \sin\psi\sin\gamma \end{bmatrix} \quad (10)$$

$$T_2 = \begin{bmatrix} \sin\psi\cos\theta \\ \sin\psi\sin\theta\sin\gamma + \cos\psi\cos\gamma \\ \sin\psi\sin\theta\cos\gamma - \cos\psi\sin\gamma \end{bmatrix} \quad (11)$$

$$T_3 = \begin{bmatrix} -\cos\theta \\ \cos\theta\sin\gamma \\ \cos\theta\cos\gamma \end{bmatrix} \quad (12)$$

3 SOFTWARE DESIGN

3.1 Microcontroller software design

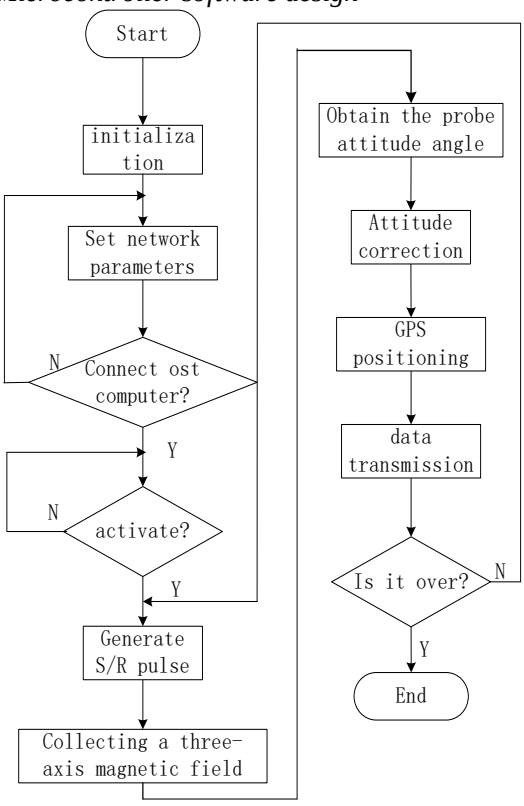

Fig. 5. Microcontroller Software Flow Chart

The lower part of the device adopts STM32 as the microprocessor of the magnetic measuring device, which has the advantages of high performance, strong real-time performance, low power consumption, convenient low-voltage operation, and easy development. The microprocessor module works closely with other modules. For example, the attitude measurement module measures the real-time data of the magnetic probe on the surface of the water: the acceleration and angular velocity of each axis, and the attitude angle of the probe is sent to the microcontroller through the quaternion attitude solution algorithm. The signal acquisition module converts the magnetic field analog quantity measured by the magnetic probe into a digital quantity and sends it to the microprocessor module, and the microprocessor module transforms the three components of the magnetic field of the carrier coordinate system into a geographic coordinate system through the three-dimensional rotating coordinate transformation. The wireless transmission module performs remote display[5].Similarly, the real-time accurate positioning obtained by the GPS module can also be analyzed and processed by the wireless transmission module to the mobile terminal or the computer. The lower machine software flow chart is shown in Figure 5.

3.2 PC software design

The upper computer software of the magnetic measuring device is realized by LabVIEW programming. The software has the functions of connection and startup with WIFI, network port parameter setting, geographic location of magnetic measuring device, attitude angle display, magnetic field strength waveform display and data storage.

The control interface of the three-component water surface magnetic measuring device based on the magnetoresistive sensor is mainly composed of a control area and a display area.The control area mainly includes the operation buttons and network port parameters of the system.The display area includes real-time measurement values of the magnetic field strength, continuous recording waveforms,attitude angles,and the geographic location of the magnetic measurement device.The LabVIEW host computer interface is shown in Figure 6.

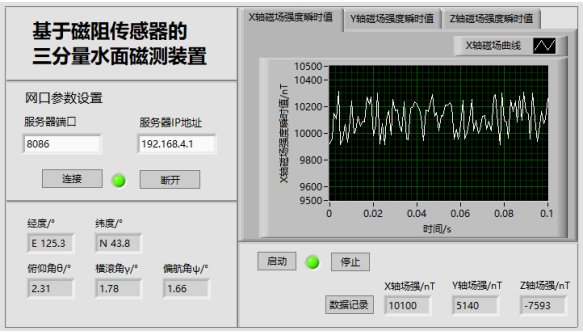

Fig.6. LabVIEW Control Interface

The x-axis magnetic flux density in the LabVIEW host computer interface refers to the measured value of the magnetic flux density in the north direction of the magnetic measuring device; while the y-axis magnetic flux density refers to the measured value of the east direction ; the z-axis magnetic flux density refers to the measured value of the Downward direction.

4 EXPERIMENTAL RESULT

4.1 Test results and analysis

The system parameter test was tested in a laboratory environment at a temperature of 25.10 ℃. The 1m long signal shielding line is used to connect the magnetic probe to the microprocessor to reduce the interference of the spatial magnetic field signal. The measured data of the measured magnetic measurement system are shown in Table 1.

TABLE I System parameter test

Performance parameter	Typical value	unit
Sensitivity	20	nT
Linearity	2.3n	%FS
Linear measu-rement range	-200000—+200000	nT
Operating temperature	-35—+85	℃
Working power consumption	0.6	W

4.2 Field test

The three-component water surface magnetic measuring device based on the magnetoresistive sensor mainly relies on the surface drag measurement to detect the magnetic field distribution of the underwater ferromagnetic substance. Next, an experiment is performed to eliminate the fixed magnetic field, and the three-component magnetic anomaly value of the ferromagnetic substance is determined.

In a magnetically shielded laboratory, a square sink of 100 cm x 100 cm x 100 cm was taken and water was injected until the water level reached 80 cm. A cylindrical magnet having a diameter of 3.2 cm and a height of 0.6 cm was placed in a water tank for experimental measurement. The magnetic measurement test measurement diagram is shown in Figure 7 and Figure 8.

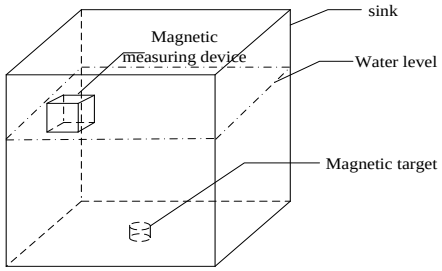

Fig.7. a three-dimensional schematic diagram of the magnetic test

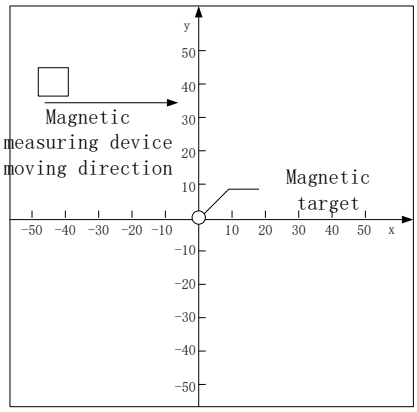

Fig.8. Schematic diagram of magnetic test

In the experiment, the parallel movement from the edge of the center of the sink began with 5cm as the moving unit until it moved to the other edge. A total of 20 sets of data were measured. After repeated measurements, the data was processed by matlab.The three component magnetic anomaly values are taken as the vertical coordinates while the distance as horizontal coordinates.And the magnetic field distribution map is plotted as shown in Fig. 9.

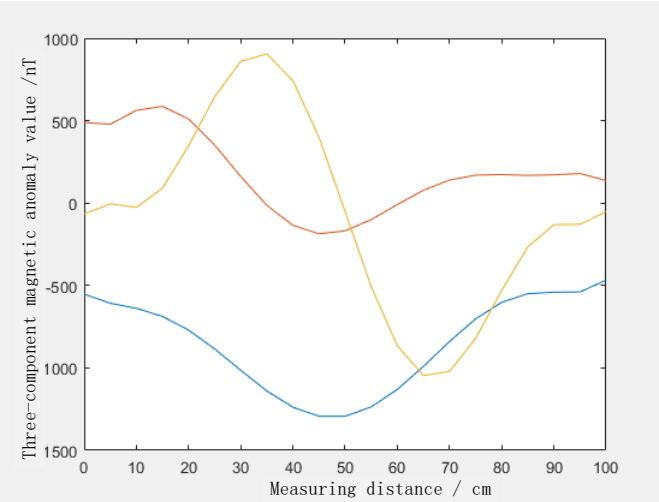

Fig. 9 .Magnetic field distribution

Under the MFC framework, three-dimensional imaging is drawn, and the obtained data is consistent with the data of Fig.9, indicating that the magnetic measuring device can provide effective normal magnetic anomaly data.

5 IN CONCLUSION

This design of the three-component means a water-based magnetic magnetoresistive sensor, by measuring the water drag achieved in three-component magnetic field data acquisition geographic coordinate system, the magnetic range of up to ± 2Gs; using a wireless transmission module record and transmit magnetic field value in real-time, and the continuous working time can reach 24h; the S/R pulse circuit is used to improve the working precision, and the magnetic measurement sensitivity is better than 20nT. In addition, the magnetic measuring device is small in size and extremely portable, and can conveniently and reliably perform surface magnetic measurement work.

The device can realize magnetic field detection of underwater ferromagnetic substances, and can transmit experimental data to the mobile phone terminal or the computer end remotely. This is also important for the detection of underwater magnetic materials and the detection of underwater magnetic field distribution.

References

[1] Huang Kongyao, Zhang Xueting, Zhou Qiaozhen, Tang Yong. Electronic System Design of Three-component Magnetometer for Offshore Bottom[J]. Instrumentation Technology and Sensors, 2009(07): 26-29.

[2] Wu Xiuwen, Zhang Songyong, Xue Yimeng. Research on Three-component Magnetometer Based on Fluxgate and Acceleration Sensor[J].modern electronic technology,2013,36(22):96-98

[3] ZHANG Ronghui, JIA Hongguang, CHEN Tao, ZHANG Yue. Attitude calculation of strapdown inertial navigation system based on quaternion method[J].Optics and Precision Engineering,2008(10):1963-1970.

[4] Zhang Mengying,Zeng Cheng,Di Susu,Wang Yunrui.Inertial positioning algorithm based on multi-sensor filtering fusion[J].Application of Electronic Technique,2017,43(10):86-88+98.

[5] Wu Dengyun. Development of magnetoresistive three-component magnetometer [D]. Jilin University, 2009.

Design of Visual Evoked EEG Acquisition and Color Resolution System

Wang Ziang; Dong Zequn; Song Hongzhen; Cai Jing;
(College of Instrumentation & Electrical Engineering, Jilin University)

***Abstract*-This paper designs a set of high-standard brainwave acquisition system through OPENBCI open source experimental platform, and designs an experimental paradigm of color recognition through the study of color imaging EEG signals, and collects different colors of EEG under different prompt information. signal. The processing is performed by different color EEG signals, and the feature signal is used as the source signal, and the Euclidean distance, PCA and other algorithms are used for feature extraction. Through SVM, Ensemble Bagged Trees and other machine learning algorithms for learning classification, and finally achieve good experimental results, that is, generally applicable to most people, thus achieving color resolution.**

***Keywords*- EEG signals; feature extraction: machine learning; color resolution**

I. INTRODUCTION

THE brain-computer interface is a device that converts electrical signals collected from the human brain into control commands and directly transmits them to a computer or other machine [1]. Its function is to establish an AC control channel independent of the human brain and electronic devices. It can effectively help deaf people with severe physical disabilities. Studying brain-computer interface has important effects and significance for brain research, physiological research and clinical disease diagnosis [2]. Brain-computer interface research involves neuroscience [3], signal detection, Signal processing, control implementation and many other areas. In the past few decades, the research and development of BCI technology has been very rapid, and as an emerging technology, it is receiving more and more attention.

The obvious use of BCI technology is to provide a new type of compensation function and external information exchange for those who have normal thinking but lack of motor function. At present, neuromuscular disorders, including cerebral palsy, multiple sclerosis, spinal cord injury, amyotrophic sclerosing and muscle dystrophies affect 2 million to 3 million people in the United States alone, and more in the world [4]. Many of them do not need an auxiliary information exchange device, and most of the rest can use one or several of the traditional auxiliary devices currently available (synthesizing input devices such as speech synthesizers, joysticks or mice, keyboard intensifiers) , suction switch, etc.). For most users, the speed and accuracy of these traditional devices is better than the EEG-based information exchange under current development conditions.

II. SYSTEM DESIGN

This paper introduces an open source experimental platform based on OPENBCI and a color resolution system based on MATLAB pattern recognition to realize the function of judging the color seen by the human eye by analyzing signals. The design hardware circuit has a simple structure, and is divided into two modules: an electroencephalogram induction module, an EEG acquisition module, and a communication module. The software structure is divided into two parts: signal processing module and EEG resolution human-computer interaction module. The EEG inducing module uses the OLED display as the stimulator, and the EEG signal acquisition module selects the OPENBCI open source experimental platform based on the ads1299 chip and the four-channel EEG acquisition device, and the communication module uses Bluetooth communication. The signal processing module uses MATLAB for signal filtering and feature extraction for machine learning. The human-computer interaction module uses an OELD display to display data.

III. EEG SIGNAL ACQUISITION

A. EEG-Evoked Stimulator

According to the frequency of the stimulation signal, the visual evoked potential can be divided into the steady-state visual evoked potential SSVEP and the transient visual evoked potential TSVEP [5]; the former refers to the visual stimulation mode with a frequency less than 2 Hz; the latter uses the visual stimulation frequency higher than 4Hz. When the frequency is less than or equal to 2 Hz, the stimuli appear one after another, and when the second stimulus occurs, a series of stimuli in the cortex disappear, and the VEP waveform we are studying is a steady-state visual evoked potential. The detection of visual evoked potentials is an important approach to visual function research [6]. The effects of different visual evoked potentials depend on different stimulation times and frequencies. The visual stimulator is an important part of the brain-computer interface system. Through stable and reliable visual stimulation, the action potential generated by the human brain will become stable, which is also the action potential we need. The experimenter stares at the flash, which causes eye strain and interferes with the results of the experiment, so this article needs to choose a soft stimulator as a stimulus. So we use the computer's display screen 10hz to flash as a stimulator.

B. EEG Signal Acquisition

We use the OPENBCI open source experimental platform based on ADS1299 to collect EEG signals for us. The OpenBCI open source experimental platform is an open source brain-computer interface device with moderate price, but zero drift and low temperature drift, and the signal-to-noise ratio is very high. He can be used to collect EEG EEG in different situations of 1-8 channels, which has a more convenient experience. It can also acquire four-channel, six-channel and eight-channel low-noise, 24-bit simultaneous sampling with a delta-sigma analog-to-digital converter. The open source lab platform includes a programmable gain amplifier (PGA), an internal reference, and an onboard oscillator. And the chip ADS1299 has all the usual functions required for extracranial electroencephalography (EEG) and electrocardiogram (ECG) applications. With its high level of integration and performance, the ADS1299 is capable of building scalable medical instrumentation systems with significantly reduced size, significantly reduced power consumption and overall cost [7].

C. EEG Signal Transmission

The signal transmission part uses the Bluetooth module as a communication module, and the Bluetooth module is a PCB board integrated with Bluetooth function, used for short-range wireless communication, and is divided into a Bluetooth data module and a Bluetooth voice module according to functions. The Bluetooth module refers to the basic circuit set of the integrated Bluetooth function [8], which is used for wireless network communication and can be roughly divided into three types: the data transmission module remote control module. The general module has semi-finished properties and is processed on a chip basis to make subsequent applications simpler. The process of subject brain wave acquisition is shown in Figure 1.

Fig.1 Subject's process of brain wave acquisition

IV. SIGNAL PROCESSING

A. Signal Preprocessing and Feature Extraction

The signal processing part is all based on MATLAB. First, we first perform signal preprocessing. Because the EEG signals we collected were induced by 10hz light, we performed a bandpass filter of 6-14hz to analyze the specific signal of SSVEP at 10hz.

Secondly, the signal feature extraction is performed. The most accurate algorithm we use is Mean Absolute Deviation. The Chinese translation is the average absolute deviation. The calculation method of Mean Absolute Deviation reverses this proper noun [9]. First calculate the deviation deviation, then turn the negative number into a positive number (absolute value) Absolute, and then calculate the average number Mean. The formula for calculating the simple average difference is as follows:

$$A.D. = \frac{\sum |X - \overline{X}|}{n}, \quad (1)$$

Where A.D. is the average difference; X is the flag value; $\bar{x}$ is arithmetic mean; $|x - \bar{x}|$ is absolute deviation; n is the number of items.

The weighted average difference is calculated as follows:

$$A.D. = \frac{\sum |X - \overline{X}| f}{\Sigma f}. \quad (2)$$

The main feature of the average absolute dispersion is that it is not affected by extremely large or extremely small values. At the same time, its calculations make use of all observations. At last. Its absolute value is somewhat difficult to handle. There are two effects of the average absolute dispersion. The first one is that the average difference calculation is simple and clear. The second is the average difference, which can include the difference of the mark values of all the units in the whole, which more accurately reflects the degree of dispersion of the overall unit mark values.

In addition to the average absolute dispersion, we also use a variety of feature extraction algorithms, using Euclid Distances, Frequency Magnitude, Frequency Ratio, IQR, Kurtosis Feature, Maxfreq, Mean, Median, PCA, Quantile[10] and other features. The extracted algorithm.

B. Classification of EEG signals

After feature extraction, this paper uses these features to classify various EEG signals. We use a linear SVM support vector machine [11]. This algorithm machine learning algorithm is the best for classifying EEG signals [12]. . Specifically, for the second-class classification problem, the training set T={(x1,y1),(x2,y2),⋯,(xN, yN)}， its category yi∈{0,1}，The linear SVM learns to get the separated hyperplane:

$$w \cdot x + b = 0 \quad (3)$$

And the corresponding classification decision function:

$$f(x) = \text{sign}(w \cdot x + b) \quad (4)$$

Therefore, there is a separation hyperplane as shown in Figure 2:

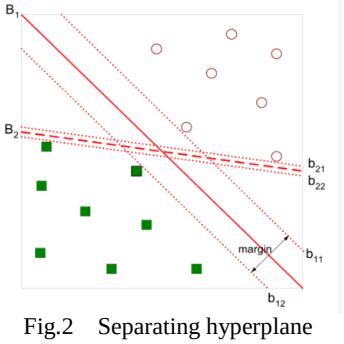

Fig.2 Separating hyperplane

Intuitively, the classification of hyperplane B1 is better. The two different categories of sample points closest to the separated hyperplane are called support vectors, and two long bands parallel to the separated hyperplane are formed. The distance between the two is called margin. Obviously, the margin is bigger, and the confidence in the classification is higher. It is easy to get by calculation:

$$\text{margin} = \frac{2}{||w||} \quad (5)$$

It can be observed from the above figure that sample points other than margin do not contribute to the determination of the separation hyperplane. In other words, the SVM is determined by a very important training sample (support vector). At this point, the SVM classification problem can be described as maximizing all classifications. 2/|(|w|)|（Equivalent to minimization 1/2*（|(|w|)|）） 2； Constrained optimization problem for linear classification:

$$\text{s.t. } yi(w \cdot xi+b)-1 \geq 0 \quad (6)$$

Introducing Lagrange multipliers for each inequality constraint$\alpha i \geq 0, i=1,2,\cdots,N$； construct a Lagrangian function:

$$L(w,b,\alpha) = \frac{1}{2}|w|^2 - \sum_{i-1}^{N} a_i y_i (w \cdot x_i + b) - 1 \quad (7)$$

According to the Lagrangian duality, the original constrained optimization problem can be equivalent to the extremely small dual problem, and L(w,b,α) is biased to w and b and equal to 0. Substituting into the Lagrangian function (3), the dual problem becomes much simpler, equivalent to the optimization problem:

$$s.t. \sum_{i=1}^{N} \alpha_i y_i = 0 \quad (8)$$

$$\alpha_i \geq 0, i = 1,2 \ldots N \quad (9)$$

In addition to support vector machines, we also use machine learning algorithms such as Bagged Trees and KNN for color classification recognition [13].

V. INTERACTION INTERFACE

Finally, we created a human-computer interaction interface for displaying brainwaves and displaying the results of the final signal processing. We use C# as a programming language to design a human-computer interaction interface [14]. C# is an object-oriented, high-level programming language that runs on the .NET Framework [15]. It is scheduled to appear on the Microsoft Professional Developer Forum (PDC). C# is the latest achievement of Microsoft researcher Anders Hejlsberg. C# seems to be strikingly similar to Java; it includes procedures such as single inheritance, interfaces, almost the same syntax as Java, and compilation into intermediate code. But C# is significantly different from Java. It draws on one of Delphi's features and is directly integrated with COM (Component Object Model), and it is the protagonist of Microsoft's .NET windows network framework.

The C# language abstraction hierarchy is high and basically only one (object-oriented), the runtime supports rich (garbage collection, etc.), and the class library is rich. Therefore, it is eager to learn, easy to use, while taking into account the operational efficiency, try to optimize. C# is similar to Java. After compilation, it is not the machine code, but the meta-command running in the virtual machine. It has made more considerations for security, no pointers, no direct manipulation of memory, and automatic memory management.

The human-computer interaction interface can display the waveform of the EEG signal, and can adjust the size, and can also display the result of the classification and judgment of the last EEG signal. The specific finished product of the human-computer interaction interface is shown in Figure 3.

Fig.3 C# human-computer interaction interface

In order to select different calling methods according to different needs in the later stage, we have created two ways of connecting human-computer interaction interface with MATLAB. The first way is to use MATLAB and C# mixed programming method, you need to use pupple to generate a dll file from MATLAB [16], and then reference it in C# form program. This method is very strict on C# and MATLAB versions. Very strict requirements, the version of .NET is required to be no larger than the .NET version of the dll file generated by MATLAB, so sometimes there are many errors involved in the program to modify. In C# programming, the dll file that is called can be used as a CLASS to achieve the target [17], and the second is to open the MATLAB file directly.

VI. TEST RESULTS

We allowed the subjects to experiment in a dark, sound-proof environment that collected EEG signals from subjects who saw different color stimulators that were 10hz flashing. We collected a total of 1080s red, green and blue SSVEP EEG signals, preprocessed these signals, and then extracted their features with more than ten different feature extraction algorithms, and put them into the machine learning model for training. Finally, using another signal to judge, the feature extraction algorithm machine learning algorithm and the results obtained are shown in Table 1.

Table 1 Test result table

Feature Type	Classifier Type	Accuracy
Euclid Distances	Simple Tree	54.00%
Frequency Magnitude	Complex Tree	42.80%
Frequency Ratio	Ensemble Bagged Trees	53.30%
IQR	Cubic SVM	95.40%
Kurtosis Feature	Ensemble Boosted Trees	61.20%
Maxfreq	Linear SVM	37.20%
Mean	Fine Gaussian SVM	65.10%
Mean Absolute Deviation	Fine Gaussian SVM	98.10%
Median	Quadratic SVM	68.10%
PCA	Ensemble Subspace KNN	86.70%
Quantile25	Cubic SVM	75.90%
Quantile75	Fine Gaussian SVM	79.10%
Shannon Entropy	Ensemble Bagged Trees	76.10%
Skewness	Ensemble Bagged Trees	55.90%
Spectral Entropy	Medium Gaussian SVM	43.20%
Standard Deviation	Ensemble RUSBoosted Trees	96.30%
Svd	Ensemble Bagged Trees	89.40%

It can be seen from the above diagram that some feature extraction algorithms and machine learning algorithms have higher matching, so the learning efficiency and classification effect of machine learning algorithms are better, and the accuracy is higher. However, some machine learning algorithm learning features and feature extraction algorithms are not so good, so the machine learning algorithm is less accurate in classification. When we actually use it, we should select several groups with higher accuracy to continue the test.

VII. CONCLUSION

From the above experiments, for the commonly used extraction algorithm and machine learning algorithm, the combination of Mean Absolute Deviation and Fine Gaussian SVM has higher recognition accuracy and stability than other operators; the accuracy of recognition color can reach 90 %, the system effectively recognizes the colors as red green and blue, the flicker frequency is 10hz, and the recognition detection time is less than 3s, which has high accuracy and stability. The expanded work can be applied to embedded systems for faster color classification.

References

[1] Yan Jingyan. Information Dimensions and Interaction Design Principles [J]. Packaging Engineering, 2018(16): 57-68.

[2] He Chao, Tang Wenhui, Ping Yazhen, Chen Wenjin, Huang Cheng, Xu Lei. Research on augmented reality technology and its educational training status [J]. Electronic World, 2018 (15): 13-15.

[3] Jiang Lei, Zhang Hai, Zhang Wei, Wu Wei, Sun Qicun, Li Haibin.Analysis of the Evolution of Brain-Computer Interface Research and Knowledge Mapping of Educational Application Trends——Based on the Research of SCI and SSCI Journals in 1985-2018[J]. Journal of Education, 2018, 36 (04): 27-38.

[4] Chen Liusong, Yang Li, Zhang Yu, Liu Li. Mixed Programming Technology and Application of C# and Matlab Based on .NET Assembly[J].Control and Information Technology,2018(02):44-46+64.

[5] Cao Yan. Research on micro-electric stimulation information feedback and neural information reduction in implantable brain-computer interface [D]. Zhejiang University, 2016.

[6] Tang Anzang1, Luo Rong2, Dong Xiaoli3, Liu Wei1. Application of multifocal visual evoked potentials in children with cerebral palsy[J/OL]. West China Medical Journal, 2016(06):1-6[2018-08-24].http://kns.cnki.net/kcms/detail/51.1356.R.20160614.2243.010.html.

[7] Zhang Rui. Auxiliary research on brain-computer interface function for severely disabled people [D]. South China University of Technology, 2016.

[8] Wang Jiang, Zhang Huiyuan, Li Fang, Zhang Bingwen, Li Peng.Study on semi-supervised learning algorithm in brain-computer interface[J].Electronic Measurement Technology,2014,37(05):9-12.

[9] Xie Hong, Li Yanan, Xia Bin, Yao Nan. Front-end design of wearable EEG signal acquisition system based on ADS1299[J].Application of Electronic Technique, 2014, 40(03): 86-89.

[10] Li Chenggang, Zhao Jiabao, Chen Zhaorong.Application of Visual C# and Matlab Mixed Programming in Visualization Software[J]. Software, 2012, 33(02): 78-79+83.

[11] Hou Bingwen. Feature extraction and pattern classification of motion imaging brain-computer interface [D]. Xidian University, 2012.

[12] Ye Ning. Key Technology and Experimental Research of Brain-Computer Interface Based on EEG Signal [D]. Northeastern University, 2010.

[13] Huang Anhu. Classification and identification of P300EEG evoked potential and its application in brain-computer interface [D]. Shandong University, 2008.

[14] Lu Jinglei. Classification of P300 EEG Signals Based on Support Vector Machine [D]. Northwestern Polytechnical University, 2005.

[15] Dong Guojun. Research on Bluetooth wireless communication technology and its application [D]. Tianjin University, 2004.

[16] He Qinghua. Experimental study of brain-computer interface based on visual evoked potentials [D]. Chongqing University, 2003.

[17] Zhou Jixian. Clinical identification of neuromuscular dysmotility in sheep[J]. Foreign Veterinary Medicine. Livestock and Poultry Diseases, 1996(02): 28-30.

Research on Bluetooth-based Unwired Dynamic Electrocardiograph

Zhou Lu-jia; Duan Rong-zhou; Dong Wei-hao

(College of Instrument science and Electrical Engineering, Jilin University, Changchun 130026,China)

***Abstract*——In order to monitor ECG(Electrocardiograph) signal of sub-healthy people in a real-time way, the research used the integrated chip of ads1191 to collect two heart signals(RA and LA),which was transmitted to the MSP430F2132 via SPI and then to the computer by Bluetooth technology. The required heart rate was obtained by using low-pass filter to eliminate interference signal, and using the second order difference method to monitor the position of R wave in the ECG waveform. Instead of using lead wire between Electrode patch and electrocardiograph, this research avoids interference caused by it effectively, and meets the needs of daily wear for its smaller size and lower power. Under the battery power supply of 1000mAh, the system can work continuously for 48h, ensuring the wearer's normal data transmission within the range of 3-4m.**

***Key words*——medical equipment; dynamic electrocardiograph; SPI; Bluetooth technology; second-order difference; no lead wire.**

I.PREFACE

BECAUSE the heart disease has features of suddenness, is difficult to cure, and the risk of heart disease population increased greatly[1], Long term monitoring of ECG has important clinical value. Dynamic electrocardiograph is a kind of instrument which can be worn and recorded for a long time for clinical diagnosis. However, the traditional ECG monitoring equipment is large and expensive[2]. Patients need to connect many lead wires with monitoring devices to obtain the desired ECG signals. The presence of lead wires leads to inconvenience to patients, especially at home. In addition, as the patient's actions will lead to the electrode paste's loosening or falling off, which will cause some interference or interrupt the recording of ECG signal and affect the quality of the collected signal[3].

This paper presents a design of a dynamic electrocardiograph based on Bluetooth technology and without lead wire to improve some problems of traditional dynamic electrocardiograph. The transmission and reception of ECG signals can be realized by wireless transmission instead of the traditional lead wires. It avoids the above problems caused by the pulling of the traditional lead wires, and fully consider for patients, so that the patients can monitor the ECG at anytime and anywhere in their normal work and life.

II. SYSTEM OVERALL STRUCTURE DESIGN

The Bluetooth-based unwired dynamic electro-cardiograph has the following modules: Electrode paste connection module, ECG acquisition module, main control unit module, wireless transmission module and power management module. The whole instrument structure is shown in Figure 1. Two ECG signals (RA and LA) are collected by ECG acquisition chip ADS1191. The chip is connected with micro-controller through SPI transmission mode. After analysis and processing by microcontroller MSP430, ECG signal is sent to data receiver (such as computer) through Bluetooth module for storage analysis ECG signal (such as heart rate, alarm and location of R wave).

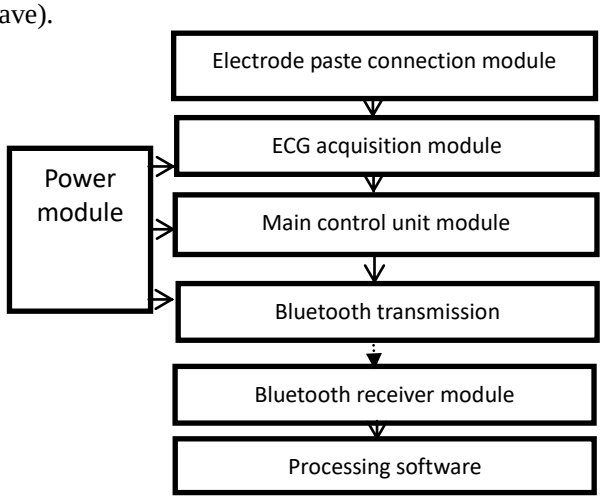

Fig.1 Block diagram of the whole system structure

Note: RA: Fourth intercostal spaces at the right border of sternum; LA: Fourth intercostal spaces at the left border of sternum[4];

III. HARDWARE CIRCUIT DESIGN

A. ELECTRODE PASTE CONNECTION MODULE

The AgCl electrocardiogram electrode was selec-ted with a diameter of 55mm.

B. ECG ACQUISITION MODULE

ECG acquisition circuit generally includes preamplifier circuit, filter circuit, main amplifier circuit, level boost circuit and AD conversion circuit. The preamplifier amplifies the signal differently, the filter eliminates baseline drift and power frequency noise, and the main amplifier and the level boost circuit amplify the signal further[5]. But considering the portability requirement of the system, we choose the high integration level chip ADS1191.

ADS1191 provides a highly flexible input multiplexer for each channel that can be tested independently of the internally generated signals. It covers an area of about 5mm * 5mm, and each channel has a power of as low as 335μW. It includes all the functions required for portable, low-power medical electrocardiograms, exercise and fitness applications, such as high gain, high input impedance, high CMRR(Common Mode Rejection Ratio), low noise, and low drift.

C. MAIN CONTROL UNIT MODULE

For wearable ECG devices such as dynamic electrocardiograph, power consumption and volume are the two most important considerations in chip selection[6]. Because MSP430F2132 has a total of 28 pins and smaller size in the same series of Microcontrollers, which meet the requirements of portability of design products, so choose this type of microcontroller as the main control unit. Its wiring diagram with ADS1191 is shown in Figure 3.

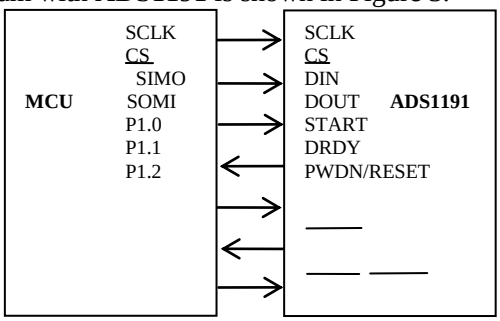

Fig.2 Schematic diagram of connection between main control module and ADS1191

MSP430F2132 communicates with ADS1191 in SPI mode, and selects P3.1, P3.2, P3.3, as SPI communication interface (because only for ADS1191, chip selection signal can not be connected), the START pin of P1.0 of MCU is set to high level to start the conversion. Read DRDY pin from P1.1 to low level, indicating that data conversion is complete and waiting to read data. PWDN/RESET is chip reset / sleep pin.

D. BLUETOOTH TRANSMISSION MODULE

Bluetooth technology is a low-cost wireless transmission application technology supporting short distance communication[7]. The PW-01 Bluetooth module with low power consumption mode is selected, and its connection with MSP430 is shown in Figure 3. The P3.4 of MSP430F2132 is connected to the receiving and sending ports corresponding to P3.5 and Bluetooth module. The P3.4 and P3.5 of MSP430F2132 are connected to the receiving and sending ports of Bluetooth module.

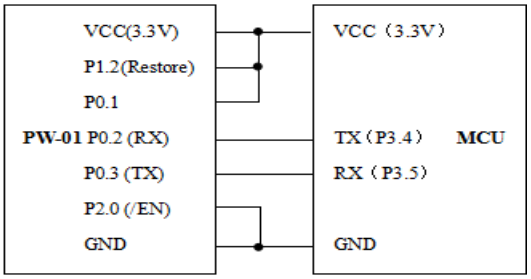

Fig.3 Schematic diagram of connection between Bluetooth module and master control module

E. BLUETOOTH RECEIVER MODULE

The PW-01 Bluetooth module is connected with the USB To TTL module to transmit the received data to the PC.

Connect the PW-01 P1.2 with VCC to enable the Bluetooth module to work, and the PW-01 P2.0 with GND to make the Bluetooth module work properly (instead of in low power mode).

F. POWER MANAGEMENT MODULE

Based on the following advantages, lithium battery power supply is used:

(1) High specific energy: high storage energy density, that is, more power stored in unit volume. The required battery is small in size and suitable for wearable portable devices under the same power requirements.

(2) Long service life: slower performance.

(3) It has good safety performance and low working environment requirements[8].

IV. SYSTEM SOFTWARE DESIGN

A. SYSTEM SOFTWARE FLOW CHART

After the system is powered on, the ECG acquisition chips ADS1191, SPI and Bluetooth are initialized. Then the command is sent by MSP430F2132 to make ADS1191 start acquisition. The data is amplified and filtered by ADS1191. The collected ECG signals are transmitted to MCU by SPI communication mode. The collected ECG signals are processed by MSP4302132 again and sent by serial port. In order to ensure the success of Bluetooth connection, the data is sent to the PC for signal processing and waveform drawing. In order to achieve low power consumption of the whole system, the transmission and reception of ECG data are triggered by interruption. The system software flow chart is shown in Figure 4.

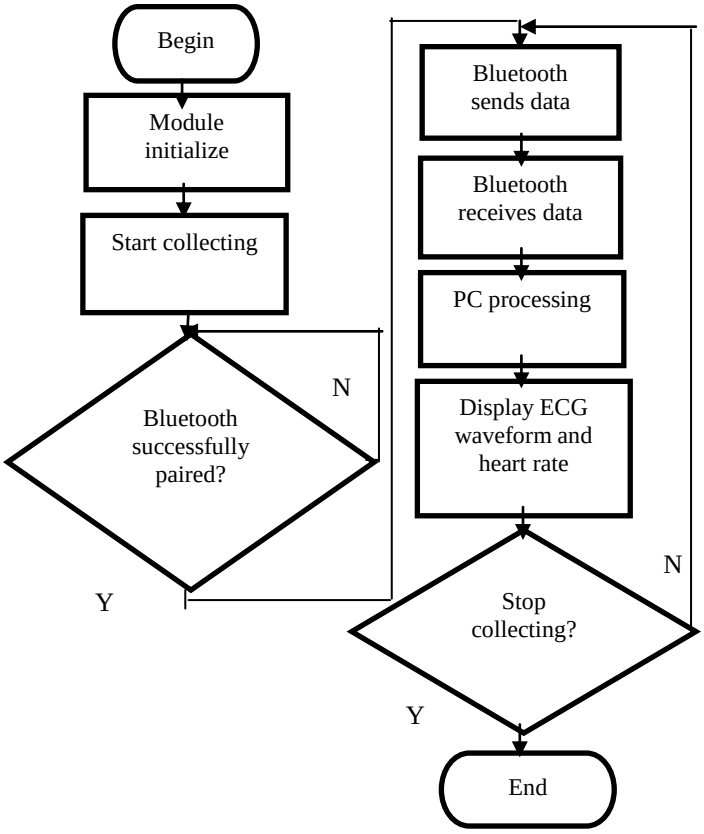

Fig.4 System software flow chart

B. ADS1191 FLOW CHART

The initialization operation is carried out according to the ADS1191 official chip manual. The ADS1191 initialization flow chart is shown in Figure 6. Internal clock is used here. ADS1191 has two reading modes: (1) RDATAC (Read data continuously): when running this mode, the register only needs to be set once, and no subsequent reconfiguration is required. This mode converts the data into the output register and can be directly removed. (2) RDATA (Read data): between the conversion cycles, we need to change or read register values. Because it is necessary to continuously collect ECG signals to observe the characteristics of ECG signals, continuous reading mode is adopted.

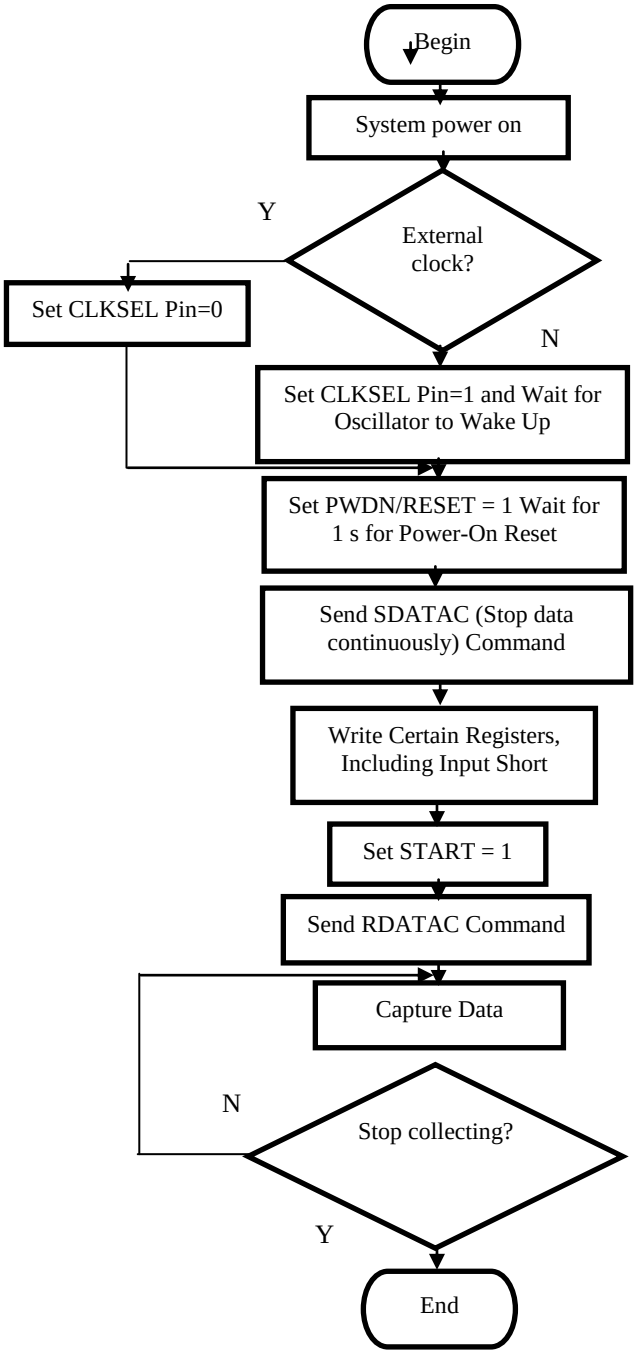

Fig.5 Initial flow chart of ADS1191

Note: According to the Chip Manual, the above instructions will take a certain clock cycle to take effect after they are sent, so there is a need to increase the delay between instructions.

V. ECG SIGNAL PROCESSING DESIGN

LabVIEW is a graphical software development platform with test and measurement as its main application. It provides a simple, convenient and user-friendly development environment for engineering research[9].

LabVIEW development software tools need three parts, namely the program front panel, block diagram program and icon / connection port. The function of the program front panel is the same as that of the real instrument front panel, and can set values and display output data on the program front panel, while the control and display icons can appear on the front panel; block

diagram program consists of nodes and data connections, equivalent to the source code of traditional programs; icon /connection port equivalent The parameters of subroutines in traditional programming languages.

A. FILTERING POWER FREQUENCY INTERFERENCE

By analyzing the spectrum of ECG signal, we can get the frequency components of ECG signal in each waveform: QRS waveform in 3-40HZ band, P wave and T wave in 0.5-10HZ band[10]. Because the system is portable and does not consider the right leg drive connection, it only needs to accurately detect the required the number of R wave and other information to calculate the heart rate, so it can not consider the impact of baseline drift, only need to consider the main interference: power frequency interference.

Power frequency interference is caused by electromagnetic radiation around the measuring environment. The main component of electroma-gnetic radiation interference is 50HZ power frequency. To sum up, a low pass filter with cut-off frequency of 45HZ is used to filter power frequency interference.

B. DETECTION OF R WAVE LOCATION

In the whole electrocardiogram, R wave is the most obvious and easy to identify, and the basic function of dynamic electrocardiograph - heart rate detection, is based on the number of R waves, therefore, the detection of the position of R wave is very important.

The main methods used in R-wave position detection are differential threshold method, wavelet transform method and neural network[11]. Among them, the differential threshold method is widely used for its advantages of fast computation and easy implementation. The basic idea is that the position of the highest point of R-wave corresponds to the position of the second-order difference minima. The minimum points of the second-order difference in a period of time are calculated and the search interval of R-wave is determined according to these minima. The maximum amplitude of the signal searched in this interval is the location of R-wave[12]. Each location of the R wave is combined into an array so as to get the number of R waves in a period of time.

C. HEART RATE CALCULATION

Heart rate (heart beats per minute) is calculated mainly by the number of R waves detected and the time taken to detect them. According to the heart rate of the normal people, the heart rate is too fast or slow to give an alarm.

VI. EXPERIMENTAL RESULTS AND ANALYSIS

The system uses LabVIEW as the upper computer. The front panel of the system is shown in Fig. 6. The ECG waveform and heart rate can be displayed normally, and it has the alarm function when the heart rate is not in the normal range.

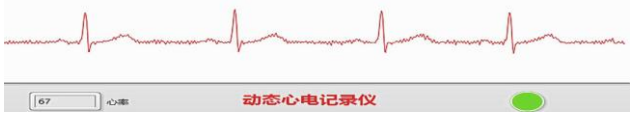

Fig.6 Upper computer software

In order to compare the differences more clearly, it is concluded that the heart rate of two testers (A, B) was measured at different time intervals (morning, noon and evening) by this system and Myrie iMEC 10 ECG monitor. The results are shown in Table 1 and Table 2.

TABLE 1
Heart rate test comparison of A tester

Tester	Test time	Test instrument	Heart rate	Error
A	morning	Instrument1	72	1.36%
		Instrument2	73	
	noon	Instrument1	75	0
		Instrument2	75	
	evening	Instrument1	74	1.33%
		Instrument2	75	

TABLE 2
Heart rate test comparison of B tester

Tester	Test time	Test instrument	Heart rate	Error
B	morning	Instrument1	78	2.50%
		Instrument2	80	
	noon	Instrument1	85	1.16%
		Instrument2	86	
	evening	Instrument1	82	1.20%
		Instrument2	83	

Note: instrument 1 indicates the system, instrument 2 indicates Myrie iMEC 10 ECG monitor.

According to Table 1 and Table 2 and the physiological condition of the human body, the heart rate is the lowest at the beginning of the morning, normal at noon, the brain begins to rest at night, heart rate will also be reduced. The design system can complete the normal heart rate calculation, and the error between the system and the Myrie iMEC 10 ECG monitor is less than 2.50%.

Tests show that when Bluetooth is connected in 3.3V mode, the current measured by milliampere meter is 12.41mA, ADS1191 and MSP430F2132 is 8.35mA, totaling 20.76mA. The system is powered by batteries with a capacity of 1000mAh, which can ensure uninterrupted operation within 2 days. Using Bluetooth 4.0 communication protocol, the transmission distance within 3-4m without data loss, to ensure that in the scope of family activities, anytime and anywhere ECG monitoring.

VII. CONCLUSION

This design starts from the user wear experience and focuses on the low power consumption and portability of the whole system. By choosing the low-power chip MSP430F2132 and PW-01 Bluetooth module to realize the low-power consumption of the system; By choosing the small-volume function module and using RA and LA as the two inputs of ECG acquisition chip ADS1191 to realize the portability of the system; the upper computer software achieves the drawing of ECG waveform , the display of heart rate and the alarm function of abnormal heart rate.

The whole system realizes the basic function of ECG with a simplified structure. Under the power supply of 1000mAh battery, the system can work continuously for

48h, which can ensure the normal data transmission within the range of 3-4m and meet the needs of daily wear. However, due to the reasons of welding technology and filtering, the collected ECG waveform still has a small amount of burr, and there is a small deviation in heart rate calculation, which needs further optimization and improvement.

REFERENCE

[1] Chen Wei-wei, Gao Run-lin, Liu Li-sheng, Zhu Man-lu, Wang Wen, Wang Yong-jun, Wu Zhao-su, Li Hui-jun, Gu Dong-feng, Yang Yue-jin, Zheng Zhe, Jiang Li-xin, Hu Sheng-shou. Summary of China cardiovascular disease report 2017[J].Chinese Circulation Journal,2018,33(1)：1-8.

[2] Song Han. Wireless data transmission design of ecg Holter system[D].Changsha：College of Information Physics, Central South University,2009.

[3] Ling Zhen-bao, Li Shu-yan, Zhang Ming, Li Dong-shi. Holter monitor based on ZigBee technology without lead wire design[J].Application of electronic technology,2015,41(08)：66-69.

[4] Li Shu-yuan, Wu Shui-cai, Bin Guang-yu, Bin Guang-hong, Cai Bao-long. Design and implementation of wearable wireless low-power ecg recorder[J].China Medical Devices,2015,30(03)：21-23,30.

[5] Li Shu-yuan. Research on wearable intelligent ecg equipment[D].Beijing：College of Life Science and Bio-engineering, Beijing University of Technology,2015.

[6] Xu Bu-wei. Design of ecg acquisition and display system based on Android system[D].Chengdu：College of Electronic Engineering, University of Electronic Science and Technology of China,2013.

[7] Peng Bao-ji. Design and implementation of portable electrocardiograph based on bluetooth and Android[D].Changchun：College of Communication Engineering, Jilin University,2014.

[8] Jiang Zhe-min. Design and implementation of wearable wireless low-power ecg recorder[J].Premiere,2016,88(01)：7-7.

[9] Su Na. Development and application of virtual instrument LabVIEW[J].Computer CD Software and Applications,2013,16(23)：131-132.

[10] Peng Fei-wu, Xiong Ping, Cai Xiao-zhu, Liu Jian-ting, Fu Wei.Noise and interference in the detection of ecg signal and its elimination method[J].Chinese Medical Equipment Journal,2007,28(09)：72-74.

[11] Huang Yue. Research and development of a portable dynamic ecg monitoring system[D].Changchun：College of Instrument Science and Electrical Engineering, Jilin University,2013

[12] Wang Bu-qing, Wang Wei-dong. Research on R wave detection algorithm in virtual ecg analyzer based on LabVIEW[J].Science Technology and Engineering,2006,6(21)：3401-3404.

Human positioning fan based on infrared scanning

Saikun Liu; Ziheng Qu; Anlai Mao
(College of Instrument Science and Electrical Engineering, Jilin University,changchun,130021)

***Abstract*—The electric fan has the characteristics of simple operation, safety and reliability. Aiming at some shortcomings of traditional electric fan, a variety of sensors are added to carry out intelligent transformation. STC89C52 single chip microcomputer is used as the core, and stepper motor is used to control the fan swing. In the process of fan swing, infrared sensor is used to identify human body in the environment, and the fan speed is automatically adjusted according to the room temperature collected by DS18B20. Intelligent effect.**

***keywords*—Singlechip Control system Intelligence Infrared**

I. INTRODUCTION

WITH the development of science and the improvement of people's living standards, products tend to be automated, intelligent, environmentally friendly and humanized. In recent years, the price level of air conditioning has been declining, more and more people begin to use air conditioning, which is a big impact on the fan industry, but the powerful function of air conditioning is at the cost of high energy consumption and closed space. In contrast, the electric fan ventilation is better and low power consumption is still a great advantage, we design the intelligent positioning fan in this context[1].

This design is to monitor the temperature in real time. When the temperature is lower than the lower limit temperature, the system automatically turns off the fan. When the temperature rises above the lower limit temperature, the fan rotates at a lower speed. When the temperature is higher than the upper limit temperature, the fan rotates at a higher speed. When the body is detected, the fan will activate the function of shaking head.

II. SYSTEM DESIGN

A. System overall design

The system is based on STC89C52 single chip microcomputer, which mainly completes the functions of collecting, processing and displaying the external environment temperature signal. Data collection of external environment temperature through DS18B20 sensor. Using long-distance DS18B20 to measure body surface temperature, the detected temperature is converted into digital signal, and the input digital signal is analyzed and processed by single chip microcomputer[2].

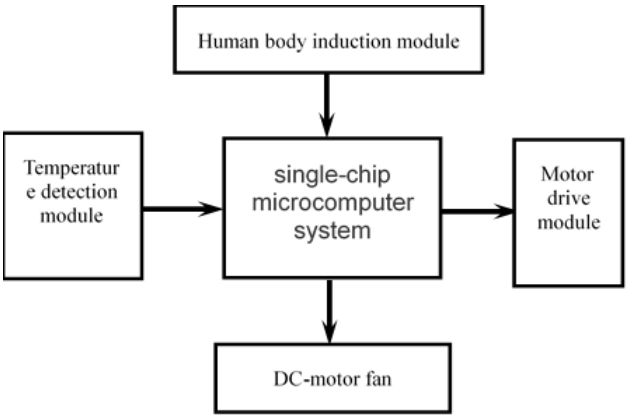

Fig. 1. System Block Diagram.

B. single-chip microcomputer system

STC89C51 single chip microcomputer is used as the core of the whole system. The smallest system of single chip microcomputer consists of single chip microcomputer, reset circuit and clock circuit.

Reset circuit is to determine the working state of the microcontroller and complete the start-up process of the microcontroller. The reset signal is produced when the single-chip microcomputer is connected with the power supply, and the start-up of the single-chip microcomputer is completed to determine the starting working state of the single-chip microcomputer. After the microcontroller works in the clock circuit, the reset operation can be completed by continuously giving two machine cycles of high level at the RESET terminal. This design uses an external manual key reset circuit, which needs to be connected with pull-up resistance to improve the output of high-level value[3].

The clock circuit is an oscillation circuit, which provides a sine wave signal to the single chip microcomputer as a reference to determine the execution speed of the single chip microcomputer. XTAL1 and XTAL2 are the input and output of the reverse amplifier, respectively. The oscillation frequency of the external quartz crystal oscillator is 12MHZ, and one oscillation period is 1/12us.

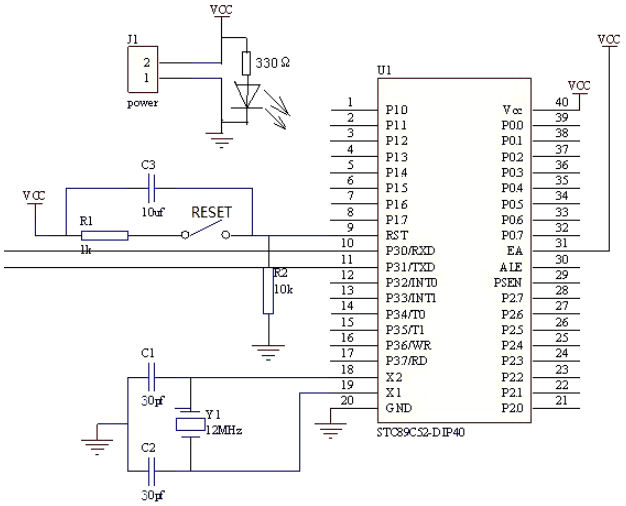

Fig. 2. single-chip system.

C. Temperature detection module

DS18B20 digital temperature sensor collects the field temperature, and sends the measured data to STC89C52 microcontroller. After processing, the current temperature value is displayed.DS18B20 can be used in two ways, one is to use power supply mode, at this time DS18B20 one foot ground, two feet as a signal line, three feet connected to power. The other is parasitic power supply mode, as shown in Figure 3[4]. The MCU ports shown are connected to a single-wire bus, and a MOSFE can be used to pull up the bus in order to provide enough current in an effective DS18B20 clock cycle. When DS18B20 is in write memory operation and temperature A/D conversion operation, the bus must have a strong pull-up, pull-up time up to 10 us. The VDD terminal is grounded when parasitic power is supplied. Because the single wire system has only one line, the sending interface must be three state[4].

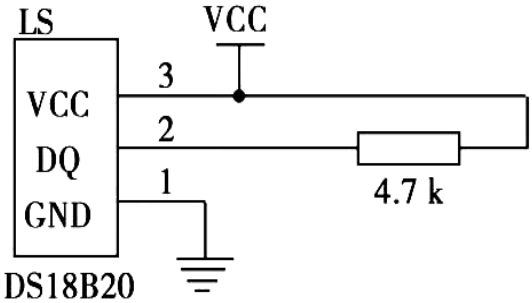

Fig. 3. Temperature detection module.

D. DC-MOTOR Fan

Through the DC motor PWM control system, the speed control and stop of the DC motor can be realized, and the intelligent control of the motor can be easily realized. PWM (Pulse Width Modulation) is a voltage regulation method by controlling the switching frequency of DC power supply with fixed voltage to change the voltage at both ends of the load so as to meet the control requirements. In the PWM drive control adjustment system, the power supply is turned on and off at a fixed frequency and the "on" and "off" time of a cycle is changed as needed. By controlling the duty cycle of the DC motor, the speed control of the motor is realized[5].

E. Human body induction module

HC-SR501 is an automatic control module based on infrared technology, the body has a constant body temperature, usually at 37 degrees, so it will emit a specific wavelength of 10UM or so, passive infrared probes work by detecting infrared rays emitted by the human body. About 10UM of the infrared emitted by the human body is gathered through the Phenanthrene filter and then gathered onto the infrared induction source. Pyroelectric devices are commonly used in IR sources, this component loses its charge balance when the infrared radiation temperature of the human body changes, after releasing the charge outward, the subsequent circuit can generate signals after being detected and processed[6].

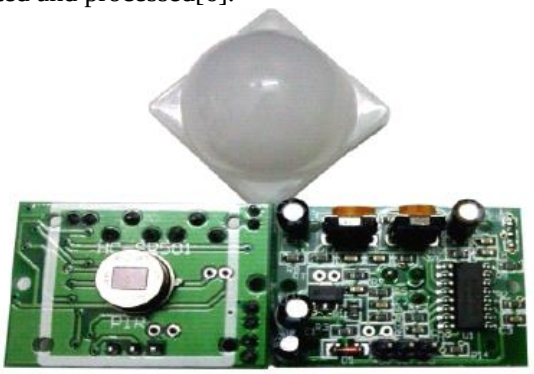

Fig. 4. Human body induction module.

F. Motor Drive Module

The motor drive module adopts ULN2003, ULN is an integrated Darlington IC with a coil-free back-EMF diode that can be used to drive relays. ULN2003 has the characteristics of high current gain, high working voltage, wide temperature range and strong load capacity.,It is suitable for all kinds of systems requiring high speed and high power driving, so ULN2003 is used as driving chip for high current load. ULN2003 has 16 pins, 7 in, 7 out, 1 GND and 1 COM. The input can be directly connected to the MCU pin using TTL level control, the output terminal is connected to a driving circuit (which can be connected to a stepping motor, a DC motor, etc.). The COM pin can be connected to VCC for driving current[7].

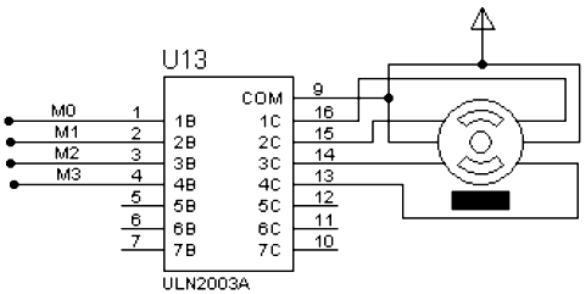

Fig. 5. Motor Drive Module.

III. SOFTWARE DESIGN

System software design is mainly programmed in C

language, debug in uVision4 uVision4 environment. It mainly includes the main control program, step motor driver, DC motor speed control program, temperature acquisition module program and display program.

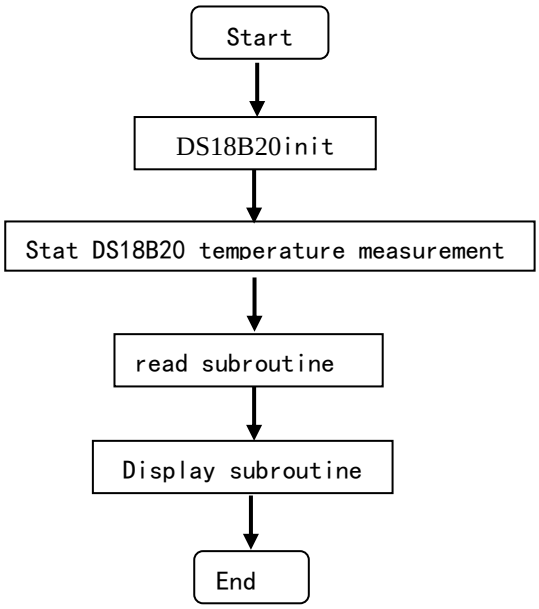

Fig.6.DS18B20 program flow chart

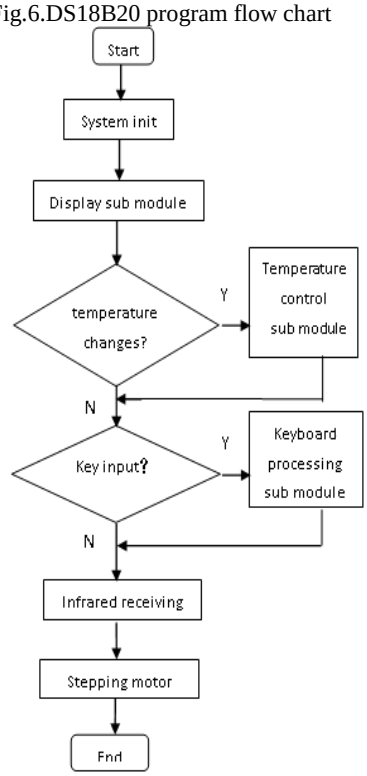

Fig.7. System Software Flow Chart.

IV. Test result

Fig.8. System physical diagram.

Related parameters	
Recognizable distance	<0.5m
Temperature precision	0.1℃
Step angle	0.9 °

Fig.9. Related parameters.

Through the actual test, the design can identify the human body in the environment and control the fan shaking head;It can automatically adjust the multi-gear speed of the fan according to the ambient temperature. When the temperature is lower than the set lower limit temperature, the system automatically shuts down the fan to rotate. When the temperature rises above the lower limit temperature, the fan rotates at a lower speed. When the body is detected, it will start the function of the fan shaking head to achieve the intelligent operation effect.

V. Conclusion

This design realizes the intelligent control of the fan. The shortcomings of traditional electric fans are intelligently reconstructed. Taking infrared sensor as the key point to recognize human body in the environment, using 51 single chip microcomputer as the core, using stepper motor to carry infrared sensor and control fan swing, scanning the general position of human body in the process of fan swing, and then using the room temperature collected by DS18B20 to automatically adjust the fan speed to achieve intelligent effect.the production of physical objects. The designed system meets the task requirements.

References

[1] Meng Jianyuan, Hu Lingyan. Model Design and Testing of Human Sensory Intelligent Fan [J]. Electronic Testing, 2017, (01): 15 + 17.

[2] Xu Zhigang, Huang Tao. Intelligent Fan Based on Single Chip Microcomputer [J] Electronic Design Engineering, 2016, 24 (11): 154-156, 159.

[3] He Li Min. Design of single chip application system [M]. Beijing: Tsinghua University press.2006.

[4] Ma Yunfeng, the interface design between MCU and digital temperature sensor DS18B20 [J].Computer Measurement and Control, 2007,10(4):278-280.

[5] Wang Su.Research on PWM Speed Regulation of DC Motor and Realization of MCU Control[J].Electromechanical Engineering Technology, 2008(11): 82-84+95+110.

[6] Li Zhenxing, Tan Hong, Li Kaicheng, et al. Application of Human Tracking Motor Control Based on Pyroelectric Infrared Sensors [J]. Electrical Measurement and Instruments, 2017, 54 (10): 108-112.

[7] Zheng Zhenjie, Jiang Yanxuan, You Dezhi.Single chip microcomputer combined with ULN2003 to drive stepping motor[J].Motor technology, 2010 (06): 44-46.

[8] Application of Ming Degang.DS18B20 in Single Chip Microcomputer Temperature Control System [J].Journal of Guizhou University (Natural Science Edition), 2006, (01)

Design of Public Bicycle Protection System

Xiaodan He, Wei Wei, Xiaolong Zhang
(College of Instrumentation & Electrical Engineering,Jilin University,Changchun 130012,China)

***Abstract*—In recent years, public bicycles have been widely used in major cities, but it is a difficult thing to monitor its status in real time.So it is important to design a system to monitor the status of the public bicycles in real time.After collecting the vibration signal by the SW-18010P vibration sensor, the 51 MCU processes the data and controls the alarm module. At the same time, the infrared scanning tubes scan the rear wheel of the bicycle in real time.If foreign object is detected, the serial port camera will be controlled to take photos and then transfer the photos to a remote desktop through the SIM900 module.After that, the LabVIEW software processes the image data automatically. An alert is issued when the similarity is less than the expected value. The result shows that the system is easy to maintain and has low power consumption with simple circuit and good real-time performance.**

***Keywords*—Vibration sensor Infrared scanning tube GPRS Digital image processing**

I. INTRODUCTION

WITH the development of society and the improvement of people's living standards, traffic congestion and smog have gradually become huge problems that restrict the further development of major cities. Therefore, public bicycles have gradually entered thousands of households as a clean, environment-friendly and convenient means of transportation.The widespread use of public bicycles has facilitated the travel of residents, but it also brought about huge regulatory problems, such as the damage of bicycle body, the private locks on the rear wheels and so on.The public bicycle protection system can monitor the status of the public bicycle in real time. When the system detects that the public bicycle is in an abnormal state, it can issue an alarm in time.It has strong real-time performance, high reliability, and is convenient for maintenance and management of the staff.This paper aims to design a public bicycle protection system,combining infrared scanning technology,GPRS technology and digital image processing technology to realize the supervision and maintenance of public bicycles.

II. SYSTEM DESIGN

The overall design of the system includes an acquisition module,a control module, an image acquisition and transmission module, a data processing module, and an alarm indication module. The overall block diagram of the system is shown in Figure 1.

First,the vibration sensor collects the vibration signal.If thevibration of the public bicycle is detected, it will control the alarm indication module to issue an alarm.At the same time, the infrared scanning tubes detect the foreign object on the bicycle in real time. When the foreign object is preliminary detected, the 51 MCU controls the alarm indication module to issue an indication signal and send a control signal to the STM32 MCU to start the image acquisition and transmission module.Finally,the acquired image data is processed by the data processing module.

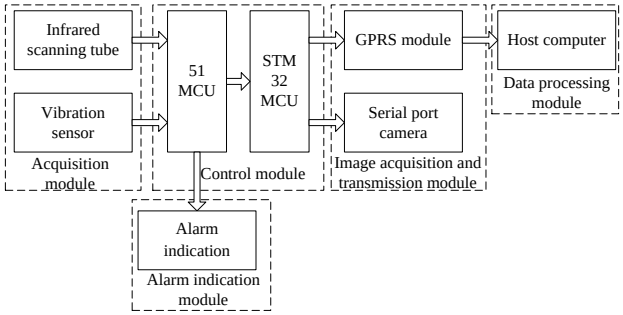

Fig.1 System block diagram

III. HARDWARE DESIGN

A. Vibration Alarm Circuit

The SW-18010P vibration sensor outputs a high level when the vibration is not detected, otherwise,it outputs a low level.The output pin of the sensor is directly connected to a certain pin of the single-chip microcomputer, and the state of the pin is detected by the single-chip microcomputer.If a high level is detected, the indicator light will be off; otherwise, the indicator light will be illuminated.So the systemcan indicate whether there is a vibration in the environment.

The sensor can be used in various situations where vibration can be detected.It has the advantages of high sensitivity, digital switching output, and small size. The vibration alarm circuit is shown in Figure 2.

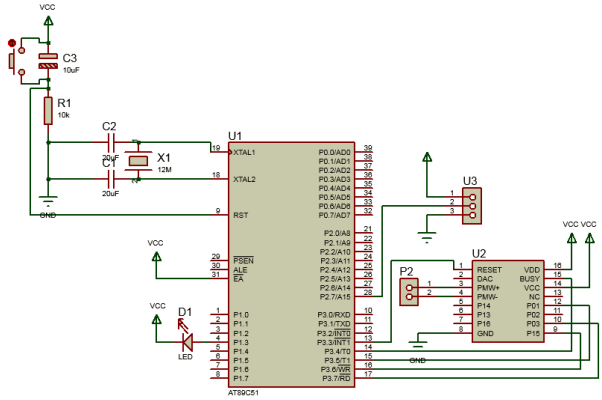

Fig.2 Vibration alarm circuit

B. Infrared Scanning Circuit

The receiving angle of the Infrared receiver diode is about 37°, and we use 6 pairs of infrared scanning tubes to detect foreign objects.The Infrared Light Emitting Diode continuously emits infrared rays.If there is no foreign object , the Infrared receiver diode will detect the infrared signal, and the OUT pin will output a high level; otherwise, the Infrared receiver diode will not detect the infrared signal,and the green indicator light of the module will be illuminated.At the same time the OUT pin outputs a low level[1].

The infrared scanning tubes have the advantages of adjustable detection range and high sensitivity.They can be applied to obstacle avoidance, infrared detection and so on[2]. The infrared scanning circuit is shown in Figure 3.

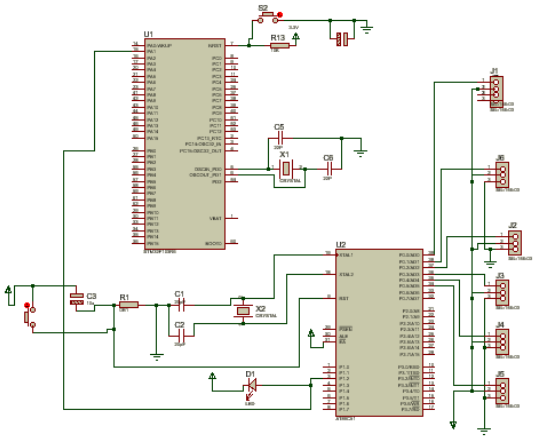

Fig.3 Infrared scanning circuit

C. Image Acquisition and Transmission Module

C1. Image Acquisition

The OV2640 is a digital image sensor belonging to the CMOS type. The sensor's size is small and it has low operating voltage. The data format of the output image includes YUV (422/420), YCbCr422, RGB565, and JPEG formats. If the image is output in JPEG format directly, the amount of data can be greatly reduced, and network transmission is facilitated.

The OV2640 reads pixels line by line. The line output sequence is that when HREF (line synchronous signal) goes high, it outputs one byte of image data on each PCLK clock. The frame output timing is that when the HREF is low, it does not perform operations, otherwise,it starts reading a line of pixels.It can read a frame of image by repeating the above operation .

The data stream saved in .jpg format starts with 0XFF, 0XD8,and ends with 0XFF, 0XD9[3].

C2. Image Transmission

GPRS is one of the Radio Packet Switching technology based on the GSM system.It supports the specific point-to-point and point-to-multipoint services and transmits data in "packet" form. The technology transmits data at the speed of 56~115Kbps, and has four frequency bands of 850/900/1800/1900MHz. It has built-in Transparent transmission protocol and can be used for long-distance communication or control[4].

The system uses the AT command as a connection and communication command between the GPRS module and the STM32 microcontroller[5]. The image acquisition and transmission module circuit is shown in Figure 4.

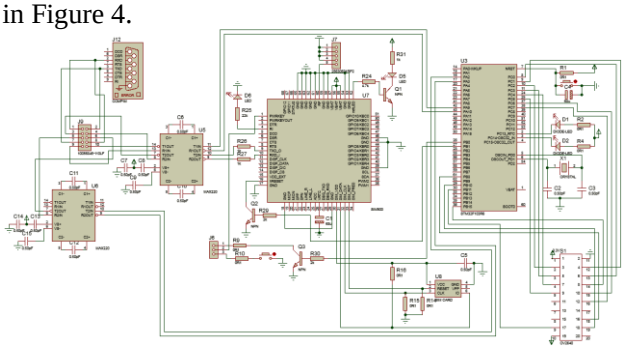

Fig.4 Image acquisition and transmission module

IV. SOFTWARE DESIGN

A. Digital Image Processing Program

A color picture file of a specified path is stored in MATLAB as a three-dimensional array, in which stores the position information and color information of each pixel[6]. Use the fspecial function provided by the MATLAB software to calculate the sobel operator template, and thenfilter the red, green and blue components of the picture by the sobel operator in the x and y directions respectively. Record the obtained values respectively as Rx, Ry, Gx, Gy, Bx, By[7].

Definition vector:

$$\mathbf{u}=\frac{\partial \mathrm{R}}{\partial \mathrm{x}}\mathbf{r}+\frac{\partial \mathrm{G}}{\partial \mathrm{x}}\mathbf{g}+\frac{\partial \mathrm{B}}{\partial \mathrm{x}}\mathbf{b} \tag{1}$$

$$\mathbf{v}=\frac{\partial \mathrm{R}}{\partial \mathrm{y}}\mathbf{r}+\frac{\partial \mathrm{G}}{\partial \mathrm{y}}\mathbf{g}+\frac{\partial \mathrm{B}}{\partial \mathrm{y}}\mathbf{b} \tag{2}$$

Define variables:

$$\mathrm{gxx}=\mathbf{u}\bullet\mathbf{u}=\left|\frac{\partial \mathrm{R}}{\partial \mathrm{x}}\right|^2+\left|\frac{\partial \mathrm{G}}{\partial \mathrm{x}}\right|^2+\left|\frac{\partial \mathrm{B}}{\partial \mathrm{x}}\right|^2 \tag{3}$$

$$\mathrm{gyy}=\mathbf{v}\bullet\mathbf{v}=\left|\frac{\partial \mathrm{R}}{\partial \mathrm{y}}\right|^2+\left|\frac{\partial \mathrm{G}}{\partial \mathrm{y}}\right|^2+\left|\frac{\partial \mathrm{B}}{\partial \mathrm{y}}\right|^2 \tag{4}$$

$$\mathrm{gxy}=\mathbf{u}\bullet\mathbf{v}=\frac{\partial \mathrm{R}}{\partial \mathrm{x}}\frac{\partial \mathrm{R}}{\partial \mathrm{y}}+\frac{\partial \mathrm{G}}{\partial \mathrm{x}}\frac{\partial \mathrm{G}}{\partial \mathrm{y}}+\frac{\partial \mathrm{B}}{\partial \mathrm{x}}\frac{\partial \mathrm{B}}{\partial \mathrm{y}} \tag{5}$$

Then the angle of the direction in which the color changes the fastest is

$$\theta_1=\frac{1}{2}\arctan\left[\frac{2\mathrm{gxy}}{(\mathrm{gxx}-\mathrm{gyy})}\right] \tag{6}$$

The value of the color change rate in the direction of θ1 is

$$\mathrm{F}(\theta_1)=\left\{\frac{1}{2}\left[(\mathrm{gxx}+\mathrm{gyy})+(\mathrm{gxx}-\mathrm{gyy})\cos 2\theta_1+2\mathrm{gxy}\sin 2\theta_1\right]\right\}^{\frac{1}{2}} \tag{7}$$

Since the tangent function has periodicity, it is necessary to calculate θ_2, $F(\theta_2)$ by rotating 90° again.

Select the valueof the maximum color change rate in $F(\theta_1)$ and $F(\theta_2)$, anduse the mat2gray function to convert the matrix composed of the values with the highest color change rates into grayscale images, which are the edges of the original image[8].

In order to judge the difference between the two images, the edge grayscale images of the two images are correspondingly subtracted.The pixels with the same grayscale equal to 0 after subtraction,which is displayed as black, and the pixels with different grayscales equal to a non-zero real numberafter subtraction, which is displayed as the gray level corresponding to the number. If the result after subtraction is a negative real number, the valuestored in the array is also zero, which is displayed as black.Therefore, the grayscale image obtained by subtracting the second image from the first image is added to the grayscale image obtained by subtracting the firstimage from the second image, and the number of all approximate zero valuein the obtained two-dimensional array as a percentage of the total number of pixels in the image is the similarity between the two images. The greaterthe similarity is, the more pixels with similar colors in the two images there are, that is, the difference between the two images is small; the smaller the similarity is, the fewer pixels with similar colors in the two images there are, that is, the difference between the two graph is larger. The flow chart is shown in Figure 5.

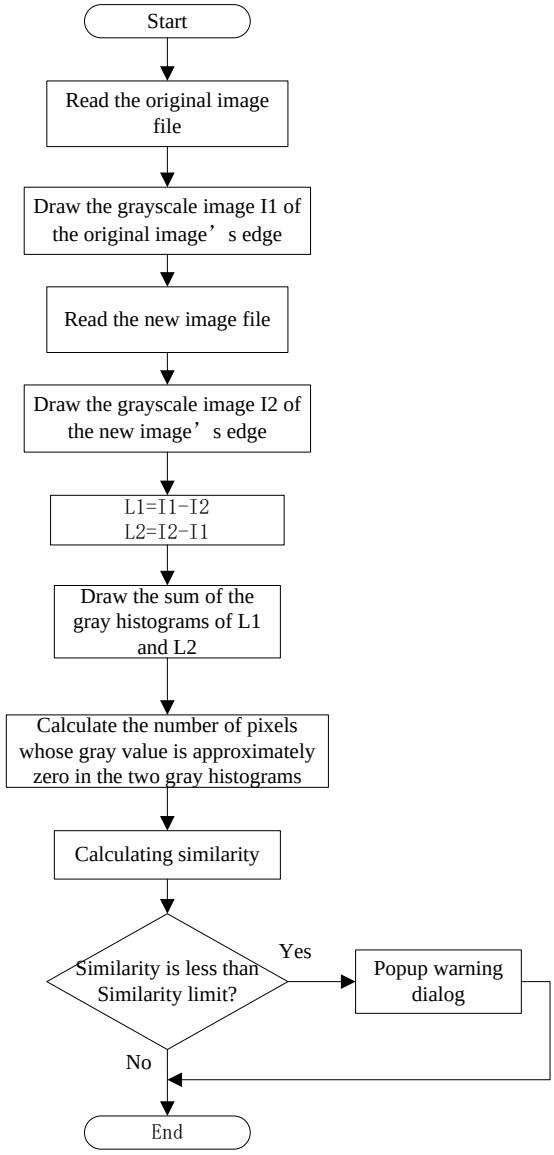

Fig.5 Flow chart

B. LabVIEW Master Computer Program Design

Use the MATLAB Script to edit the MATLAB program in it or directly call an existing MATLAB file[9]. It has explicit requirements for the type of input and output data. In order to match the variables in the LabVIEW program with the variables in the MATLAB program, there are a series of corresponding controls and program for data type conversion. It is simple and practical to use this method to achieve mixed programming of LabVIEW and MATLAB , but it still depends on the operating environment of MATLAB. The MATLAB Script can be used to easily complete the digital image processing function, and design a friendly human-machine interaction interface which can meet the requirements of the system function[10]. The MATLAB Script program is shown in Figure 6.

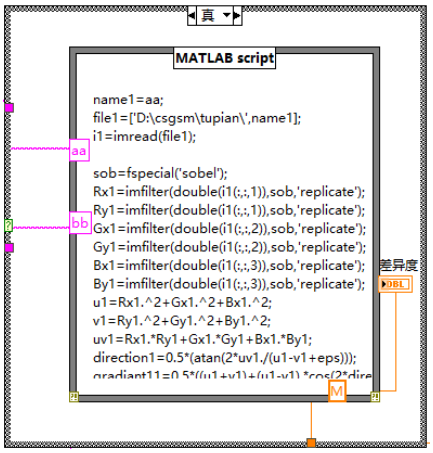

Fig.6 Matlab script

Name the original image file as 01.jpg.Starting with the number of 01,in the while loop structure the feedback node is used to generate the arithmetic progression column which is sequentially adding with the number of cycles. These numbers are respectively connected with '.jpg' to form a file name. Use the "Judge whether the file exists" control to determine whether the image file that MATLAB needs to process exists. If it exists, execute labview to call the MATLAB program for digital image processing; otherwise,it will wait for the next picture to be transmitted to the master computer. The system interface is shown in Figure 7, and the overall program is shown in Figure 8.

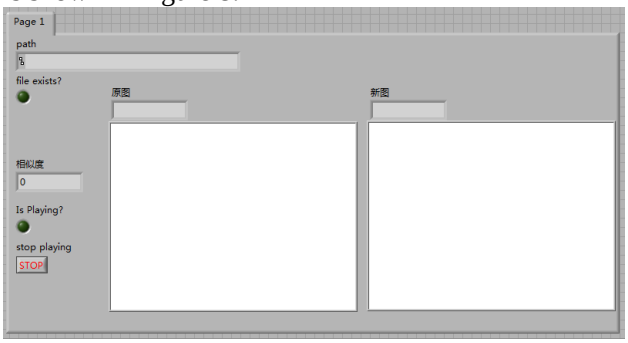

Fig.7 System interface

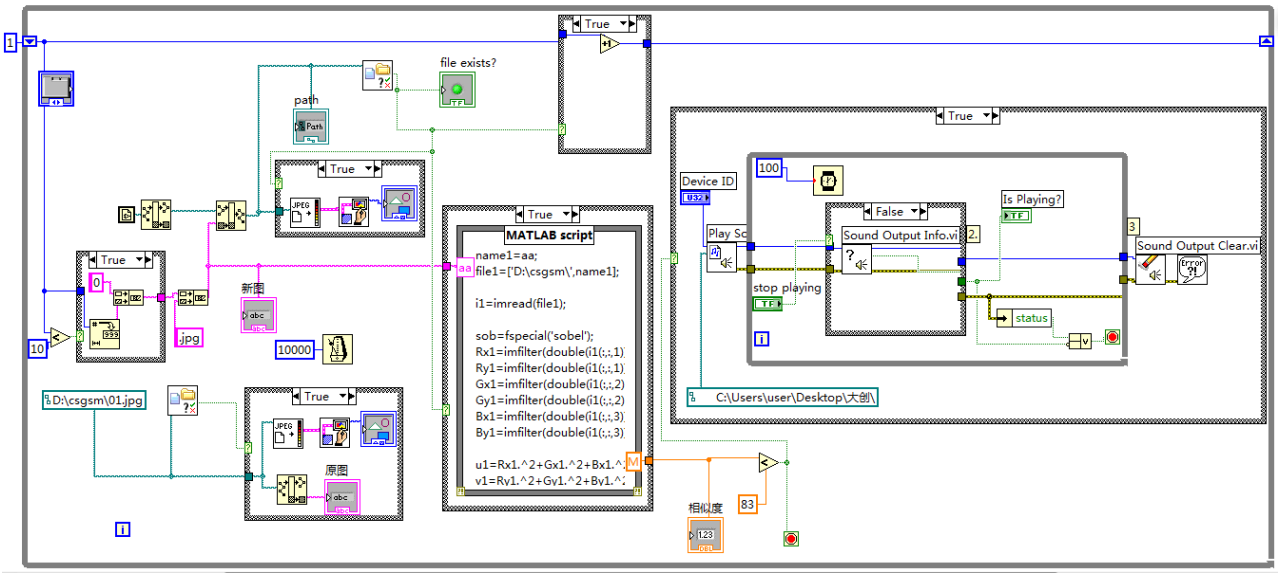

Fig.8 Overall program

V. TEST RESULT

After continuous debugging and improving, the system finally achieves the expected goals. After the system is powered on, if the public bicycle body vibrates violently, the system alarm indicator will light up and a warning tone will sound; otherwise, the system alarm indicator will be off and no warning tone will be played. When the infrared scanning module preliminarily detects that there is a foreign object on the rear wheel of the bicycle, the serial port camera takes a picture of the current state of the rear wheel and transmits the image data to the remote desktop through the GPRS module[11]. LabVIEW calls the image file to calculate the similarity between the received image and the original image through the MATLAB algorithm. When the similarity is less than the predetermined value, the program issues an alarm[12].

The picture of the two unlocked bicycle rear wheels is shown in Fig. 9, and the gray histogram of the edge image after abstracting is shown in Fig. 10.

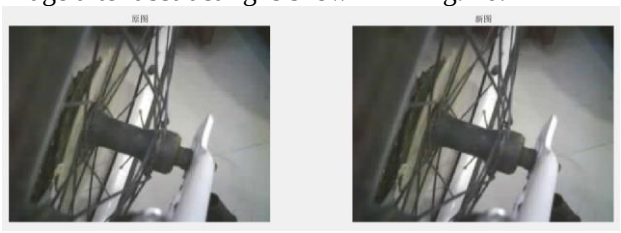

Fig.9 Photos

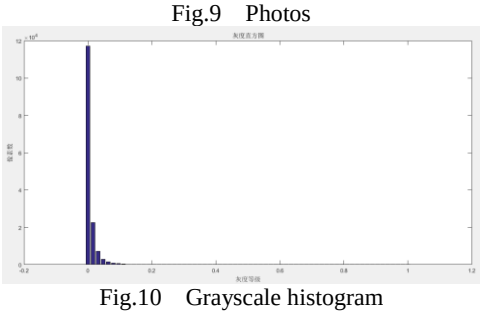

Fig.10 Grayscale histogram

An unlocked bicycle rear wheel and a locked bicycle rear wheel pictures are shown in Fig. 11, and the gray histogram of the edge image after abstracting is shown in Fig. 12.

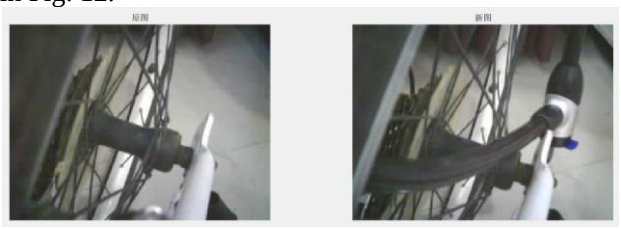

Fig.11 photos

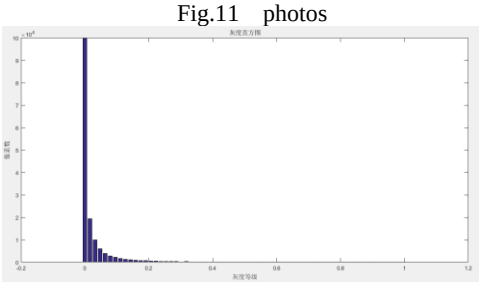

Fig.12 Grayscale histogram

After continuous testing, the similarity of the two un-locked bicycle rear-wheel images in the same condition is 95.7%.As for a locked bicycle rear wheel picture and another unlocked bicycle rear wheel picture,the similarity is 83.9%.Therefore,the picture similarity limit can be set to 90.0%.When the system detects that the similarity between the original picture and the new picture is greater than 90.0%, the system does not issue an alarm. Otherwise, an alarm is issued to alert the staff. The alarm phenomenon is shown in Figure 13.

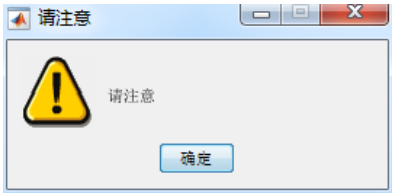

Fig.13 Alarm

VI. CONCLUSION

The public bicycle protection system uses a vibration sensor to collect the vibration signal.When the signal is detected,the system controls alarm indication module to issue an alarm. At the same time, the infrared scanning tubes detect whether there is foreign matter in the rear wheel of the bicycle in real time. When the foreign object is preliminary detected, the image acquisition and transmission module is started. Finally,the acquired image data is processed by the data processing module.When the calculation result indicates that foreign matter appears on the rear wheel of the bicycle, the system sounds an alarm tone.

The public bicycle protection system can monitor the status of the public bicycle in real time.It will issue an alarm and send the information to the management personnel in time if the bicycle is in abnormal condition. The system has low power consumption and strong real-time performance.It is convenient to use, and can reduce unnecessary manpower input.It can effectively protect social property , reduce public property losses, and has great practical significance.

References

[1] Tang Yuan, Zhou Wei, Duan Wubin, Liu Wei. Infrared and ultrasonic hybrid obstacle avoidance intelligent car based on single-chip control [J]. China Equipment Engineering. 2018(12): 179-180.

[2] Peng Meiding, Deng Peng. Design of intelligent infrared obstacle avoidance car based on single chip microcomputer[J].Wireless Interconnect Technology.2017(03):74-76+104.

[3] Zhang Wei, Lu Guangsheng, Hao Jinghua. A human body sensor design based on serial camera image comparison[J]. Electronic Technology and Software Engineering. 2014(19):97.

[4] Jiang Qishi. Design and implementation of general wireless data acquisition and control system based on GPRS [D]. Zhengzhou University. 2012.

[5] Cui Boliang, Wang Yaonan, Wang Lei, Chen Sisi. Implementation of Image Monitoring Terminal Based on GPRS Wireless Transmission[J]. Computer Measurement & Control. 2008, 16(12): 1865-1867.

[6] Liu Li, Su Fu, Tian Fang, Lu Ajuan. Image Region Extraction Based on Matlab[J].Modern Electronics Technique.2013,36(08):117-120.

[7] Wei Wei. Common Image Edge Detection Method and Matlab Research[J].Modern Electronics Technique.2011,34(04):91-94.

[8] Tu Wangming, Wei Youguo, Shi Shaomin. Application of MATLAB in Digital Image Processing[J].Microcomputer Information.2007(06):299-300+23.

[9] Li Ning, Zhang Yuanpei, Zhu Lijun. Using MATLAB Script Node in LabVIEW[J]. Instrumentation Standardization and Metrology. 2003(05): 17-19.

[10] Xu Ming, Yu Yeming. Calling of MATLAB in LabVIEW[J]. Journal of Shandong University of Technology(Natural Science Edition).2005(04):92-95.

[11] Feng Sheng. Design and implementation of wireless image transmission system based on GPRS [D]. Tianjin University.2016.

[12] Hu Youlan, Peng Tianhao, Zhu Liuying. Mixed Programming of MATLAB and LabVIEW and Its Application in Control System[J].Machine Tool & Hydraulics.2009,37(10):209-212.

A Review of Tunable Diode Laser Absorption Spectroscopy Interference Processing Algorithm

Kang Jiawen, Meng Dezhuang , Wang Hongwei
(College of Instrumentation & Electrical Engineering, Jilin University, Changchun 130000, China)

***Abstract*—One of the most common limits to gas sensor performance is the presence of unwanted interference fringes arising, for example, from multiple reflections between surfaces in the optical path. Additionally, since the amplitude and the frequency of these interferences depend on the distance and alignment of the optical elements, they are affected by temperature changes and mechanical disturbances, giving rise to a drift of the signal. In this paper, some algorithm for removing the interference fringe of TDLAS signal is introduced, these methods can ameliorate the interference distortion pointedly, and improve the accuracy of sensors.**

***Keywords*—TDLAS signal process sensor interference fringe**

I.INTRODUCTION

GAS composition analysis is widely used in the fields of chemical industrial production[1,2] and atmospheric composition detection[3,4]. Many methods of gaseous molecules analysis have been developed, including chemical sensors[5,6], gas chromatography[7,8], absorption spectroscopy[9,10]. Among them, the TDLAS (tunable diode absorption spectroscopy) technique[11,12] is commonly applied in trace gas analysis instruments with its remarkable advantages[13]. Since gas absorption reacts with transitions between various possible energy levels of gas molecules or atoms, it can directly give the structure information of detected gas molecules, in this way, absorption spectroscopy can be utilized to identify different gas types. Many industrial or environmental gases, such as methane (CH_4), propane (C_3H_8), acetylene (C_2H_2), carbon dioxide (CO_2), ammonia (NH_3), etc. all have intrinsic absorption in the near-infrared range.

In the development of TDLAS, many methods of improving system accuracy and measuring resolution has been proposed[14,15], which can be divided into two classes: software processing and hardware based. In the hardware-based approach, a class of methods by adding a reference optical path[16], while effective, inevitably increases the complexity of the system and increases the cost of the sensor[17]. On the other hand, although these white noise and baseline shifts can be meliorated by improving the optical path[18,19] or using better electronic components, this hardware units has reached the technical bottleneck and there is limited scope for research. These years, data processing[20,21] technology continues to evolve, many effective data analysis algorithms have emerging in some fields like image processing, some of them have been introduced or modified into TDLAS system to the deal with the disturbances in absorption peaks or second harmonic signals, also some algorithm have been proposed to address the pertinent issues in TDLAS signals, these algorithms have been experimental demonstrated their applicability.

II.INTERFERENCE FRINGE PROBLEM IN TDLAS SYSTEM

Due to the strong coherence of the laser[22,23], the detection sensitivity of TDLAS technology is severely restricted by optical interference. Especially at low concentration, this disturbance lead to baseline fluctuation and cause error in waveform extraction[24]. These optical interferences may come from the multiple reflections on the reflecting or scattering surfaces in the light path[25,26], then shows a periodic fluctuation like sine function in measurement signal. Unlike the electrical noise, optical interference the effect of interference fringes is in the low frequency segment and has a large amplitude, it may be difficult to distinguish the location of signal peaks under some extreme cases. Even if the comprehensive algorithm such as wavelet transform can do the work of interference fringe removing, it can't reach a high-precision extraction in many special situations. In some studies, some strategies for removing optical interference have been proposed[27,28], and these targeted algorithms have unexpected effects compared to common methods.

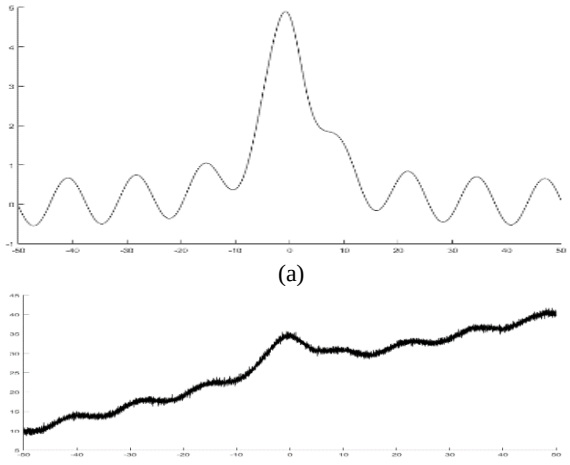

(a)

(b)

Fig.1.Signal simulation. (a) Simulink ofinterference fringe; (b) interference fringe disturbof white noise.

III. Interference Fringe Remove Algorithm

In some practical case[29], the white noise removal algorithm can not effectively remove the interference fringes especially under a serious polluted, it is hard to ensure the accuracy of signal extraction[30]. Therefore, after the noise reduction, the following algorithms can be used to remove the interference fringes. The Levenberg-Marquardt nonlinear fitting and the semi-parametric interference-immune algorithm can do this work, respectively from the perspective of time domain and frequency domain.

A. Levenberg-Marquardt Nonlinear fitting

Levenberg-Marquardt (L-M) algorithm[31] is the most widely used nonlinear least-square algorithm, which uses the gradient and iteration to find the largest (smallest) value, and then obtains the optimal solution of the requested parameters. YAN Jie et al[32]. and Wagner S et al[33]. use this algorithm for TDLAS curve-fitting, this algorithm convergent fast, and has both the advantages of gradient method and Newton method[34,35]. However, one obvious drawback of L-M is that is that this iterative fit requires a large amount of computation. Since the second-harmonic signal 2f, which is not a particularly complex function, has not too much parameter to be estimated, this method is useable for the TDLAS signal processing. But even so, in this paper, it mentions that the algorithm requires around 60,000 operator operations (for the processor) in a single iteration, so this algorithm is better suited for situations where there is good hardware support.

Theory and method

Because of the extensive use of L-M algorithm, the specific mathematical principles of the algorithm are not elaborated here, but simply introduce the general iteration steps:

a. Select initial value x^0 and termination conditionε, calculate$e^0 = \|Y - f(x^0)\|$and let$\lambda_0 = 10^{-3}$;
b. Compute the Jacobian matrix $J_x{}^k$ and construct the incremental equations;
c. Solve the incremental equation, obtain Δ^{k+1};
d. If $\|Y - f(x^0)\|$less than or equal to e^k, forward to e; else let $\lambda^{k-1} = 10\lambda^k$ and go back to a;
e. If $\|\Delta^k\|$ less thanε, stop iteration and output the result; else let $\lambda^{k-1} = 10\lambda^k$ and go back to b;

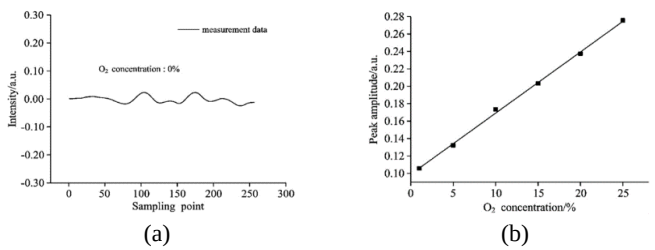

(a) (b)

Fig. 2. (a) Zero concentration fringe. (b) Relationship between the peak amplitude and gas concentration. This figure was adapted from Ref.[47].

Experiment and results

The baseline noise is measured at first. As shown in the Figure.9 (a), at a concentration of zero, the measured signal still shows pronounced fluctuation after smoothing filtered (which filtered out most of the high-frequency electronic noise).

In non-zero concentration experiment, the fitted and actual peak amplitudes show a 15% concentration error (the author mentions this is the result of reducing the computational complexity of the L-M algorithm). After error correction, the measured nonlinearity between the gas concentration and the calculated concentration is 1.08%. It is worth noting that this figure is 0.103% in the EMD algorithm experiment. However, because of the different measurement equipment and the different function area of the two algorithms, Comparison of these two values does not make much sense (eg: the two measurements may not use the same smoothing algorithm).

B Semi-Parametric Interference-Immune Algorithm

Michelucci and Venturini proposed a novel semi-parametric algorithm to eliminate the signal distortion and background fluctuation caused by interference, it has a significant effect for dealing with strong interference signal. Compared with some of above time-domain algorithm, this method starts from the frequency domain to solve the problem that the time domain algorithm is not good at. For severely polluted signal (even though the signal amplitude is ten times smaller than the fringes), the time-domain waveform has been severely disturbed and the conventional time-domain fitting makes it difficult to restore the signal itself, but these disturbances are easily distinguishable in frequency, independently of the amplitude of the interferences. In general, the desired signal in TDLAS system, like absorption peak and second-harmonic waveform, can be modeled using known linear type, and it easily to calculate the DFT of model function, therefore, the DFT of the measurement signal can be fitted to obtain the line type parameters, and this algorithm no need to enter parameter. However, for general spectrum fitting algorithms, when the signal interference is too weak, the contribution of the undesired factors on the frequency spectrum is not obvious, this method is hard to be applied.

Theory and method

This algorithm is to obtain the parameters by fitting the DFTs of model function and measured signal, using the parameters to reconstruct the corresponding line shape. The steps of the algorithm are summarized in the figure. First of all, in order to improve the accuracy and reduce the window effect when measuring the signal DFT, the author chooses Tukey window (Figure.9 (a)) as the compensation window[36,37], so that the signal decreases rapidly to zero on the sides. The next step is to determinate the optimal cut-off point i_0 so as to maximize the coefficient of determination R^2 obtained by fitting the

DFT for i >i_0 to the functional form of the Fourier transform of the line shape. At every measurement, the $i_0$is recalculated to guarantee the algorithm won't be influenced fringes change in time, solving long-time stability problems arising from changes over time of the background, like thermal drift. The final step, fitting of DFT, uses the DFT of model function to fit the DFT of the measured signal so as to obtain the parameters to determine the target signal. The algorithm flowchart is shown in Figure.9 (c).

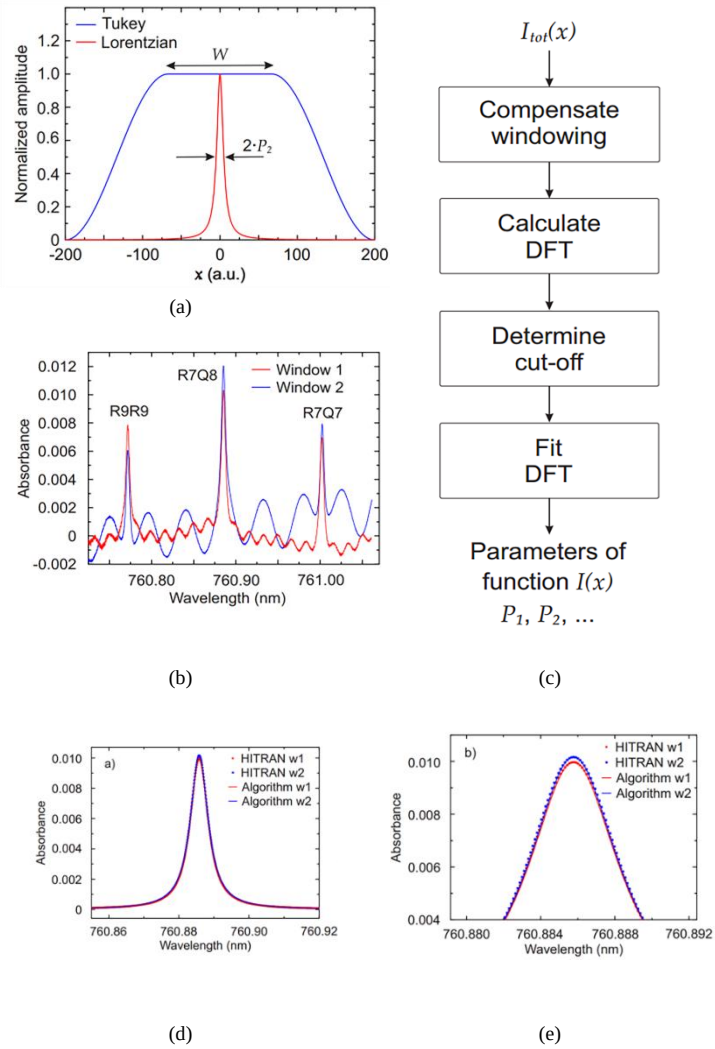

Fig. 3. (a) Turkey Window (b)Deliberately made interference fringe(c) Algorithm flowchart (d) Experimental result (e) Detail of processed signal.

Experiment and results

In the simulation, the author simulates three background interference to test algorithm: periodic disturbance, weak disturbances of large FSR, a complex disturbance with summing of 100 cosine function. The result of simulation shows the discrepancy between the results obtained with the algorithm and the expected values for the line parameters is less than 0.3%. As long as the background interference has no fitting obstacle in the spectrum, the algorithm can perform signal extraction well and this process has little affected by the interference amplitude.

Deliberately made interference fringes is utilized to testing the practicality of the algorithm, the measured signal is shown in Figure.9 (b), two different windows interfere with two different intensity fringes, despite the strong fluctuation, the extracted line shows a remarkable agreement with the expected curves from the HITRAN database[38], with deviation of the area of 0.1%. And the experimental result is shown in Figure.9 (d) and (e). These experiments show that the algorithm can effectively improve the system accuracy in the case of strong interference, and solve the background fluctuation of the signal in a targeted manner. On the other hand, more experiments remained to be performed to test the performance of this algorithm under the interference of other features.

C. Partial least squares method

The least squares method (CLS) is a commonly used algorithm for commercial instruments based on spectral inversion concentrations, but the least squares method has better fitting characteristics only when the number of independent variables is small. In the statistical analysis of near-infrared spectral data, high-dimensional numbers are the basic features, and there is often a certain correlation between independent variables, which leads to serious collinearity problems. At this time, the ordinary least squares method will have a pathological solution. Partial least squares (PLS) solves this problem by orthogonal projection on latent variables and regression problems on one-dimensional latent variables. It can simultaneously implement regression modeling, data structure simplification, and correlation analysis between two sets of variables. A satisfactory qualitative analysis effect is obtained, and the decomposition of the spectrum and the content in the PLS is simultaneously performed, and the concentration information is introduced into the spectral data decomposition process, so that the spectral principal component is directly related to the concentration of the component to be analyzed, and the elimination can be eliminated. Interference due to interference fringes.

Theory and method

The spectrum acquired in the experiment, the concentration matrix is Y, the spectral matrix is X, and the NIPLS method is solved by multiple iterations. The principal elements t and u are extracted from the independent variable and the dependent variable {X, Y}, and the partial least squares method is used. X and Y respectively perform principal component decomposition to extract r principal components, that is:

$$X = TP^T + E = \sum_{i=1}^{r} t_i p_i^T + E$$

$$Y = UQ^T + F = \sum_{i=1}^{r} u_i q_i^T + F$$

Where T and P are the scoring matrix and the load matrix of the measurement matrix X, respectively, U and Q are the scoring matrix and the load matrix of the concentration matrix Y, respectively, and E and F are the residual matrices of the measurement matrix and the concentration matrix, respectively.

After iterative calculation, it can be obtained that:

$$\{X, Y\} \xrightarrow{PLS} \{T, W, P, Q\}$$

Where W is the weight matrix of X.

$$W = X^T U / (U^T U)$$

And T=[t_1, t_2, …, t_r], W=[w_1, w_2, …, w_r], P=[p_1, p_2, …, p_r], Q=[q_1, q_2, …, q_r]

The regression equation of Y for X is

$$Y = XB_{PLS}$$

$$B_{PLS} = W^* Q^T$$

In this function, B_{PLS} is the Partial Least Squares Regression Coefficient Matrix of Y to X, $W^* = W(P^T W)^{-1}$, P^T,Q^T is the transposed matrix of P and Q.

Experiment and results

The author uses natural gas for gas absorption experiments. Modeling with PLS first requires the calculation of the appropriate number of principal components. Cross-checking is based on the difference spectrum. The PRESS corresponding to the number of principal components is shown in Table 1. When the number of principal components is 7, PRESS has a minimum value, then the number of principal components is the best, and the principal component number is used for PLS modeling.

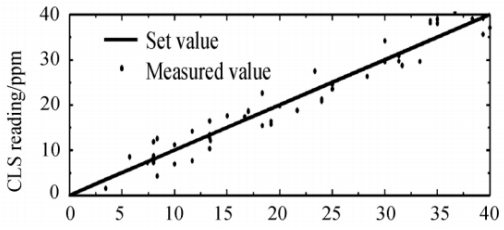

Set concentration/ppm

(a)Direct spectra deal with CLS

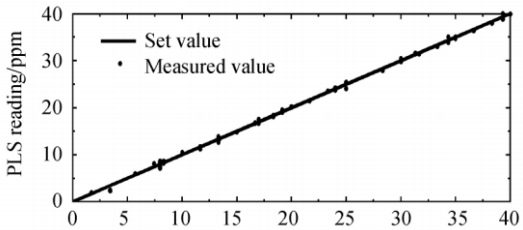

Set concentration/ppm

(b)Direct spectra deal with PLS

Fig. 4. Comparison between set value and measured value of direct spectra.

The measurement results of the analyzer show that the CLS model has a poor fit to the set value of the direct measurement spectral data processing. The correlation coefficient of the calculated CLS is 0.9580, and the measured root mean square error (RMSEP) is 2.20 ppm. The measured values obtained by the PLS model are linearly matched to the set values. The correlation coefficient of the calculated PLS is 0.9988, and the measured root mean square error RMSEP is 0.37 ppm.

IV .CONCLUSION

In this review, we first introduce the causes of the interference fringe problem in the TDLAS system and the common solutions at the hardware level. According to the shortcomings of these methods, according to some recent studies, the paper summarizes the LM nonlinear fitting, half Three post-processing algorithms: parameter immune interference algorithm and PLS partial least squares method.

LM is a widely used nonlinear least squares method for time domain fitting of signals. This algorithm has the advantages of Newton method and gradient method, and the convergence speed is fast, but this iterative fitting requires high computing power of the equipment. The semi-parametric immune interference algorithm is a spectrum fitting algorithm, which can cope with many cases that are difficult to process in time domain analysis. It has strong interference immunity to signals with strong interference, and the signal extraction is independent of the amplitude of interference. The interference fringes that need to measure the signal are easily resolved in the spectrum. If the interference fringes are small, the time domain fitting can be performed directly without analyzing the spectrum. The PLS algorithm is a multi-dependent variable regression modeling method for multiple independent variables. It avoids the storage of a large amount of reference spectral data necessary for the least squares method. The analyzer can eliminate complex differential spectroscopy systems, thereby reducing costs and improving the system. Robust and real-time effects.

In the practical application of these algorithms, the optical standard deviation interference phenomenon may increase more interference due to the uncertainty of the measurement environment. When selecting the corresponding algorithm, in addition to the experimental data given in the reference text, it should be based on the characteristics of each algorithm and Limiting judgments allows signal processing techniques to produce more useful effects.

Reference

[1] Cassidy, D. T.; Reid, J. (1982). Atmospheric pressure monitoring of trace gases using tunable diode lasers. Applied Optics, 21(7), 1185-1190.

[2] Feher, M.; Martin, P. A. (1995). Tunable diode laser

monitoring of atmospheric trace gas constituents. Spectrochimica Acta Part A: Molecular and Biomolecular Spectroscopy, 51(10), 1579-1599.

[3] Nikodem, M.; Wysocki, G. (2012). Chirped laser dispersion spectroscopy for remote open-path trace-gas sensing. Sensors, 12(12), 16466-16481.

[4] Risby, T. H.; Tittel, F. K. (2010). Current status of midinfrared quantum and interband cascade lasers for clinical breath analysis. Optical engineering, 49(11), 111123.

[5] Kluczynski, P.; Jahjah, M.; Nähle, L.; Axner, O.; Belahsene, S.; Fischer, M.; Lundqvist, S. (2011). Detection of acetylene impurities in ethylene and polyethylene manufacturing processes using tunable diode laser spectroscopy in the 3-μm range. Applied Physics B, 105(2), 427.

[6] Lackner, M. (2007). Tunable diode laser absorption spectroscopy (TDLAS) in the process industries–a review. Reviews in Chemical Engineering, 23(2), 65-147

[7] Werle, P. (1998). A review of recent advances in semiconductor laser based gas monitors. Spectrochimica Acta Part A: Molecular and Biomolecular Spectroscopy, 54(2), 197-236.

[8] Werle, P.; Slemr, F.; Maurer, K.; Kormann, R.; Mücke, R.; Jänker, B. (2002). Near-and mid-infrared laser-optical sensors for gas analysis. Optics and lasers in engineering, 37(2-3), 101-114.

[9] Wang, F.; Cen, K. F.; Li, N.; Jeffries, J. B.; Huang, Q. X.; Yan, J. H.; Chi, Y. (2010). Two-dimensional tomography for gas concentration and temperature distributions based on tunable diode laser absorption spectroscopy. Measurement Science and Technology, 21(4), 045301.

[10] Kurtz, J.; Aizengendler, M.; Krishna, Y.; Walsh, P.; O'Byrne, S. B. (2015). Flight test of a rugged scramjet-inlet temperature and velocity sensor. In 53rd AIAA Aerospace Sciences Meeting (p. 0110).

[11] Wang, F.; Wu, Q.; Huang, Q.; Zhang, H.; Yan, J.; Cen, K. (2015). Simultaneous measurement of 2-dimensional H2O concentration and temperature distribution in premixed methane/air flame using TDLAS-based tomography technology. Optics Communications, 346, 53-63.

[12] Buchholz, B.; Afchine, A.; Ebert, V. (2014). Rapid, optical measurement of the atmospheric pressure on a fast research aircraft using open-path TDLAS. Atmospheric measurement techniques, 7(11), 3653-3666.

[13] Lins, B.; Zinn, P.; Engelbrecht, R.; Schmauss, B. (2010). Simulation-based comparison of noise effects in wavelength modulation spectroscopy and direct absorption TDLAS. Applied Physics B, 100(2), 367-376.

[14] Werle, P.; Slemr, F.; Gehrtz, M.; Bräuchle, C. (1989). Wideband noise characteristics of a lead-salt diode laser: possibility of quantum noise limited TDLAS performance. Applied optics, 28(9), 1638-1642.

[15] Mueller, H. G.; Weber, J.; Hornsby, B. W. (2006). The effects of digital noise reduction on the acceptance of background noise. Trends in Amplification, 10(2), 83-93.

[16] Misiti, M.; Misiti, Y.; Oppenheim, G.; Poggi, J. M. (Eds.). (2013). Wavelets and their Applications. John Wiley & Sons.

[17] Li, J.; Yu, B.; Zhao, W.; Chen, W. (2014). A review of signal enhancement and noise reduction techniques for tunable diode laser absorption spectroscopy. Applied Spectroscopy Reviews, 49(8), 666-691.

[18] Zhang, K.; Zhang, L.; Zhao, Q.; Liu, S.; Chen, S.; Wu, Y., ...; Yang, X. (2017, October). Application of digital quadrature lock-in amplifier in TDLAS humidity detection. In AOPC 2017: Optical Spectroscopy and Imaging (Vol. 10461, p. 1046109). International Society for Optics and Photonics.

[19] Mohammad, I. L.; Anderson, G. T.; Chen, Y. (2014, June). Noise estimation technique to reduce the effects of 1/f noise in Open Path Tunable Diode Laser Absorption Spectrometry (OP-TDLAS). In Sensors for Extreme Harsh Environments(Vol. 9113, p. 91130S). International Society for Optics and Photonics.

[20] Chighine, A.; Fisher, E.; Wilson, D.; Lengden, M.; Johnstone, W.; McCann, H. (2015, September). An FPGA-based lock-in detection system to enable Chemical Species Tomography using TDLAS. In Imaging Systems and Techniques (IST), 2015 IEEE International Conference on (pp. 1-5). IEEE.

[21] Tu, G.; Dong, F.; Wang, Y.; Culshaw, B.; Zhang, Z.; Pang, T.; Wu, B. (2015). Analysis of random noise and long-term drift for tunable diode laser absorption spectroscopy system at atmospheric pressure. IEEE Sensors Journal, 15(6), 3535-3542.

[22] He, Q.; Dang, P.; Liu, Z.; Zheng, C.; Wang, Y. (2017). TDLAS–WMS based near-infrared methane sensor system using hollow-core photonic crystal fiber as gas-chamber. Optical and Quantum Electronics, 49(3), 115.

[23] Werle, P.; Slemr, F.; Maurer, K.; Kormann, R.; Mücke, R.; Jänker, B. (2002). Near-and mid-infrared laser-optical sensors for gas analysis. Optics and lasers in engineering, 37(2-3), 101-114.

[24] Frish, M. B.; Wainner, R. T.; Laderer, M. C.; Parameswaran, K. R.; Sonnenfroh, D. M.; Druy, M. A. (2011, May). Precision and accuracy of miniature tunable diode laser absorption spectrometers. In Next-Generation Spectroscopic Technologies IV (Vol. 8032, p. 803209). International Society for Optics and Photonics.

[25] Dong, L.; Tittel, F. K.; Li, C.; Sanchez, N. P.; Wu, H.; Zheng, C.; ...; Griffin, R. J. (2016). Compact TDLAS based sensor design using interband cascade lasers for mid-IR trace gas sensing. Optics express, 24(6), A528-A535.

[26] Wang, F.; Chang, J.; Wang, Q.; Wei, W.; Qin, Z. (2017). TDLAS gas sensing system utilizing fiber reflector based round-trip structure: Double absorption path-length, residual amplitude modulation removal. Sensors and Actuators A: Physical, 259, 152-159.

[27] Shao, L.; Yan, R.; Li, X.; Liu, Y. (2014). From heuristic optimization to dictionary learning: A review and

comprehensive comparison of image denoising algorithms. IEEE Transactions on Cybernetics, 44(7), 1001-1013.

[28] Gupta, K.; Gupta, S. K. (2013). Image Denoising techniques-a review paper. IJITEE, 2, 6-9.

[29] Werle, P. (1995). Laser excess noise and interferometric effects in frequency-modulated diode-laser spectrometers. Applied Physics B, 60(6), 499-506.

[30] Masiyano, D.; Hodgkinson, J.; Schilt, S.; Tatam, R. P. (2009). Self-mixing interference effects in tunable diode laser absorption spectroscopy. Applied Physics B, 96(4), 863-874.

[31] Ranganathan, A. (2004). The levenberg-marquardt algorithm. Tutoral on LM algorithm, 11(1), 101-110.

[32] Press, W. H. (2007). Numerical recipes 3rd edition: The art of scientific computing. Cambridge university press.

[33] Wagner, S.; Klein, M.; Kathrotia, T.; Riedel, U.; Kissel, T.; Dreizler, A.; Ebert, V. (2012). Absolute, spatially resolved, in situ CO profiles in atmospheric laminar counter-flow diffusion flames using 2.3 μm TDLAS. Applied Physics B, 109(3), 533-540.

[34] Wedderburn, R. W. (1974). Quasi-likelihood functions, generalized linear models, and the Gauss—Newton method. Biometrika, 61(3), 439-447.

[35] Hartley, H. O. (1961). The modified Gauss-Newton method for the fitting of non-linear regression functions by least squares. Technometrics, 3(2), 269-280.

[36] Tukey, J. W. (1967). An introduction to the calculations of numerical spectrum analysis. Spectral Analysis of Time, 25-46.

[37] Harris, F. J. (1978). On the use of windows for harmonic analysis with the discrete Fourier transform. Proceedings of the IEEE, 66(1), 51-83.

[38] Rothman, L. S.; Gordon, I. E.; Babikov, Y.; Barbe, A.; Benner, D. C.; Bernath, P. F.; ... ;Campargue, A. (2013). The HITRAN2012 molecular spectroscopic database. Journal of Quantitative Spectroscopy and Radiative Transfer, 130, 4-50

A Review of Tunable Diode Laser Absorption Spectroscopy Denoise Algorithm

Kang Jiawen, Meng Dezhuang , Wang Hongwei
(College of Instrumentation & Electrical Engineering, Jilin University, Changchun 130000, China)

***Abstract*—Gas sensor based on Tunable Diode Laser Absorption Spectroscopy (TDLAS) has been widely application. Due to the TDLAS system has dual characteristics with optical and electrical, the extracted signal tends to have a lower noise-to-signal ratio（SNR）. In the TDLAS signal processing, denoising will have a great influence on the accuracy of the system. Based on recent researches, this paper introduces these problems and presents some algorithms to deal with the corresponding issues, which have been experimentally confirmed its effectiveness. Finally, the merits and drawbacks of these algorithms are summarized in the conclusion.**

***Keywords*—TDLAS signal process sensor denoise**

I.INTRODUCTION

Gas sensors based on TDLAS (tunable diode absorption spectroscopy) technique have remarkable advantages of high sensitivity, rapid response, strong stability and high selectivity, after several years of development, it has been widely used in the fields of atmospheric composition[1-3], medical healthy[4], chemical industrial production[5-8] and detection. Because of the diversity of application environments, the detection system is unavoidable disturbed by multiple environmental noises, moreover, due to the dual nature of optics and electricity, the measurement signal incorporates numerous contributions from optical components (interference fringe) and electronic components (white noise)[9-10]. In addition, background error, which is caused from the background extraction, will also limit the detection precision of the system. Therefore, the work of signal preprocessing is necessary to improve the accuracy of TDLAS based analytical instruments.

II.FACTORS AFFECTING THE ACCURACY OF TDLAS

There are many factors that can affect the accuracy of a TDLAS system, such as white noise in electronic units, interference fringes in optical components, errors in background extraction, signal drift and atmospheric pressure changes. Some errors even come from the dust in light paths and mechanical jamming when the device is used. Among them, the first three interferences are more universal, and this article mainly introduces the researches of these three issues.

Compared with traditional signal processing, the signal obtained from the TDLAS system tends to have a lower signal-to-noise ratio (SNR) [11-12]. Due to the gas absorption is weaker in near-infrared than in mid-infrared region, the amplitudes of absorption peak is small than that in other detection methods, especially in trace gas detection, (in which TDLAS is usually applicated) second harmonic signal is so weakness that it can be easily submerged in the various noise (and spikes), these noise may come from TEC or lock-in amplifier, the 1/f noise or power supply voltage jitter. In this case, those algorithms that are most commonly used in general signal processing, like least-square method, can not efficiently extract the precise desired signal. Recent years, some advanced algorithms have been proposed or introduced into TDLAS system to processing this signal with low SNR, including Wavelet Transform(WT) [13-15], adaptive Savitzky–Golay algorithm[16-18] and EMD-FCR algorithm[19-22]. And these algorithms have been verified to be of significance for practical issues.

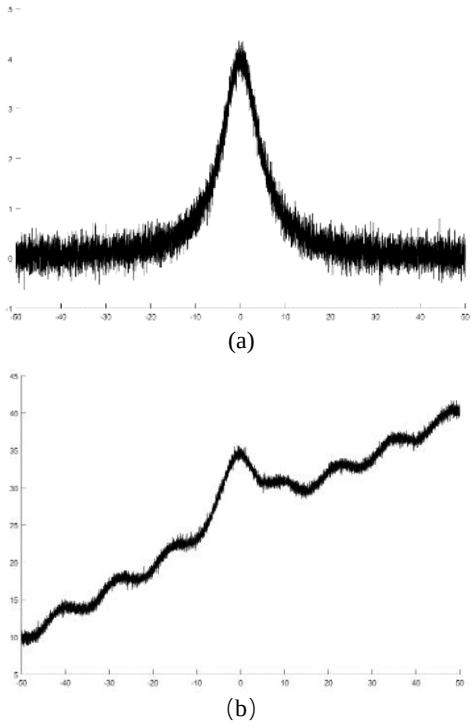

(a)

(b)

Fig.1. Signal simulation. (a) White noise; (b) Multiple interference signal.

III.Algorithms for TDLAS signal processing

Algorithms applied to denoising and signal processing have further development[23-24], the signal averaging is an early and simply method for signal processing[25-26]. Over years, many kinds of

algorithms have been developed to denoise from different perspectives, for example, the linear filters based on early filtering theory such as Wiener filter and Kalman filter[27-28], the fitting algorithms based on nonlinear regression such as least-square method and some other decomposition algorithms based on signal decomposition and reconstruction such as Empirical Mode Decomposition. In recent years, some novel strategies have been worked out to deal with the usual signal disturbances in TDLAS. In the following, this article will introduce some solutions addressing the three issues mentioned above.

Noise reduction is needed in a variety of signal preprocessing. In this section, wavelet transform, adaptive Savitzky–Golay algorithm and EMD-FCR algorithm will be introduced for the applications in TDLAS noise deduction with their particular strength. It is worth mentioning that, in addition to denoising, they can theoretically solve other interference at some degree.

A. Wavelet Transform (W-T)

In some studies, wavelet transform is introduced into TDLAS sign analytical process[29], which has been widely used in other signal processing filed Wavelet analysis is a signal time-frequency analysis method for processing local or transient signals. It origins from Fourier algorithm transformation, and combines the thought of signal stretching and translation, has dual locality in time domain and frequency domain. This variable resolution analysis method focuses on both the low-frequency trend and high-frequency detail of signal.

Because of the special characteristic in time-frequency relationship, the wavelet-based scenarios can be an effective approach to modeling the absorption signal, and to work out the complicated situation: The amplitude of absorption signal peak is very small, but also contains the low-frequency fluctuations (caused by temperature drift, interference fringes), and the high-frequency abrupt signal (mainly Gaussian white noise). The WT offers a window that varies with signal frequency band, allowing different scales of noise to be resolved into different sub-bands. As a result, time resolution becomes better at high frequency and frequency resolution is improved at low frequency[30-32]. As a result, wavelet denoising is a powerful tool to extract desired signal from severer noise pollution. However, one of the drawbacks of wavelet transform is that its choice of parameters has a strong subjectivity. Human error will greatly affect the decomposition performance of the algorithm. In this part, we mainly introduce the studies of wavelet transform to deal with the noise of low-SNR situation, in which the experimental process and data have significant reference for further research, and the application of removing background will be introduced later in this article.

Theory and method

In this paper, only the key concepts of wavelet transform are presented, detail mathematical treatment can be found in the references. The basic principle of wavelet analysis is described to choose a mother wavelet basis function, making scale change and time shift to form a series of related functions to analyze the approximation of data. Combined with the parameter transformation in this series of functions (that is, wavelet transform)， the analyzed signals can be mapped into different frequencies.

Wavelet analysis process can be understood as the window observation process, setting a fixed size analysis window, the resolution of the window and the time-frequency localization characteristics can be changed by adjusting the window shape, which achieve the variable resolution analysis. The method of variable resolution analysis can obtain both the low frequency information and high frequency information, analyze the general characteristics and signal details of the detected signal. The electrical noise of signal is contained in the high-frequency part in general. The flow chart of the wavelet transform is shown in Figure.2.

Experiment and results

Hua XIA et al. introduced the wavelet transform to deal with low-SNR signal in TDLAS system. The parameter selecting and steps of procedure are shown in Figure.4. In this experiment, wavelet basis sym6 and decomposition scale six was used, and just reserve and reconstruct approximation coefficient a term of absorption signal only in the certain frequency. After signal reconstruction, the signal with WD and without WD had been compared in Figure.3, it shows that the wavelet denoising can strikingly optimize the signal.

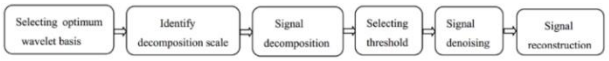

Fig. 2. The flow chart of wavelet transform.

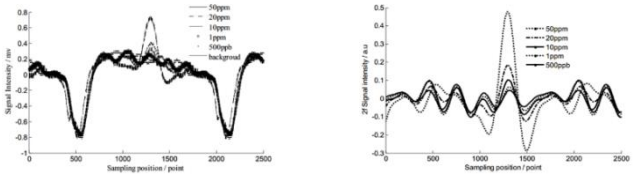

(a) (b)

Fig. 3. WD signal and without WD signal

Chuan-Tao Zheng et al. also studied the application of wavelet-denoising-assisted wavelength modulation technique in TDLAS-based near-infrared CH4 detection device. Furthermore, more detailed experimental data was listed to confirm the improvement of WD for polluted signal. A comparison between the sensing performances under the cases of using WD and without using WD is tabled below.

Besides, in this experiment，the sample gas was set up in two groups, a low-concentration group (scale of 0–1 kppm) and a high-concentration group (scale of 0–50 kppm),in this way, the accuracy and respond time index of WD signal and without-WD signal is also be contrast in this two situation. Firstly, when WD is used, over the whole range of 0–50 kppm, the absolute detection error is less than 5% under high

concentration range. For the 1 ppm and 3 ppm gas samples, the detective errors with WD are 14.3% and 9.3%, which are up to 58% and 21% when WD is unused. Secondly, the respond time of the sample concentration change from 10ppm to 15ppm is about 8.0s, when the concentration increases from 2 to 3 kppm, the response time is about 6.0s. Experimental results demonstrate that the wavelet denoising method has a strong practical significance, especially in low-concentration gas detection, the quality of the signal has been significantly enhanced.

B. adaptive Savitzky–Golay algorithm

S-G filter is a classic smoothing denoising method[33], one of the common pretreatment methods in spectrum analysis[34]. Jing song Li et al. proposed a simple but robust modified adaptiveSavitzky–Golay (S-G) algorithm for TDLAS signal processing, which shows unique superiority When temporal resolution and lower system cost are priorities. This approach is developed from S-G smoothing filter, the S-G filter using the least squares fitting coefficient as filter response function, is a smoothing filtering method for high frequency noises, as for basic S-G filter, its effectiveness is found to be strongly dependent on the window size. As explained above, one of the difficulties in TDLAS signal processing is that the noise can obtain various of multi-frequency components, A fixed window is hard to match each of these signal segments. This new method presents a variable window and gives two additional criteria for TDLAS signal processing to determine the optimal window size. Compared with many preset parameters of wavelet transform, this adaptive algorithm reduces the subjective error.

Theory and method

The basic method of the S–G algorithm obtains the following steps: (i) selecting window size (ii) selecting polynomial function for the data point in window (iii) correct the data point at the center of the selected interval by the polynomial coefficients as shown in Figure.4). And shifting the analysis window to the right by one data point, repeating above process. In this modified approach, two criteria be introduced to work out the optimal window size, “PolyFit” and a threshold “Th”. “Ploy fit” is a signal segment in a polynomial function, which we regard as noiseless, in a process of a segment of data, correlation coefficient R between the “PolyFit” and the same segment in the S–G-filter-smoothed data is utilized to assess the optimal filtering parameters (instead of SNR).In fact, this condition is valid for noise reduction, while not credible for signal preservation. The threshold “Th”, which defined as the difference of peak heights between “PolyFit” and the S–G filtering smoothed data, is used to ensure filtering parameters without excessive signal distortion. by this means, each data interval can be modified under an optimal window size, potential signal distortion can be alleviated in signal processing. The flow chart of the modified algorithm is shown in Figure.5.

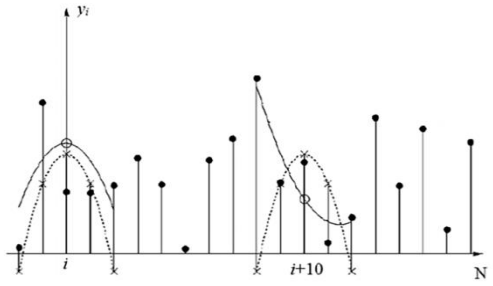

Fig. 4. Polynomial fitting of S-G filter.

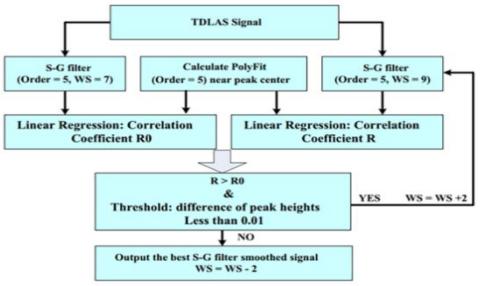

Fig. 5. Flow chart of adaptive Savitzky–Golay algorithm.

Experiment and results

A series of experiments have been performed to investigate the effectiveness of the algorithm and its applicability in various situations, for example, suitability evaluation for absorption spectra with different lineshapes under the different pressures (between a few mbar and 1 bar). These experimental results indicate that the developed algorithm is reliable for practical application, and this method could also be used to construct an optimal calibration model for TDLAS spectra with different background structural characteristics (linear or nonlinear baseline drift). However, it should be pointed out that when it applying to the simulated signals with different sampling points, one has to compromise between noise reduction and temporal resolution.

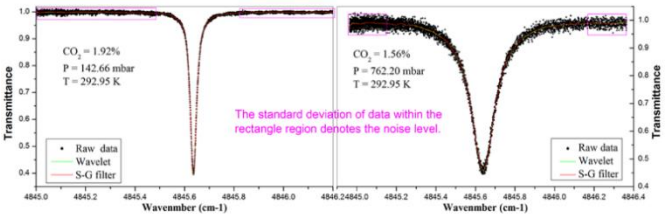

(a)

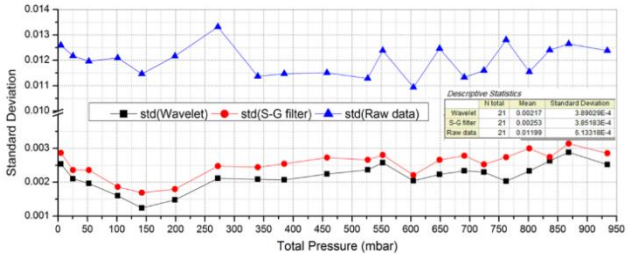

(b)

Fig. 6. (a) Raw signal and processed signal by Wavelet and S-G filter under different noise level. (b)Standard deviations of three sets of data under different pressure.

Specially, at a concentration of 1.5% of CO2, the filter results of this developed algorithm are compared with wavelet transform-based filter where Stein thresholding policy, wavelet db10, and decomposition level 6 are used in this filter, Figure.6 (a) and (b). The wavelet filter shows a stronger ability of noise reduction, the SNR enhancement factor is 5.5 and the S–G filter is 4.7. But the method requires more parameters to be specified (such as wavelet basis, threshold estimation, and decomposition scale), in addition, this method saves time costs and is easier to implement.

C. EMD-FCR Algorithm

EMD algorithm is a time domain decomposition method based on the time scale features of the processed data. It had been widely applied in many fields[35-38] with its excellent performance in processing non-stationary and non-linear signal. In theory, EMD algorithm is able to decompose any complicated signal into finite IMFs and any preset basis functions are not required[39-41], the decomposition of signals depends only on the nature of signal itself, which is the essential difference from wavelet transform. Y Meng et al. introduced this method into TDLAS, and Yunxia Meng et al. proposed a modified algorithm that combined with EMD, S-G filter (which already mentioned above) and cross-correlation operation, referred to EMD-FCR algorithm. This new method has better applicability for second harmonic signal processing and improves the system accuracy.

Theory and method

The essence of EMD is: Using the thought of stationary time series(STS) to decompose a frequency irregular wave into multiple regular wave and residual wave (original waveform = Σ IMFs + residual wave), Figure.7 (a).Each IMF must meet two conditions: 1) In the whole data set, the number of extrema and the number of zero crossings must either equal or differ at most by one; 2) at any point, the mean value of the envelope defined by the local maxima and the envelope defined by the local minima is zero.

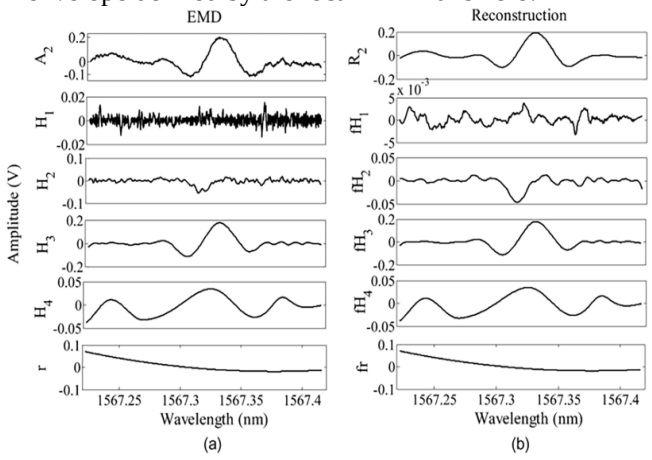

Fig. 7. (a) The signal decomposition into IMF. (b) Reconstructed IFM after S-G filtering. This figure was taken from Ref. [42].

In EMD-FCR algorithm, each IMF needs to be filtered by S-G filter (Figure.7 (b)), then perform cross-correlation calculations to obtain the cross-correlation coefficients between original signal and each filtered IMFs. At last, each filtered IMF is weighted by its corresponding correlation coefficient and then added up to reconstruct a new signal. A portion of noise in original signal is removed by S-G filter, the remaining noise have a low correlation with second harmonic signal so that it accounts for a small proportion of reconstruction signal. In this way, majority noise is suppressed. It is worth notion that some researches indicate that mode mixing problem may occur during the decomposition processing of EMD algorithm.

Experiment and results

The algorithm is assessed by simulation and experiment respectively, in the two tests, EMD-FCR was compared with Wiener filter, Kalman filter and Wavelet filter. The results indicated that EMD-FCR performed best in both of them (Table.1 and Figure.8 (a)). By this method, the SNR was significantly improved from 7.32 dB to 14.31 dB and the MDL decreased from 18 ppm to2 ppm with SNR = 3dB.

Table 1SNR and residual sum of squares (SSR) of different filters.

Filter	Wiener	Kalman	Wavelet	EMD-FCR
SNR_1(dB)	14.17	11.21	13.26	14.82
$SSR_1(V^2)$	0.0287	0.3010	0.0027	0.0014
SNR_2(dB)	14.02	11.81	13.96	14.31
$SSR_2(V^2)$	0.9859	0.7523	0.5943	0.2538

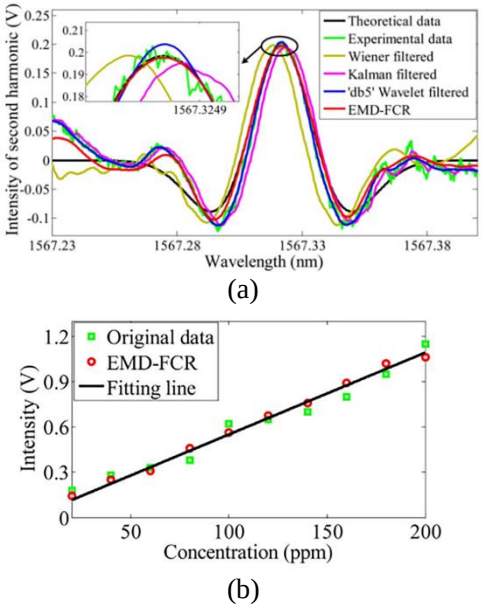

Fig. 8. (a) Performance of different method. (b)Relationship between the second harmonic intensity and gas concentration..

In further research, demodulation error experiment verified its reliability for long-hours work, the errors of second harmonic intensity in 50 minutes is only 2:113× 10^{-5} V. Vary-concentration experiment

indicated that the second harmonic using EMD-FCR algorithm shows the linear correlation coefficient R2 was improved from 0.93290 of the original data to 0.99297. Besides, it is worth mentioning that experiments confirmed that the EMD-FCR algorithm not only restrained the noises, the baseline drift problem of second harmonic signals is also solved.

IV. CONCLUSION

In this article, the common problems of TDLAS system is introduced, according to recent researches, we introduce several algorithms to solve corresponding issue.

For signal denoising, wavelet transform is a powerful tool, which can reach a high SNR. However, the wavelet transform algorithm relies on many parameters such as setting wavelet base and degree of decomposition, which is prone to subjective error in this process, and makes a high requirement for the user's level. Adaptive S-G filter is an improved vision of SG filter whose window size and polynomial order vary with the local feature of signal, with higher precision. Since most commercial software libraries include the function for S-G filter, this algorithm is easy to implement. However, due to its nature as a smoothing filter and its specialization in Gaussian noise, some S-G filter experiments shows that it may not work well if the signal contains larger fluctuation. The EMD-FCR algorithm is an improved algorithm based on empirical mode decomposition. Its filtering principle is signal decomposition and reconstruction, which can deal with non-stationary signals well, and the algorithm is also self-adaptive (because this decomposition depends on the characteristic of the signal itself). However, this algorithm is not perfect either, if there is a sudden change in the scale of the measurement signal, the EMD algorithm may appear modal mixture.

In solving the TDLAS signal processing problems, the optical factors, the electronic factors and the nature of the semiconductor lasers all can bring disturbance. In response to these issues, these algorithms can be used for reference or improvement, avoid weaknesses. However, in point of fact, no algorithm can solve all signal problems, which have been described by the “No Free Lunch Theorem of Optimization (NFLT), still, the strategy contained in the algorithm are not limited to the algorithm itself, for example, the schemes of correlation coefficient weight method, iteration, adaptive improvement, and problem decomposition, can have a foothold in any problem.

Reference

[1] Cassidy, D. T.; Reid, J. (1982). Atmospheric pressure monitoring of trace gases using tunable diode lasers. Applied Optics, 21(7), 1185-1190.

[2] Feher, M.; Martin, P. A. (1995). Tunable diode laser monitoring of atmospheric trace gas constituents. Spectrochimica Acta Part A: Molecular and Biomolecular Spectroscopy, 51(10), 1579-1599.

[3] Nikodem, M.; Wysocki, G. (2012). Chirped laser dispersion spectroscopy for remote open-path trace-gas sensing. Sensors, 12(12), 16466-16481.

[4] Risby, T. H.; Tittel, F. K. (2010). Current status of midinfrared quantum and interband cascade lasers for clinical breath analysis. Optical engineering, 49(11), 111123.

[5] Kluczynski, P.; Jahjah, M.; Nähle, L.; Axner, O.; Belahsene, S.; Fischer, M.; ...; Lundqvist, S. (2011). Detection of acetylene impurities in ethylene and polyethylene manufacturing processes using tunable diode laser spectroscopy in the 3-μm range. Applied Physics B, 105(2), 427.

[6] Lackner, M. (2007). Tunable diode laser absorption spectroscopy (TDLAS) in the process industries–a review. Reviews in Chemical Engineering, 23(2), 65-147

[7] Werle, P. (1998). A review of recent advances in semiconductor laser based gas monitors. Spectrochimica Acta Part A: Molecular and Biomolecular Spectroscopy, 54(2), 197-236.

[8] Werle, P.; Slemr, F.; Maurer, K.; Kormann, R.; Mücke, R.; Jänker, B. (2002). Near-and mid-infrared laser-optical sensors for gas analysis. Optics and lasers in engineering, 37(2-3), 101-114.

[9] Wang, F.; Cen, K. F.; Li, N.; Jeffries, J. B.; Huang, Q. X.; Yan, J. H.; Chi, Y. (2010). Two-dimensional tomography for gas concentration and temperature distributions based on tunable diode laser absorption spectroscopy. Measurement Science and Technology, 21(4), 045301.

[10] Kurtz, J.; Aizengendler, M.; Krishna, Y.; Walsh, P.; O'Byrne, S. B. (2015). Flight test of a rugged scramjet-inlet temperature and velocity sensor. In 53rd AIAA Aerospace Sciences Meeting (p. 0110).

[11] Wang, F.; Wu, Q.; Huang, Q.; Zhang, H.; Yan, J.; Cen, K. (2015). Simultaneous measurement of 2-dimensional H2O concentration and temperature distribution in premixed methane/air flame using TDLAS-based tomography technology. Optics Communications, 346, 53-63.

[12] Buchholz, B.; Afchine, A.; Ebert, V. (2014). Rapid, optical measurement of the atmospheric pressure on a fast research aircraft using open-path TDLAS. Atmospheric measurement techniques, 7(11), 3653-3666.

[13] Lins, B.; Zinn, P.; Engelbrecht, R.; Schmauss, B. (2010). Simulation-based comparison of noise effects in wavelength modulation spectroscopy and direct absorption TDLAS. Applied Physics B, 100(2), 367-376.

[14] Werle, P.; Slemr, F.; Gehrtz, M.; Bräuchle, C. (1989). Wideband noise characteristics of a lead-salt diode laser: possibility of quantum noise limited TDLAS performance. Applied optics, 28(9), 1638-1642.

[15] Mueller, H. G.; Weber, J.; Hornsby, B. W. (2006). The effects of digital noise reduction on the acceptance of background noise. Trends in Amplification, 10(2), 83-93.

[16] Misiti, M.; Misiti, Y.; Oppenheim, G.; Poggi, J. M. (Eds.).

(2013). Wavelets and their Applications. John Wiley & Sons.

[17] Li, J.; Yu, B.; Zhao, W.; Chen, W. (2014). A review of signal enhancement and noise reduction techniques for tunable diode laser absorption spectroscopy. Applied Spectroscopy Reviews, 49(8), 666-691.

[18] Zhang, K.; Zhang, L.; Zhao, Q.; Liu, S.; Chen, S.; Wu, Y., ...; Yang, X. (2017, October). Application of digital quadrature lock-in amplifier in TDLAS humidity detection. In AOPC 2017: Optical Spectroscopy and Imaging (Vol. 10461, p. 1046109). International Society for Optics and Photonics.

[19] Mohammad, I. L.; Anderson, G. T.; Chen, Y. (2014, June). Noise estimation technique to reduce the effects of 1/f noise in Open Path Tunable Diode Laser Absorption Spectrometry (OP-TDLAS). In Sensors for Extreme Harsh Environments(Vol. 9113, p. 91130S). International Society for Optics and Photonics.

[20] Chighine, A.; Fisher, E.; Wilson, D.; Lengden, M.; Johnstone, W.; McCann, H. (2015, September). An FPGA-based lock-in detection system to enable Chemical Species Tomography using TDLAS. In Imaging Systems and Techniques (IST), 2015 IEEE International Conference on (pp. 1-5). IEEE.

[21] Tu, G.; Dong, F.; Wang, Y.; Culshaw, B.; Zhang, Z.; Pang, T.; Wu, B. (2015). Analysis of random noise and long-term drift for tunable diode laser absorption spectroscopy system at atmospheric pressure. IEEE Sensors Journal, 15(6), 3535-3542.

[22] He, Q.; Dang, P.; Liu, Z.; Zheng, C.; Wang, Y. (2017). TDLAS–WMS based near-infrared methane sensor system using hollow-core photonic crystal fiber as gas-chamber. Optical and Quantum Electronics, 49(3), 115.

[23] Werle, P.; Slemr, F.; Maurer, K.; Kormann, R.; Mücke, R.; Jänker, B. (2002). Near-and mid-infrared laser-optical sensors for gas analysis. Optics and lasers in engineering, 37(2-3), 101-114.

[24] Frish, M. B.; Wainner, R. T.; Laderer, M. C.; Parameswaran, K. R.; Sonnenfroh, D. M.; Druy, M. A. (2011, May). Precision and accuracy of miniature tunable diode laser absorption spectrometers. In Next-Generation Spectroscopic Technologies IV (Vol. 8032, p. 803209). International Society for Optics and Photonics.

[25] Dong, L.; Tittel, F. K.; Li, C.; Sanchez, N. P.; Wu, H.; Zheng, C.; ...; Griffin, R. J. (2016). Compact TDLAS based sensor design using interband cascade lasers for mid-IR trace gas sensing. Optics express, 24(6), A528-A535.

[26] Wang, F.; Chang, J.; Wang, Q.; Wei, W.; Qin, Z. (2017). TDLAS gas sensing system utilizing fiber reflector based round-trip structure: Double absorption path-length, residual amplitude modulation removal. Sensors and Actuators A: Physical, 259, 152-159.

[27] Shao, L.; Yan, R.; Li, X.; Liu, Y. (2014). From heuristic optimization to dictionary learning: A review and comprehensive comparison of image denoising algorithms. IEEE Transactions on Cybernetics, 44(7), 1001-1013.

[28] Gupta, K.; Gupta, S. K. (2013). Image Denoising techniques-a review paper. IJITEE, 2, 6-9.

[29] Werle, P.; Slemr, F. (1991). Signal-to-noise ratio analysis in laser absorption spectrometers using optical multipass cells. Applied optics, 30(4), 430-434.

[30] Masiyano, D.; Hodgkinson, J.; Tatam, R. P. (2008). Use of diffuse reflections in tunable diode laser absorption spectroscopy: implications of laser speckle for gas absorption measurements. Applied Physics B, 90(2), 279-288.

[31] Bomse, D. S.; Stanton, A. C.; Silver, J. A. (1992). Frequency modulation and wavelength modulation spectroscopies: comparison of experimental methods using a lead-salt diode laser. Applied optics, 31(6), 718-731.

[32] Hennig, O.; Strzoda, R.; Mágori, E.; Chemisky, E.; Tump, C.; Fleischer, M.; ...; Eisele, I. (2003). Hand-held unit for simultaneous detection of methane and ethane based on NIR-absorption spectroscopy. Sensors and Actuators B: Chemical, 95(1-3), 151-156.

[33] Le Barbu, T.; Vinogradov, I.; Durry, G.; Korablev, O.; Chassefière, E.; Bertaux, J. L. (2006). TDLAS a laser diode sensor for the in situ monitoring of H2O, CO2 and their isotopes in the Martian atmosphere. Advances in Space Research, 38(4), 718-725.

[34] Weibring, P.; Richter, D.; Fried, A.; Walega, J. G.; Dyroff, C. (2006). Ultra-high-precision mid-IR spectrometer II: system description and spectroscopic performance. Applied Physics B, 85(2-3), 207-218.

[35] Buchholz, B.; Kühnreich, B.; Smit, H. G. J.; Ebert, V. (2013). Validation of an extractive, airborne, compact TDL spectrometer for atmospheric humidity sensing by blind intercomparison. Applied Physics B, 110(2), 249-262.

[36] Michelucci, U.; Venturini, F. (2017). Novel Semi-Parametric Algorithm for Interference-Immune Tunable Absorption Spectroscopy Gas Sensing. Sensors, 17(10), 2281.

[37] Wang, J.; Yu, D.; Ye, H.; Yang, J.; Ke, L.; Han, S.; ...; Chen, Y. (2011, November). Applications of optical measurement technology in pollution gas monitoring at thermal power plants. In 2011 International Conference on Optical Instruments and Technology: Optical Systems and Modern Optoelectronic Instruments (Vol. 8197, p. 819702). International Society for Optics and Photonics.

[38] Reid, J.; Labrie, D. (1981). Second-harmonic detection with tunable diode lasers—comparison of experiment and theory. Applied Physics B, 26(3), 203-210.

[39] Xia, H.; Dong, F. Z.; Zhang, Z. R.; Tu, G. J.; Pang, T.; Wu, B.; Wang, Y. (2010, November). Signal analytical processing based on wavelet transform for tunable diode laser absorption spectroscopy. In Advanced Sensor Systems and Applications IV (Vol. 7853, p. 785311). International Society for Optics and Photonics.

[40] Zheng, C. T.; Ye, W. L.; Huang, J. Q.; Cao, T. S.; Lv, M.; Dang, J. M.; Wang, Y. D. (2014). Performance improvement of a near-infrared CH4 detection device using wavelet-denoising-assisted wavelength modulation

technique. Sensors and Actuators B: Chemical, 190, 249-258.

[41] Li, J.; Deng, H.; Li, P.; Yu, B. (2015). Real-time infrared gas detection based on an adaptive Savitzky–Golay algorithm. Applied Physics B, 120(2), 207-216.

[42] Meng, Y.; Liu, T.; Liu, K.; Jiang, J.; Wang, R.; Wang, T.; Hu, H. (2014). A modified empirical mode decomposition algorithm in TDLAS for gas detection. IEEE Photonics Journal, 6(6), 1-7.

2D -EEG Imaging Optimization Analysis Based Kriging Interpolation

Jifeng Hu; Fenghua Liu; Jianfa Meng

（jilin university instrument science and engineering institute,changchun,130021）

***Abstract*—Electroencephalogram (EEG) is produced by cerebral cortical neurons which contains information of physiology and disease. With the development of computer image processing technology, EEG imaging technology tends to be ripened. It has extremely wide application and important significance that EEG imaging method is used to analysis and diagnosis brain diseases in clinical and medical research. In this paper, the Ordinary Kriging Interpolation(OKI) method based on Gaussian variogram model is used to conduct EEG imaging. Through fitting the covariance function in variogram model, we get the functional relationship of the nugget C_0 and the correlation length a ,and use the Mean Kriging Variance(MKV) as the error evaluation criterion,.The nugget C_0 and the correlation length a can reach optimal values when MKV approaches zero and also Gaussian variogram model can reach optimize. Applying the optimal Gaussian model variogram to OKI, we will achieve optimal 2D-EEG imaging. The experiment result shows that the MKV of 2D -EEG Imaging based on Gaussian model variogram will be minimal through using this method.**

***Keywords* —EEG 2D-imaging Kriging interpolation variogram optimize**

1. INTRODUCTION

EEG is a weak, non-stationary and pseudo-random bioelectric signal produced by cerebral cortical neurons and it has abundant information about brain activity. With the development of information technology in recent years, the development of EEG processing technology has been greatly accelerated. EEG imaging analysis and its application in clinical research has increasingly become the focus of study[1].EEG imaging has great significance for targeting lesions such as cerebrovascular disease, hydrocephalus, brain tumors[2-7]and the clinical medical research on the characteristic of epilepsy, stroke and other diseases[8-13].

In 1989,Lee S H,Ko H W,Yoo S Kand others developed a computerized EEG imaging system with IBM PC AT. They used inverse distance weighted interpolation method to weight each interpolation point with its nearest four points and they successfully discovered the EEG imaging[14] technology. In 2011,Yang Qi,Wang Xiaofeng and others used the statistical analysis method of the mixed-effect polynomial regression model adopting the use of high-density electroencephalograms to describe changes in corresponding dynamic sources of EEG imaging during submaximal muscle contraction [15].In 2015,Paul Fergus, David Hignett and other scholars studied the epilepsy. The results showed that EEG imaging with the k-nearest neighbor interpolation method in most cases can effectively increase the sensitivity and reduce the errors[16].In 2017,Indian scholar Taran Sachin, Australian scholar Siuly Siuly, Turkish scholar Sengur A and other scholars used radial basis kernel function of IMF1 to classify EEG of different moving image tasks. This method showed better performance in accuracy and sensitivity of classification compared with the existing method [17].

Based on the above research, this paper optimizes the OKI algorithm based on Gaussian model variogram, and establishes the functional relationship between the parameters of the variogram using the method of data fitting and combining the MKV. Finally we achieve optimal 2D-EEG imaging.

2. METHOD

2.1 Ordinary Kriging interpolation

Kriging interpolation is a spatial interpolation algorithm that was first proposed by French statistician Matheron to perform unbiased optimal estimation of regionalized variables within a limited area [18-20].

The OKI method has the following constraints [21]:

$$E\left[Z\left(x+h\right)-Z\left(x\right)\right]=0 \qquad (1)$$

$$Var\left[Z\left(x+h\right)-Z\left(x\right)\right]=2\gamma\left(h\right) \qquad (2)$$

On the above equation, $Z\left(x+h\right)$ and $Z\left(x\right)$ are measured at the $x+h$ and x positions respectively, $\gamma\left(h\right)$ is the variogram corresponding to distance h .

The estimated value of the test point $Z^*\left(x_0\right)$ can be obtained from the measured value of the sample points $Z\left(x_i\right)$:

$$Z^*(x_0)=\sum_{i=1}^{n}\lambda_i Z(x_i)$$
$$\sum_{i=1}^{n}\lambda_i=1 \quad (3)$$

On the above equation λ is a weight coefficient.

The variance of the estimate is:

$$S=Var\left[Z^*(x_0)-Z(x_0)\right]=\sum_{i=1}^{n}\lambda_i\gamma(h_i)+L \quad (4)$$
$$(h_i=x_0-x_i)$$

Where L is the Lagrangian multiplier which is introduced to find the variance minimum value under constraints.

According to OKI, the estimated values of N test points can be acquired from the measured values of n sampling points $(N>>n)$.At the same time, it can also be used for EEG imaging. The MKV of the N test points is shown in equation (5).

$$\overline{S}=\sum_{l=1}^{N}S_l/N=(\sum_{l=1}^{N}\sum_{i=1}^{n}\lambda_{il}\gamma(h_{il})+\sum_{l=1}^{N}L_l)/N \quad (5)$$

Using the MKV method as the criterion of the EEG imaging system, when $\overline{S}=0$, It is regarded as the best EEG imaging.

2.2 Select the variogram model and determine the optimal relationship

It can be seen from equations (4) and (5) that the MKV has a close association with $\gamma(h)$ .The variogram is used to characterize the spatial variability of the region, and the variogram of an region is defined by the following equations:

$$\gamma(h)=Var[Z(x)]-C(h)$$
$$C(h)=Cov\left[Z(x+h),Z(x)\right] \quad (6)$$

In practical application, in order to simplify the calculation, the following variogram model is usually selected[21].

Gaussian model:

$$\gamma(h)=C_0+C_1\left[1-e^{-(h/a)^2}\right]$$
$$C(h)=C_1e^{-(h/a)^2} \quad (7)$$

Exponential model:

$$\gamma(h)=C_0+C_1\left[1-e^{-h/a}\right]$$
$$C(h)=C_1e^{-h/a} \quad (8)$$

Spherical model:

$$\gamma(h)=C_0+C_1\left[1.5(h/a)-0.5(h/a)^3\right](0\le h\le a)$$
$$\gamma(h)=C_0+C_1(h>a)$$
$$C(h)=C_1\left[1-1.5(h/a)+0.5(h/a)^3\right](0<h\le a) \quad (9)$$

The nugget C_0 in the formula is the deviation of the variogram caused by the error of sample points and the variability of the short distance. The correlation length a means that when the distances between two samples are greater than or equal to a definite distance, the sample points are independent of each other.

$C_0+C_1=Var[Z(x)]$ is called the sill.

It can be concluded that the values of the nugget C_0 and the correlation length a determine the value of $\overline{S}$. After comparison, Gaussian model is adopted in this paper. When C_0 and a reach optimization, the MKV approaches zero, which is shown in equation(10).

$$\overline{S}=(\sum_{l=1}^{N}\sum_{i=1}^{n}\lambda_{il}(C_0+C_1\left[1-e^{-(h_{il}/a)^2}\right])+\sum_{l=1}^{N}L_l)/N=0 \quad (10)$$

2.3 The nugget C_0 and the correlation length a optimal value acquisition

For n sample points, taking the distance h between any two sample points as the abscissa, and the value obtained from $C(h)$ in equation (6) as ordinate. Through quadratic curve fitting we obtain an approximate variogram of the sample region. The result is shown in Fig.1.

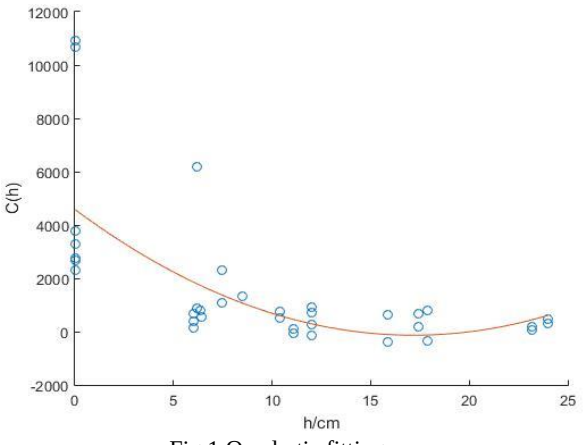

Fig.1 Quadratic fitting curve

The fitting polynomial is as following:

$$C(h)=m_2h^2+m_1h+m_0 \quad (11)$$

The relationship between a and C_0 is:

$$C_0 = Var[Z(x)] - \frac{\left(m_2 h^2 + m_1 h + m_0\right)}{e^{-(\frac{h}{a})^2}} \quad (12)$$

For different distances h, a and C_0 have a similar relationship, so we take the average value h_0 of all h into the above equation to get the optimal relationship between a and C_0, which is the following equation:

$$C_0 = Var[Z(x)] - \frac{\left(m_2 h_0^{\,2} + m_1 h_0 + m_0\right)}{e^{-(\frac{h_0}{a})^2}} \quad (13)$$

The relationship between a and C_0 is shown in Fig.2:

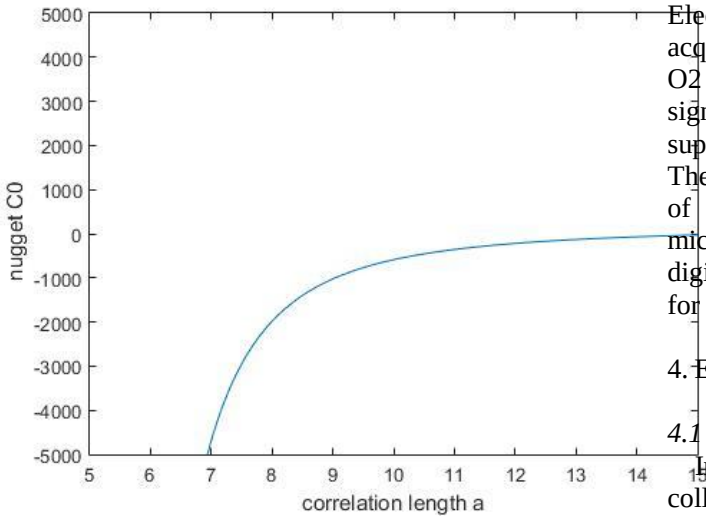

Fig.2 a - C_0 Relationship curve

It can be found the optimal values of C_0 and a by calculating equation (14).

$$C_0 = Var[Z(x)] - \frac{\left(m_2 h_0^{\,2} - m_1 h_0 + m_0\right)}{e^{-(\frac{h}{a})^2}}$$

$$\overline{S} = \left(\sum_{l=1}^{N}\sum_{i=1}^{n}\lambda_{il}\left(C_0 + C_1\left[1 - e^{-(h_{il}/a)^2}\right]\right) + \sum_{l=1}^{N} L_l\right) / N = 0 \quad (14)$$

The OKI used the optimized the nugget C_0 and the correlation length a has achieved optimization and using the results of the interpolation to 2D-EEG imaging for analysis of clinical diseases is relatively better.

3 .EEG SIGNAL ACQUISITION SYSTEM

Fig.3 shows a block diagram of an EEG acquisition system, which consists of acquisition electrodes, pre-filter amplification unit, AD conversion unit, microprocessor unit, Bluetooth communication unit, and host computer signal processing unit[3].

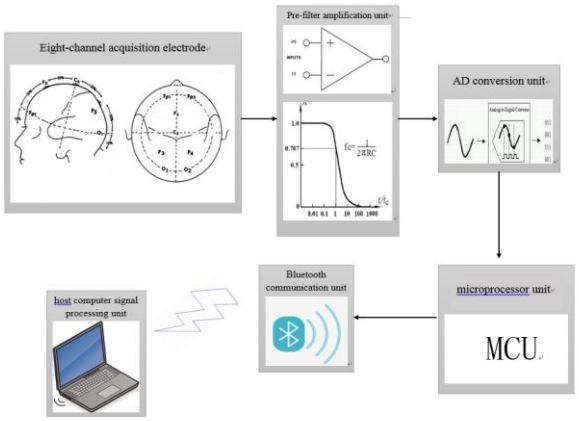

Fig.3 System block diagram

According to the International 10-20 System Electrode Placement Method, we choose eight acquisition electrodes Fp1,Fp2, Fz, Cz, P3, P4, O1, and O2 to collect EEG at the same time[22-23]. The useful signal is amplified while the noise of high frequency is suppressed through the pre-filter amplification unit. Then the AD conversion unit converts eight channels of analog EEG into digital signals. Finally the microprocessor unit is responsible for receiving these digital signals and transmitting it to the host computer for processing through Bluetooth communication[24].

4. EXPERIMENTS

4.1 EEG SIGNAL

In order to perform 2D-EEG imaging,The EEG collected at electrode location Fp1, Fp2, Fz, Cz, P3, P4, O1, and O2 by the acquisition system is shown in Fig. 4.

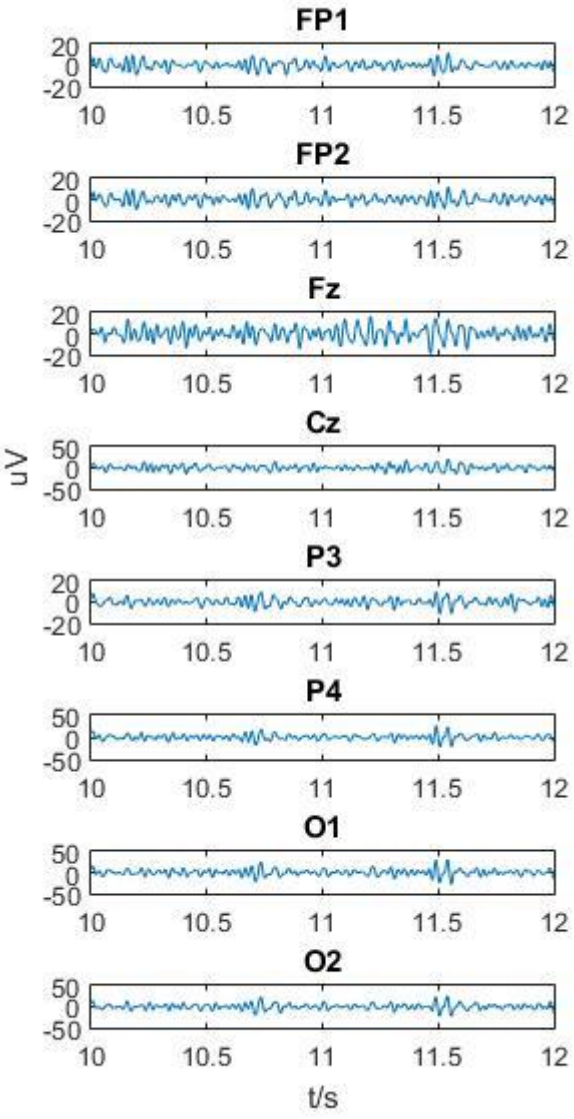

Fig.4 EEG signal

4.2 Variogram model selection

The selection of the variogram model in OKI has important significance for interpolation. Fig. 5, Fig. 6, and Fig.8 show the EEG imaging results and the corresponding variance distributions , variogram models are Gaussian model, exponential model, spherical model respectively.

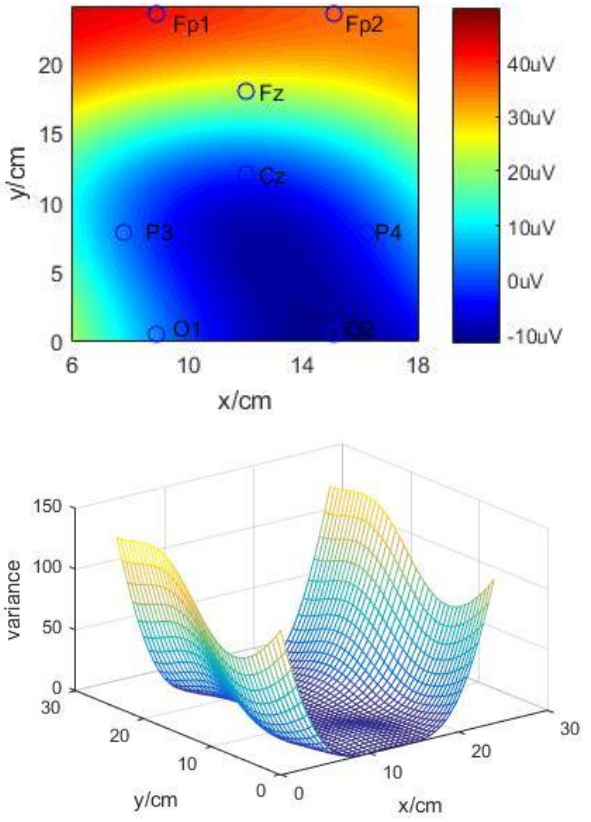

Fig.5 2D -EEG Imaging of Gaussian model and variance distributions map

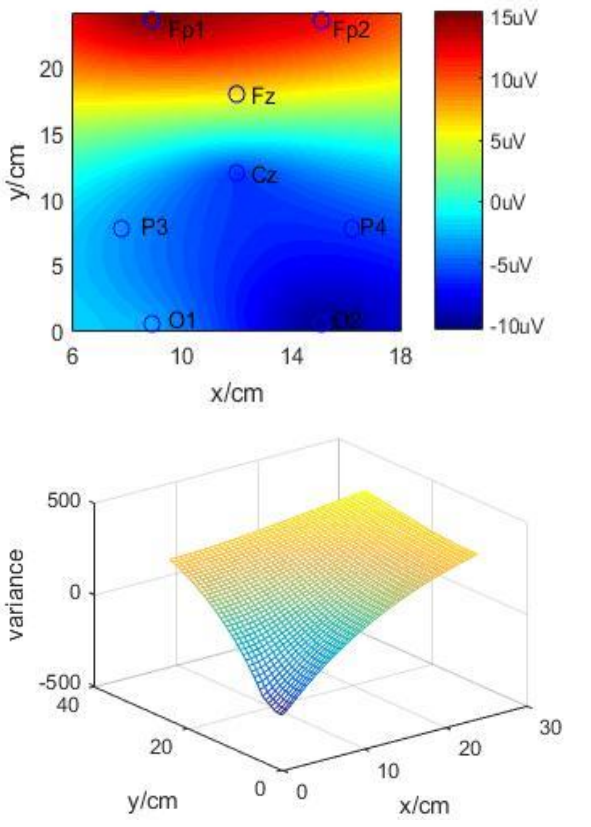

Fig.6 2D -EEG Imaging of Exponential model and variance distributions map

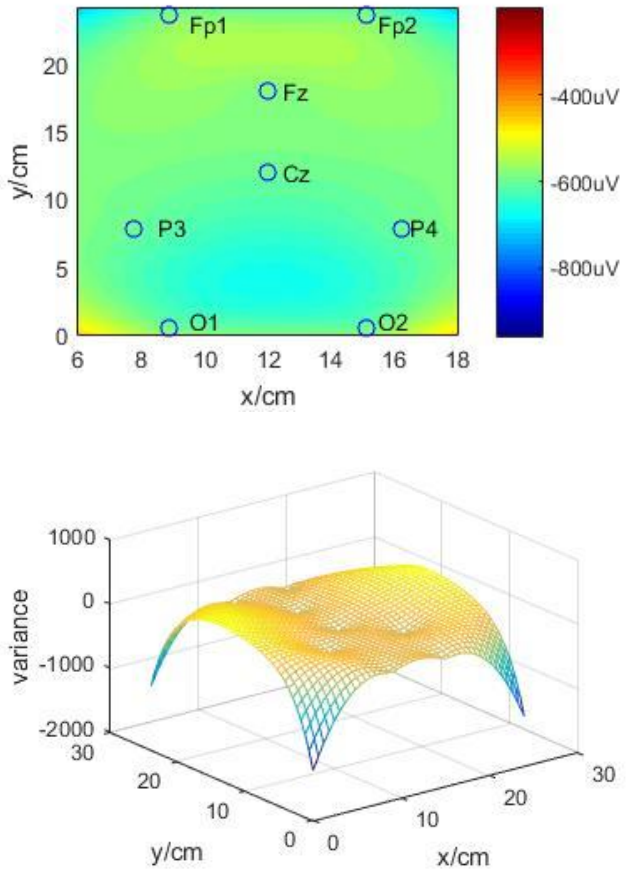

Fig.7 2D -EEG Imaging of Spherical model and variance distributions map

The distribution of the variance is shown in Figure 11:

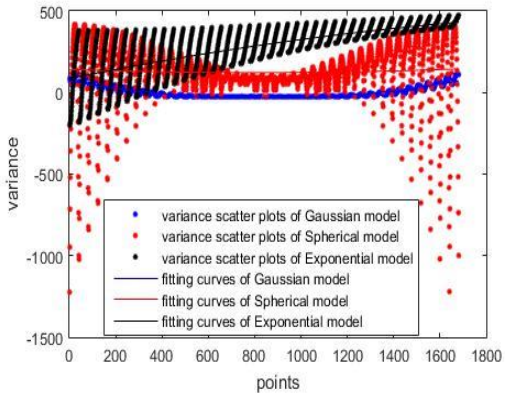

Fig.8 Variance scatter plots and fitting curves of different models

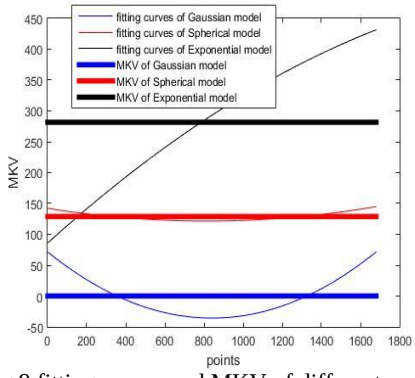

Fig.9 fitting curves and MKV of different models

From Fig.5 to Fig.9 the error of each test points in the Gaussian model is near zero, and the MKV is significantly lower than the other two models. Therefore, the variogram model used in the OKI is Gaussian model.

4.3 Optimal value determination

In the equation (10) , the correlation length a and the nugget C_0 are chosen different values, the consequence are shown in Fig10.

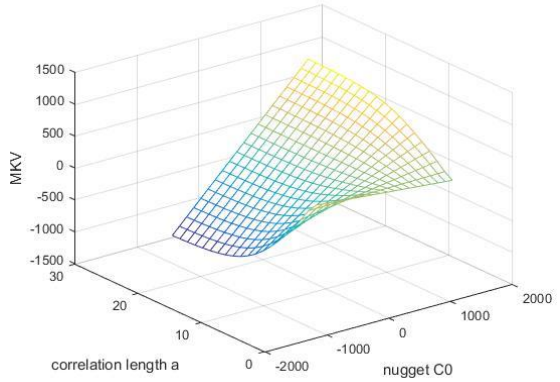

Fig.10 MKV distribution

Simultaneously equation 13 and equation 10 can get equation 14,which is shown in Fig11.

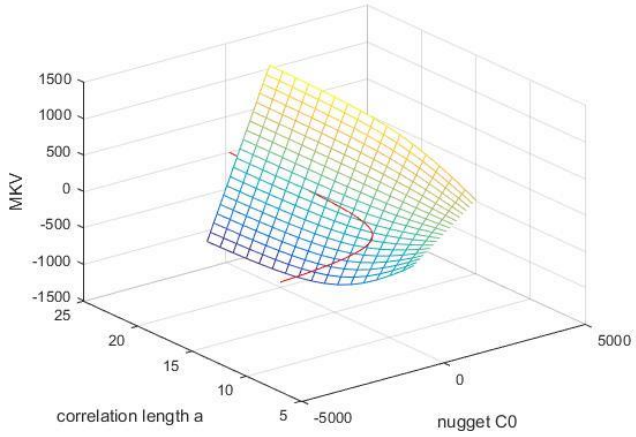

Fig.11 The intersection of the surface and the curve reflects the optimal value of the correlation length a and the nugget C_0 when the MKV $\overline{S}$ approaches zero.

4.4 Result analysis

Fig.12 shows the 2D-EEG imaging and corresponding error distribution maps in the experiments, when the correlation length a and the nugget C_0 are near the optimal value.

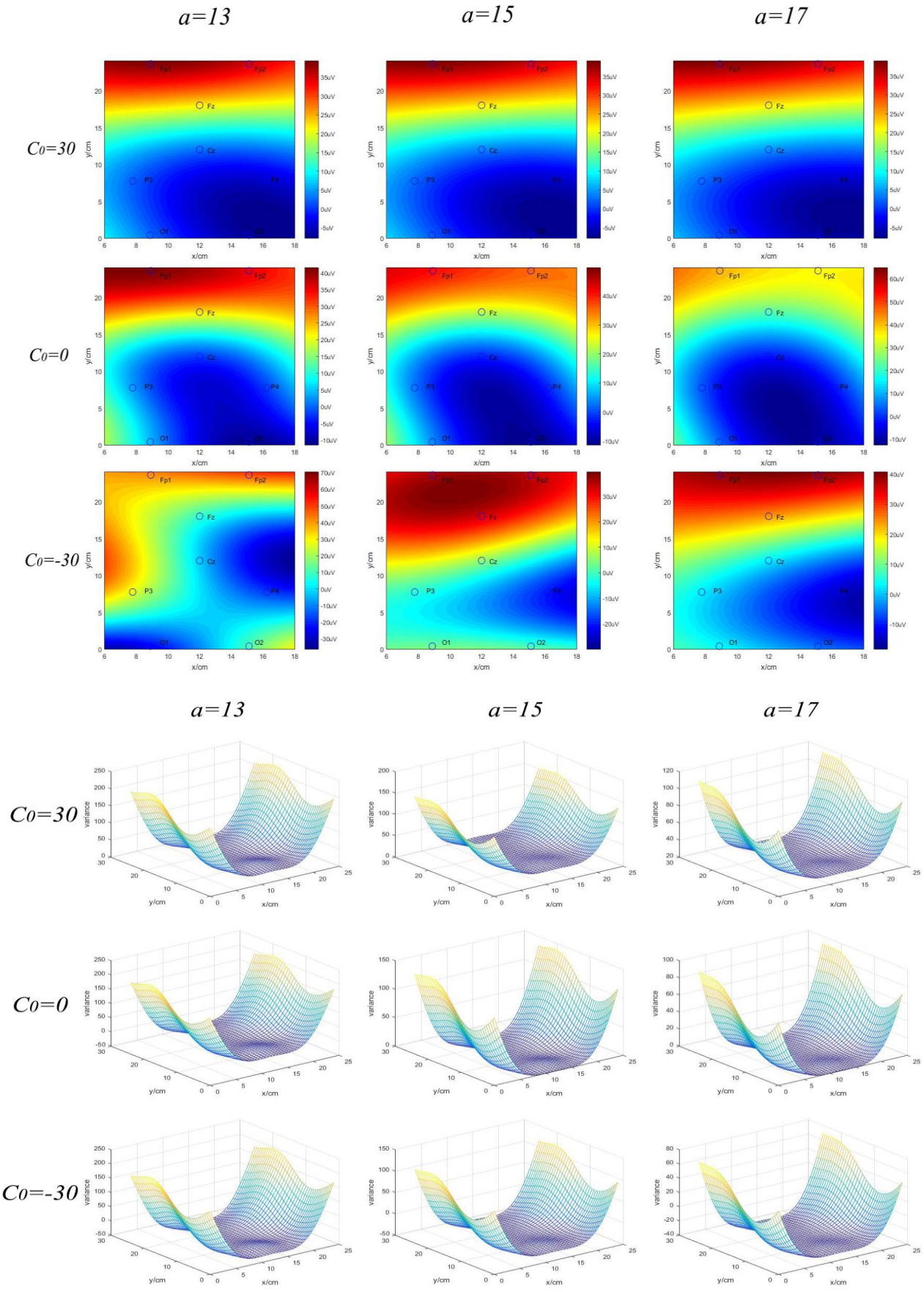

Fig.12 2D -EEG Imaging and variance distributions map

Table 1

The corresponding MKV in the above figure

	a =13	a =15	a =17
C_0 =30	74.7711	56.4347	45.5476
C_0 =0	48.7676	28.7943	16.9354
C_0 =—30	22.7640	1.1540	-11.6768

Based on the above experiments, a successive approximation method is used to obtain the optimal a and C_0 values when the MKV approaches zero[25].

Fig.13 is the optimal 2D -EEG Imaging and variance distributions map for a healthy male adult tester when the optimal values of a and C_0 are taken when the M KV approaches zero:

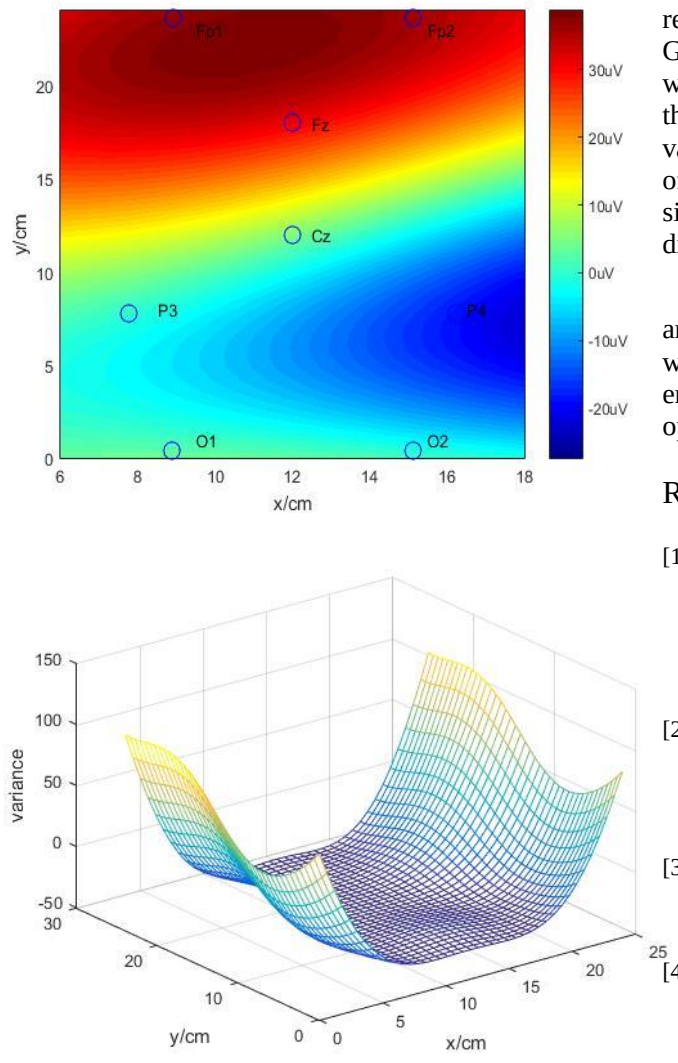

Fig.13 optimal 2D -EEG Imaging and variance distributions map

5. CONCLUSIONS

In this paper,we present a optimal 2D -EEG imaging method based on OKI.

The variance of 2D -EEG imaging using Gaussian variogram model is minimal with the experimental comparison. Then we fit the covariance function in Gaussian variogram model and get the functional relationship of the nugget C_0 and the correlation length a. The MKV is the error evaluation criterion, the nugget C_0 and the correlation length a will reach optimal values when MKV approaches zero and Gaussian variogram model can reach optimize. Finally we achieve optimal 2D-EEG imaging based on OKI through applying the optimal Gaussian model variogram to OKI. This method improves the accuracy of 2D-EEG imaging, making it easier to analyze EEG signals and obtain the information of physiology and disease from EEG signals.

However, it is obviously not enough to use MKV as an error evaluation criterion for 2D-EEG imaging. We will add the gradient of variance distribution as another error evaluation criterion criterion for 2D-EEG imaging optimization.

REFERENCES

[1] Hosseini,S.A.H.,Sohrabpour,A.,&He,B.(2018).Elect-romagnetic source imaging using simultaneous scalp EEG and intracranial EEG: An emerging tool for interacting with pathological brain networks. *Clinical Neurophysiology*, 129(1),168-187.

[2] Zhisuo,Z.,Ping,H.,& Jifen,Z.(1996). Contrastive analysis of BEAM, EEG and CT in ischemic cerebrovascular diseases. Chinese Journal of Stroke and Nervous Diseases,01,27-28.

[3] Chen,L.,Zhang,Q.,Wang,X.,&Luo,Q.(1994). Investigation of cerebrograph imaging system.He Jishu /Nuclear Techniques,17(5),277-280.

[4] Aoki,Y.,Kazui,H.,Tanaka,T.,Ishii,R.,Wada T.,Ikeda,S.,Hata,M.,Canuet,L.,Musha,T.,etal. (2013). EEG and Neuronal Activity Topography analysis can predict effectiveness of shunt operation in idiopathic normal pressure hydrocephalus patients.Neuroimage-Clinical,3,522-530.

[5] Bajaj,V.,Guo,Y.H.,Sengur,A.,Siily,S.,&Alcin,OF.(2017).A hybrid method based on time-frequency images for classification of alcohol and control EEG signals.Neural Computing&Applications, 28 (12),3717-3723.

[6] Seo,J.G.,Kang,K.,Jung, J.Y.,Park,S.P.Lee,M.G.,& Lee,H.W.(2014).Idiopathic Normal Pressure Hydro-cephalus, Quantitative EEG Findings, and the Cer-ebrospinal Fluid Tap Test: A Pilot Study.Journal of Clinical Neurophysiology,31(6),594-599.

[7] Ailing,Z.(2012). Application of EEG Topography in the Diagnosis of Brain Tumors. World Journal of Integrated Traditional Chinese and Western Medi-cine,7(05),441-442.

[8] Lu,Y.,Worrell,G.A.,Zhang,H.C.,Yang,L., Brinkma-nn,B.,Nelson,& C.,He,B.(2014).Noninvasive imag- ing of the high frequency brain activity in focal epilepsy patients.IEEE Transactions on Biomed- ical Engineering,61(6),1660-1667.

[9] Coito,A.,Michel,C.M.,van Mierlo ,P.,Vulliemoz S.,& Plomp,G.(2016).Directed Functional Brain Connectivity Based on EEG Source Imaging: Meth- odology and Application to Temporal Lobe Epile- psy.IEEE Transactions on Biomedical Engineering,63(12),2619-2628.

[10] Beniczky,S.,Rosenzweig,I.,Scherg,M.Jordanov,T.,etal.(201 6).Ictal EEG source imaging in pre- surgical evaluation: High agreement between a- nalysis methods.Seizure-European Journal Of E- pilepsy,43,1-5.

[11] Del Felice,A.,Storti,S.F.,&Manganotti,P. (2015).Sleep affects cortical source modulari- ty in temporal lobe epilepsy: A high-density EEG study.Clinical Neurophysiology.126(9),1677- 1683.

[12] GuhathakurtaDebarpan,Dutta,&Anirban(2015).Coutationa l Pipeline for NIRS-EEG Joint Imaging of tDCS-Evoked Cerebral Responses An Application in Ischemic Stroke.Frontiers In Neuroscience, 10,261.

[13] Antelis,J.M.;Montesano,L.,Ramos-Murguialday,A.,Birbau mer,N.;& Minguez,J.(2017).Decoding Upper Limb Movement Attempt from EEG Measurements of the Contralesional Motor Cortex in Chronic Stroke Pa-tients.IEEE Transactions On Biomedical Engineering.64(1),99-111.

[14] Lee,S.H.,Ko,H.W.,Yoo,S.K.,Kim,W.K.,Lee,H.S.,&Lee,H. Y.(1989).Development of a computerized EEG imaging system with a personal computer.Yonsei Medical Journal,30(1),45-53.

[15] Yang,Q.,Wang,X.,Fang,Y.,Siemionow,V.,Yao,W.,&Yue,G. H.(2011).Time-dependent cortical activation in voluntary muscle contraction.The open neuroimaging journal,5,232-9.

[16] Fergus,P.,Hignett,D.,Hussain,A.,Al-Jumeily,D.,&Abdel-A ziz,K.(2015).Automatic Epileptic Seiz- ure Detection Using Scalp EEG and Advanced Art- ificial Intelligence Techniques.BioMed Research International,986736.

[17] Taran,S.,Bajaj,V.,Sharma,D.,Siuly,S.,& Sengu-r,A.(2018).Features based on analytic IMF for classifying motor imagery EEG signals in BCI applications.Journal of the International Measurement Confederation,116,68-76.

[18] Davis John C(2002).Statistics and Data Analysis in Geology.New York:John Wiley&Sons,57-61.

[19] Li,L.,& Jianping,H.(2008). Application of Kri- ging Interpolation Algorithm in Contour Line Drawing. Journal of Tianjin Institute of Urban Construc- tion,14(1),68-71.

[20] Teng,X.,Jinhui,L.,Dianqing,L.,& Lei,S.(2016). Exploration Location Optimization Method Based on Ordinary Kriging Method.Journal of Wuhan Unive-rsity,49(5),714-39.

[21] Renduo,Z.Spatial Variation Theory and Applic-ation.Beijing: Science Press.

[22] Fahua,Z.,Lin,S.,& Xiaofen,X.. Study on Scalp Elect-roencephalography.(2017).Electronic Technolo- gy Application,43(12):3-8.

[23] Dezhong,Y. Research on the Setting of "Reference Electrode Location" in EEG Record.(2002). Clinical Journal of Neuroelectrophysiology.03:132-136.

[24] Shuiming,C.,Yinshan,G.,Yunfei,Z.,Jiandong,Y.,& Yunjia,W.(2015). Design of New Type of Power Acquisition Terminal Test Device Based on ARM. Electrical Technology.01:91-94.

[25] Changfeng,M.(1999).A Successive Approximation Method for Solving Simple-Boundary Constrained Optimization Problems. Mathematics for Comput- ational Mathematics in Colleges and Universiti- es.02:170-177. KV approaches zero:

Design of Ground Target Tracking System Based on Quadrotors

Yang Sien , Song Xingke，Tang Zhao, Wang Shilong
(*jilin university instrument science and engineering institute,changchun,130021*)

***Abstract*—Aiming at the defects that the current UAV tracking system is affected by the surrounding environment and the tracking accuracy is low, a four-rotor aircraft that can automatically identify and track ground targets is designed. Firstly, the flight principle of the four-rotor aircraft is analyzed to obtain the aircraft dynamics model. Then the computer vision technology is used to obtain the position parameters of the ground moving target, and the attitude of the aircraft is adjusted. Finally, the four-rotor aircraft will automatically take off, identify and track the ground target. After testing, when the aircraft takes off, the height axis overshoot is less than 8%. In the process of tracking, the roll axis error is less than 13cm, and the pitch axis error is less than 10cm, so as to achieve the requirement of stable tracking of ground targets.**

***Key words*— Four-rotor aircraft; Computer Vision; PID Controller; Battery Compensation**

I.INTRODUCTION

THE four-rotor aircraft is the simplest and most popular type of multi-rotor aircraft. Its four rotors are symmetrically distributed in the form of "十" or "X". Compared with helicopters, the four-rotor aircraft is simple in structure and suitable for the application in complex and small environment. Besides,The flight stability of the aircraft is better, and the ground effect is not obvious when landing [1]. Combining the above advantages, the four-rotor aircraft is used as an emerging air mobile platform in various fields, carrying various corresponding mission loads, and is widely used in film and television aerial photography, power cruise, intelligence surveillance, battle damage assessment, etc.So it's said that the four-rotor aircraft has extremely high application value and broad application prospects.

At present, there are many kinds of airborne monocular vision tracking methods.There is a commonly used method ,the optical flow sensor method [2], which uses the variation of pixels in the image sequence in the time domain and the correlation between adjacent frames to find the previous frame and the current frame. The method is used for calculating the motion information of an object between adjacent frames, but it has strict requirements on the target texture and low tracking accuracy;Another important method is simultaneous positioning and map creation methods based on image feature points [3]. Measuring the surrounding environment data through the sensor, the method gradually estimate its position and motion and depict the surrounding environment and map. The method has strict requirements on the performance of sensors and processors; The paper[4] designs a series of the ground mark composed of concentric rings to control the attitude of the aircraft in order to minimize the distance by calculating the distance between the center of the image and the center of the concentric circle; The text [5] designs a square ground mark by calculating the distance between the centroid. The aircraft is controlled to adjust the attitude, but this method uses the image features as input and the attitude parameters of the aircraft cannot be obtained.

The four-rotor aircraft tracking system designed in this paper effectively compensates for the defects of the optical flow sensor method and other methods, and makes full use of advanced computer vision technology to optimize the control algorithm and improve the tracking while acquiring target position information and aircraft attitude information.So the accuracy and system reliability are improved obviously.

II.PRINCIPLE AND ALGORITHM

2.1 Quad rotor attitude control principle

The aircraft adopts the X-type electric four-rotor structure and establishes the X-Y-Z coordinate system using the center of the aircraft as the origin (as shown in Figure 1). The angle that the body rotates around the X-axis is the roll angle. The angle that the body rotates around the Y-axis is the pitch angle. and the angle rotated around the Z-axis is the yaw angle (Yaw).The three angles are collectively referred to as Euler angles.

During the hovering process, the lift generated by the four rotors to the body is equal to the weight of the body itself. The rotors **M1** and **M3** rotate clockwise, and the rotors **M2** and **M4** rotate counterclockwise. The rotational inertia of each rotor is equal, which can offset the body's spin.

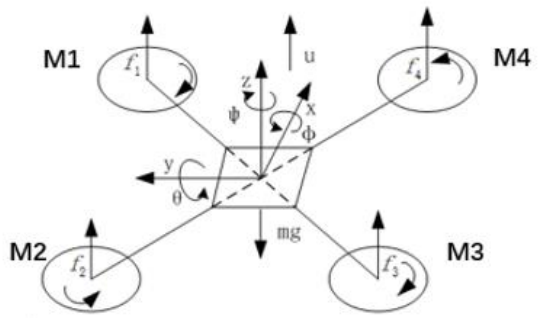

Figure 1 Spiral model of four-rotor aircraft

When flying vertically, the speed of the four rotors is increased at the same time, so that the pulling force **u** becomes larger. When **u**>**mg**, the flight is upward; When flying along the pitch angle, the rotational speeds of the rotors **M2** and **M3** increase simultaneously , and the rotational speeds of the rotors **M1** and **M4** decrease simultaneously. So the value of **f2+f3** increases, the value of **f1+f4** decreases, and the aircraft flies forward; When flying along the roll angle,the rotational speeds of the rotors **M3** and **M4** increase simultaneously, and the rotational speeds of the rotors **M1** and **M2** decrease simultaneously, making the value of **f3+f4** increases, the value of **f1+f2** decreases.The aircraft flies to the left;When flying along the yaw angle, the rotational speeds of the rotors **M2** and **M4** increase simultaneously, and the rotational speeds of the rotors **M1** and **M3** decrease simultaneously, so that the value of **f2+f4** increases, the value of **f1+f3** decreases and the aircraft rotates counterclockwise in the horizontal direction.

2.2 PID control algorithm

The PID controller has achieved very good control effect in the continuous control system and it has been widely used. The time domain differential equation of the PID controller is shown in Equation 1.

$$u(t) = K_p[e(t) + \frac{1}{T_i}\int e(t)dt + T_d\frac{de(t)}{dt}] \quad (1)$$

In the equation, K_P is the scale factor, T_i is the integration time constant, T_d is the differential time constant, $u(t)$ is the control volume, $e(t)$ is the amount of deviation between the expected value and the actual output value.

The schematic diagram of the PID control algorithm is shown in Figure 2.

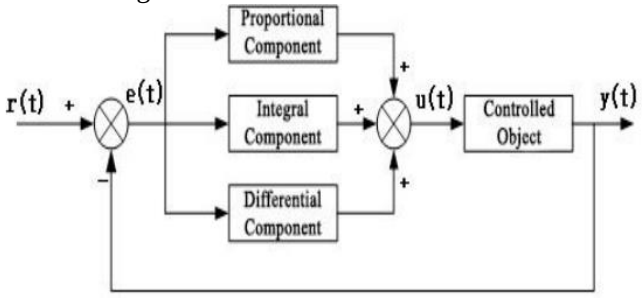

Figure 2 The schematic diagram of the PID control algorithm

In the figure, $r(t)$ is the expected value, $y(t)$ is the actual output value.

Equation (1) describes an analog PID controller that needs to be converted to a digital PID controller in computer control.

$$u_k = K_p\left[e_k + \frac{T}{T_i}\sum_{i=0}^{k} e_i + \frac{T_d}{T}(e_k - e_{k-1})\right] \quad (2)$$

Where, T is the sampling period, u_k is control volume.

In this paper, the PID algorithm is used for the control of the height, roll and pitch of the four rotor aircraft. Therefore, $r(t)$ is the height value or position coordinate expected by the aircraft. $y(t)$is the actual altitude value or position coordinate of the aircraft. $u(t)$ is the PWM (Pulse Width Modulation) duty cycle for controlling the four motor speeds of the aircraft. The controlled object is the four motors of the aircraft.

2.3 Open Source Computer Vision Library

Open-CV is an open source cross-platform computer vision library that runs on Linux, Windows and Mac OS operating systems. It consists of a series of C functions and a small number of C++ classes, and provides interfaces for languages such as Python, Ruby, and MATLAB. There are many general algorithms for image processing and computer vision. For the system with high real-time requirements of the aircraft, using computer vision technology to process the image can quickly obtain the tracking target position information to control the attitude of the aircraft in real time [6], so this paper uses Open-CV to realize the image processing of the system.

III.SYSTEM DESIGN

3.1 System Architecture

The whole system consists of control module, ranging module, image acquisition and processing module, and its overall block diagram is shown in Figure 3.

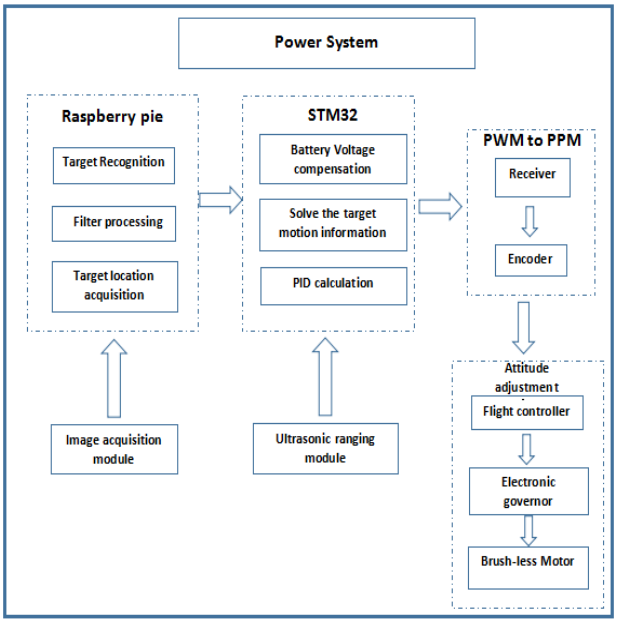

Figure 3 Overall system block diagram

3.2 Hardware design

3.2.1 Control module

The control module is composed of a central controller STM32 and a flight controller. After receiving the position information of the moving target, the STM32 performs solution calculation, and then calculates the moving direction, speed and acceleration of the target, and obtains a suitable roll value, pitch value and the yaw value through the PID control algorithm. According to the height measured by the distance measuring module, the corresponding throttle value is obtained, and then the four attitude values are sent to the encoder, and the encoder will have four postures. The PWM signal corresponding to the value is converted into a PPM signal and transmitted to the flight controller;The flight control board integrates a barometer, a 3-axis gyroscope, a 3-axis accelerometer, and various communication interfaces such as SPI and I2C, and the main control chip has a fast calculation speed. With powerful data processing capability, it can meet the requirements of the four-rotor aircraft as a hard real-time system. When the flight control board receives the PPM control signal, it converts the attitude values into Euler angle outputs and changes the four rotor speeds of the aircraft in order to achieve posture adjustment.

3.2.2 Ranging module

The ranging part adopts the HC-SR04 ultrasonic ranging module. The module's ranging range is 2~400cm; the IO port TRIG triggers the ranging, giving a high level signal of at least 10 microseconds.The module automatically sends eight 40KHz square waves and automatically detects whether there is a signal return.If any, the module outputs a high level through the IO port ECHO, and the high level duration is the time from the transmission to the return of the ultrasonic wave.Therefore, the test distance = (high time sound speed) / 2.

$$h = \frac{v \bullet t}{2} \tag{3}$$

Where ‘h’ is the height of the aircraft;’t’ is the time interval between the sound wave emitted and received;’v’ is the speed at which the sound travels in the air, taking 340 m/s.

3.2.3 Image acquisition and processing module

The image acquisition and processing section uses a monocular camera and a Raspberry Pi. The monocular camera has 8 megapixel resolution and auto-dimming and auto-focusing functions, which can effectively reduce the impact of aircraft vibration and the light intensity changes on the image acquisition during flight. So it has strong anti-interference ability,which meets the requirements of this system. Raspberry Pi uses ARMv7-based 32-bit Broadcom BCM2836 quad-core processor, loading Ubuntu operating system,which make it easy to use and develop. With 4 USB interfaces, the Raspberry Pi is easy to connect external devices and communicate with the main controller; Powered by a 5 V DC power supply, it can be powered directly from the aircraft, so it is compact and easy to carry.

3.3 Software design

The software design of the system is mainly divided into two parts. One is to control the four-rotor aircraft to achieve fixed-high flight and tracking flight; the other is to identify the ground moving target and obtain and solve its position information. Program flow chart is shown in Figure 4.

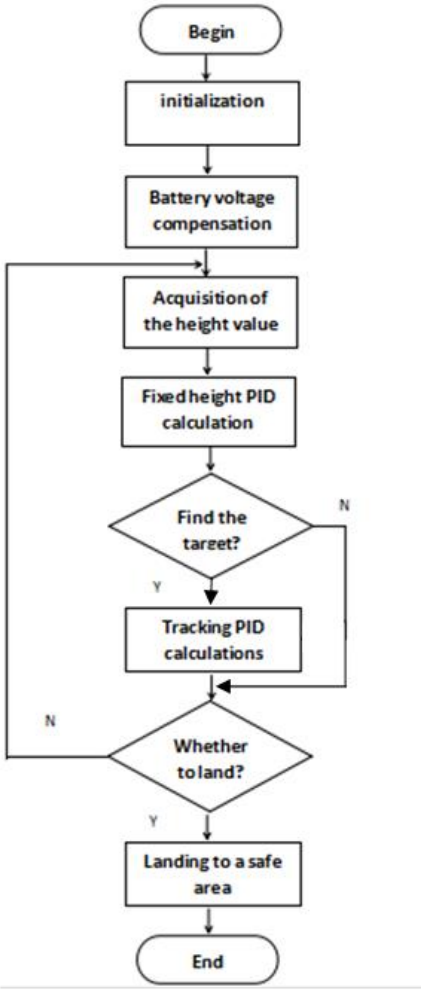

Figure 4 Program flow chart

3.3.1 Flight with a fixed height

During the flight, the ultrasonic ranging module measures the current flight altitude of the aircraft in real time, and transmits the altitude value to the main controller STM32. The main controller uses the positional PID algorithm to calculate the height direction PID, and finally converts the calculated result into the corresponding throttle value in order to control the speed of the rotor to change the height of the aircraft.

The expected and actual values of the flight height of the aircraft are used as the input and feedback of the PID controller respectively. The positional PID algorithm is shown in formula (2). $u(k)$ is the final control amount.

The relationship between the PWM control signal of the motor and the motor speed is affected by the battery output voltage. On the one hand, due to the internal resistance of the battery, a voltage drop occurs at the output of a large current, which lowers the output voltage. On the other hand, as the working time is extended, the amount of charge of the battery decreases, resulting in a decrease in the output voltage [7]. These two reasons will make the battery output voltage not constant, which causes the take-off stability and overshoot height to be different when the aircraft takes off at the same throttle value with different battery voltages. The system will use 11.4V to 12.6V as the normal working range of the battery, with 0.1V as the unit, with overshoot and rise time as the standard to test the ideal throttle value under different battery voltages. The test results are shown in Table 1(In appendix).

3.3.2 Tracking the ground target

After the target is recognized, the BGR color space image obtained by the camera is first converted into an HSV color space image, as shown in FIG. 5(a). Then the target threshold is set and the mask is constructed according to the threshold.The original image and the mask are performed the bit operation then the image after bit processing is shown in Figure 5(b). In the next step, the image and the set core are convoluted, firstly subjected to etching treatment, and the region with small gray value is enhanced and expanded to remove relatively bright noise; then the expansion processing is performed to enhance the expansion of the region with large gray value and connect areas of similar color. The process of first eroding and then expanding is called the morphological opening operation, and the image after the opening operation is shown in Fig. 5(c). Obviously, it can be seen that after the open processing, the noise in the image can be effectively filtered out, and the accuracy of the target recognition is improved. Finally, the minimum circumscribed circle of the target is made, and the target position is the center of the circumcision, and the Raspberry Pi sends the center information to the STM32 main controller to perform PID calculation.

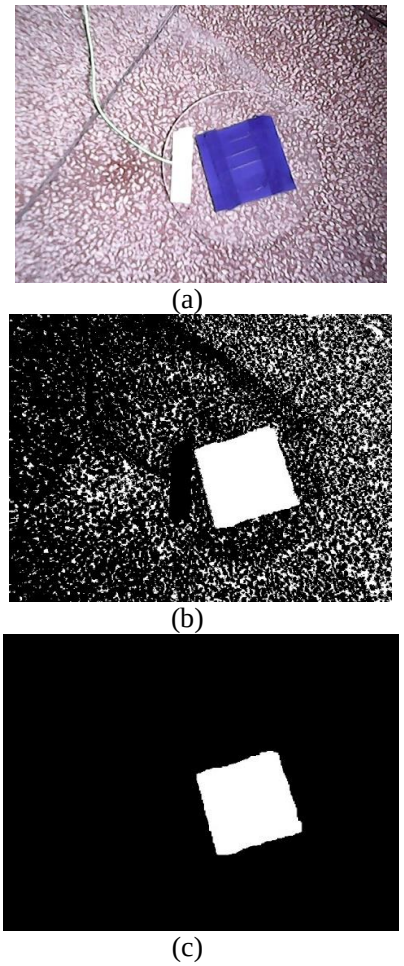

(a)

(b)

(c)

Figure 5 Image processing process diagram

3.4 Flight altitude information and analysis

In order to achieve short takeoff time, small overshoot, high stability during flight, etc., the coefficients Kp, Ki and Kd in the aircraft height axis PID controller are adjusted multiple times according to the PID parameter setting rules, and the altitude during flight is observed through the ground station. The information and the curve of the height change with time (as is shown in Figure 6), it can be seen from the figure that the overshoot is less than 8% during takeoff, the steady state error is less than 5%, and the flight stability is high. It can effectively avoid the problem of losing the target due to high instability during the tracking of the target.

Figure 6 Flight height curve of the aircraft

3.5 Target tracking information and analysis

During the tracking process, the target motion information is collected in real time through the monocular camera and transmitted to the Raspberry Pi. By constructing the plane rectangular coordinate system, the position coordinate x and the pitch direction position of the target relative to the aircraft in the roll direction can be obtained. The coordinates y are then calculated by the PID controllers in their respective directions to calculate the roll value and the pitch value. By adjusting the parameters of the PID controllers of the roll and pitch directions Kpx, Kix, Kdx and Kpy, Kiy, Kdy multiple times, the recognition speed is fast, the reaction is sensitive, and the tracking stability is high. Fig. 7(a) is a graph showing the variation of the roll direction deviation x with time in the tracking process, and Fig. 7(b) is a graph of the pitch direction deviation y as a function of time.

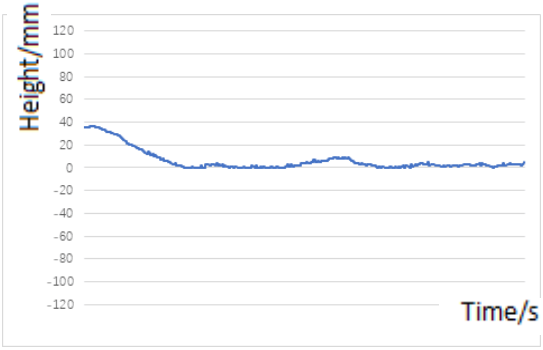

(a)

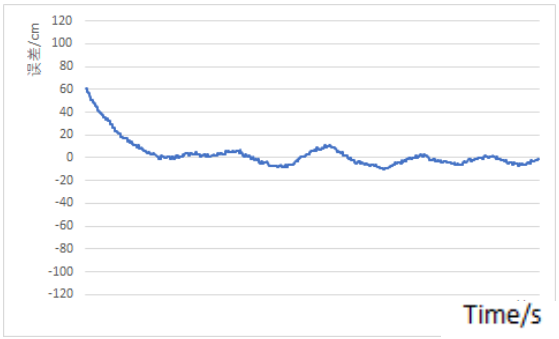

(b)

Figure 7 tracking error curve

According to the analysis of the figure, after the aircraft takes off, the target can be quickly identified and locked. The x-axis deviation does not exceed ±13cm during the tracking process, and the y-axis deviation does not exceed ±10cm. It has high reliability and anti-interference ability. Which can meet the requirement to stably track ground targets.

IV Conclusion

Based on the ground target tracking system of the four rotor aircraft, the ultrasonic module is used to acquire its own height information, and the camera module is used to obtain the target position information. Combined with computer vision technology, the functions of autonomous takeoff, automatic identification and tracking of targets are realized, and the speed is fast and stable. High and reliable, it realizes the automation and intelligence of the aircraft in the tracking process, and provides a reliable basis for the further development of the four rotor aircraft.

References

[1] Zhuang Chaowei, Jiang Bingyan, Zhao Dangjun, Han Jingxuan. Four-rotor aircraft controller based on tracking differentiator[J].Computer Simulation,2015,32(05):114-118.

[2] YUE Ji-long,ZHANG Qing-jie,ZHU Hua-yong.Research Progress and Key Technologies of Micro-miniature Four-rotor UAV[J].Electronics Optics & Control,2010,17(10):46-52.

[3] Honegger D,Meier L,Tanskanen P,etal.An open source and open hardware embedded metric optical flow CMOS camera for indoor and outdoor applications[C]//IEEE International Conference on Robotics and Automation.Piscataway,USA:IEEE,2013:1736-1741.

[4] Grzonka S,Grisetti G,Burgard W.A fully autonomous indoor quadrotor[J].IEEE Transactions on Robotics,2012,28(1):90-100.

[5] Lange S,Sunderhauf N,Protzel P.A vision based on board approach for landing and position control of an autonomous multirotor UAV in GPS-denied environments[C]//International Conference on Advanced Robotics.Piscataway,USA:IEEE,2009:674-679.

[6] Santamaria-Navarro A,Andrade-Cetto J.Uncalibrated imagebased visual servoing[C]//IEEE International Conference on Robotics and Automation.Piscataway,USA:IEEE,2013:5247-5252.

[7] Sun Ning,Fang Yongchun.Overview of Control Methods for a Class of Underactuated Systems[J].Journal of Intelligent Systems,2011,6(03):200-207.

[8] SUKTHANKAR R.PCA-SIFT:A More Distinctive Representation for Local Image Descriptions［C］// Proceedings Conference Computer Vision and Pattern Recognition．Washington，DC:IEEE，2004: 511-517．

[9] Du Cong.Discussion on Open-CV Computer Vision Library[J].Science and Technology Information,2016,14(28):7-8.

[10] Li Yanhui,Tang Shengjing,Yang Shengyi,Liu Chao,Liu Yangyang.Modeling and experiment of four-rotor power system based on voltage compensation[J].System Engineering and Electronics,2014,36(05):934-939.

Table 1 Battery voltage compensation table

Voltage value	12.6	12.5	12.4	12.3	12.2	12.1	12.0	11.9	11.8	11.7	11.6	11.5	11.4
Throttle value	1272	1280	1300	1308	1312	1326	1330	1336	1342	1349	1354	1363	1372
Tr(s)	2.4	2.3	2.4	2.5	2.3	2.4	2.5	2.4	2.4	2.3	2.4	2.4	2.5
Δ（%）	10.2	10.3	10.2	10.3	10.4	10.2	10.3	10.4	10.4	10.3	10.3	10.4	10.4

Note: Tr is the rise time and Δ is the overshoot

Multi-degree-of-freedom manipulator trajectory planning method based on genetic algorithm

Wang Hualiang; Yin Guanxu; Liu Qian
(College of Instrument Science and Electrical Engineering, Jilin University, Changchun 130061, China)

***Abstract*—This article is aimed at how to achieve a fast and efficient trajectory for a robot with six degrees of freedom commonly used in industry.The robot D-H coordinate system constructed in this paper utilizes the D-H modeling method.The robot is analyzed using positive kinematics. Taking the shortest time as the goal of optimization, introducing a genetic algorithm while considering the constraint relationship of multiple nodes. Finally, the optimal joint angle of a set of mechanical arms is obtained through simulation analysis, which satisfies the shortest movement time of the mechanical arm.**

***Key words*—six-degree-of-freedom manipulator; positive kinematics; trajectory planning; Matlab simulation**

1. INTRODUCTION

WITH the development of science and technology, the mechanical arm has been applied to many fields, and a robot with high degree of freedom has been developed to accomplish high-complexity tasks. As the degree of freedom increases, the link motion has stronger coupling [1]. Therefore, it is difficult to solve the trajectory planning problem of multi-constrained multi-body systems with multi-parameters, strong coupling and nonlinear motion [2]. How to improve the efficiency of path planning is of great significance to the working efficiency and motion accuracy of the mechanical arm system.

2. KINEMATICS ANALYSIS OF A SIX-DEGREE-OF-FREEDOM MANIPULATOR

Robot kinematics is a method of analyzing the relationship between the pose of a robot and each of its joints and robots. It is divided into two categories, positive kinematics and inverse kinematics [3-4]. The forward kinematics analysis robot can obtain a positive kinematics solution of the robot. This method starts from the beginning of the robot and passes through each joint.

And the variable reaches the end to calculate the transformation matrix of the end pose. According to the DH modeling analysis method [5], a reference coordinate system is established for the robot arm, as shown in Fig. 1 below. The DH parameters are shown in Table 1.

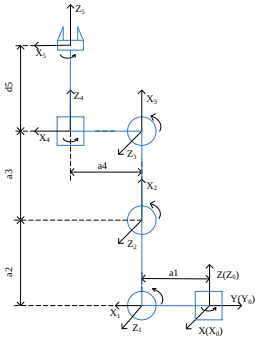

Fig. 1.Six-degree-of-freedom manipulator model

Table 1 Robot DH parameters

Link number	θ	d	a	α	Joint limit
1	θ1	0	a1	-90 °	-180 ~180 °
2	θ2	0	a2	0	-135 ~135 °
3	θ3	0	a3	0	-135 ~135 °
4	θ4	0	a4	90 °	-135 ~135 °
5	θ5	d5	0	0	-180 ~180 °

$$T_{i-1}^{i}=\begin{pmatrix}\cos(\theta_i) & -\sin(\theta_i)*\cos(\theta_i) & \sin(\theta_i)^2 & a_n*\cos(\theta_i)\\ \sin(\theta_i) & \cos(\theta_i) & -\cos(\theta_i)*\sin(\theta_i) & a_n*\sin(\theta_i)\\ 0 & \sin(\theta_i) & \cos(\theta_i) & d_n\\ 0 & 0 & 0 & 1\end{pmatrix}$$

where:

Ti_{i-1}: coordinate transformation matrix of coordinate system i to i+1

d_n: the distance between two adjacent joints X_i and X_{i+1} axes;

a_n: the distance between two adjacent joints Z_i and Z_{i+1} axes;

θ_i: the angle between the two axes of X_i and X_{i+1}, which is right-handed around the Z-axis as a positive direction;

α_i: The angle between the two axes of Z_i and Z_{i+1}, which is right-handed around the X-axis in the positive direction.

$$^{R}T_{H}=\begin{bmatrix}n & o & a & p\\ 0 & 0 & 0 & 1\end{bmatrix}=\begin{bmatrix}n_x & o_x & a_x & p_x\\ n_y & o_y & a_y & p_y\\ n_z & o_z & a_z & p_z\\ 0 & 0 & 0 & 1\end{bmatrix}$$

where $\boldsymbol{p} = [p_x, p_y, p_z]^T$ is the position vector of the end effector relative to the base coordinate system. $n=[n_x, n_y, n_z]^T$, $o=[o_x, o_y, o_z]^T$, $a=[a_x), a_y, a_z]^T$ is the pose vector of the end effector relative to the base coordinate system.

According to the robot in the initial state, the DH coordinate system shown in Fig. 1 and the manipulator parameters in Table 1 are selected, and the forward kinematics model is established, as shown in Fig. 2.

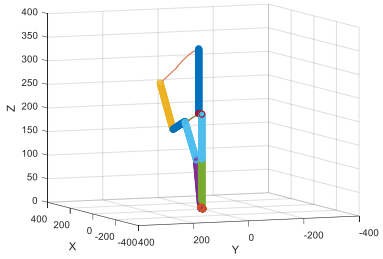

Fig.2.Joint motion trajectory simulation

3.OPTIMIZATION OBJECTIVE FUNCTION

The object of this paper is the six-degree-of-freedom manipulator. The speed of the steering gear of each joint is constant. It can be known that the coordinate system at the end of the manipulator is a rotating system, so the change of the fifth joint will not affect the change of the end, and thus can be ignored. .

3.1 Constraints

(1) Joint constraint: The genetic algorithm is actually planned to be the joint angle, so the genetic algorithm should take into account the positive and negative limits of the joint angle when generating the population individual and encoding the individual population. The positive and negative limits are shown in Table 1 above.

(2) Spatial position constraints:

$$F1=\sqrt{(x-xf)^2+(y-yf)^2+(z-zf)^2}$$

Where: the end of the arm is in real time (x, y, z) And target point (xf, yf, zf)

F1 is the deviation between two points.

(3) Rod length physical constraints:

$$l_{\max} \le l_{cur} \le l_{\max}$$

(4) where: lmax is the distance from the end of the initial pose arm to the origin of the base coordinate system, lcur is the real-time moving distance from the end of the arm to the origin of the base coordinate system, and lobj is the end of the arm to the base The distance from the origin of the coordinate system.

3.2 fitness function

In order to find a set of joint angles at which the robot arm can reach the target point and spend the shortest time, the fitness function can be set to:

$$Fit=\begin{cases}\alpha\cdot max(|\theta_1/\omega_1|,|\theta_2/\omega_2|,|\theta_3/\omega_3|,|\theta_4/\omega_4|)+\beta\cdot F1 & l_{obj}\le l_{cur}\le l_{\max}\\ \alpha\cdot max(|\theta_1/\omega_1|,|\theta_2/\omega_2|,|\theta_3/\omega_3|,|\theta_4/\omega_4|)+\beta\cdot F1+\gamma & else\end{cases}$$

In this paper, the robot arm movement time is optimized, but the premise of optimizing the motion time is that the end of the arm must reach the target point, so the weight coefficient in the fitness function should be satisfied. $\beta \ge \alpha$ The greater the weight coefficient, the more important it is to be given priority. In the formula γ As a constant, it can be adjusted according to the optimization effect.

4.OPTIMIZING TRAJECTORY BASED ON GENETIC ALGORITHM

In this paper, after several simulations, the genetic algorithm is optimized, and N=100 is the population size of the genetic algorithm.Using binary coding, the genetic algebra is g=500, the recombination crossover probability is 0.7, and the mutation probability is 0.5.At the same time, continuously adjust the weight coefficient, and finally determine the weight coefficient $\alpha=1$, $\beta=100$, β ratio α The reason for the large amount is that the penalty function becomes small when the end of the arm approaches the target point. In order to make the error as small as possible, a certain degree of amplification error is required to make the objective function relatively large. However, when the joint angle does not satisfy the constraint, in order to eliminate the population, it is necessary to make the evaluation fitness relatively small, so a larger constant can be added after the objective function. γ , taken in this article $\gamma=1000$ The reason why the objective function is not directly equal to a larger constant is to increase the diversity of the individual population and speed up the convergence.

The above process was designed by Matlab, and the simulation results of the shortest path of the manipulator time were analyzed. The simulation results are shown in Figures 3 and 4 below:

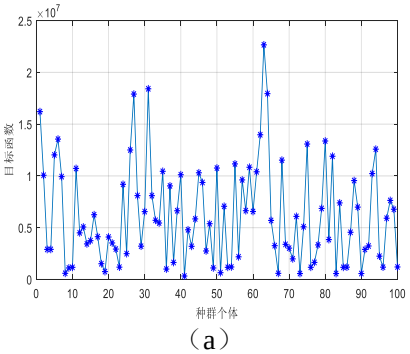

（a）

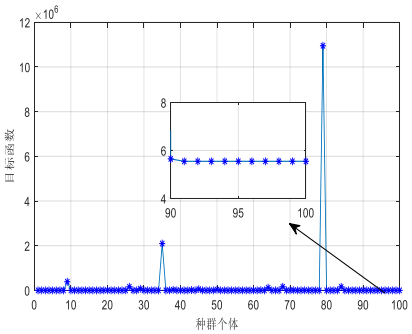

（b）

Fig. 3(a) Distribution of individual objective function of the first generation population of GA algorithm (b) Distribution of individual objective function of the 500th generation of GA algorithm

Figure 3(a) shows the distribution of the objective function of the first generation population of the genetic algorithm. It can be seen from the figure that the objective function is randomly distributed and presents disorder. With the increase of genetic algebra, the genetic algorithm gradually converges. (b) When the 500th generation, the objective function has mostly concentrated on a certain value, which verifies the convergence of the genetic algorithm.

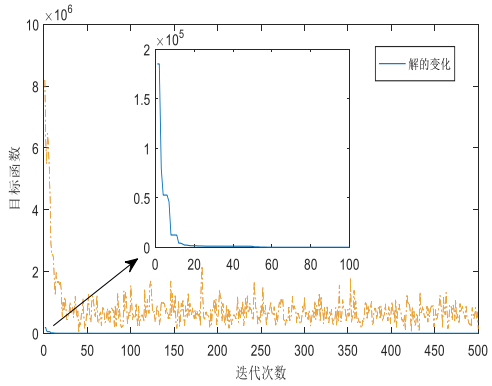

（a）

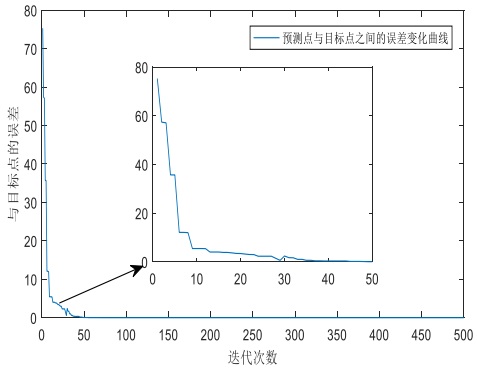

（b）

Figure 4 (a) Genetic Algorithm Performance Tracking
(b) Error variation during iteration

It can be seen from Fig. 4(a) that the genetic algorithm discussed in this paper has superior performance and fast convergence, which can meet the requirements of robot arm trajectory planning and design. It can be concluded from Fig. 4(b) that as the number of iterations increases, the end of the arm becomes closer to the target point and eventually stabilizes at the target point. Through Matlab programming simulation, a set of optimal solutions is finally obtained.

5.IN CONCLUSION

In this paper, the positive kinematics of the manipulator is simulated and analyzed, and the positive kinematics model of the six-degree-of-freedom manipulator is built. Secondly, the genetic algorithm is used for path planning for the six-degree-of-freedom manipulator. It can be seen from the simulation analysis that the genetic algorithm can improve the speed and efficiency of the trajectory planning, and provides reference and reference for the trajectory planning of the robot arm.

References

[1] Hu Youzhong. Optimal trajectory planning of mechanical arm based on dynamics [D]. Zhejiang University, 2016.

[2] Peng Daihui, Zou Xianchun, MATLAB2013 practical tutorial, Beijing Higher Education Press, 2014.8, 221 P

[3] Reynoso-Mora P, Chen W, Tomizuka M. On the time-optimal trajectory planning and control of robotic manipulators along predefined paths[C]// American Control Conference. IEEE, 2013:371-377. Zhang Xiulin. Based on heredity Algorithmic robot arm time optimal trajectory planning [D]. Lanzhou University of Technology, 2014

[4] Zhang Xiulin. Time-optimal trajectory planning of manipulator based on genetic algorithm [D]. Lanzhou University of Technology, 2014.

[5] Zhou Gaofeng, Zhu Qiang, MATLAB Engineering Basic Application Tutorial [J] Mechanical Industry Press, Beijing.2015.1:207

The Design and Research of Rehabilitation Training System Based on Kinect

Zhang Xinhao; Tao Jin; Liu Junlin
（jilin university instrument science and engineering institute,changchun,130021）

***Abstract*—Aiming at demand for rehabilitation training of patients with motor dysfunction, a rehabilitation training system based on Kinect somatosensory device was designed. The system collect human real-time skeleton data with Kinect, calculate the Angle between feature nodes, and form the Angle sequence. The DTW algorithm is used to compare the similarity between the measured Angle sequence and the standard action sequence of the action library, judge whether the action is standard and output the evaluation results.It is easy to use and low cost, which improves the fun of the training process. The test results show that the system realizes the rehabilitation training guidance for the patients with sports disorder through human-machine interaction, which has a positive influence on the rehabilitation training process.**

***keywords*—Kinect; Rehabilitation Training; DTW Algorithm; Human-computer Interaction**

I. INTRODUCTION

REHABILITATION training is an important part of medical services and has always been a hot spot in the medical field. At present, the majority of domestic medical rehabilitation still adopts the traditional rehabilitation training method, but it is limited by the training place, medical equipment, physician level and so on, and cannot have a good training effect. Foreign countries have preliminarily built an industrial chain of medical and rehabilitation big data: from sensor research and development to intelligent wearable devices and detection devices to intelligent analysis of data storage to big data, all of which have begun to take shape. With the development of science and technology, new interactive technology has entered people's attention, and more and more people use this technology for body sense rehabilitation training[1]. TAYLOR M J et al. first confirmed the feasibility of Kinect in the field of rehabilitation[2-3], and then WANN J P[4] etal. proposed visual rehabilitation treatment.

One of the important tasks to realize the new rehabilitation training is to complete the action recognition. At present, there are some problems in some popular visual recognition.The action recognition based on monocular vision is vulnerable to the influence of light , color and other environmental factors,while the recognition based on binocular vision can largely avoid these influences, but the calculation process is relatively complex[5]. In addition, traditional human motion recognition is difficult to complete the task of continuous motion recognition[6]. With the advent of Kinect depth somatosensory camera, more and more researchers have realized that depth images and skeleton information can change the application status in the field of motion recognition.

It will be a new attempt in the field of medical rehabilitation to study an efficient and accurate motion recognition algorithm, and to combine 3d somatosensory technology with computer vision algorithm. Therefore, we designed a system of rehabilitation training assessment based on Kinect to liberate rehabilitation training to communities and families. Thiscan not only alleviate the work of medical staff, but also let patients experience more funin the rehabilitation training,which hasa positive impact on the entire rehabilitation trai-ning process.

II. OVERALL SYSTEM DESIGN

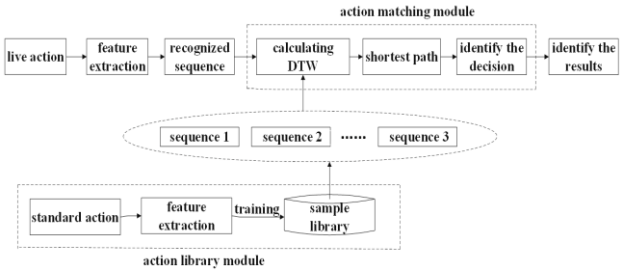

Fig. 1. System structure diagram

This rehabilitation training system mainly consists of four modules: training guidance module, motion matching module, training evaluation module and motion library module. The figure above shows the relationships among the modules.

--Action library module. The non-specific person recognition template training method is adopted, and the standard movements provided by rehabilitation training physicians are input by multiple people. The movements of multiple people are integrated, the common features are extracted, and the bone node data of movement movements are recorded to form the standard movement templates.

--Training guidance module. Patients are provided with recorded standard movements video, and corresponding text and voice instructions are provided simultaneously during the training to regulate the training movements of patients.

--Action recognition module. By reading the real-time bone node data of patients, extracting the coordinates of feature nodes and transforming them into Angle sequences, DTW algorithm was used to match the Angle sequences with the sample sequences in the sample database to make decisions.

--Training evaluation module. All motion data of patients were collected, training scores were calculated, and rehabilitation training data were analyzed and evaluated. The evaluation results are directly reported

to the patients or the treatment staff and used as the basis to determine the next treatment plan.

III. FEATURE EXTRACTION AND MODEL CONSTRUCTION

A. Action Feature Extraction

The Kinect sensor is connected with the computer through the data cable, and installed in the front of the computer screen. The human body stands straight in the right position, so that the Kinect can obtain the bone nodes of the whole body. The data collected by Kinect was transmitted to the front-end system through the interface function, and the figure of human skeleton was obtained in the computer.

Establish the three-dimensional space coordinate system of Kinect with camera space. Take the left direction of the radiation direction following the Kinect as the X axis, the upper direction of the radiation direction as the Y axis, and the irradiation direction as the Z axis, and obtain the coordinates of each skeleton node of the human body in this coordinate system.

Since the real-time coordinate data of each node obtained by Kinect is greatly affected by individual differences, in order to reduce such errors, the coordinate changes of joints in the process of motion are converted into the Angle changes to study, that is, the Angle is selected as the motion feature. By calculating the Euclidean distance between the bone nodes and using the triangle cosine theorem, the Angle between the two nodes can be obtained.

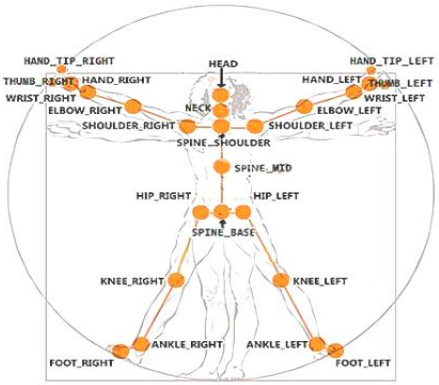

Fig. 2. 25 nodes obtained by Kinect

Euclidean Distance is a commonly used Distance definition, which is the real Distance between two points in an n-dimensional space. Suppose there is some point x and y, then the Euclidean distance between these two points[7].

$$d_{(x,y)} = \sqrt{\sum (x_i - y_i)^2}\, i = (0,1,2,\ldots,n)$$

Taking the left arm movement of the human body as an example, the left shoulder joint point, the left elbow joint point and the left wrist joint point are selected, which are set as J1(x1,y1,z1), J2(x2,y2,z2) and J3(x3,y3,z3) respectively. Suppose the length of connection points J1 and J2 is D1, the length of connection points J2 and J3 is D2, and the length of connection points J_1 and J_3 is D_3. According to the Euclidean distance formula,

$$D_1 = \sqrt{(x_2 - x_1)^2 + (y_2 - y_1)^2 + (z_2 - z_1)^2}$$

$$D_2 = \sqrt{(x_3 - x_2)^2 + (y_3 - y_2)^2 + (z_3 - z_2)^2}$$

$$D_3 = \sqrt{(x_3 - x_1)^2 + (y_3 - y_1)^2 + (z_3 - z_1)^2}$$

Then, the value of the flexor and extensor of elbow joint can be calculated by the cosine theorem. The formula is as follows:

$$\beta = \arccos \frac{D_1^{\,2} + D_2^{\,2} - D_3^{\,2}}{2 D_1 D_2}$$

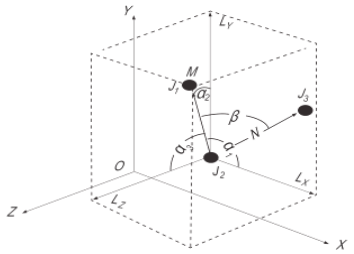

Fig. 3. Spatial Angle diagram

B. Action Modeling

The action process can be decomposed into a series of frames, each of which contains a static position, so the dynamic action can be regarded as a combination of a series of static positions, which means that the expression of the action has the property of time duration[8]. Kinect can obtain data of about 30 frames per second. It takes every 3 frames as a sampling period for data collection, and takes an average of 30 frames as the total length of the motion template. As time goes on, the static position will generate a set of vectors composed of the node Angle scalar at the same sampling interval. This set of vectors reflects the change process of action. Take the change of the Angle of the left shoulder joint when the left hand is lifted as an example, only 4 frames (frame 1, 10, 20 and 30) are intercepted below to show the motion process:

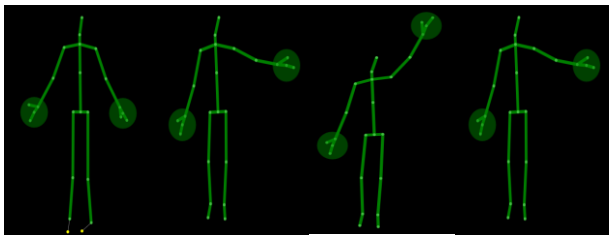

Fig. 4 Schematic diagram of left hand lifting

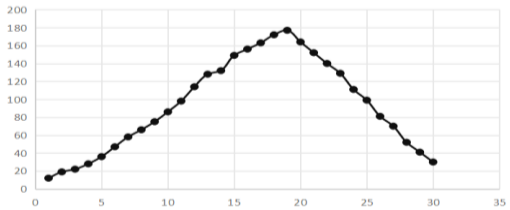

Fig. 5. Angle change curve of left shoulder joint

As shown in the figure, as the joint angle changes over a period of time during body movement, an angle change curve will be generated, namely the joint angle time series, which is a one-dimensional vector of time. Like the trajectory of the end of the limb during movement, the joint angle curve can reflect the

movement trend. Therefore, we use the joint angle time series as the characteristic parameter of limb movements. If the duration of the maintenance dimension of a movement is X, the dynamic motion features can be abstracted into the following formula:

$$A=[\theta_1,...\theta_i...\theta_M]$$

Where, A represents the time series of a joint, and is a column vector of length X; M is the number of nodes selected.

IV STANDARD TEMPLATE TRAINING

B. Action Library Composition

According to the requirements of patients, rehabilitation physicians design a set of standard rehabilitation training movements. Many individuals conduct motion input, extract motion features, and calculate the Angle sequence according to the coordinate relations between the bone nodes, as the standard movement template. The 3d animation video is also produced and played on the system interface to guide the movements of patients. This design selects 12 professional rehabilitation exercises, as shown in the following table.

TABLE I
Rehabilitation training movement

Serial number	Action name	Action interpretation
1	left shoulder joint abduction	the body upright, left arm unbend along the lateral carried the body's center line and movement rang e 0 ° ~ 180 °
2	left elbow flexion	the body upright, his left arm, hand, and shoulder l evel, forearm along the el bow bend inward, the mo vement range of 0 ° ~ 18 0 °
3	carpal flexion	the body upright, left arm unbend carried forward, the left palm upward alon g the wrist rotation, move ment range -70 °~70 °
4	the body turn right	the body upright, left arm unbend and shoulder lev el, spin to the right, mov ement range 90 °~ 180 °
5	stance knee	stand upright with the rig ht leg standing still, with the left leg bent naturall y and lifting forward slo wly until the knee is at t he same height as the hi p. (to his left knee and l eft hip joints with linear axis, the left leg vertical standing of 0 °, up to 9 0 °), the movement range of 0 ° ~ 90 °
6	stance and ankle	body straight, right leg str aight, left leg straight for ward and slowly raise, un til the ankle of the angle is greater than 45 °.
7	sitting position bend your knees	with the body in a sitting position, the upper body is upright with the right leg falling naturally and the left leg behind the bo dy slowly to the minimu m angle of the knee.
8	seat stretch ankle	the body remains in a sitt ing position with the upp er body upright, the right leg drooping naturally, a nd the left leg slowly lift ing forward of the body until the angle of the ank le joint is maximum.

B. Construction of Standard Action Templates

If the original bone data collected by the Kinect sensor is directly used as the characteristic parameter, 60 different coordinate data points of 3 dimensions will be generated in each frame. The computational complexity of the model is high, and the information is highly redundant, which leads to the difficulty in training samples and affects the precision and timeliness of the recognition algorithm. Therefore, it is a problem that needs to be considered to express

various behavioral gestures of the human body through feature parameters. We need to accurately select the node of human characteristics, so that it can not only accurately describe the behavioral gestures of the human body, but also avoid data redundancy.

Through the analysis of the test results, the Angle changes of the shoulder, elbow, knee and ankle joints were the largest. Therefore, on the premise of ensuring the effect of rehabilitation training and the accuracy of motion recognition, their characteristics are set up to improve the scientific evaluation. The characteristic node is shown in the following table:

TABLE II
characteristic nodes

Serial number	Node name	The field name
1	under the neck vertebrae	SPINE_SHOULDER
2	left hand joints	HAND_LEFT
3	left wrist	WRIST_LEFT
4	left elbow	ELBOW_LEFT
5	left shoulder joint	SHOULDER_LEFT
6	left hip	HIP_LEFT
7	left knee joints	KNEE_LEFT
8	left ankle	FOOT_LEFT

Kinect can obtain data of about 30 frames per second. It takes every 3 frames as a sampling period for data collection, and takes an average of 30 frames as the total length of the motion template. A total of 16 joint angles were selected from the table, and the motion was analyzed according to the time sequence of Angle. According to the three-dimensional space coordinates of the feature nodes, the Angle between the feature nodes of the standard action is calculated. As shown above, the Angle time series can be formed. This design of an action sequence template structure can be expressed as

$A=[\theta(1,1),\theta(1,2)\ldots\theta(1,16);\theta(2,1),\theta(2,2)\ldots\theta(2,16);\ldots;\theta(30,1),\theta(30,2)\ldots\theta(30,16)]$

In order to make the system test result more stable, the selection of standard action template is very important. This design adopts the template training method of non-specific person recognition. According to the standard movements provided by rehabilitation training physicians, multiple people are used to input, integrate the movements of multiple people, extract the common features, and form the standard motion template. The system adopts the gradual fuzzy clustering method to extract motion template. We defined 8 actions in 8 categories, and selected 8 clustering centers, whose indicators can reflect the characteristics of this class. Input the standard action, extract the Angle sequence data of the action, and cluster the sample to the nearest cluster center. The new clustering center is determined according to the classification results, and the indexes are the average of the corresponding indexes of all samples in this class. The training is repeated by many people until the standard action sample is enough, and the construction of the standard action template of the action library is completed.

V IMPLEMENTATION OF DTW ALGORITHM

The test sample has similar characteristics with the standard sample, but due to the difference in the speed of movement of different patients, the corresponding test sample length is also different, so the similarity between the two cannot be compared with the traditional European distance. To solve this problem, DTW algorithm is adopted in this system.

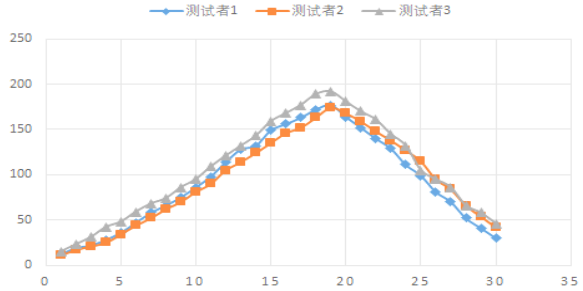

Fig. 6. Angle sequence of three different testers

The standard sample Angle sequence in the test sample and action library is defined as Q(q1, q2...qn) and C(c1, c2...cn). The length is n and m. A matrix grid is constructed. The matrix elements (I,j) represent the distance d(qi,cj) between the points of qi and cj, namely the similarity of these two points. The smaller the distance, the higher the similarity. To determine the similarity of two sequences is to find a path in this network to minimize the distance between Q and C.

The cumulative distance can be calculated by the iterative formula:

Q and C match one by one from the beginning (0,0), and select the next point closest to each other until (n, m). The distance calculated before will be accumulated, and the cumulative distance is the total distance, that is, the similarity between the sequence Q and C. The system calculates the shortest distance value. If it is less than the set threshold value, the template match is considered. Otherwise, no template match is considered.

The threshold judgment is determined by the following formula:

$$K=\begin{cases}1, & d>D\\ 0, & d\le D\end{cases}$$

According to the comparison between the calculated minimum distance d and the set standard threshold d, the data of K is obtained and calculated. When K is true, the action is correct, and when K is false, the action is incorrect.

VI TRAINING GUIDANCE AND EVALUATION

According to the requirements of patients, the rehabilitation physician designed a set of standard movements, and played each standard rehabilitation training movements successively in the form of video. If the patient can complete this movement, he/she will immediately enter the instruction of the next movement. If he/she fails to complete this movement within the specified time, he/she will repeat this

movement, if he/she still fails, he/she will automatically enter the next movement, so as to realize the assistance and guidance for the patient's rehabilitation training.

Fig. 7. Subject interface

The DTW distance can be used to measure the similarity between the patient's movements and the standard movements. We assigned different weights to the difficulty of the rehabilitation training movements, and evaluated the effect of the rehabilitation movements by using the weighted parameter score. The final evaluation score is divided into 5 grades according to the interval. Corresponding training evaluation and rehabilitation guidance are given for different grades. After the training, the evaluation of training results is fed back through the chat window and PDF document.

Specifically, the evaluation method of different actions is the same, but the threshold value of the parameter score and the weight value of the score are different. The DTW distance value of 8 actions was set as the evaluation parameter value, denoted as Di={d1,d2... D8}. The score of the system action evaluation parameter is calculated by Di. The parameter score is:

$$s = d_i - \eta$$

Based on healthy η after many experiments to select threshold, according to the condition changes, it is a experience. Parameter threshold set for H={η1, η2...η8}. Different actions to choose different η, calculation method for the same.

By calculating the parameter score, we can get a set of parameter score Sp={s1,s2,s3...s8}. Since the si is not the same as each other, and their contribution to the measurement of the performance evaluation results is different, the sum of the parameters can not be directly used to evaluate the performance score, and the difference can be reduced by giving different weights to each parameter. The setting of the weight value should take into account the volatility of each parameter in the action evaluation. The setting with high volatility has a larger weight and the setting with low volatility has a smaller weight. After several tests, the corresponding weight values were matched for each parameter score, and a weight set W={w1,w2,w3... w8}, and the

$$\sum_{i=1}^{8} \omega_i = 1$$

The normalized score is calculated according to each parameter score and its corresponding weight

$$Score = \sum_{i=1}^{8} (s_i \times w_i)$$

VII THE SYSTEM TEST

In order to test the stability and reliability of the system, 20 healthy subjects aged from 20 to 40 were selected in the preliminary test of the system, among which 20 were male and 20 were female. The subjects stood about 2m away from the Kinect device and were tested according to the system instructions. Repeat the test 100 times for 8 standard actions. Compare the accuracy of the action recognition and system evaluation scores, and the test results are shown in the following table:

TABLE III
test results

Action number	Action name	The field name		Recognition rate
		Total number	Correct number	
1	left elbow flexion	200	196	98.0%
2	carpal flexion	200	192	96.0%
3	stance knee	200	188	94.0%
4	stance and ankle	200	191	95.5%
5	sitting position bending knees	200	196	98.0%
6	seat stretch ankle	200	193	96.5%
7	seat stretch ankle	200	190	95.0%

It can be seen from the results in the table that the recognition rate of the 8 actions is 94.0% or above. The test sample data is evaluated and calculated. The results are shown in the figure.

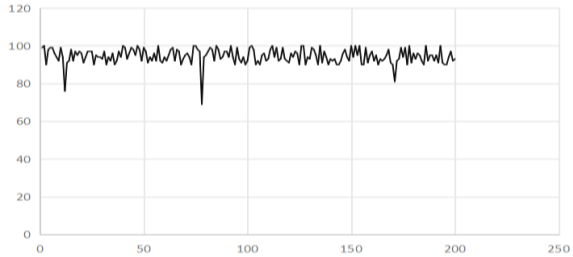

Fig. 8. Evaluation results

VIII. CONCLUSION

Based on the use of Kinect device to extract the topological structure of human skeleton, this paper proposes a motion model to extract human motion features based on the Angle sequence of nodes. We have fully analyzed the characteristics of the motion model, extracted the commonness of the motion features, abstracted the specific human movement process, and found that the action recognition essentially needs to solve the classification of one-dimensional time-varying signals. Therefore, the

relationship between Angle timing and motion features is found by taking the Angle parameters of the nodes in the process of human movement as the entry point. On this basis, multiple comparisons are made, with Angle timing as the parameter and DTW algorithm combined to realize human motion recognition, so as to improve and improve the accuracy of recognition matching. In addition, we also tried to design a scientific and effective rehabilitation training evaluation system by combining the relatively scientific evaluation criteria of rehabilitation training.

References

[1] Zhou Liu, Wang Yinghua, Liu Qiang, et al. Application of virtual reality technology in sports rehabilitation [J]. China tissue engineering research and clinical reversion,2007,11(5):957-960.

[2] TAYLOR MJ, MCCORMICK D,SHAWIS T,et al.Activitypromoting gaming systems in exercise and rehabilitation[J] . Journal of Rehabilitation Research & Development, 2011, 48(10): 1171-1186.

[3] Wang Jing, Ma Jingquan, Chen Changxiang. Study on the effect of body sense game Kinect on improving the executive function of stroke patients [J] Chinese journal of rehabilitation medicine,2014,29(8):748-751.

[4] WANN J P,TURNBULL J D.Motor skill learning in cerebralpalsy:movement,action and computer-enhanced therapy［J］. Baillieres Clin Neurol,1993,2(1):15-28.

[5] Bai Dong tian. Static gesture recognition and continuous motion recognition of upper limbs based on KINECT [D]. Beijing: Beijing institute of technology, 2016.

[6] Mao Yijie. Research on human continuous motion recognition based on kinect [D]. Chengdu: university of electronic science and technology, 2017.

[7] Tang Xuan Huang Rangnian, Zhou Sha. Study on motion recognition system of shoulder periarthritis rehabilitation training based on Kinect[J]. Modern computer (professional edition),2014(23):53-55.

[8] Motion recognition based on Kinect skeleton information[D]. Shanghai: donghua university, 2014

Research on Dimensional Measurement Technology Based on Monocular Vision

Zhang TianLong; Zhong DianShi; Gong JingXuan
（*jilin university instrument science and engineering institute,changchun,130021*）

***Abstract*—With the rapid development of science and technology , the industrial field has become increasingly refined in product manufacturing, stringent in product appearance design, high requirements on machining and assembly accuracy, and in most cases, real-time testing is required in the production .This design is based on the monocular vision measurement technology and develops a set of visual precision measurement system.The feature points of the optical probe are collected through the contact between the optical probe and the object under test. The feature points are optimized and extracted through image processing to obtain the spatial coordinates of the feature points.The system can be set up on site to realize on-line measurement.**

***keywords*—Single-camera vision The image processing Measurement Optical probe**

I. INTRODUCTION

WITH the rapid development of the world's science and technology, the manufacture of large and giant products in the aerospace, military and civilian fields is refined, the design of the product is more and more complex, the processing and assembly precision requirements are higher and higher, and in most cases, Real-time inspection at the production and use site. Modern detection technology is the basis of industrial development. Measurement accuracy and efficiency determine the development level of manufacturing industry and even science and technology to a certain extent. Nowadays, technology should be able to adapt to the rapid development of manufacturing industry, and according to the requirements of the development of advanced manufacturing technology and the development law of precision measurement technology itself, constantly develop new measurement principles and test methods[1].

The visual measurement method is a light and convenient measurement technology, and has the advantages of high measurement accuracy, on-line detection, etc., and meets the requirements for measurement accuracy and measurement range in modern industrial production processes. More and more are applied to product quality inspection and parameter measurement. Common visual measurement methods include monocular vision measurement, binocular vision measurement, and structured light vision measurement. Binocular vision can achieve higher precision, but it has the disadvantages of complicated structure and long measurement time compared to monocular vision. The structural light vision measurement has strong anti-interference ability, but the calibration of the measurement system is difficult. In contrast, monocular vision has the advantages of simple structure and high flexibility, and overcomes the defects that most current visual coordinate measuring systems cannot measure the occlusion surface, high-gloss surface and small measurement range, and are inconvenient for on-line measurement[1].

II. SYSTEM DESIGN AND OPTICAL PROBE PROCESS

A. System composition

The hardware part of the monocular vision measurement system designed in this paper is composed of auxiliary measuring rod, CCD camera and bluetooth; the software part is realized by computer programming, including image processing and PC design. The Bluetooth module is used to realize the communication between the auxiliary measuring rod and the computer, and the auxiliary measuring rod wireless remote control CCD camera is taken to take a picture, and the computer adjusts the number of the characteristic points of the auxiliary measuring rod and the luminous intensity. The CCD camera transmits the acquired image to a computer, and the coordinates of the measurement point are obtained by computer programming.

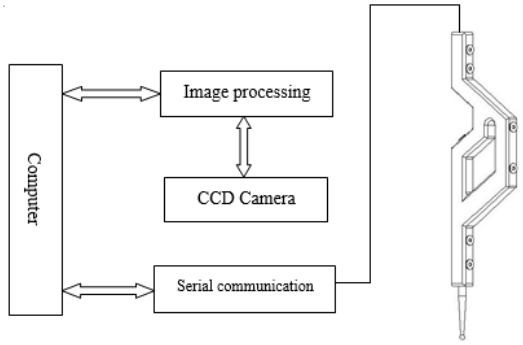

Fig.1 Monocular vision measurement system.

B. Optical probe process

The bright spot on the traditional optical probe consists of the marked LED point source. Due to the uniformity of the point source illumination and the symmetry about the center of the bright spot, the extraction of the point source imaging center becomes an important factor limiting the accuracy of the system. In order to reduce the noise brought by the surrounding environment to the captured image, the optical feature point uses SE3470 infrared light-emitting diode, matched with the filter of the corresponding wavelength, which can filter the interference of visible light and improve the accuracy and stability of the

measurement system. Figure 2 shows the photoelectric characteristics of the infrared light-emitting diode SE3470. The figure shows that the luminous intensity is approximately proportional to the luminous current in the range of its effective luminous current. The luminous brightness can be adjusted by adjusting the current.

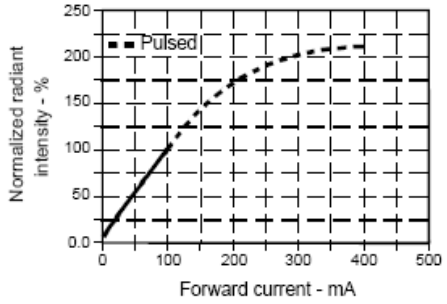

Figure 2 SE3470 luminous intensity versus current curve.

In the process of measuring the measured point, the probe needs to be manually operated to make contact with the object to be tested. In order to facilitate the operation and ensure the measurement accuracy, the material of the probe is required to be light in weight and small in deformation, and the carbon fiber material is rigid and strong. Lightweight and has a small coefficient of expansion compared to stainless steel, which makes it the material of choice for making probes. Six infrared light-emitting diodes are used as feature points, and there is a known constraint relationship with the probe.

III. IMAGE PROCESSING

A. .Threshold segmentation method for image segmentation

In order to obtain the two-dimensional coordinates of the feature points in the image coordinate system, it is necessary to separate the feature points from the background. This paper adopts a basic image segmentation method-threshold image segmentation method. The basic principle is to select one or more gray thresholds in the gray image range, compare the gray values of each pixel in the image with the threshold, and divide the corresponding pixels in the image into two or more types according to the comparison result. Therefore, the image is divided into regions that do not overlap each other, and the purpose of image segmentation is achieved.

B. Maximum inter-class variance method

The largest interclass variance method, also known as the Otsu method, or Otsu for short, is a global-based binarization algorithm proposed by the Japanese scholar Otsu. It can automatically select the threshold. The threshold selection criterion is to make the target area and the background area two areas. The variance between classes is the largest, thus minimizing the probability of misclassification[2].

We acquire optical feature point images using a camera with a resolution of M*N. Suppose $f(x,y)$ is the pixel point (x,y)gray value, if the threshold is T and there are $N_a$pixels in the image which meet the conditions $f(x,y)<T$,$N_b$pixels in the image which meet the conditions $f(x,y)>T$, The proportion of the total of the two categories is ω_a and ω_b, The proportion of pixels with a gray value of $i$is ω_i,and the relationship among them is as follows:

$$\omega_a = \frac{N_a}{M\cdot N} = \sum_{i=0}^{T-1}\omega_i = \omega(T) \quad (1)$$

$$\omega_b = \frac{N_b}{M\cdot N} = \sum_{i=T}^{255}\omega_i = 1-\omega(T) \quad (2)$$

$$N_a + N_b = M\cdot N \quad (3)$$

$$\omega_a + \omega_b = 1 \quad (4)$$

We suppose the average gray value of the two categories isverage gray value of the two categories is μ_a and μ_b,and the average is μ,so we obtain the following equations:

$$\begin{cases} \mu_a = \frac{1}{\omega_a}\sum_{i=0}^{T-1} i\omega_i = \frac{\mu(T)}{\omega_a} \\ \mu_b = \frac{1}{\omega_b}\sum_{i=T}^{255} i\omega_i = \frac{\mu-\mu(T)}{1-\omega_a} \\ \mu = \omega_a\cdot\mu_a + \omega_b\cdot\mu_b \end{cases} \quad (5)$$

We define Inter-class variance as follows:

$$\sigma_B^2 = \omega_a(\mu_a-\mu)^2 + \omega_b(\mu_b-\mu)^2 = \omega_a\omega_b(\mu_a-\mu_b)^2 \quad (6)$$

The equivalent formula can be expressed as follows:

$$\sigma_B^2 = \omega_a\omega_b[\mu_a-\mu_b]^2 = \frac{[\mu\omega(T)-\mu(T)]^2}{\omega(T)[1-\omega(T)]} \quad (7)$$

It can be seen that the Inter-class is a variable related to T. The traversal method can be used to obtain the threshold T which maximizes the variance between classes. The threshold is the optimal threshold. Selecting this threshold can best extract the feature points from the background region.

C. Gaussian surface fitting and localization algorithm

Gaussian surface fitting and localization algorithm is an algorithm for feature point location using all pixel information in feature point images. It makes full use of the gray point distribution information of feature points, and has small requirements on the symmetry of feature point images. Strong anti-interference ability and high positioning accuracy. The basic principle is as follows [3]:

We assume that the pixel point gradation value of the coordinate position (x,y) in the two-dimensional gray image of the optical feature point is $f(x,y)$, it can be expressed as a two-dimensional Gaussian function,as follows:

$$f(x_i,y_i) = G\cdot e^{-\frac{1}{2(1-\rho)^2}\left[\left(\frac{x_i-x_0}{\sigma_x}\right)^2 - 2\rho\left(\frac{x_i-x_0}{\sigma_x}\right)\left(\frac{y_i-y_0}{\sigma_y}\right)+\left(\frac{y_i-y_0}{\sigma_y}\right)^2\right]} \quad (8)$$

In the equation: G is the amplitude of the Gaussian distribution, $G=\frac{K}{2\pi\sigma_x\sigma_y\sqrt{1-\rho^2}}$, ρis the Gaussian

function correlation coefficient; (x_0, y_0) is the Gaussian function extreme point coordinates; σ_x and σ_y are the standard deviation in the direction x、y ,respectively.

Take the logarithm of both sides of the formula（8）, expand the squared item, and then multiply both sides by $f(x,y)$,

The result is obtained as follows :

$$f\ln(f) = ft_1 + ft_2 x + ft_3 y + ft_4 xy + ft_5 x^2 + ft_6 y^2 \quad \text{……（9）}$$

Where :

$$t_1 = \ln(G) - \frac{x_0^2}{2(1-\rho^2)\sigma_x^2} + \frac{\rho x_0 y_0}{(1-\rho^2)\sigma_x\sigma_y} - \frac{y_0^2}{2(1-\rho^2)\sigma_y^2} \quad (10)$$

$$t_2 = \frac{x_0^2}{(1-\rho^2)\sigma_x^2} - \frac{\rho y_0}{(1-\rho^2)\sigma_x\sigma_y} \quad (11)$$

$$t_3 = \frac{y_0^2}{(1-\rho^2)\sigma_y^2} - \frac{\rho x_0}{(1-\rho^2)\sigma_x\sigma_y} \quad (12)$$

$$t_4 = \frac{\rho}{(1-\rho^2)\sigma_x\sigma_y} \quad (13)$$

$$t_5 = -\frac{1}{2(1-\rho^2)\sigma_x^2} \quad (14)$$

$$t_6 = -\frac{1}{2(1-\rho^2)\sigma_y^2} \quad (15)$$

Substituting the coordinates and gray values of n pixel points in the image into the matrix equation,we obtain:

$$\begin{bmatrix} f_1\ln(f_1) \\ f_2\ln(f_2) \\ \vdots \\ f_n\ln(f_n) \end{bmatrix} = \begin{bmatrix} f_1 & f_1x_1 & f_1y_1 & f_1x_1y_1 & f_1x_1^2 & f_1y_1^2 \\ f_2 & f_2x_2 & f_2y_2 & f_2x_2y_2 & f_2x_2^2 & f_2y_2^2 \\ \vdots & \vdots & \vdots & \vdots & \vdots & \vdots \\ f_n & f_nx_n & f_ny_n & f_nx_ny_n & f_nx_n^2 & f_ny_n^2 \end{bmatrix} \cdot \begin{bmatrix} t_1 \\ t_2 \\ \vdots \\ t_6 \end{bmatrix}$$

……（16）

The corresponding vector equation can be written as:

$$b = At \quad (17)$$

If we use far more than 6 sets of data to locate the optical feature point centroid in the calculation process, there will be an overdetermined system of equations, According to the knowledge of linear algebra,we know there is no exact solution to the overdetermined system of equations. It is necessary to find the least squares solution of the system of equations with the norm as the constraint. Solving equations by least squares method based on constraints,we obtain (x,y) as follows:

$$x_0 = -\frac{t_3t_4 - 2t_2t_6}{4t_5t_6 - t_4^2} \quad (18)$$

$$y_0 = -\frac{t_2t_4 - 2t_3t_5}{4t_5t_6 - t_4^2} \quad (19)$$

(x_0, y_0) is the center position coordinates of optical feature points.

D. Bicubic Interpolation

The feature point imaging center is determined by the constraint-based least squares method. Therefore, by using the bicubic interpolation subdivision method in the feature point imaging region to increase the number of effective pixel points, the positioning accuracy of the feature points is further improved.

The basic principle of the bicubic interpolation method is to fit the data by selecting the 4*4 pixel points adjacent to the pixel to be obtained by selecting the interpolation basis function [4], as shown in the figure.

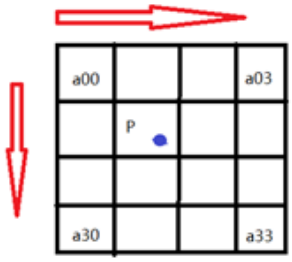

Fig.2 Bicubic Interpolation

Not only the influence factor of the pixel value of the surrounding pixel is considered, but also the influence of the pixel value change rate of the pixel between adjacent points is included in the pixel value to be sought. Bicubic interpolation is performed by the following bicubic basis function [4], where a = 0.5:

$$S(\omega) = \begin{cases} 1 - 2|\omega|^2 + |\omega|^3 & |\omega| < 1 \\ 4 - 8|\omega| + 5|\omega|^2 - |\omega|^3 & 1 \le |\omega| \le 2 \\ 0 & |\omega| > 2 \end{cases} \quad (20)$$

This formula can be used to calculate the weight of the interpolation point, and then use the formula to calculate $f(x,y)$, the gray value of the interpolation point pixel.The result is as follows:

$$f(x,y) = A \cdot B \cdot C \quad (21)$$

where: $x = i + u,\ y = j + v\ \ (0 < u, v < 1)$

$$A = \begin{bmatrix} S(1+v) \\ S(v) \\ S(1-v) \\ S(2-v) \end{bmatrix}^T \quad (22)$$

$$B = \begin{bmatrix} f(i-1,j-1) & f(i-1,j) & f(i-1,j+1) & f(i-1,j+2) \\ f(i,j-1) & f(i,j) & f(i,j+1) & f(i,j+2) \\ f(i+1,j-1) & f(i+1,j) & f(i+1,j+1) & f(i+1,j+2) \\ f(i+2,j-1) & f(i+2,j) & f(i+2,j+1) & f(i+2,j+2) \end{bmatrix}$$

…… （23）

$$C = \begin{bmatrix} S(1+u) \\ S(u) \\ S(1-u) \\ S(2-u) \end{bmatrix} \quad (24)$$

Then the pixel value of the interpolation point is obtained.

IV. CCD CAMERA CALIBRATION

The traditional camera calibration method has higher precision, but it need more requirements on the device and the operation is more complicated. Although the self-calibration method is simple in operation, the accuracy of the result is not very well. This paper chooses Zhang Zhengyou's calibration method ,this method can overcome the shortcomings of the two and combine the advantages of both at the same time.The camera model is as shown below:

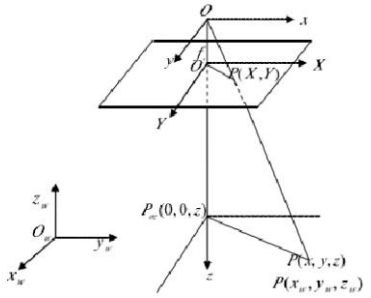

Fig. 3. The camara model

The main coordinate system involved is as follows:

Three-dimensional world coordinate system $O_w - X_w Y_w Z_w$: the external 3D world coordinate system of the camera using the auxiliary measuring rod as a reference.

Camera coordinate system $O_c - X_c Y_c Z_c$: Taking the camera's optical center as the origin of the coordinate system, the distance from the CCD image plane to the origin is f, which is the effective focal length of the ideal imaging system, and the axis of the coordinate system coincides with the optical axis

Image plane coordinate system $O - uv$: In the two-dimensional coordinate system established by the CCD image plane, the origin is in the upper left corner of the image plane, and the u-axis and the v-axis form a coordinate system. The former is the horizontal axis, and the latter is the vertical axis, and the direction is rightward and downward.

Camera image coordinate system $O' - XY$: The two-dimensional coordinate system is also disposed on the CCD image plane, where in the intersection of the optical axis and the image plane is defined as the origin O' , and the axes X and Y are parallel to the axes x and axes y, respectively.

A. Rigid transformation(From the world coordinate system to the camera coordinate system)

The point in the world coordinate system where any point is converted to the camera coordinate system can be described by a rotation matrix R and a translation matrix t. The following rigid body transformation formula exists:

$$\begin{bmatrix} x_c \\ y_c \\ z_c \end{bmatrix} = R \begin{bmatrix} x_w \\ y_w \\ z_w \end{bmatrix} + t \qquad (25)$$

where R is a 3x3 rotation matrix, T is a three-dimensional translation vector, in the form of homogeneous coordinates:

$$\begin{bmatrix} x_c \\ y_c \\ z_c \\ 1 \end{bmatrix} = \begin{bmatrix} R & \mathrm{t} \\ 0_3^{\mathrm{T}} & 1 \end{bmatrix} \begin{bmatrix} x_w \\ y_w \\ z_w \\ 1 \end{bmatrix} \qquad (26)$$

B. Perspective projection（Camera coordinate system to the ideal image coordinate system）

Perspective projection is a method of transforming the coordinates of a camera's coordinate system into the coordinates of the camera image coordinate system,Using the weak perspective imaging model, which assumes that all feature point depth information is the same, then according to the POS algorithm,Pose from Orthograohy and Scaling,proportional orthogonal projection iterative transformation algorithm, we can see that the projection point and phase points meet the following proportional relationship:

$$\frac{f}{Z_c} = \frac{x_u}{X_c} = \frac{y_u}{Y_c} \qquad (27)$$

Among them, (X_c, Y_c, Z_c) is the image coordinates of the camera coordinate system, then the above relation into homogeneous coordinates is:

$$Z_c \begin{bmatrix} x_u \\ y_u \\ 1 \end{bmatrix} = \begin{bmatrix} f & 0 & 0 & 0 \\ 0 & \mathrm{f} & 0 & 0 \\ 0 & 0 & 1 & 0 \end{bmatrix} \begin{bmatrix} x_c \\ y_c \\ z_c \\ 1 \end{bmatrix} \qquad (28)$$

C. Digital Image（Ideal image physical coordinate system to pixel coordinate system）

The origin of the camera image coordinate system, that is, the focus of the optical axis and the planar plane should ideally be located in the center of the image, but due to the limitations of the camera manufacturing process, there are generally deviations.

If the coordinates of the camera image coordinate system (x, y) and the origin point in the image coordinate system (U, V) are (U0, V0), the image plane of each pixel in the x-axis, the physical size of the y-axis direction dx, dy, any one of the image pixel satisfy the following relationship in two coordinate systems:

$$\begin{cases} u = \dfrac{x_u}{dx} + u_0 \\ v = \dfrac{y_u}{dy} + v_0 \end{cases} \qquad (29)$$

Turn it into homogeneous coordinates and matrix form:

$$\begin{bmatrix} u \\ v \\ 1 \end{bmatrix} = \begin{bmatrix} \dfrac{1}{dx} & 0 & u_0 \\ 0 & \dfrac{1}{\mathrm{dy}} & v_0 \\ 0 & 0 & 1 \end{bmatrix} \begin{bmatrix} x_u \\ y_u \\ 1 \end{bmatrix} \qquad (30)$$

From equations (27), (29) and (30), a mapping of a t hree-dimensional spatial coordinate point to the actual image pixel coordinate point is obtained as follows：

$$Z_c\begin{bmatrix}u\\v\\1\end{bmatrix}=\begin{bmatrix}\frac{1}{dx}&0&u_0\\0&\frac{1}{\mathrm{dy}}&v_0\\0&0&1\end{bmatrix}\begin{bmatrix}f&0&0&0\\0&f&0&0\\0&0&1&0\end{bmatrix}\begin{bmatrix}R&t\\0^T&1\end{bmatrix}\begin{bmatrix}x_w\\y_w\\z_w\\1\end{bmatrix} \quad (31)$$

$$=\begin{bmatrix}\alpha&0&u_0&0\\0&\beta&v_0&0\\0&0&1&0\end{bmatrix}\begin{bmatrix}R&t\\0^T&1\end{bmatrix}\begin{bmatrix}x_w\\y_w\\z_w\\1\end{bmatrix}=M_1M_2\tilde{x}_w$$

M1 and M2 are the internal and external parameters of camera calibration, where M1 is the internal parameters of the camera, M2 is the external parameters, including rotation matrix and translation matrix.

V. Experiment and Data Analysis

The interface diagram is designed based on the MATLAB platform. From this interface, we can see that software can control the opening of the camera, control the exposure time, collect images, extract the center of mass, and calculate the distance.The brightness of the glow point can be adjusted by Bluetooth communication.

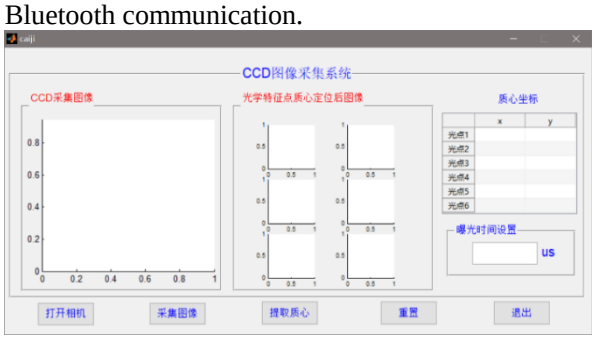

Fig.4 GUI interface for upper computer

After the system is completed, the measurement system is tested, and the upper and lower surfaces of an object are measured with 20 sets of data respectively, the results are as follows:

Table 1 400mm standard gage measurement oriented in parallel Xc(mm)

	400mm standard gauge block		
	Group 1	Group 2	Group 3
1	400.01	400.03	399.99
2	400.03	399.99	400.02
3	400.00	400.02	400.04
4	400.02	400.07	399.99
5	400.04	400.03	399.93
6	399.98	400.08	400.01
7	400.05	399.98	399.98
8	400.02	400.03	399.97
Average	400.02	400.03	399.99
Standard deviation	0.02	0.04	0.03
U_{95}	0.06	0.11	0.07

Table2 400mm standard gage measurement oriented in parallel Yc(mm)

	400mm standard gauge block		
	Group 1	Group 2	Group 3
1	400.04	400.03	399.99
2	400.03	400.07	400.02
3	400.01	400.04	400.04
4	400.06	400.01	399.99
5	400.02	400.07	399.93
6	400.01	400.06	400.01
7	400.05	400.03	399.98
8	400.07	400.05	399.97
Average	400.01	400.05	399.99
Standard deviation	0.02	0.02	0.04
U_{95}	0.08	0.09	0.11

After measuring the size of the standard gauge block with an accuracy of 0.01mm, the result meets the requirements.

VI. Conclusion

In this paper, a measuring system of monocular vision measuring principle based on optical probe is studied, and the design and fabrication of optical probe are accomplished, and the luminous intensity of feature points can be adjusted.Control the exposure time of the camera to achieve the optimal feature point extraction.In this paper, a vision measurement algorithm based on optical probe is presented, the principle of monocular vision measurement is studied in detail, and the spatial coordinate of the measured point is calculated by using the orthogonal iterative algorithm to solve the position relation matrix and finally using the solved rotation and movement matrix.

In order to further improve the measurement accuracy of the whole system and achieve subpixel positioning of the centroid of the optical feature point, a Gaussian surface fitting method based on double three interpolation is proposed to locate the centroid of the optical feature point.Using Matlab to program the algorithm proposed in this paper, design GUI interface, control the camera image acquisition and processing, and finally obtain the measurement results.Through the analysis of the experimental results, the feasibility of the measurement system is verified.

References

[1] Liu Changying, Research on Key Technologies of Large Size Monocular Vision Measurement [D]. Harbin: Harbin Institute of Technology, 2006.

[2] Qi Lina, Zhang Bo, Wang Zhankai.Application of Maximum Inter-class Variance Method in Image Processing[J].Radio Engineering,2006(07):25-26+44.

[3] Lü Rui,Wang Junwei,Shao Wei.Study on Gaussian Surface Fitting and Location Algorithm Based on Bilinear

Interpolation[J].Machine Tool & Hydraulics,2013,41(03):83-85.

[4] Wang Huipeng, Zhou Lili, Zhang Jie. A Region-Based Bicubic Image Interpolation Algorithm[J]. Computer Engineering, 2010, 36(19): 216-218.

Study on Intelligent Battery Charging System Based on Switching Power System

Liang Peipei,Chu Xunyu,Li Mengqi,Liu Weiping
(Jilin University College of Instrument Science and Electrical Engineering,Changchun 130026,China)

***Abstract*—With the rapid development of power electronics technology, the performance of high frequency switching power supplies have been continuously improved. Due to its high efficiency, small size and large output voltage range, high-frequency switching power supply has been widely used in various household appliances or industrial electronic equipment. In order to solve the problem that the battery car capacitance is damaged for the reason that charging voltage of the battery charging systems used in the market is not matched with the model of the battery car capacitance,this article proposes a new battery charger that can detect the capacity of the battery and provides a specific charging voltage and current by considering the capacity and mode of battery car capacitance ,which makes the charging process more efficient and safe.The battery charging system proposed in this article use NCP1654 as the core control chip, and the Boost Chopper is used to conduct the main circuit. The new silicon carbide semiconductor device is used as the main switching device to turn alternating current into direct current. When the AC voltage on the power supply side changes from 180V to 260V, the device can operate normally. The intelligent battery car charging system outputs two DC voltages, 42v and 27v, respectively, and the maximum output current are both 2A. The load regulation is 0.1, and the peak-to-peak value of output noise ripple voltage is less than 1.5V. The protection circuit in the charging device not only prevents spike voltage and surge current from disturbing the circuit during start-up, but also prevents over charge problem. Considering the user experience of the intelligent battery charging system, the touch screen is selected as the operation interface. In addition, the STM32 demoboard is used to detect the output voltage and output current, control the output voltage amplitude of the charging system. In addition, the STM32 also functions to detect the output voltage and current and control the amplitude of the output voltage. After testing, the battery charging system reached the design requirements and can be put into use.**

***Keywords*—Switching Mode Power Supply;Boost Chopper;STM32**

I. INTRODUCTION

BATTERY cars are the tools that people often use today. Designing a charger that is efficient and meets different charging currents is of great significance to facilitate people's travel. Most of the battery charging piles available in the market can only meet a specific current and voltage demand, and the core part of the charging pile - the switching power supply can not guarantee a certain voltage regulation rate and load adjustment rate, which will bring the charging process unsafe, Reduce the risk of battery life and other hazards. This paper refers to a new battery car charging device that can detect the battery capacity of the battery, thus providing a specific charging voltage and current, making the charging process more efficient and safe. The core of the charging device, the switching power supply, ensures that the battery's voltage regulation and load regulation are kept within a small value. At the same time, overcurrent protection, short circuit protection and overshoot protection are also provided.In addition, the battery car charging device can also reasonably predict the service life of the battery by detecting the battery capacity and the length of use of the battery, and reminding the user to change the old battery of the battery at the right time[1].

II. OVERALL DESIGN

A. System Design Block Diagram

The system consists of the main circuit, control circuit, A/D conversion module, controller, display screen, operation interface, etc. The system structure is shown in Figure 1.

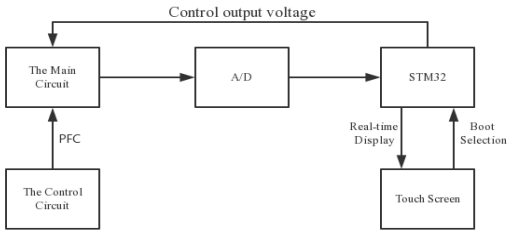

Fig. 1. System design block diagram.

B. Start Protection Circuit

The inrush current is caused by a sudden change in voltage. The surge current rises very quickly and has a very short duration, but the damage is very large. In order to prevent or reduce the damage of the surge current, the varistor, common mode inductor and other original components are commonly used in the switching power supply to form a start protection circuit, as shown in Figure 2[5]. The varistor and the thermistor form a lightning protection unit to suppress overvoltage pulses and surge currents generated by the circuit during startup. The common mode inductor, X capacitor and Y capacitor form a π-type filter-shaped circuit EMI unit to suppress common mode interference, radiation and surge current[2].

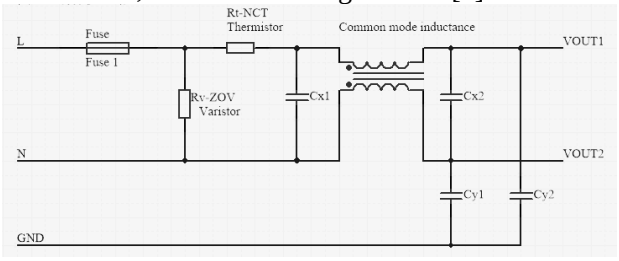

Fig. 2. Start protection circuit diagram.

C. Main circuit design

The boost type PFC circuit is selected in the system main circuit design. The basic principle is shown in Figure 3. The input Vin is the 24V sinusoidal AC voltage signal output by the isolated transformer. The sinusoidal half-wave voltage signal with a frequency of 100HZ is output through the rectifier bridge, and then the signal is BOOST transformed. The PWM signal drives the switch tube. When the switch tube is turned on, the input voltage is charged to the inductor through the switch tube, and the diode is turned off. At this time, the voltage stored in the output capacitor is supplied with the output voltage; when the switch tube is turned off, the energy stored in the inductor is continued. The flow diode and the stored energy stored in the capacitor together supply the output voltage, so that the output voltage is higher than the input terminal, and the boosting purpose is achieved.

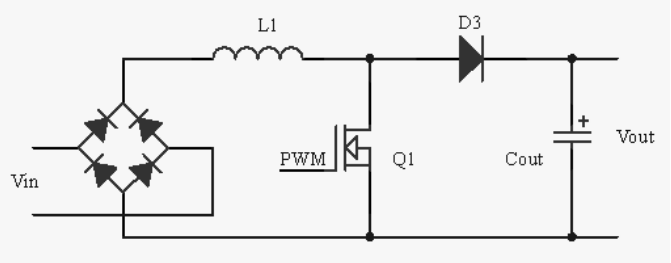

Fig. 3. Main circuit topology.

D. Selection of Energy Storage Inductance

The BOOST circuit has two modes of operation, namely current continuous mode (CCM) and current interrupt mode (DCM). When the CCM stabilizes, the current flowing through the inductor does not cross zero, and the DCM will have a current zero crossing after the circuit is stable. In the case of a large power supply with a high switching frequency, CCM is generally used to reduce the peak current flowing through the inductor and the current stress experienced by the device in the circuit.

Considering the worst case conditions, the input voltage is Vin=20V; the output voltage Vout=42V; the maximum output power is Pout max=100W; the efficiency is η=0.9; according to the working mode of the selected control chip, the switching frequency is determined to be 65kHz. The current ripple coefficient was set to r = 0.36.

Under this condition, the duty cycle of the switching device is 0.326, and the calculation method is as shown in (1):

$$D = \frac{V_{out} - \sqrt{2}V_{in}}{V_{out}} \qquad (1)$$

Where D represents the duty cycle of the switching device, V_{out} represents the output voltage of the switching circuit, and V_{in} represents the input voltage of the switching circuit.

The peak current flowing through the inductor is 7.857A, which is calculated as shown in (2):

$$I_L = \frac{\sqrt{2}P_{outmax}}{\eta \times V_{in}} \qquad (2)$$

Where I_L represents the current flowing through the inductor, P_{outmax} represents the maximum output power, η represents the efficiency of the switching circuit, and V_{in} represents the input voltage of the switching circuit.

The inductance of the energy storage inductor is $50uH$, and the calculation method is as shown in Equation 3:

$$L = \frac{V_{on} \times D}{r \times I_L \times f} \qquad (3)$$

Where L represents the inductance value of the energy storage inductor, V_{on} represents the effective value of the input voltage of the switching circuit, r represents the current ripple coefficient, I_L represents the current flowing through the inductor, and f represents the switching frequency.

Therefore, in the case where the current is kept continuous, the inductance value is selected to be 50 μH[3].

E. Control Chip Selection

The NCP1654 is a controller for power factor correction circuits in continuous conduction mode[9]. It controls the power switch conduction time (PWM) in a fixed frequency mode and relies on the instantaneous coil current.

The chip operates in an average current continuous conduction mode with extremely fast transient response, very low startup current, and very low shutdown current. The internal 1.5A push-pull output circuit gate drive, fully integrated 65/133/200KHz oscillator, three closed-loop PWMs for periodic duty cycle control. The external design components of the circuit are few, with input current detection, over current limitation, over voltage protection, hysteresis undervoltage lockout, etc., and soft start function for smooth start operation. The chip pins are shown in Figure 4.

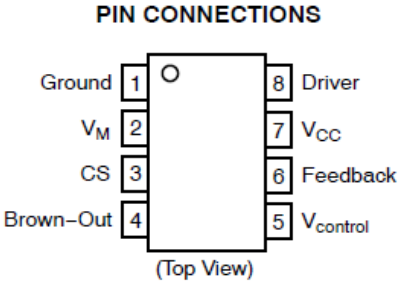

Fig. 4. Power chip pins.

Pin6 (Feed Back): This pin receives the feedback signal VFB, which is proportional to the output voltage of the PFC circuit. This information is used for two output adjustments. Features output overvoltage protection (OVP) and output undervoltage protection

(UVP). When VFB is greater than 105% VRef, OVP is activated and the drive output is disabled; when VFB is less than 8% VRef, the device enters shutdown low power mode.

Pin5 (Vcontrol/Soft-Start): This pin Vcontrol voltage directly controls the input impedance. This pin is usually connected to an external capacitor Control to limit the Vcontrol bandpass to less than 20Hz, which is approximately unity power factor. The device provides Vcontrol <0.7V when there is no output and is turned off when the Vcontrol circuit is grounded. When the chip is powered up, Vcontrol gradually increases with the 20mA current source. When VFB is greater than 95% VRef, an increasing linear control duty cycle is obtained as a function of time, thus reducing the voltage and current stress on the MOSFET. , the soft start function is implemented.

Pin4 (Brown Out): The voltage signal detected by Pin4 is proportional to the average input voltage. A grounding resistor network and capacitor need to be connected between Pin4 and ground. When VBO <0.7V, the circuit uses education to detect low input, turn off the output drive and keep it low until VBO exceeds 1.3V (0.6V hysteresis).

Pin3 (current detection input): The current source of this pin is proportional to the induced current ICS of the inductor current. It has overcurrent protection. When ICS>200mA, overcurrent protection is activated and the drive output is disabled.

Pin2 (multiplier voltage): This pin provides VM for PFC duty cycle modulation, input impedance, RM ground, CM ground, otherwise the current works in peak mode.

Pin1 (GROUND): Ground.

Pin8 (DRIVE): Gate drive current capability (±1.5A).

Pin7 (VCC): Connect to the power supply -0.3, +20V[4].

The core part of the control circuit is the NCP1654 power chip. The typical control application circuit is shown in Figure 5.

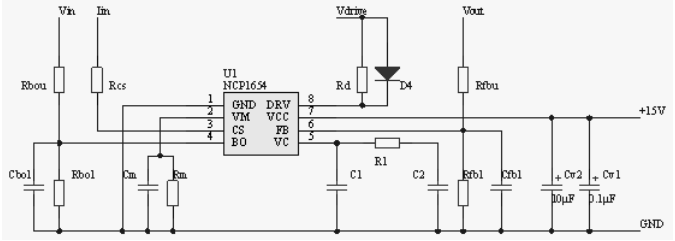

Fig. 5. Control circuit design.

F. Switching Device Selection

The maximum output voltage of the power supply is 42V, and the maximum actual leakage current of the switch is about 8A. The actual voltage and current have spikes, and the voltage and current values must be left with a certain margin. In order to reduce switching loss and conduction loss, it is necessary to select a device with a small on-resistance.

Here IRF540N switch tube is selected, the maximum withstand voltage is 100V at normal temperature, and the maximum on-current is 23A, and the maximum voltage required for the switch in the main circuit is 42V, the maximum current is 8A, and the margin is sufficient; its maximum leakage source The on-resistance RDS(ON)=77mΩ has a small loss. Therefore, it is appropriate to select the switch tube here[5].

G. Freewheeling Diode Selection

The output freewheeling diode selects C4D10120D. The reverse blocking voltage has a limit of 1200V and can withstand a current limit of 18A. In the actual circuit, the current and voltage are the same as those of the switch tube, and in extreme cases, 8A and 42V respectively. Therefore, the device is selected here to meet the design requirements[6].

H. Sampling Circuit Design

Voltage sampling by means of resistor divider, as shown in Figure 6, the sampling point voltage is stabilized within 3.3V, and then through the AD sampling chip inside the STM32, the voltage at the sampling point is worth, and then according to the proportional relationship of the resistor divider Voltage value.

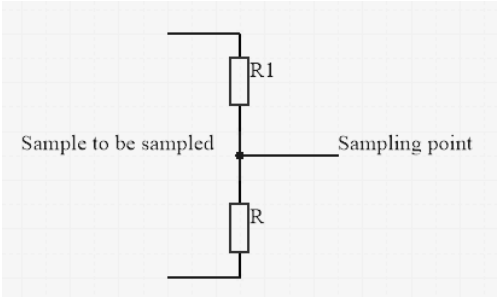

Fig. 6. Voltage sampling principle.

The current sampling is performed by means of a differential amplifying circuit. As shown in Figure 1.7, a sampling resistor is connected in series at the current to be sampled, and the voltage across the sampling resistor is used as two input terminals of the differential amplifying circuit respectively, and the voltage difference is stabilized by the differential amplifying circuit. Within 3.3V and there is a significant difference, after the voltage difference is obtained by the AD sampling of the STM32, the current value is obtained according to the proportional relationship of the differential amplifying circuit and the magnitude of the sampling resistance value.

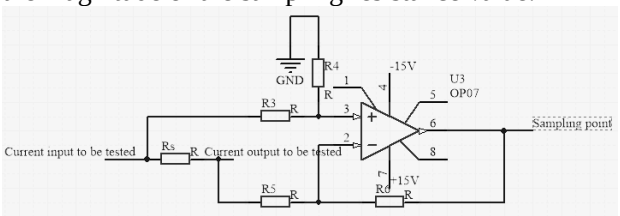

Fig. 7. Current sampling principle

I. Drive Circuit Design

In order to control the on/off of the control circuit through the pin of the microcontroller, it is necessary to design a special drive circuit to control the large voltage through a small voltage. In this part, the triode is controlled by the signal of the single-chip microcomputer, and then after the relay coil side is energized, the normally open switch on the switch side

is closed, and the main circuit is turned on[7].

In combination with the previous part, there is ±15V dual power supply in the total design of the system. Therefore, +15V is used as the driving circuit power supply. The relay of NXJ-3Z1-DC12V specification is selected. The rated voltage is 12V DC, the operating voltage is 9.0V DC, the highest voltage. At 13.2V, the coil resistance is 160Ω (1±10%). The triode is selected from the commonly used s8050, and the β value is 160~300. Other parameters also meet the requirements of various indicators. The drive circuit is shown in Figure 8[8].

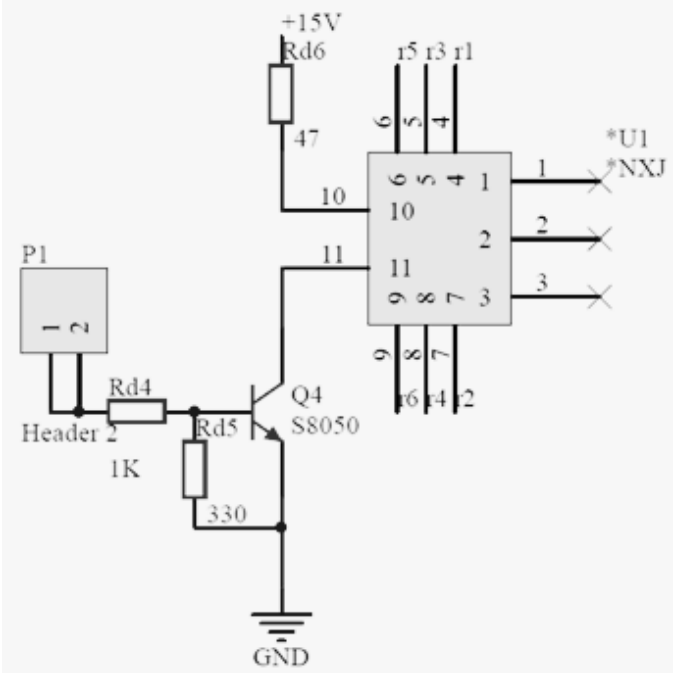

Fig. 8. Drive circuit principle.

The three normally open switches of the relay are respectively connected in series to the input and output of the main circuit and the power supply part of the control circuit to reduce the energy and mutual interference consumed when the circuit is not working.

To ensure that the collector current does not exceed the limit, take R_{d4} equal to 1 kΩ [9].

In order for the relay to work properly, Conditional Formula (4), Equation (5), and Equation (6) are satisfied.

$$\beta \times I_b < I_c \quad (4)$$

$$9.0 < U_{VCC} - I_c \times R_{d6} < 13.2 \quad (5)$$

$$I_b = \frac{U_i}{R_{d4} + R_{d5}} \quad (6)$$

Where β represents the amplification factor of the triode, I_b represents the base current of the triode, and I_c represents the collector current of the triode.

According to the calculation result, R_{d5}=330Ω and R_{d6}=47Ω[10].

III. SOFTWARE SIMULATION

A. Main Circuit Part

The rectifier bridge is usually used to directly convert the AC voltage into a DC ripple waveform. If it is ideally idling, when the whole circuit starts to work stably, the voltage across the filter capacitor is approximately the amplitude of the input AC voltage[6]. After the load is applied, the voltage will decrease accordingly. Only when the value of the input AC voltage is greater than the voltage across the filter capacitor on the output side of the rectifier bridge, current is injected from the grid, causing the input current to have a value only near the peak of the input voltage. The simulated waveforms of the input voltage and current are shown in Figures 9 and 10.

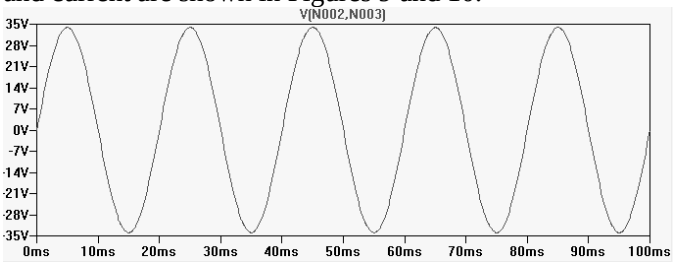

Fig. 9. Input current waveform before correction

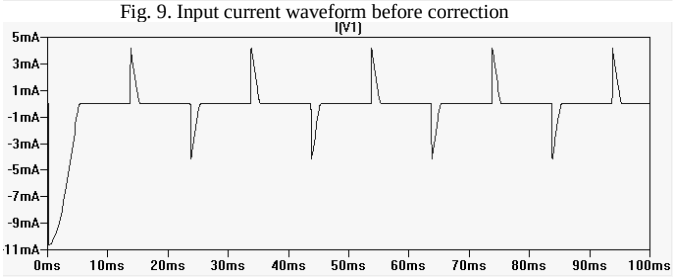

Fig. 10. Input current waveform before correction.

B. Main Circuit Combined With Control Circuit Part

The main function of the control circuit is to achieve no phase difference between the input side current and voltage, and the waveform does not produce distortion. Therefore, on the input side, the input voltage is sampled, as the object of current waveform tracking, the input current is sampled, and the input current tracking input voltage waveform is formed to constitute a current control loop; and the voltage on the output side is introduced to the amplitude of the input side current. Regulation, forming a voltage control loop. The internal and external control loops work together to achieve the function of PFC and output constant voltage. The corrected input voltage and input current waveforms are shown in Figures 11 and 12[11][12].

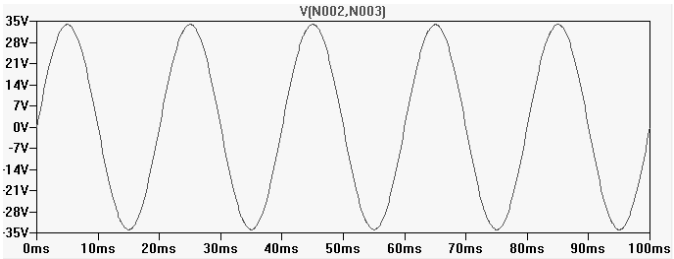

Fig.11. Corrected input voltage waveform..

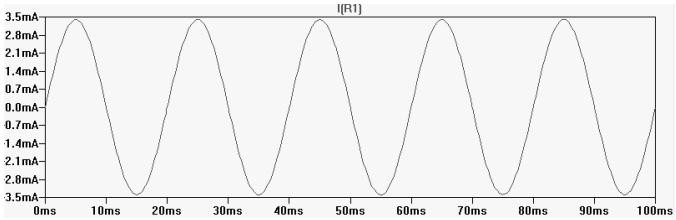

Fig. 12. Corrected input current waveform..

IV. PROGRAMMING

The overall design flow of the system is shown in Figure 13. The system's workflow and display are combined with the STM32 chip and touch screen display. The STM32 collects the user's information, thereby controlling the main circuit and the control circuit to work. The main circuit output voltage and current are sampled and then fed back to the user through the display screen in real time. With a battery life estimation function, the battery life can be roughly estimated by the length of time the battery has been used, and the user can also choose whether to use this function[13].

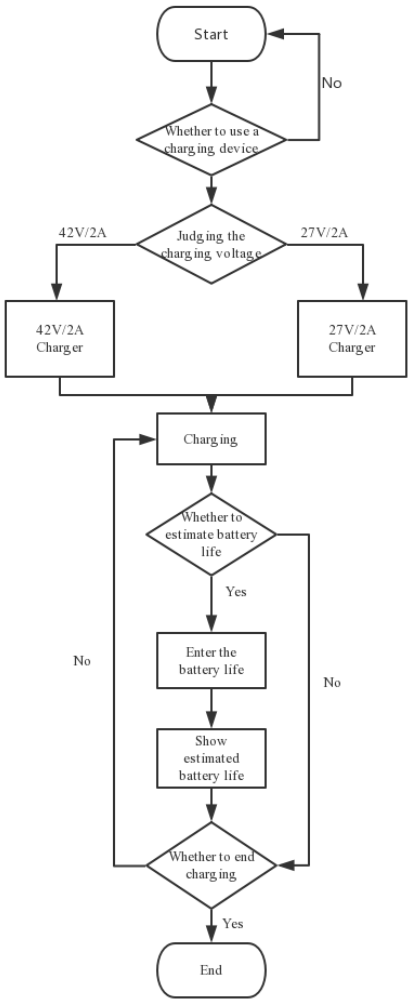

Fig. 13. System Flow

V. SUMMARY

The test data shows that when the converter is operating normally and stably, the power factor is above 0.8 and the converter efficiency is above 0.8. At the same time, under normal working conditions, the peak-to-peak voltage of the two output voltages is within 1.5V, the output current is up to 2A, and the harmonic factor is less than 6%. The harmonics of the visible current have been greatly reduced. The voltage regulation rate and load regulation rate are all within 8%, which meets the design requirements.

References

[1] Shi Huangxia,He Ying,Dong Xiaohong. The Overview of Power Electronics Soft Switching Technology[J].Microprocessors,2013,34(04):1-6.

[2] Liu Jianfeng.The Research on the Development Status of Power Electronic Technology Application System in China[J].Digital Technology and Application,2013(05):230+232.

[3] Wang Xiao-ming the Chinese People's Armed Police Forces Academy Staff Office Langfang,China. Switching Power Supply for Low Power Experiments[A]. IACSIT、IEEE China Council、IEEE Beijing Section、Sichuan Computer Federation.Proceedings of 2010 3rd IEEE International Conference on Computer Science and Information Technology VOL.8[C].IACSIT、IEEE China Council、IEEE Beijing Section、Sichuan Computer Federation:,2010:3.

[4] Yu-jie Fang 1,3,a,Bing-hua Su 2,3,b and Ling-xia Hang 1,c 1 Shaanxi Province Thin Film Technology and Optical Test Open Key Laboratory,Xi'An Techological University,Xi'An 710032,China 2 School of Optoelectronics,Beijing Institute of Technology,Beijing 10081,China 3 Zhuhai Campus of Beijing Institute.... Study of switching power supply ripple rejection[A]. Hong Kong Education Society,Hong Kong.Lecture Notes in Information Technology—Proceedings of 2012 International Conference on Future Electrical Power and Energy Systems(ICFEPES 2012)[C].Hong Kong Education Society,Hong Kong:,2012:5.

[5] Wang Peikang,Zheng Feng,Yang Xiaoyu,zhang yu,Wang junfei,Qiao Yanpeng,Peng Genzhai.A method for adjusting the impedance of common mode noise source and optimizing the performance of EMI filter[J]. Proceedings of the CSEE, 2014, 34(06): 993-1000.

[6] Xu Xiaoning.Research on Reliability Design of Switching Power Supply[J]. Electric Drive Automation,2009,31(03): 27-31.

[7] Zhang Hao,Xu Longhu.Analysis of Active Power Factor Correction Technology and Control Method[J].Journal of Shanghai University of Electric Power,2009,25(03):201-207.

[8] Gao Chao.A new high-performance AC/DC power factor correction switching converter based on one-cycle control technology and active floating-charge technology[J].Journal of Chongqing University(English Edition),2008(02):119-124.

[9] Wang Yu,Gao Wengen.Research and Implementation of Active Power Factor Correction Circuit[J].Journal of Chongqing Technology and Business University(Natural Science Edition),2017,34(05):75-81.

[10] Wu Xiaojun,Qin Kaiyu,Tang Bo.EMI filter design [J]. Electronic test, 2011 (07): 75-80+113.

[11] SHINPEI OMATA,TOSHIHISA SHIMIZU. Design Method for EMI Filters Connected to Both dc and ac ports of a Residential-Use Photovoltaic Power Conditioner[J]. Electrical Engineering in Japan,2016,197(2).

[12] Zhang Jiayong.Switching Power Supply Measurement System Based on STM32 and C++builder [D]. Guangxi Normal University, 2015.

[13] Ling Zhenbao,Cao Shuanglan,Chang Le,Wang Yi,Huang Jintao.Charger Design with Function of Detecting Battery Capacity[J].Journal of Jilin University(Information Science Edition),2010,28(01):100-105.

Design of Radio Energy Transmission System Based on 51 Single Chip Microcomputer

Jiahui Xu; Zhipeng Zhou; Xiangjiang Liu; Defeng Xu
（jilin university instrument science and engineering institute,changchun,130061）

***Abstract*—This design mainly uses the principle of electromagnetic coupling to realize the transmission of electric energy through the electromagnetic induction of the primary and secondary coils. The radio energy transmission system based on this method is mainly composed of three parts, namely, an energy transmitting end, an induction coil, and an energy receiving end. When an alternating current is applied to the transmitting coil, the current will form an alternating magnetic field in the medium surrounding the coil, and the receiving coil generates an induced electromotive force in the alternating magnetic field to supply power to the mobile device or battery. The device takes the transmitting module and the receiving module as the core, and the PMW wave generated by the 51 single-chip microcomputer is transmitted to the driving tube MOSFET through push-pull, and the direct current is converted into high-frequency alternating current through the rectifier circuit for wireless transmission.**

keywords—electromagnetic induction wireless charging resonant coupling

0. INTRODUCTION

NOWADAYS, almost all electronic devices, such as mobile phones, MP3s and notebook computers, are mainly charged with one end connected to an AC power source and the other end connected to a portable electronic device to charge a wired battery. This method has many disadvantages. Firstly, frequent plugging and unplugging can easily damage the motherboard interface. In addition, incorrect use may also bring about the risk of electric shock. Therefore, the non-contact inductive charger was born at the end of the last century. With its advantages of convenient carrying, low cost, and no wiring, it has quickly attracted attention from all walks of life. At present, the technology of wireless charging has begun to be used in mobile phones, and the farther the distance of wireless transmission, the higher the energy consumption of the device. [1]To achieve long-distance high-power wireless electromagnetic conversion, it is necessary to overcome the high energy consumption of the device. Therefore, the realization of high-efficiency energy transmission of wireless charging is the primary problem that needs to be solved in the popularization of wireless chargers. On the other hand, the problem to be solved is to establish a unified standard so that different types of wireless chargers can be connected with different electronic products,thereby realizing wireless charging.

1 EXPERIMENTAL SCHEME

1.1 general plan introduction

The theoretical basis of the magnetic resonance coupled radio energy transmission technology is the "coupled mode theory". If the resonant frequency of the energy transmitting device and the receiving device are the same, the transmitter generates an alternating magnetic field at the specific resonant frequency, and the transmitting device first generates self-resonance in the alternating magnetic field and generates an alternating magnetic field of the same frequency as the receiving device. When it is close to the transmitting device, self-resonance is also generated. The receiving device continuously accumulates energy and transmits it to the load, so that wireless transmission of energy can be realized. The overall topology of the circuit is shown in Fig.1

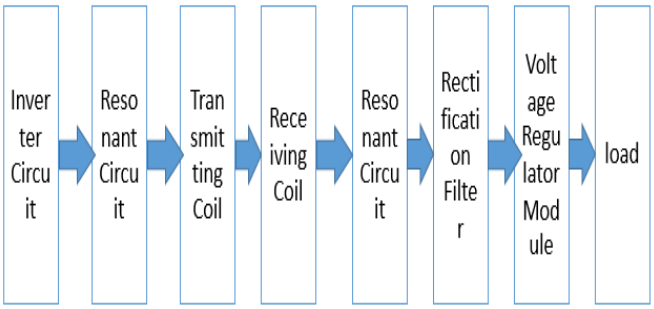

Fig.1 The overall circuit topology

1.2 waveform generator circuit

Solution 1: Using a quartz crystal oscillator, this oscillator is fabricated based on the piezoelectric effect of a quartz crystal piece. This quartz crystal piece generates mechanical vibration under the action of an external alternating electric field. When the frequency of the alternating electric field is the same as the natural frequency of the quartz crystal, the vibration becomes very strong, which is the reaction of the crystal resonance characteristic. Although the square wave frequency stability generated by the quartz crystal oscillator is high, it is not easy to adjust the frequency.

Solution 2: The 51 (single chip microcomputer) SCM is used to generate the PWM signal with adjustable duty cycle, and the pulse width debugging (PWM) wave outputted by the single-chip microcomputer in the comparison mode is used to realize the working principle of D/A conversion.

Solution 3: Using the NE555 time base circuit to generate the PWM signal, adding a diode and potentiometer to the 555 timer running in the alien mode, a wide-band modulator with adjustable efficiency coefficient can be generated. Waveform to

500KHZ. This scheme has simple frequency adjustment and simple circuit. The disadvantage is that the power consumption is too large.

Consider the above three solution and choose solution two.

1.3 driving circuit scheme

Solution 1: The driving circuit is composed of a buffer, a resistor and a pair of small power switching transistor pairs. When the control signal is low, the same direction buffer outputs a low level, the a point potential is low, the base potential of the bipolar transistor is low, and the base current flowing through the NPN type transistor is approximately zero, the triode The cutoff is equivalent to a large resistance in series between the collector and the emitter, and the current flowing through the PNP type transistor quickly reaches saturation, the triode is saturated and turned on, the gate of the P-channel insulated gate field effect transistor is approximately grounded, and the triode is turned off; When the signal is high, the same direction buffer outputs a high level, the a point potential is high, the base potential of the bipolar transistor pair is high, and the base current flowing through the NPN type transistor quickly reaches saturation, the triode The saturation is turned on, and the base current flowing through the PNP transistor is approximately zero, the transistor is turned off, and the gate potential of the insulated gate field effect transistor is approximately equal to +9 V, and the field effect transistor is turned on. The resistor is a pull-up resistor of the open-collector buffer of the open collector. The resistor is connected to the base of the power transistor, and a current-driven transistor is formed in the base loop. The transistor is a current control device, and the current flowing during saturation is large. If the drive current is not enough, the voltage will rise. If the drive current is sufficient, the saturation voltage drop is small, the switching frequency is not good, and the speed is slow.

Solution 2: Using MOS tube drive, MOS tube has strong high current and high power processing capability, very low conduction internal resistance, very low gate charge, good anti-avalanche breakdown capability, and strong driving capability. . The FET is the core of the device. Before introducing the working principle of this part, briefly explain the working principle of the MOS FET. The MOS FET is also referred to as a MOS FET, an abbreviation for Metal Oxide Semiconductor Field Effect Transistor. It is generally available in both depleted and enhanced versions. [2]In this paper, enhanced MOS FETs are used, which are classified into NPN type and PNP type. The NPN type is generally referred to as an N-channel type, and the PNP type is generally referred to as a P-channel type. For an N-channel type field effect transistor, its source and drain are connected to an N-type semiconductor, and for a P-channel field effect transistor, its source and drain are connected to a P-type semiconductor. For FETs, the output current is controlled by the input voltage (or field voltage), which means that the input current is very small or has no input current, which makes the device have a high input impedance.

The MOS tube IRF540 is used to form the driving circuit. Because the IRF540 switching tube has a turn-on time of 4nS and a turn-off time of 3nS, the theoretical switching frequency can reach several tens of megabytes, and the power consumption is low. The passing current is large and meets the design requirements.

Consider the above two solutions and choose solution 2.

1.4 receiving coil circuit

Solution 1: Full-bridge rectification, Figure 2 is the structure diagram of full-bridge rectification:

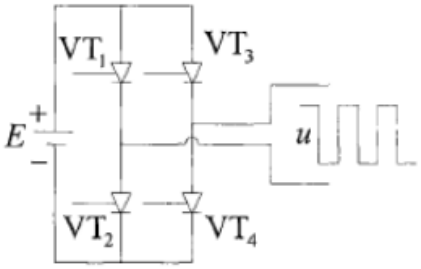

Fig.2 Full-bridge inverter circuit

The normal operation of the electronic system is inseparable from the stable power supply. Except for the use of solar cells or chemical batteries as power sources in some specific occasions, the DC power of most circuits is converted from the AC power of the power grid. The voltage waveform at the location is shown in Figure 2. The DC power supply is composed of a power transformer, a rectifier circuit, a filter circuit, and a voltage stabilization circuit. The rectifier circuit uses a unidirectional conductivity of the diode to form a rectifier circuit, which can change the AC voltage into a unidirectional ripple voltage.

The rectification (and filtering) circuit has both AC and DC quantities. Different expressions are often used for these quantities: input (AC) - with rms or maximum value; output (DC) - with average; diode forward current - with average; diode reverse voltage - The maximum value, this design is more complicated.

Solution 2: Half-bridge rectification, half-bridge rectification is to connect two diodes of bridge rectification together, two bridge rectifier circuits can be used to form a bridge rectifier circuit, and one half bridge can also form a transformer with center taps. Wave rectifier circuit. Using two diodes, a symmetrical loop is formed using the center tap of the transformer coil. This structure is simple and low in cost. The structure diagram is shown in Figure 3:

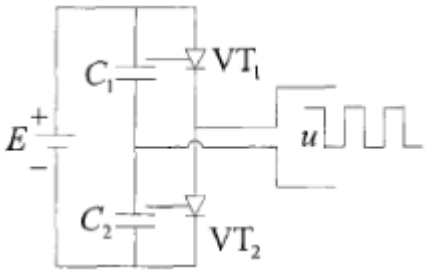

Fig.3 Half-bridge inverter circuit

Consider the above two solutions and choose solution 2.

1.5 Selection and demonstration of coils

Solution 1: Select hollow copper tube. Hollow copper tubes are convenient and generally have finished products, but the specifications and sizes are not well calculated, and the price is high.

Solution 2: Use enameled wire. The enameled wire winding method is determined by individual needs, and the number of turns can be determined by theoretical calculations, and the copper wire is convenient to purchase, and is convenient to recycle after use, thereby reducing waste of resources.

Considering the above two solutions comprehensively, solution 2 is simpler and more convenient, so choose solution 2.

1.6 Selection and demonstration of single chip microcomputer

Solution 1: 51 (single chip microcomputer) SCM, it is the most common single-chip microcomputer on the market at present. Many single-chip development boards are upgraded based on 51 single-chip microcomputers, so 51 single-chip microcomputers are more popular and resources are abundant. This single-chip microcomputer has powerful processing capacity and volume. Very small, very suitable for welding, the function is also incomparably powerful, but the disadvantage is that it is relatively energy-intensive, the memory is relatively small, and it is difficult for some complicated large-scale operations.

Solution 2: MSP430 MCU, which is a single-chip computer developed by Texas Instruments in the United States for the MCU enthusiasts. It has excellent processing power and powerful functions. The main feature is that its power consumption is very small, but the price is relatively expensive. The use of more complex, for some users who are not demanding, 51 microcontroller is more practical.

Considering the above two solutions, choose the STM series 89C51 microcontroller.

2 THEORETICAL ANALYSIS

2.1 theoretical basis of electromagnetic resonant coupling radio energy transmission system

The basic theory of electromagnetic resonance coupled radio energy transmission system is Maxwell's electromagnetic field theory. The following is a theoretical analysis of the propagation path and mode of magnetic field in the electromagnetic resonance coupled radio energy transmission process. Maxwell's electromagnetic field theory believes that the moving charge or alternating electric field can generate a magnetic field around it; and the alternating magnetic field can generate an electric field. Figure.4 is a distribution diagram of a magnetic field around a spiral coil, and H represents a magnetic field strength, and an alternating magnetic field is generated around the coil when an alternating current is passed through the spiral coil. The magnetic field strength increases as the coil distance decreases.[3]

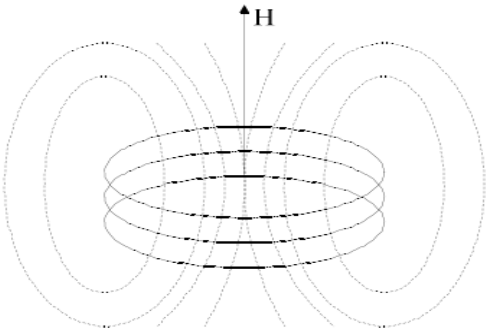

Fig.4 Magnetic field distribution around a spiral coil

The transmitting coil is regarded as a high-frequency transmitting source, and x is the distance from the receiving coil to the center of the transmitting coil. The distribution of the magnetic field around the two coils of the transmission system is as shown in Fig. 5. The magnetic field around the high-frequency source is divided into two major areas - the near field and the far field. The near field region is $\lambda/2\pi$ from the center of the transmitting coil (λ is the wavelength of the electromagnetic wave), and the far field region is $\lambda/2\pi$ from the center of the transmitting coil to infinity. There is no clear proportional relationship between the magnetic field strength and the electric field strength in the near-field region, but there is a certain proportional relationship between the two in the far-field region. Under normal circumstances, in the case of high voltage and small current, the electric field strength is much larger than the magnetic field strength; in the case of low voltage and large current, the magnetic field strength is much larger than the electric field strength.

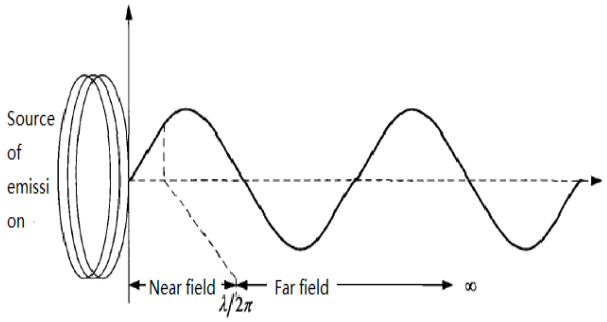

Fig.5 division of near and far field regions

2.2 lossless system two resonator mode coupling

The theoretical basis for magnetic field resonant coupled radio energy transmission is coupled model theory (CMT). Assuming that the analog signal is $a_1(t)$ and $a_2(t)$, the natural frequency is ω_1 and ω_2, the system has no loss. When the two resonators are coupled, we can get equation (1):

$$\begin{cases} \dfrac{\mathrm{d}\,a_1(t)}{\mathrm{d}t} = \mathrm{j}\omega_1 a_1(t) + \mathrm{j}k_{12}a_2(t) \\ \dfrac{\mathrm{d}\,a_2(t)}{\mathrm{d}t} = \mathrm{j}\omega_2 a_2(t) + \mathrm{j}k_{21}a_1(t) \end{cases} \tag{1}$$

Where k_{12} and k_{21} are the coupling factors of the two models, but according to the conservation of energy we can know that as time changes, the energy gradually approaches 0, so we can know:

$$\frac{d}{d\mathrm{t}}\left(|\ a_1\ |^2 + |\ a_2\ |^2\right) = 0 \tag{2}$$

Because $a_1(t)$ and $a_2(t)$ can be set to any value, the coupling relationship is:

$$k_{12} = k_{21}^* = k \tag{3}$$

From equations (1)-(3) we can know: $\omega = \frac{\omega_1+\omega_2}{2} \pm \sqrt{\left(\frac{\omega_1-\omega_2}{2}\right)^2 + |k_{12}|^2} = \frac{\omega_1+\omega_2}{2} \pm \Omega_0$ （4）

2.3 coupling of lossy system with two resonator mode

Considering the loss in a general practical system, it is easy to relate the coupling model to the current wireless power system, from which the following coupled differential equations can be obtained:

$$\begin{cases} \dfrac{\mathrm{d}\,a_S(t)}{\mathrm{d}t} = \left(\mathrm{j}\omega_S - \Gamma_S\right)a_S(t) + \mathrm{j}k_{SD}a_D(t) \\ \dfrac{\mathrm{d}\,a_D(t)}{\mathrm{d}t} = \left(\mathrm{j}\omega_D - \Gamma_D\right)a_D(t) + \mathrm{j}k_{DS}a_S(t) \end{cases} \tag{5}$$

Where $a_s(t)$ and $a_D(t)$ representing the signal source and device, $\omega_{S,D} = 2\pi \bullet f_{S,D}$ are the respective angular frequencies, $|\ K_{SD} = K_{DS}\ |$ is the coupling factors, and $\Gamma_{S,D}$ is the respective attenuation rates. The solution equations can be obtained:

$$\begin{cases} L\left(a_S(t)\right) = \dfrac{\mathrm{j}k_{SD}a_D(0) + a_S(0)\left(s+\Gamma_D - \mathrm{j}\omega_D\right)}{\left(s+\Gamma_S - \mathrm{j}\omega_S\right)\left(s+\Gamma_D - \mathrm{j}\omega_D\right) + k_{SD}k_{DS}} \\ L\left(a_D(t)\right) = \dfrac{\mathrm{j}k_{DS}a_S(0) + a_D(0)\left(s+\Gamma_S - \mathrm{j}\omega_S\right)}{\left(s+\Gamma_S - \mathrm{j}\omega_S\right)\left(s+\Gamma_D - \mathrm{j}\omega_D\right) + k_{SD}k_{DS}} \end{cases} \tag{6}$$

Here we only consider the coil S and the coil D. The single-turn coils that are transmitted and received are not considered at the same time, and it is assumed that the coil S and the coil D are identical, and the energy of the coil S is 1 when the system starts transmitting energy. In the form, we can very easily discuss the energy transfer of the coil in the case of resonance and non-resonance.

2.4 wireless transmission system working principle analysis and efficiency calculation

Turning the direct current into alternating current, through the principle of electromagnetic induction, the corresponding end of the alternating current is generated, and then the alternating current is converted into direct current by the rectifier circuit to drive the corresponding device.

The input power and output power of the system can be calculated by two types $P_{in} = U_{dc} \times I_{dg}$, $P_{out} = U_l^2 \div R_l$, where Udc and Idg are the input voltage and current of the inverter respectively, and U_l is the effective value of u_l. By measuring multiple sets of data and calculating, the output power and transmission efficiency can be obtained. The curve as a function of distance. The formula for calculating efficiency is: $\eta = \frac{U_2 I_2}{U_1 I_1} \times 100\%$

3 CIRCUIT DESIGN

3.1 Design of power conversion circuit

Since the system uses 12V DC power supply, and the power supply voltage of the MCU is 5V, it is necessary to convert the 12V voltage to 5V. [4]This design uses a three-terminal forward voltage regulator circuit, the chip model is 7805, and the circuit diagram is shown in Figure 6.

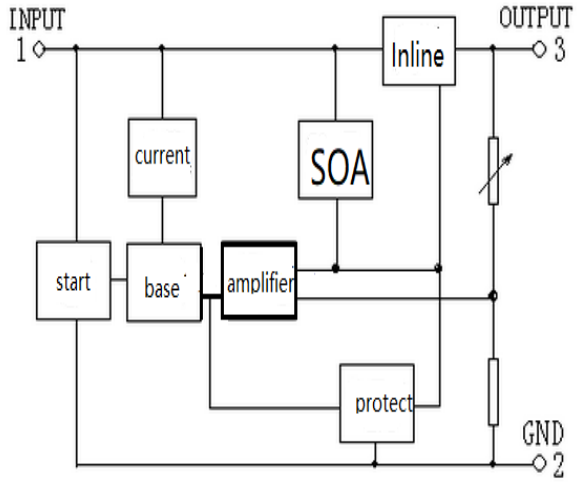

Fig.6 Forward voltage regulator

The 7805 is a TO-220 package that provides a wide range of fixed output voltages. It has a wide range of applications and includes overcurrent, overtemperature and overload protection circuits. With a heat sink, the output current can reach 1A. Although it is a fixed voltage regulator circuit, changing the external components can obtain different voltages and currents. The voltage conversion circuit is shown in Figure.7

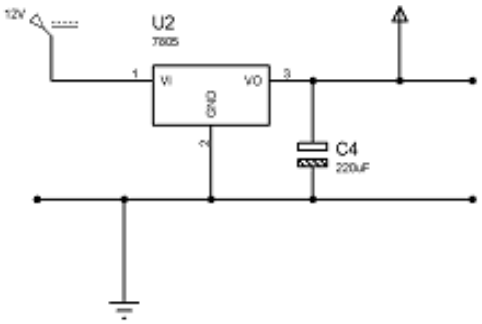

Fig.7 Voltage conversion circuit

3.2 receiving circuit design

The receiving circuit only needs to convert the energy sensed by the receiving coil, so it is relatively simple to design. The DC current and voltage are required for the load to be charged. Therefore, it is necessary to convert the energy received by the induction coil into DC power, so a rectification and filtering circuit is added to the last stage of the overall circuit. The receiving circuit is shown in Figure 8.

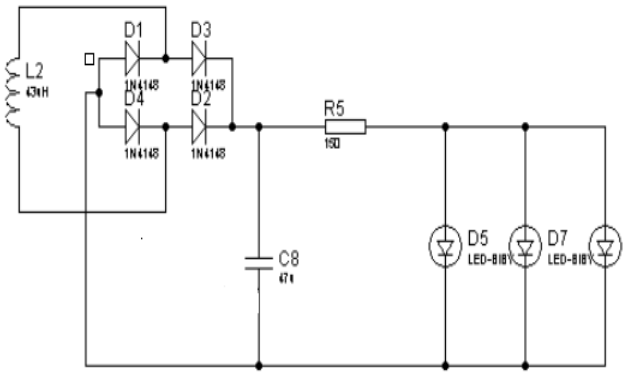

Fig.8 Receiving circuit

3.3 induction coil design

The design is made of a copper core coil with a radius of 0.2mm. The diameter of the induction coil is about 15cm, and the winding is about 34 circles. After testing, the inductance is about 43μH. The reasons for adopting such a design are as follows: a. The coil cannot be wound too little, because if the inductance is too small, the inductance is not large enough. b. The coil can't be wound too much, because if the coil is wound too much, the circuit will have too much inductive reactance due to the high resonance frequency when the circuit is in parallel resonance, resulting in less current generated in the circuit, and the generated magnetic field strength must also be It is small. [5]Combined with the actual situation, the coil we made is shown in Figure 9:

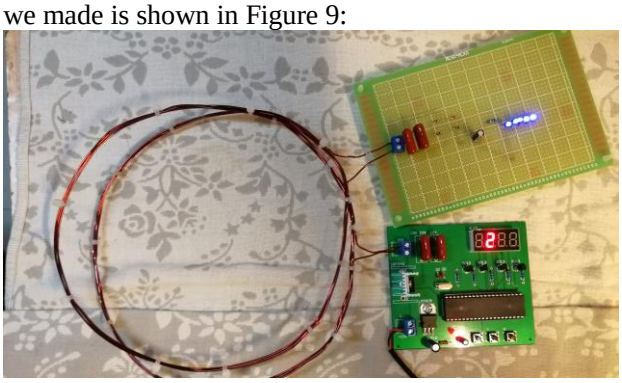

Fig.9 Induction coil

4 TEST RESULTS

The receiving end of the system uses six LED lights with a rated power of 1W as the load, and sets the frequency of the NE555 output oscillating signal to be about 440KHz.

When the distance between the transmitting coil and the receiving coil changes, the magnitude of the magnetic field strength also changes, so the magnitude of the output voltage also changes, that is, when the distance between the transmitting coil and the receiving coil increases, the magnetic field changes. Weak, the output voltage is reduced. The measured output voltage, output current, and output power are measured as shown in Table 1 at a distance of 1 cm each time.

TABLE 1 Test Data

Coil distance (cm)	output voltage (V)	Output current (mA)	output powerP(W)
0	11.6	158	1.833
1	11.5	75.9	0.873
2	11.5	42.3	0.486
3	11.0	28.6	0.315
4	10.5	16.9	0.177
5	10.5	9.2	0.097
6	10.1	5.1	0.051
7	8.7	3.0	0.026

As can be seen from the above table, as the coil distance increases, the output voltage, output current, and output power are all reduced.

5 SUMMARY AND PROSPECT

5.1 summary

In this paper, aiming at the realization of medium-range distance wireless energy transmission, electromagnetic resonance coupled wireless energy transmission technology is adopted, and the combination of theory and experiment is used to achieve the purpose of distance, efficiency and power maximization. Radio energy transmission system. In this paper, the scheme selection and design of the transmitting circuit, transmission circuit and receiving circuit in the electromagnetic resonance coupled wireless energy transmission system are introduced in detail. The functions and design principles of each module and module in the transmitting circuit are elaborated in detail. The rectification, filtering, and voltage regulator circuits have also been described in detail. Overall, the design has achieved the expected results and achieved the expected functions. Of course, there are still many areas worthy of improvement, which requires us to continuously learn and perfect.

5.2 prospects

Due to the author's relevant theoretical level, energy and time, there are still some shortcomings in the following aspects for further study.

(1) Without considering the control of the circuit, the charger is an open loop system, and the receiving end has no feedback to the transmitting end. When the system load changes, the load characteristics of the system will change. Therefore, the load characteristics of the system need to be further analyzed. .

(2) The current flowing through the wire in the device is large, and the resistor, the diode, and the triode are all energy-consuming components, so the loss on the device is large. Other methods can be used to reduce the energy loss of the entire system to increase the efficiency of the entire system.

References

[1] Allen, Richard S, Charles S. White, Margaret B. Takeda, Rewards and organizational performance in Japan and the United States,[J]. 2004, 7-14.

[2] Marylin M. Helms, A comparison, Compensation and Benefits Review [J]. 2004, 7-14.

[3] Andrews, Alice O,The effect of the chief executive officer’s financial orientation,[M]. 2000,25(1), 93-106. [4] Theresa M, Welbourne, Entrepreneurship Theory and Practice [M]. 2000,25(1), 93-106.

[4] Heneman, Robert L., Judith W. Tansky, Sheng Wang , Compensation practices in small entrepreneurial and high-growth companies in the United States and China,[M],2002,13-22

[5] Zhong-Ming Wang, Compensation and Benefits Review,[M],2002,13-22

Reseach on visual measurement technology of dimension parameters of small size parts

Jianxing Ma; Tian Li; Renliang Chen
（jilin university College of instrument Science andelectrical Engineering,changchun,130012）

***Abstract*—For using structure light sensor measurement problem of data processing in the process of small size workpieces for rapid, real-time, accurate measured workpiece size and location information, the team presents a measurement method based on MATLAB image processing method of processing data, at the same time to facilitate the practical application, the project team to design a set of control system based on Siemens S7-200 and a set of graphical user interface (GUI) based on MATLAB software applications.The final experimental results show that the system runs stably, runs fast, and the measuring accuracy can reach 1mm.Meet practical application requirements.**

***keywords*—Structural light visual image processing dimension measurement MATLAB/GUI**

I.INTRODUCTION

IN modern industrial production, a variety of product quality inspection is involved. In many cases, a non-contact, accurate and efficient measurement method is needed to meet the requirements of production quality inspection. Compared with the traditional measurement method, it can save a lot of time and manpower and have high economic benefits.Visual measurement system is composed of light transmitter, camera, image acquisition and processing system and hardware support system.The realization principle is to move the laser line emitted by the line light source, deform the structure light by the modulation of the surface information of the object under test, and use the camera to take back the structure light that is deformed, and compare and analyze the structure parameters of the system to realize the three-dimensional measurement of the object[1].

The visual measurement system based on the principle of structured light has a high application value in some environments with special requirements for the measurement system. At present, it is widely used in medicine, traffic monitoring, industry and other aspects.

Compared with the visual measurement system applied in domestic and foreign industrial systems[2], this system has more advantages in the measurement of devices with high precision, small external dimension and complex shape (multiple measured parameters).

II. PLATFORM FUNCTIONSAND DESIGN IDEAS

TO realize the integration of the system, the platform must include communication, algorithm integration, man-machine interaction and other functions, and meet the basic three features of conventional application software: simplicity, habituation and consistency[3].The specific functions are as follows:

(1) the design platform can communicate with peripheral hardware such as sensor sjg-200 and raster scale, transmit feedback data, and ensure the accuracy and real-time of data transmission.

(2) the interface integrates the independent development of image processing algorithm to realize the recognition of circle and rectangle[4];The size and location of the workpiece can be obtained and saved in real time.

(3) the interface has good human-computer interaction performance, and provides users with visual areas to facilitate users to get required information quickly.

III.DETAILED INTERFACELAYOUT DESIGN

The detection system is composed of three parts. The first part is that the structure light sensor sjg-200 is driven by the stepper motor controlled by PLC.The second part is the communication between PC and grating ruler and structure light sensor, receiving measurement information and realizing real-time communication function.The third part is based on MATLAB/GUI design interface to achieve image processing, identification information preservation, visual display and other functions.The overall structure of the test system is as follows:

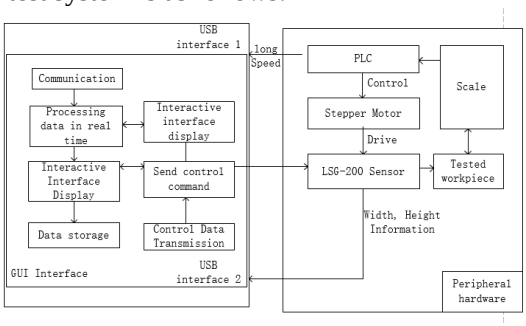

Fig.1 Image processing module

The layout of the communication module is as follows:

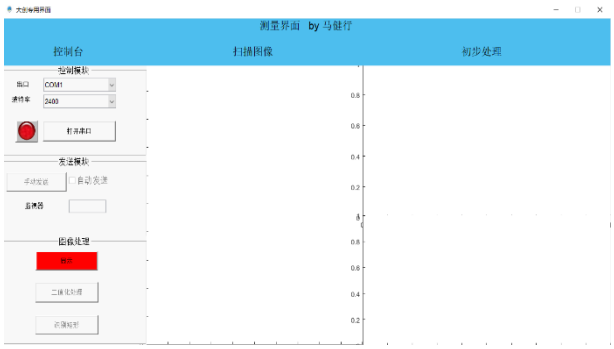

Fig.2 Communication module

The layout of the image processing module is as follows:

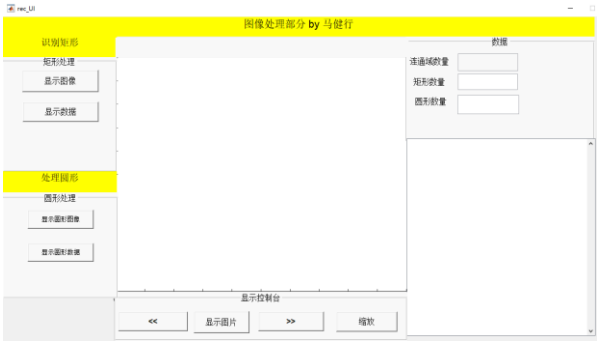

Fig.3 Image processing module

IV. IMAGE PROCESSING ALGORITHM

A.Center is Determined Based on Hough Transformation

For the circle center (Xi, Yi) with radius r, the rectangular coordinates are:

$$(a - X_i)^2 + (b - Y_i)^2 = r^2 \qquad (1)$$

Each point (Xi, Yi) corresponds to a cone in the three-dimensional space, so the point on the circular boundary intersects with the point (a, b, r)[5] in the three-dimensional coordinate system.

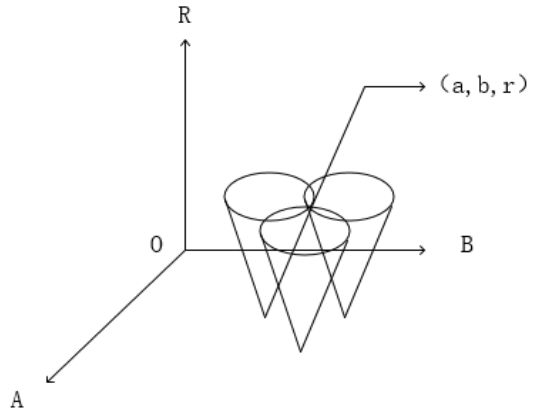

Fig.4 The boundary point of a circle on a Cartesian coordinate system is represented in the Space coordinate system

The traditional Hough transform first quantifies the circle, sets an accumulator in each quantization unit, and accumulates the corresponding quantization units mapped to the points on the circle.Increments from zero to the upper limit that the image plane can accommodate.Each increment corresponds to a planar map, resulting in a three-dimensional accumulator array[6].When all the transformations are completed, the values of all the accumulators are counted.The coordinate corresponding to the maximum accumulator is the center of the foreground image[7].Estimated running time according to its detection principle:

$$\sum_0^R 2r_0 T = R(R+1)T \qquad (2)$$

Where r0 is the given radius of foreground point, R is the range of radius change, and T is the time of each detection.

Suppose there are M boundary points, and the total detection time is[8]:

$$t_{all} = MR(R+1)T \qquad (3)$$

It can be seen that the time consuming and excessive memory consumption does not conform to the principle of software design.

Therefore, the project team proposed an improved method to obtain the boundary position information after the initial processing of point cloud, noise elimination, binarization, boundary extraction and other processes[9].

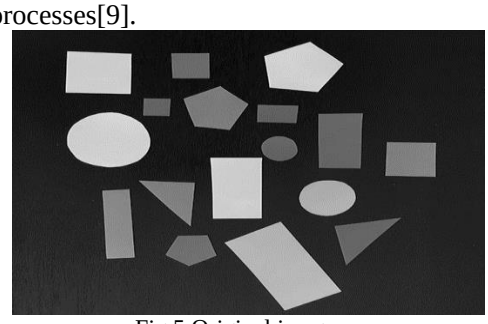

Fig.5 Original image

Consider the inherent features of the circle: a line whose distance from the center of the circle equals the radius is the tangent of the circle.Therefore, a straight line passing the center of the circle can be determined after the position information of each foreground point is added with the direction characteristic. By setting a reasonable threshold, the aggregation degree of foreground points can be counted[10].

The algorithm passes:

$$\begin{cases} a = x - r\cos\theta \\ b = y - r\sin\theta \end{cases} \qquad (4)$$

Determine the center of the circle, where $\theta = \tan^{-1}\frac{\nabla_y}{\nabla_x}$, ∇_y, ∇_x is the gradient[11].The edge points in the original image were mapped to a-b-r of the parameter space, and A certain range and step length were taken. The points in the space were mapped to the parameter space through inner circulation and outer circulation R, and the aggregation points exceeding the threshold were judged. The center of the circle was found in the parameter space[12].After treatment, the center of the circle was determined as follows:

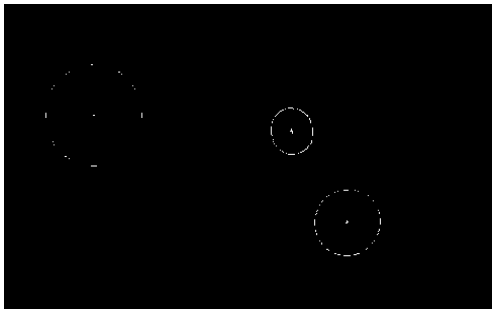

Fig.6 Center

The fitting result of the least square method is as follows:

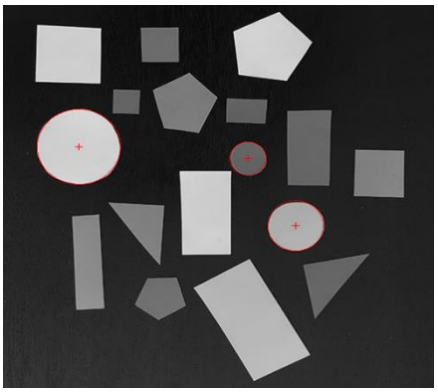

Fig7 Fitted circle

B. Detection rectangle algorithm

In this paper, the detection method of rectangle is selected according to the inherent characteristics of rectangle[13]: the distance from the center of rectangle to the boundary is the maximum and the distance from four vertices is the minimum.

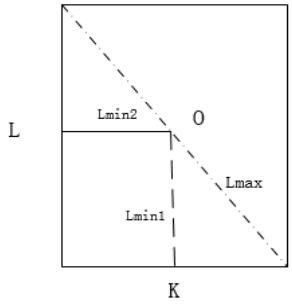

Fig.8 Schematic

The algorithm is as follows:

(1) Image preprocessing.
(2) Determine the connected domain and label the connected domain center.
(3) Canny was used to detect the boundary of the connected domain in the tested region and to refine it[14].

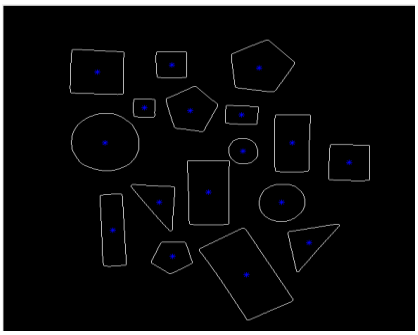

Fig.9 Preliminary processed image

(4) Polar coordinates of the difference between center and boundary coordinates can be obtained by using cart2pol function[15]:

$$[\theta, \rho] = cart2pol(\Delta y, \Delta x) \qquad (5)$$

(5) Establish the coordinate system, draw the coordinate relation of each connected domain in the coordinate system, and find the wave crest and trough (corresponding to the distance between the center point and the vertex and the distance between the center point and the boundary center)[16].
(6) Set appropriate thresholds to screen rectangles and calculate rectangle size information[17].

Calculation of rectangular length and width:

$$\begin{cases} L = 2\sqrt{{L_{max}}^2 - {L_{min2}}^2} \\ K = 2\sqrt{{L_{max}}^2 - {L_{min1}}^2} \end{cases} \qquad (6)$$

Partial results of screening are as follows:

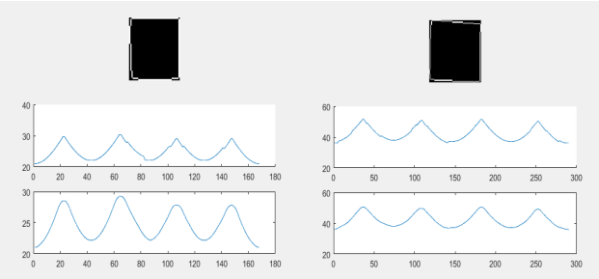

Fig.10Filtered rectangles and its relationship of $\theta - \rho$

V. Calculation Results And Comparison

To verify the reliability and practicability of the measurement system designed by the project team, three independent objects were measured.

Actual size of three objects:

Cylinder 1: radius/height: 1.25cm/0.370cm

Circle 2: radius/height: 0.95cm/0.668cm

Cuboid: length/width/height: 8.10cm/2.1cm/1.0cm

The project team got the following results after measurement:

Table.1 Cylinder 1 size information

measurement	radius(cm)	height (cm)
1	1.23	0.40
2	1.22	0.38
3	1.22	0.38

Table.2 Cylinder 2 size information

measurement	radius(cm)	height (cm)
1	0.98	0.70
2	0.97	0.68
3	0.97	0.68

Table.3 Cuboid size information

measurement	radius(cm)	width(cm)	height (cm)
1	8.08	2.04	1.02
2	8.12	2.07	1.03
3	8.11	2.08	1.01

Through the study of visual measurement technology of the external dimension parameters of small size parts, the measurement of the external dimension parameters of small size parts can be achieved. Through the processing of point cloud data, all the expected indicators can be achieved. The measurement accuracy of the 3d scanning system is 0.01cm, and the measurementrange is 10cm*5cm*5cm.

VI.CONCLUSION

Project results:

Systems.The hardware part of this project adopts screw linear track with motor to drive sensor motion, raster ruler to assist measurement, peripheral control box to control hardware part motion, and at the same time serves as the intermediary between hardware part and PC communication[18].The design of the hardware system is reasonable, stable and reliable. The design adopts modularization thinking, which can realize the rapid assembly and disassembly of the hardware system for easy application.

Software.The project team USES MATLAB as the upper computer design platform. Although MATLAB has a short board in UI design, its good image processing performance indirectly improves the accuracy of the whole system[19].Through the self-designed object recognition algorithm and object size calculation, the actual size of the measured workpiece can be obtained with the precision of 0.1mm while accurately recognizing the object shape, which meets the actual demand.

Overall cooperation.The core software of this project is MATLAB, which must process the data transmitted by sensors and process it in real time. However, due to the limitations of MATLAB itself, it is difficult to achieve real-time communication with hardware.Therefore, communication must be achieved indirectly through the intermediate control box. The project team wrote a function to access the PLC's memory to read its high-speed counter content and realized communication with the sensor through the serial port communication function to achieve the cooperation of the whole system software and hardware.

Future Expectations

Although the project team in part size measurement based on structured light technology has obtained certain achievements, but because of my professional knowledge is limited, parts for machine vision measurement still exist many problems to be solved, workpiece size measurement precision still has room for improvement, the real-time measuring process also needs to be improved.Let's sum up the problems we need to solve.

Processing time.It takes about 3 minutes to measure a 10CM workpiece. Although the accuracy meets the actual demand, there are big problems in time.Objectively speaking, the project team used the keenz ljg-200 sensor to transmit data with an upper limit. When cooperating with the stepping motor, the stepping motor should reduce the rotation speed to match the data processing speed, which directly increases the processing time of the system.Hardware locks processing time.In the future, the project team plans to optimize the algorithm to shorten the scanning process of the system and speed up the data processing.

Communication stability.As mentioned above, communication between MATLAB and hardware needs to be mediated through the intermediate control box. As the communication process is too complex, communication stability is reduced.In the actual test, PC access PLC memory failure and other problems occasionally occur, which reduces the system robustness[20].The project team plans to reduce data transmission links through direct communication between PC and hardware systems, ensure the stability of communication channels and indirectly improve data transmission accuracy.

After the research of domestic and foreign scholars in recent years, the dimension measurement technology of machine vision has been developed rapidly.We believe that with the development of science and technology, the problems in this paper will be solved smoothly.

References

[1] Xianfeng Z. 3d measurement of workpiece size based on binocular vision [D]. Zhejiang ocean college, 2014.

[2] Jianwei L, Jin L, Xinhe L,. Large industrial visual measurement system [J]. Optical precision engineering, 2010,18(1): 126-134.

[3] Jianhua Y. Research on the key technology of 3d surface measurement system based on line structure optical sensor [D]. Guangdong University of Technology,2013.

[4] Dinghai Z, Shenghua Y, Chunhua W,. Visual inspection system for on-line measurement [J] . Chinese Journal of Scientific Instrument, 1995 , 16(4):337-340。

[5] B G Batchelor, D W Braggins. Commercial vision systems in computer vision [J]. Theory and Industrial Applications, 1992:405-452.

[6] Wang Z，Shen M． Serial communication program developmentbased on Matlab GUI ［J］． Modern Electronics Technique，2010(9) : 38 － 41．

[7] Lu Guangquan, Xu Hongguo, et al. Line segment detection based onchain code detection [J]. Computer

Engineering, 2006, 32 (14): 1~3.

[8] LUO H．Study notes of Matlab GUI design［M］． 2nd ed. Beijing University of Aeronautics and Astronautics Press，2011: 87－ 673.

[9] F. Keceki, H. H. Nagel. Machine vision based estimation of pose and size parameters from a genetic work piece description [J]. IEEE Tran On robotics an Automation, 2001, 3:2159-2164.

[10] Qiuqi R．Digital image processing [M]. Electronic Industry Press，001．

[11] S.Sirkis, T. J. Lim, Displacement and Strain Measurement with automated Grid Methods [J]. Experimented Mechanics, December 1991:382-388.

[12] F.Mokhtarian, R.Suomela. Robust image corner detection through curvature scale space [J].IEEE Trans. on Pattern Analysis and Machine Intelligence. 1998, 20(12):1376-1381.

[13] A Bandera, C Urdiales, et al. Corner detection by means of adaptively estimated curvature function [J]. Electronics Letters, 2000, 36:124-126.

[14] P Reche, C Urdiales, et al. Corner detection by means of contour local vectors [J].Electronics Letters. 2002, 38(14):699-701.

[15] C Urdiales, C Trazegnies, et al. Corner detection based on adaptively filtered curvature function [J]. Electronics Letters, 2003, 39(5):426-428.

[16] D J Langride. Curve encoding and the detection of discontinuities [J]. CVGIf, 1982, 20(1):58-71.

[17] Jianping R，Bo Y．Design of automatic height detection system for cylindrical parts．Yangtze University，010，ol.6(7)：315～317

[18] Deshan D．Research and application of machine vision in non-contact detection of workpiece [J]．Beijing：Beijing University of Posts and Telecommunications，2007

[19] Mengmeng Q，Zong Q．The application of image processing technology in automatic chip size detection．Mechanical Engineering & Automation，009，Vol.10(3)：131～133

[20] Zhengda Z．Research on small size precision measurement based on image processing [J]．xian：Xidian University，2008

The Detection Robot by Magnetic Method

Xinyu Zhao, Zhi Ma, Xinchao Cui
（jilin university instrument science and engineering institute,changchun,130021）

***Abstract*—Through the analysis of current domestic and foreign mine detection techniques and mine detection methods, magnetic detection is used to combine HMC series chips into a three-axis reluctance sensor on a wheeled robot for field mine detection. Through WIFI technology for visual positioning, and the specific location of mines sent to the host computer software through GPS. The experimental results can successfully discover the landmine warning and show the specific location on the host computer software.**

***keywords*—magneto-resistive sensor mine exploration stm32 single-chip microcomputer magneto-resistive sensor three-component GPS positioning**

I. INTRODUCTION

THIS magnetic detection is one of the currently effective methods of mine detection and is currently one of the research directions of various countries. This experiment mainly uses the series chips of hmc to form a three-axis magnetoresistive sensor for mine detection and uses wheeled robots to drive the acquisition module in the field. Landmines are thus detected and the specific location of the mines is discovered and identified. suspicious metal mines are found, and the alarm position is promptly sent back on the host computer software to feedback the current position.

II. Procedure for Paper Submission

A. Hardware circuit module design

a) Collection section

The acquisition part of the robot is mainly to measure the magnetic field of the underground surface, and determine whether the magnetic field is in the range of the mine shell material to determine the position of the mine.

The magnetoresistive sensor uses a new type of thin film magnetoresistive sensor hmc1001, hmc1002 developed a three-component magnetoresistive sensor that can measure the horizontal and vertical components of the magnetic flux density and magnetic induction intensity of the underground magnetic field[1]. This type of magnetoresistive sensor is a four-element Wheatstone bridge configuration that converts a magnetic field signal into a differential output voltage signal with a sensing magnetic field as low as 30 u Gauss[2]. This kind of sensor has the characteristics of low cost and high sensitivity[3].

The signal acquisition chip selects the new high-precision, wide dynamic range AD7799 from Analog Devices, a 3-channel, 24-bit ADC that is generally suitable for low-frequency, high-precision industrial-grade conversion. It can directly measure the weak DC signal output by the sensor and contains a programmable gain amplifier. The conversion accuracy can reach 24 bits without error[4].

b) Measuring magnetic field elements

To facilitate the observation and study of magnetic fields, we decomposed the geomagnetic field into several geomagnetic elements.

In Cartesian coordinates, the x-axis is geographical north, the y-axis is geographical east, and the z-axis is vertically downward. When studying any point of magnetic field, this point is usually taken as the origin O of the Cartesian coordinate system. The magnetic field at this point is called the total vector T. The projection of T on a horizontal horizon is the horizontal component H of the geomagnetic field. The projection of T on the Z axis is the vertical component Z of the geomagnetic field. The angle D between T and H is called the magnetic dip angle. The projection of H on the X axis is the northward component of the geomagnetic field. The projection of H on the Y axis is called the eastward component of the geomagnetic field, the angle between H and X is called the magnetic declination. Therefore, geomagnetic elements mainly contain seven quantities T, H, Z, X, Y, D, and A[5].

The relationship between these elements is as follows:

$$Z = T\sin D;$$
$$H = T\cos D;$$
$$Z = H\tan D;$$
$$Y = H\sin A;$$
$$X = H\cos A;$$
$$T = \sqrt{X^2 + Y^2 + Z^2};$$

c) Magnetoresistance effect

The magnetoresistance (MR) effect refers to the phenomenon that the resistance of a conductor or semiconductor changes under the influence of a magnetic field[6].

For magnetic metals iron, cobalt, nickel and its related alloys, when the direction of the applied magnetic field is parallel to the magnetization direction inside the magnet, the resistance value of the metal is almost constant; when the direction of the applied magnetic field deviates from the internal magnetization direction of the metal, the resistance value of the metal will reduced. This is the anisotropic magnetoresistance effect of ferromagnetic metals.

The basic unit of the anisotropic magnetoresistive sensor is: A long and thin permalloy is deposited on a silicon substrate by a semiconductor process. When a certain amount of direct current is applied along the length of the permalloy, a magnetic field is applied in

the direction of the vertical current, and the resistance of the permalloy greatly changes, and this change is used to measure the magnitude and direction of the magnetic field[7].

Its change formula obeys the following formula:

$$\rho(\alpha)=\rho_{\perp}+(\rho_{\Pi}-\rho_{\perp})\cos^2\alpha$$

The resistivity (p) of the permalloy film depends on the angle between magnetization (M) and current (I).

d) Three-component magnetoresistive sensor design

In order to make the magnetic induction directions of the three magnetoresistive resistors of the three-component magnetoresistive sensor be perpendicular to each other, the requirement for placing the chip is to place it vertically at an angle of 90 degrees. The core of the HMC1001 and HMC1002 magnetoresistive sensors is the Wheatstone bridge. Permalloy has anisotropic magnetoresistance effect, which causes the output voltage of the sensor to change when the resistance of the bridge resistance changes.[8] Its internal two aluminum ring-shaped current bands (SET/RESET STRAP) will set the reset current of the sensor to correct the sensitivity of the ring current band, and it can also set and reset the polarity of the output voltage.

The magnetoresistive sensor used in this experiment is based on the working principle of magnetic thin film anisotropic magnetoresistive effect (AMR) [9].

When the energized magnetic film is placed in a different applied magnetic field, the sheet resistance will change. The bridge power supply drives the current in the thin film. When the spatial magnetic field is zero, the resistance of the four thin film resistors is R. When the external magnetic field changes, the magnetization state of the thin film changes, and the magnetization direction changes along the current direction. . The two pieces of the thin film resistance are reduced, and the magnetization direction of the other two films is opposite to the direction of the current, and the resistance value increases. The voltage output in the linear range is proportional to the measured magnetic field value[24].

$$\Delta U_O=(\Delta R/R)*U_B$$

$$\Delta U_O=U_B*M*S$$

Where R is the semiconductor film resistance S is the magnetoresistive sensor sensitivity M is the applied magnetic field value, and thus

$$M=\Delta U_O/(U_B*S)$$

That is, the output voltage signal is proportional to the applied magnetic field[10].

The magnetic signal acquisition circuit connects the three magnetic field components Z, Y, X measured by the magnetoresistive sensor to the channels 1, 2, and 3 of the AD7799, and then sends the converted digital quantity of the AD7799 to the STM32 microcontroller for subsequent analysis and processing. Simultaneously connecting the set reset band of the two magnetoresistive magnetic sensors, the same set reset signal can be obtained, and the synchronization on the set reset timing is maintained. That is, the S/R-(A) of the HMC 1002 is connected to the S/R+ (B) of the HMC 1002, and the S/R- of the HMC 1001 is connected to the HMC 1002S/R-(B) at the same time. The same S/R pulse is applied to the HMC1001 S/R+ and HMC1002S/R+(A). HMC1001 and HMC1002 signal output X, Y, Z three components are respectively connected to the AD7799 three input channels, AD7799 self-calibration and other functions, can automatically eliminate the zero error and full-scale error, and reduce the impact of temperature drift.

The following figure shows the internal structure of the AD7799, which consists of analog multiplexers, input buffers, programmable gain amplifiers, integrated modulators, programmable digital filters, nine state control registers, serial interfaces, and clock generators.

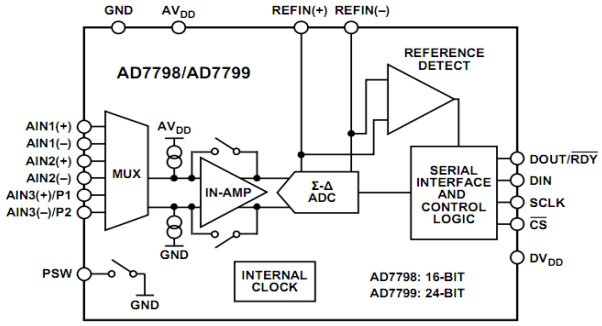

Figure 1 The internal structure of AD7799

e) Set reset circuit

As the applied magnetic field is strong enough during the experiment, the easy axis of the sensor will jump and the characteristics of the sensor will reverse. If the reset function is not set, the measured value of the sensor will become inaccurate. As a result, the error is large. Therefore, in the actual circuit, a set reset pulse is used to generate an external strong recovery magnetic field, and the MCU is used to control the turn-on and turn-off of the MOS transistor to charge and discharge the capacitor, so that a strong magnetic field is generated to make the polarization directions of the magnetic domains uniform. This can increase the sensitivity of the sensor while eliminating the effects of temperature drift.

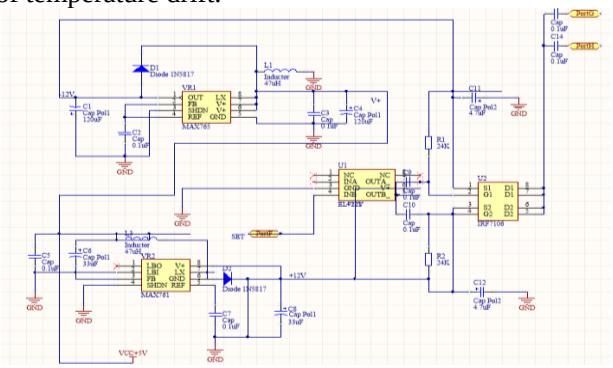

Figure 2 Set reset circuit

f) Power section

For the robot, the power module is a vital part of his work. First, the power supply must provide a stable jitter-free power signal to ensure that all parts can

operate stably at the rated voltage, and secondly, accurate measurements can be made. deal with. The power module can convert the input voltage to the standard voltage required by each device such as +5V, +3.3V.

In the acquisition circuit because the chip IRF7106 need to use positive and negative voltage of 12v to charge and discharge the capacitor to generate a sharp pulse with an amplitude of 24v. Therefore, in the actual design, the MAX761 is used to convert and generate +12V voltage. The working principle of this circuit is as follows: L is the energy storage inductance in the circuit, LX is taught to connect the drain of the internal N Channel FET, and D is the fast recovery diode. When the internal FET is turned on, the inductor L stores energy and continues until the FET is turned off. The inductor begins to release energy through the diode D and charges the capacitor.

MAX761 input voltage range is 2 ~ 16.5V, output voltage is 12V, built-in 1A MOSFET, application requires lower energy, V + by the internal resistor divider and reference voltage, the voltage value is stable at 12V output.

The circuit diagram is as follows

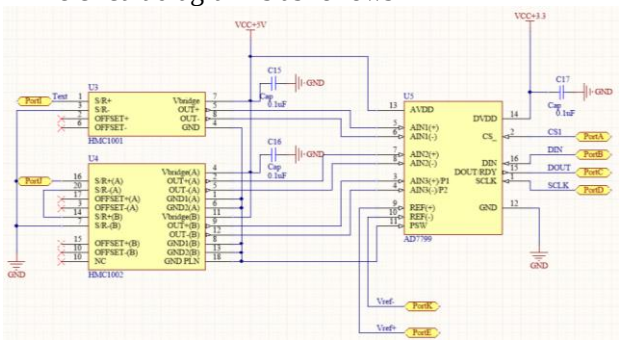

Figure 3 AD7799 connection diagram

For the -12V power supply, the MAX765 is used for design. The principle of conversion is the same as above and is not repeated here.

The circuit diagram is as follows

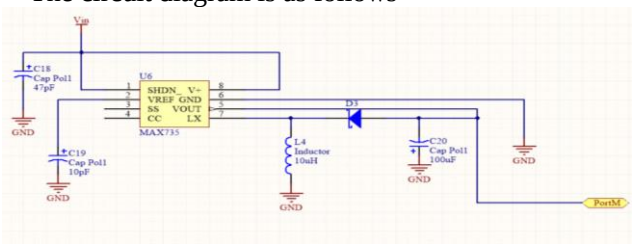

Figure 4 Power circuit

g) AD acquisition module

The AD acquisition module is an important part of the acquisition part and is divided into AD initialization, acquisition measurement, and read-write data.

Initialization and acquisition measurements configure the AD7799's internal registers, mode registers, and communications registers.

The mode register is used to proofread the working polarity of the AD7799, set the AD7799's internal amplification gain through the bridge output signal range, and select its signal input channel. The U/B bit selects unipolar or bipolar, and the AD7799 selects the bipolar input based on the bridge voltage output of the magnetoresistive sensor. The G2, G1, and G0 bits are used to set the internal gain of the AD7799 because the full-scale output voltage of the bridge is >64mV, so 32-bit gain is selected by KEIL programming and the internal buffer is selected when the BUF bit is 1. In order to make the input voltage fluctuate little and the current is large, CH x selects the three-channel acquisition to perform the data input of the three components of the X-axis, Y-axis, and Z-axis.

The upper four MD x bits of the configuration register set the operating mode of the AD7799. During initialization, zero correction and internal full-scale correction are performed. At the same time, the AD7799 is configured as a continuous measurement mode. FS3-FS0 determines the conversion rate of the AD7799. Here 16HZ conversion rate acquisition.

h) Action section

The robot is a movable car programmed by Arduino. It can control the robot's movement and direction control through the host computer software and connect to the host computer through WIFI video for long distance observation to determine the specific location of the mine.

Arduino is a popular MCU-based system development platform. It has the advantages of simple use, multiple functions, and low cost. In this experiment, the Arduino UNO R3 control board was combined with the WIFI module, and the 720P high-definition camera was used with the 2-DOF steering platform to complete the design of the action part. The PC software controlled by it was compatible with the win7 win8 win10 64-bit system[11].

i) Use of GPS

The main functions of the GPS part of this experiment are as follows:

The remote location of the object is achieved, and the data of the GPS module is received by the single-chip microcomputer for processing, and the position and time information of the suspicious mine when the alarm occurs is obtained.

The position resolution and positioning accuracy algorithm based on ARM's GPS positioning module gives it the ability to locate long distances. The data receiving device is installed on the object to be tracked. The receiving device analyzes the positioning information of the object to be tracked by receiving signals generated by the GPS module, and transfers the packaged data to the stm32 single chip microcomputer to obtain the time and status information of the object to be measured. (longitude, latitude, altitude, etc.) Then sent to the upper computer through the Bluetooth device to get the robot's positioning information[12].

The GPS positioning module consists of a data receiving device and a data processing device. The data receiving device includes a GPS receiver, a wireless RF module, and a power supply. The data processing device is composed of an ARM microprocessor and a peripheral circuit when it is

submerged[13].

In this experiment, the GPS module was selected as a general-purpose module that uses the serial port for communication control. The baud rate is 115200[14], the data bit is 8 bits, no check bit, and 1 stop bit. The data is transmitted in ASCII code.

j) Factors Affecting GPS Positioning Accuracy

There are several kinds of errors in GPS positioning affect the positioning accuracy, mainly include:

1. The satellite clock skew, which includes the clock difference between the satellite and the satellite and the clock time difference between the satellite and the receiver, causes the inaccuracy of the distance between the computing receiver and the satellite and the inaccuracy of the pseudorange. Positioning accuracy and thus influence;

2. Ionospheric error, in the process of signal transmission, refraction occurs from one medium to another, increasing the distance between the computing receiver and the satellite;

3. Ephemeris error, the ephemeris is the trajectory map of the satellite, ephemeris error refers to the satellite does not follow a certain trajectory, resulting in inaccurate distance between the calculation receiver and the satellite;

4. Receiver errors, data received by the receiver may cause data loss, etc., and cannot guarantee that the received information is accurate.

At present, algorithms for GPS data processing include algorithms such as least square method, particle filter algorithm, and Kalman filter[15].

k) Analysis of GPS data

GPS consists of three sections: The satellite constellation (space section) functions to provide GPS receivers with a fixed-frequency conductive message. The role of the ground control/detection network (control section) is mainly to control the GPS satellite constellation and to detect whether the GPS satellite constellation is operating in a normal state. The user receiving device (device segment) usually refers to the GPS receiver and is applied in the positioning module[16].

The GPS receiver belongs to the user receiving device of the global positioning system.

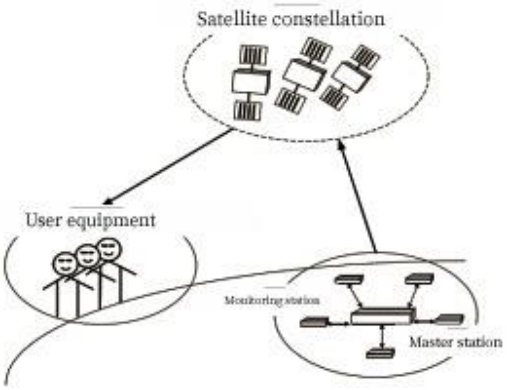

Figure 5 Data receiving device diagram

For parsing GPS data:

In this experiment, the statement in the $GPGGA format is used. The standard format is:

$GPGGA,(1),(2),(3),(4),(5),(6),(7),(8),(9),M,(10),M,(11),(12)*hh(CR)(LF)

The meaning of each symbol in the formula:

(1) Positioning UTC time, type double;

(2) The dimension (ddmm.mmmm) is of type double;

(3) North latitude or south latitude (N/S), type char;

(4) The precision (ddmm.mmmm) type is double;

(5) East or West Longitude (E/W), type char;

(6) The quality factor 0 represents no positioning;

(7) The number of available satellites of type int;

(8) Horizontal accuracy factor;

(9) Antenna elevation, m, type double;

(10) The height of the ellipsoid of the earth relative to sea level;

(11)(12) Generally not used. (CR)(LF) is carriage return and line feed[17].

l) Bluetooth module

Bluetooth technology is a kind of wireless communication technology. The working frequency band is in the globally-available 2.4 GHz ISM frequency band. It adopts a fast identification and frequency hopping scheme, so that Bluetooth has good anti-jamming capability and system stability[18]. Bluetooth technology can realize wireless communication in a small area and communication technology of autonomous networking of a small network[19].

This experiment uses an external STM32 microcontroller to develop and configure the Bluetooth module through the host control interface, so that the Bluetooth module and the computer communicate wirelessly, return the required data and send corresponding control information.

The common Bluetooth module integrates a baseband controller, data memory, program memory, radio frequency interface, and external I/O ports.

The RF module performs functions such as mixing, filtering and power amplification. It is responsible for demodulating the received high-frequency signal (2.4GHz) into an IF signal and transmitting it to the Bluetooth baseband controller. The low-IF signal from the Bluetooth baseband controller is modulated to 2.4GHz high-frequency signal and transmitted[20]. The RAM is used for data processing and temporary storage in Bluetooth communication. The internal Flash loads the protocol of the underlying hardware of the Bluetooth module and the program developed for the Bluetooth module[21].

The function of the Bluetooth module is determined by the Bluetooth protocol loaded on the processor at the factory. The Bluetooth protocol running on the chip is mainly divided into three categories: 1. Standard HCI, 2. Serial port function, 3. Integrated application program[22]. The standard HCI Bluetooth chip does not have an application protocol loaded, but the Bluetooth module can be developed through the HCI interface to implement certain specific functions in the Bluetooth protocol. Its serial port function regards the Bluetooth module as a wireless serial port device,

emulates the RS232 function, and loads the serial port simulation protocol RFCOMM on the Bluetooth module[23]. The integrated application is integrated with certain application functions on the Bluetooth module[24].

This experiment uses the HC05 Bluetooth module, the operating voltage is 3.3v, and the serial baud rate is 115200b/s. The Bluetooth chip communicates with the SCM through the serial port. At the same time, the Bluetooth module communicates with the PC through the serial port[25]. The two Bluetooth modules communicate wirelessly[26]. The Bluetooth serial debugging software can control the Bluetooth chip through the AT command, and the Bluetooth module serial communication design steps: Initialize the HC05 Bluetooth chip, query the available Bluetooth addresses, send requests, allow Bluetooth connections, transfer data, and disconnect.

In the experiment, the detected alarm signal and the time and position information received by the GPS are wirelessly transmitted to the host computer through Bluetooth.

B. software design

The experimental microcontroller uses the STMF103VET6 minimum system board.

The STM32F103xE enhanced family integrates a high-performance 32-bit ARM Cortex-M3 RISC core operating at 72 MHz, high-speed embedded memory(Flash memory and SRAM are up to 512k and 64k bytes respectively), and two APB bus enhancement I/O and peripherals[27].

This experimental program is based on the IDE integrated development environment of KEIL MDK5. The debugger uses JLINK. The firmware library uses ST official 3.5.0 library[28].

At the time of design, research and development were carried out on the module programs such as Bluetooth transmission, GPS positioning, ADC acquisition, delay processing, and USART configuration. Finally, they were brought together to form the final program for experimental debugging.

C. Data processing method

After the experimentally measured data is transmitted back through Bluetooth, the corresponding data processing is performed. First, the returned X Y Z axis 4-digit hexadecimal number is converted into a decimal number for processing, and then the corresponding environment and temperature compensation are performed. Based on the experimental environment and temperature, the relevant data is searched for software precision compensation in the range of 20 to 25 degrees Celsius. The basic magnetic field data is compensated based on the data collected without the experimental object. Repeat calibration in different environments to ensure the data is close to the true value. The compensation data is as follows:

In the range of 20 to 25 degrees Celsius

$$X = X_{CE} + 1817(nT);$$
$$Y = Y_{CE} + 23340(nT);$$
$$Z = Z_{CE} + 40572(nT);$$

Where CE is the measured value and XYZ corresponds to Hx, Hy, and Hz, respectively.

In the experimental environment, the measured environmental magnetic field interference is relatively small relative to the magnetic field of the object to be tested, and the interference caused by the environmental magnetic field can be ignored.

The above processing data is processed as follows:

$$H_{\text{xout}} = H_X * 1.2 - 5554;$$
$$H_{\text{yout}} = H_Y + 4880;$$
$$H_{\text{zout}} = H_Z + Z_{OFF};$$
$$Z_{OFF} = \tan a * (|X\max| + |X\min|) /2 - (Z\max + Z\min) /2;$$

Where a is the geomagnetic dip.

D. Commissioning results and analysis

The relevant accuracy test is performed on the robot, and the operation result is subjected to temperature compensation and environmental magnetic field compensation, thereby improving the accuracy and accuracy of the magnetic measurement, reducing false alarms and improving sensitivity.

The same object to be tested is detected by different routes, and the results can be found and alarmed, and the returned position information is consistent; when the two objects to be tested are 15 cm in diameter, they are respectively placed at different positions to be detected. However, if they are stacked together, or if they are partially overlapped together, only one object to be tested can be detected, resulting in a lower accuracy. For the case of multiple objects to be tested, when the object to be tested is separated by more than 20 cm, it can be detected separately, and other stacking situations will be greatly reduced. However, in view of the location and number of mines under actual conditions, it is rare to bury multiple mines in the same vertical direction. Therefore, the error rate for this case is within the range allowed by the current accuracy. At the same time, this is also the next problem and direction of improvement, improving detection accuracy and reducing false positive rate.

III CONCLUSION

The acquisition module is based on the structure and characteristics of the three-component magnetoresistive sensor. It uses the magnetic sensor to construct the magnetic field signal detection part, and uses the high-precision AD chip AD7799 to collect and process the signal. STM32F103VET6 single-chip microcomputer for digital signal processing and control of related modules[29]. On the basis of hardware design and debugging, the main program of KEIL software is used to design the data acquisition, GPS positioning, Bluetooth transmission and other functions. Based on the acquisition part, the mobile part of the robot is designed using ARDIUNO microcontroller. Through the host computer software to control the robot's forward, backward, left and right

movement, rotating camera angle and other functions. And to a certain extent, it can measure buried metal mine simulation objects, return their current GPS information, and issue an alarm.

Reference

[1] Xuefei Wang, Cheng Song. Research on key technologies of assisted GPS positioning system, 2009.2.

[2] HONEYWELL,CROSSAXISEFFECTFORAMRMAGNETICSENSORS,http://www.honeywell-sensor.com.cn,2004

[3] Kardach.J.Bluetooth architecture overview . IntelTechnology Journal Q2,2000

[4] Arnold Gum,Mario Proietti,Dan Hoskins,B.Ohm.E911 Roundtable[J].GPS World.2002.

[5] Jipeng Lin, Jun Wang, Zhenbao Ling. HMC1001 Magnetoresistive Sensor and Application.2002

[6] Xianmin Ma, Lichao Yan. Based on USB interface; Bluetooth wireless module design. 2004.4

[7] Jun Wang, Dengyun Wu, Development of magnetoresistive three-component magnetometer.

[8] HONEYWELL,1-and2-AXISMagneticSensorsHMC1001/1002HMC1021/1022,http://www.honeywell-sensor.com.cn,2004

[9] ANALOGDEVICE,AD7798/AD7799 DATASHEET,http://www.analog.com,2005

[10] Dong Tian. Design of three-dimensional magnetic field measurement system based on magnetoresistive sensor. 2010

[11] Feng Li, Han Xu. Design and implementation of Bluetooth-based ECG acquisition and transmission system. 2012.11

[12] Ruiqi Cai. Principles and applications of Arduino, 2011.8

[13] Qun Zhang, Bu Yang, Zhengyan Zhang. Design and implementation of serial communication for Bluetooth module. 2012

[14] RASHID R A , YUSOFF R . Bluetooth performance analysis in personal area network (PAN) [J] . RF and MicrowaveConference , 2006

[15] Jun Jing, Xiaoyu Ma. Research on portable ECG acquisition and analysis system based on STM32 and Bluetooth 4.1.2016.5

[16] Yuanyao Lu, Yuzhu Bai. Research on GPS based positioning and navigation technology based on embedded.2011

[17] Zhenlin Lu, Minghui Zhang. Research on real-time detection system of smart car based on Bluetooth technology. 2010

[18] Youxun Zheng, Zongbo Li. Research on GPRS Data Transmission Technology Based on STM32 Microprocessor. 2012

[19] Wei Zhuang, Zhenrong Li. Research on Key Technologies of Bluetooth-based Wireless Communication Chips. 2010.4

[20] Haoqiang Tan. C Programming (Third Edition). Beijing: Tsinghua University Press, 2005.

[21] Hongli Zhou, Wei Zhao. Bluetooth interface design and data transmission based on single chip microcomputer. 2008.6

[22] Honeywell． 1- and 2-Axis Magnetic Sensors HMC1001 /1002 //1021 /1022［EB / OL］.［2011 －5］.http: / / www. honeywel1．com.

[23] Bluetooth TM，Specification Volume 1 Specification of the Bluetooth System Core，Version 1.1. 2001

[24] Yusen Sun, Fengying Yue, Yonghong Li. Digital magnetometer based on magnetoresistive sensor. Liu Li, Liu Xiao's design. 2014.1

[25] Bluetooth specifications Version 2． 0 + EDR． 370-650． http: / /www．docin． com /p- 57455142． html ［ DB /OL］ .

[26] Qiang Meng, Hui Xu. Based on STM32 data acquisition and display system. 2013.5

[27] Wenzhao Liu, Tiejun Yu. Design and Implementation of GPS Positioning System Based on ARM.2014.5

[28] Yonghong Li, Shengfei Zhao. Design and implementation of data acquisition and storage system based on STM32.2014.5

[29] Wujie Zhang, Yimin Nan. Implementation of application programming technology based on STM32F103VB. 2009.10

Design of Transistor Characteristic Graphic Instrument Based on Virtual Instrument

XieLaibin; WangXingda; LiuXu
(School of Instrument Science and electrical engineering, Jilin University,Changchun 130026)

***Abstract*—Based on the virtual instrument technology and ideas, this article designs a transistor characteristic grapher. With the common computer, data acquisition card and host computer, real-time rendering and observation of various transistor characteristic curves are realized. The host computer was written using LabVIEW software, and the data acquisition was done using the domestic data acquisition Casmercohua USB-4220. After testing, the meter can measure BJT with a certain output power. The drawn curve is close to the characteristic curve provided by the official.**

***Key words*—virtual instrument transistor LabVIEW characteristic curve**

0 INTRODUCTION

THE invention of transistors is a milestone in the field of science and technology. Before the emergence of transistors, electronic devices used vacuum tubes. Compared with vacuum tubes, transistors have smaller size, lower power consumption, larger amplification, higher switching frequency, higher reliability, easy integration, and No. The advantages of preheating can be achieved. Because of its various advantages, transistors have replaced vacuum tubes which are close to the bottleneck in technology. Now, transistors have been widely used in various fields of people's production and life, and become one of the most important components in electronic and electrical sciences. A transistor is a semiconductor device, which mainly amplifies, switches and stabilizer in the circuit. In a broad sense, transistors include all electronic and electrical components based on semiconductor materials, including diodes, transistors, silicon controllers and so on, but what is commonly referred to as transistors are transistors BJT.

Bipolar Junction transients consists of two opposite PN junctions, which can be divided into NPN tube and PNP tube according to the polarity differences, and silicon tube and germanium tube according to the materials used. Bipolar transistor is a kind of current control device, which controls relatively large collector current through weak base level current. Due to the effect of small current controlling large current, it can be regarded as current amplifier device, whose amplification factor ranges from dozens to thousands of times.

As an early device, bipolar transistor is the basis of our study of various power devices, so we first plan to study BJT.

The transistor characterizer is a special instrument used to visually observe various characteristic curves of the transistor, such as output characteristic curve, input/transfer characteristic curve, etc[1]. In view of the status of the transistor in the field of modern electronics, the importance of its measuring instruments is unknown.

In the 1970s, based on the principle of JT1 tube characteristic tracer, Shanghai radio 21 factory successfully developed the QT2 transistor characteristic tracer. In the 1980s, a batch of tracer represented by XJ4810 came out, further improving the measurement range and precision of the homemade transistor characteristic tracer. Now, the transistor characteristic tracer is developing toward the intelligence, the virtualization direction, many manufacturers have built the embedded computer into the pictograph, has improved the function and the practicability of the pictograph greatly. Based on this, we designed a transistor characteristic graphical instrument based on virtual instrument.

1 TECHNICAL INTRODUCTION AND RESEARCH OBJECTIVES

1.1 Virtual instrument technology

Virtual Instrument technology USES highly integrated modular hardware circuits and equipment, and combines efficient and flexible software to realize the functions of various traditional instruments[2]. The concept of virtual instrument was first proposed by National Instruments (NI) of the United States. Then, it caused a big change in the traditional instrument measurement technology, which led to the irresistible introduction of computer technology into the field of measurement instrument, and pioneered the field of electronic measurement where "software is the instrument"[3]. There are three main components of virtual instrument: computer as the basic carrier; Software as the core of the whole instrument; High-performance A/D acquisition and signal conditioning circuits are key links. The common virtual instrument structure is shown in figure 1.

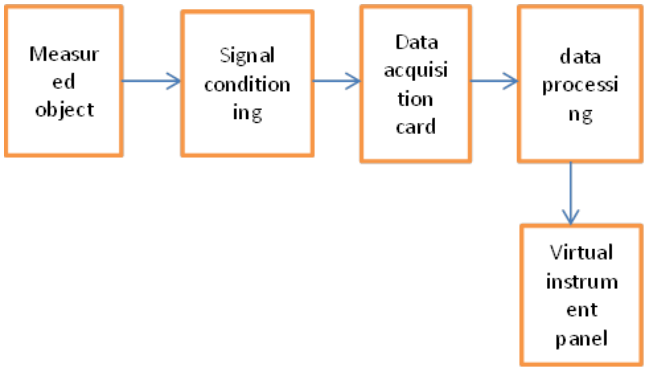

Fig.1 Common virtual instrument structure block diagram

Virtual instruments have the following advantages:

(1) High performance

Compared with the embedded controller of the traditional instrument, the computer or workstation used by the virtual instrument completely inherits the advantages of the ready-made PC technology and has obvious advantages in computing speed and various tasks processing[4].

(2) Small size and high integration

Unlike traditional measuring instrument of discrete, virtual instrument technology requirement for each kind of equipment is a main computer and a peripheral circuit, while a computer on the footprint and value tend to be greater than a traditional instruments, but through the use of appropriate bus protocol, allows a computer to control multiple peripheral hardware circuit to work at the same time, the user can add or reduce hardware circuit according to the requirements.

(3) Flexible combination, strong expansion, new product development cycle short

Different from the independent development of each device in the traditional instrument development, the development of virtual instrument only needs to follow the same bus protocol, and on this basis, appropriate software and hardware development can be carried out to improve the existing equipment at a very low cost or carry out the research and development of a new product[5].

1．2 LabVIEW

LabVIEW is by NI company launched a program development environment, and general development environment using text-based compiled languages are different, used by LabVIEW is a graphical compilation language (G language), the programming language to make program becomes vivid image, is also more convenient for people to understand, is produced by the LabVIEW programming file suffix for VI, LabVIEW will edit the program can also generate independent executable file, for developers to program directly to become an independent instrument panel[6]. The LabVIEW programming interface and its program control front panel are shown in FIG. 2 and FIG. 3 respectively.

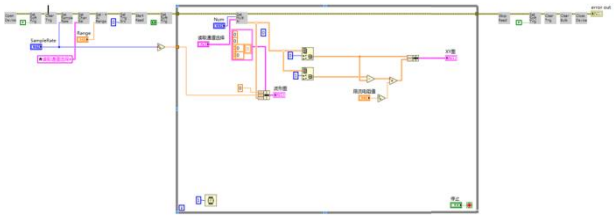

Fig.2 Programming interface

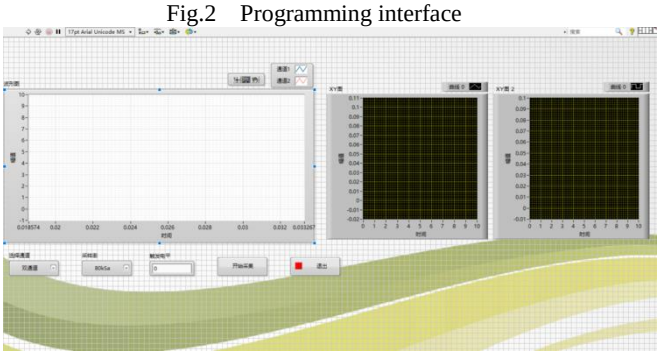

Fig.3 The front pane

1．3 The research target

To develop a transistor graphical instrument based on virtual instrument technology, the precision and power range is not very high, and the volume is much smaller than the traditional graphical instrument. By combining the data acquisition card and the computer equipped with LabVIEW software, the transistor transfer characteristic curve can be seen intuitively.

Type of measurement curve: BJT input characteristic curve, BJT output characteristic curve

The main work:

On hardware, a signal generator capable of generating current, voltage step wave and synchronous scanning voltage respectively is constructed. The lower computer and communication system can receive the upper computer instruction and set the parameters of the hardware circuit.

On the software, LabVIEW is used to write the upper computer, which communicates with the lower computer controller through the network port and controls various parameters of the graphical instrument. The data collected by the acquisition card can be received and displayed on the screen in the form of curve. Write down the program of the lower computer to generate various waveforms required by the measurement transistor, control the switching devices in the circuit, and change the circuit measurement mode and signal amplitude.

2 THE OVERALL SCHEME OF THE INSTRUMENT IS SHOWN

Tracer basic structure as shown in figure 4, the computer through the front-end ports and communication hardware circuit, control circuit work each work parameters, is responsible for the hardware circuit of signal and the signal conditioning, amplification, and then applied to the measured tube, various parameters of the measured tube through USB4220 acquisition card collection, and handed back

to the computer via USB, processing and display, so as to complete a survey of the transistor.

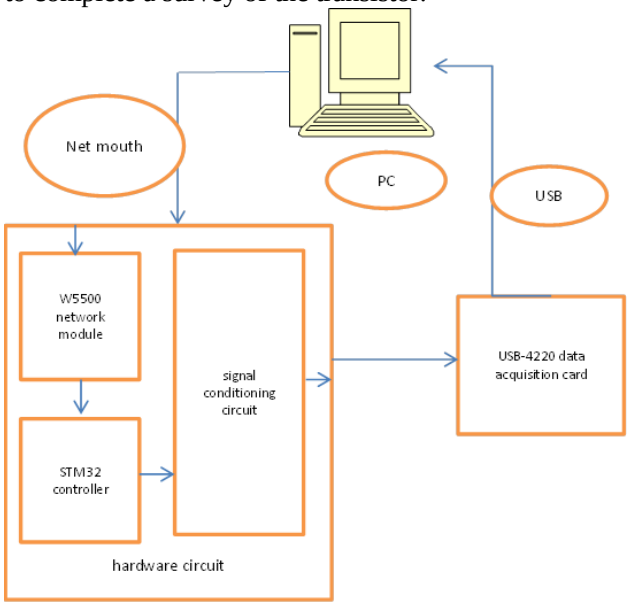

Fig.4 Basic structure of the graphic instrument

2．1 *Software solutions*

（1） Upper computer scheme

The upper computer is written by LabVIEW software, which is mainly divided into two parts: hardware circuit control, receiving and processing the data returned by the acquisition card. USB4220 acquisition card factory information is included in the detailed module subvi, these function modules subvi use calls dynamic link library (DLL) functionality, not making it easy for users to modify, but the user can according to need to the corresponding combination of these functions to achieve different functions, combined with LabVIEW inside other functions to achieve the goal of data receiving, processing and display[7].

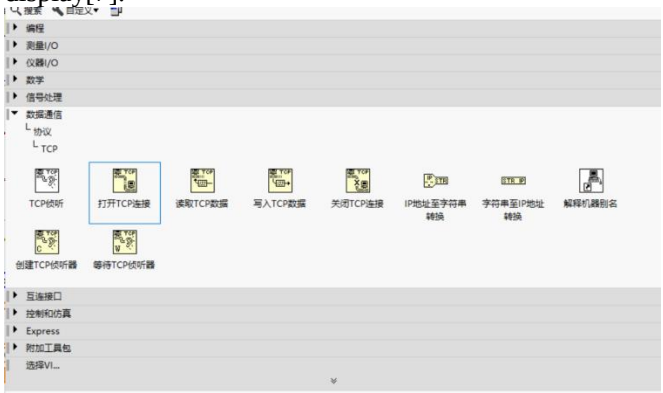

Fig.5 TCP functions in LabVIEW

（2） Lower computer scheme

The controller of the lower computer is STM32F103ZET6 type controller. STM32 series controller is a high-performance, low-power and low-cost embedded micro-controller launched by ST company, based on the ARM cortex-m kernel. The STM32F103ZET6 model controller selected in this design contains two D/A channels, which can be used to generate step signals and scan signals simultaneously[8].

2．2 *Signal conditioning circuit program*

Signal conditioning circuit structure as shown in figure 6, the steps of the STM32 produce signals through the proportion of adjustable in-phase amplifier circuit amplifier to a specified amplitude, magnification of adjustment is through the analog switch chip CD4051 to select different access circuit resistance, and analog switch chip control can make side by STM32 I/O port to control, so as to realize the program control circuit parameters. After the step signal is amplified by the same phase amplifier circuit, it is decided to enter the inverting circuit according to the measurement of NPN tube or PNP tube, enter the voltage-current conversion circuit, and then enter the power amplifier circuit. The net power amplified signal can be applied to the transistor as the output signal[9]. The principle of collector voltage sweep signal is roughly the same as that of step signal, but the link of voltage and current conversion is not discussed here.

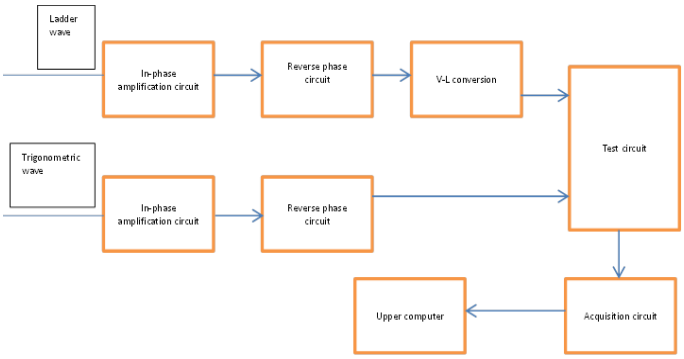

Fig.6 Hardware circuit diagram

2．3 *Acquisition card selection*

The acquisition card selected in this design is the smekehua usb-4220 data acquisition card, which is classified as synchronous channel sampling, and the acquisition card has ultra-low noise and high precision. The usb-4220 model has a 12-bit resolution and a sampling rate of up to 500K[10], which is sufficient to meet the design requirements. The acquisition card is shown in figure 7.

Fig.7 Smaikohwa usb-4220 acquisition card

2．4 *Measurement and collection of BJT*

The graphic instrument can measure the output curve and transfer curve of BJT. The mapping of each

curve corresponds to different measurement circuits, as well as different signal acquisition circuits.

BJT output characteristic curve of surveying and mapping as shown in figure 8, the transmitter earth, ladder level base on current signal, the collector connecting current-limiting resistor, current-limiting resistance applying steps and at the other side current signal synchronization 'triangle wave voltage signal, the triangular wave for special-shaped triangle wave here, in passing zero with zero value in a short period of time. This is because the output characteristic curve drawing, need to exert different respectively in the base level of drive current collector voltage - current curve drawing, the base level of drive current from one value to another value, the collector voltage at zero, and the actual letter circuit, steps base at current value can't be a moment change, need a transition time, and when the use is shown in figure 9 triangle wave as the collector signal, as a result of the triangular wave zero only for an instant, is likely to cause the base level signal switching, collector voltage at zero, so that the output characteristic of draw curves between adjacent curves' wired '. By changing to the waveform shown in figure 8, the collector voltage can be kept at zero at the time of base step signal switching, so as to eliminate the phenomenon of "connection". When measuring, CH2 directly collects collector voltage as the physical quantity of X axis. The difference between CH1 and CH2 is divided by R to obtain collector current, which is considered as the physical quantity of Y axis.

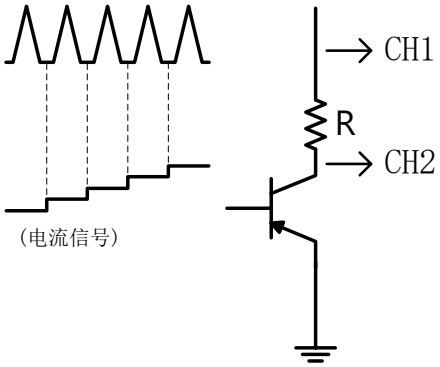

Fig.8 BJT output characteristic mapping

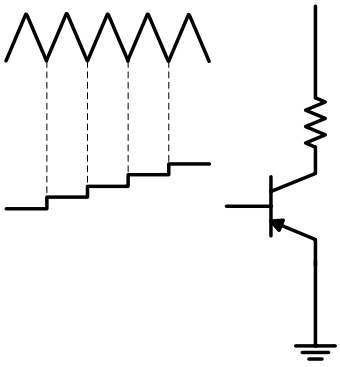

Fig.9 Use general triangular wave mapping

3 GRAPHIC INSTRUMENT STRUCTURE DESIGN

3．1 Hardware circuit (signal conditioning part)

（1） An in-phase amplifier with controllable amplification

The maximum value of step signal and scan signal generated by STM32 is only 3.3v. In order to make the signal amplitude higher, amplification needs to be carried out, and the amplification factor needs to be controlled by the upper computer. FIG. 10 shows the controllable in-phase amplification circuit. In the figure, CD4051 is an analog switch chip. One channel from CHAN0 to CHAN7 is selected to connect to COM pin according to the level signals of A, B and C pin. Assuming that the external resistance of the chip selected channel is R, the calculation formula of the circuit amplification factor is A_v=1+R/R_33. In the circuit, R33 is 10K, and different resistance values are assigned to R25 to R32 respectively, so that different amplification multiples can be obtained for the circuit and different voltage amplitudes can be obtained for the output signal.

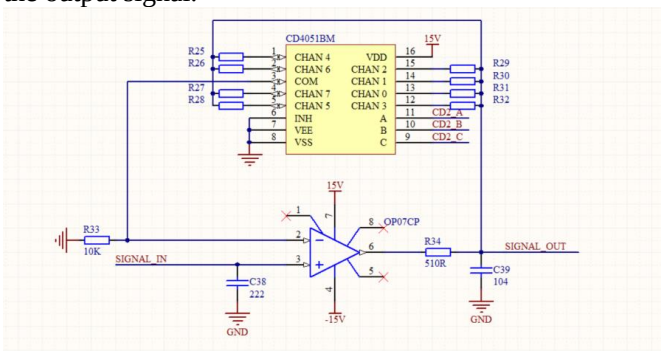

Fig.10 Adjustable in phase amplifying circuit

Since the supply voltage of CD4051 is 15V, if the enabling end A, B and C are determined to be high, the input voltage of 15V is required. The output voltage of GPIO port of STM32 is only 3.3v, so the drive circuit needs to be set. The driving circuit structure is shown in figure 11. Take the CD2_A port as an example. When the output of STM32 corresponding pin is high, Q5 leads and CD2_A sends low level. When STM32 output is low, Q5 closes, and CD2_A is connected to 15V through 10K pull-up resistance, and the output is approximately 15V.

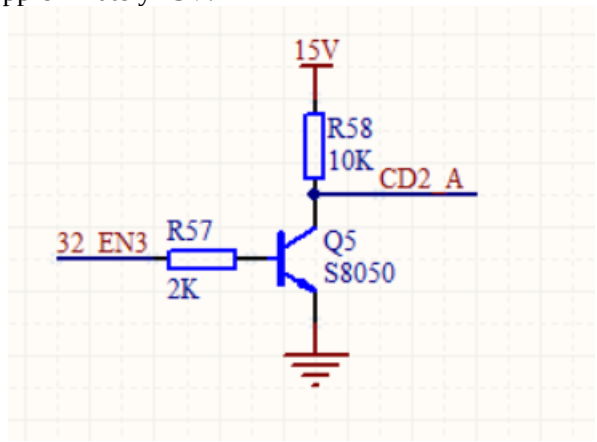

Fig.11 CD4051 enable terminal driver circuit

（2） Inverse-phase amplifier circuit

The output signal of the in-phase amplifier circuit is the positive voltage signal. If the pnp-type BJT or

p-type MOSFET are measured, the negative voltage signal is required. Then the inverse-phase amplifier circuit is required to invert the signal. As shown in figure 12, if R35=R36=10K, the input and output relation is U_out= -u_in[11].

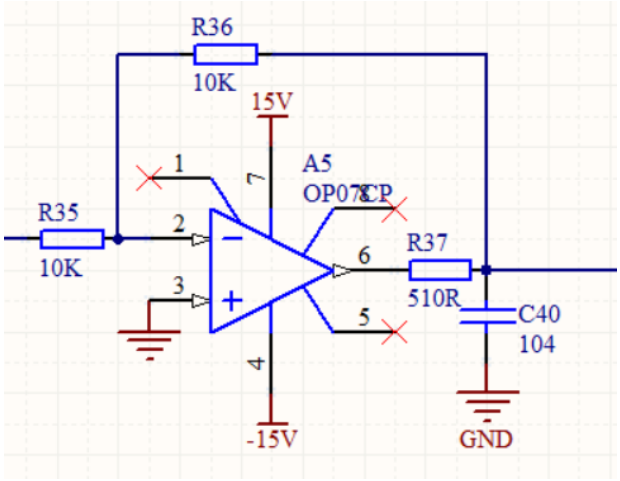

Fig.12 Reverse phase circuit

（3） Voltage - current conversion circuit

Since BJT is a current control transistor, its base step signal should be current signal, so a voltage - current conversion circuit should be set. The voltage-current conversion circuit is shown in figure 13. R33=R34=R35=R36=10K, with Ui= u1-u2. It is assumed that CD4518 access resistance is R. It can be seen that, when R is constant, the output current and input voltage show a linear relationship, and at the same time, CD4518 can choose the resistance of different resistance values to adjust the output current range to adapt to different models of BJT[12].

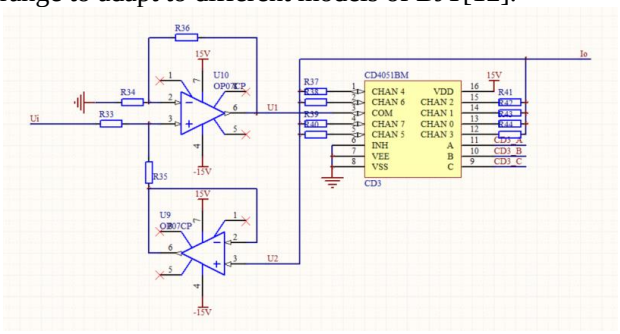

Fig.13 Voltage current conversion circuit

（4） Filtering in the circuit

In this circuit, since the signal is generated by D/A of STM32, there is almost no clutter interference in the initial signal. However, the switching power supply chip used in the circuit will produce high-frequency noise on the power supply voltage of the operational amplifier. The frequency is about 500KHz.

① Operation amplifier OP07 supply voltage is + / -15v. In the design, 100nF+10 negf capacitance is parallel to the positive and negative power pins of each amplifier, which is used to filter the high-frequency clutter of the amplifier.

②Signal noise processing: due to the operation of the power supply and various factors, noise is inevitable to be mixed into the signal. Therefore, RC filtering processing is carried out at the output end of each circuit link (or directly shunt capacitance to ground, as the case may be).

3．2 PC software

The signal collection part is combined with the data of the acquisition card usb-4220, and by using the operation function of the acquisition card provided by the manufacturer, the data of any channel can be directly collected and the waveform of this channel can be drawn. However, this design does not use the image with time as the abscissa, taking the output characteristic curve as an example, the abscissa is the collector - transmitter (drain - source) voltage, and the ordinate is the collector (drain) current, so the signals on two channels need to be integrated into a set of data and output on the same image. This function can be implemented by the 'XY graph' control in LabVIEW. Two groups of independent data are combined into clusters through the 'binding' function, and input into the 'XY graph' control, then the data can be displayed in the image in the form of independent points or wires.

3．3 Lower computer software

This part of the program block diagram decodes the data transmitted from the network port by STM32 and positions the corresponding GPIO pin to control the signal conditioning circuit topology. When the circuit structure is changed, enter the signal generation module and survey the transistor, the upper computer sends the instruction, and the lower machine generates the waveform according to the instruction content.

4 JOB ANALYSIS

After the system is built, it is necessary to first observe whether the two synchronous signals generated meet the requirements, and then measure them. You can use the oscilloscope directly or use the usb-4220 acquisition card to observe the two signals. The waveform is shown in figure 14. Triangle wave and stepped wave noise are small, signal synchronization is good, to meet the requirements, fully meet the needs.

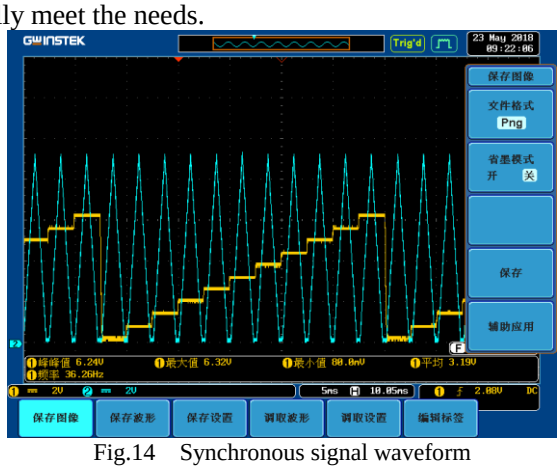

Fig.14 Synchronous signal waveform

5 CONCLUSION

This design provides the design idea of a transistor graphics instrument and the initial realization of the transistor device characteristics measurement and curve drawing, the test data is true, but there are still the following deficiencies.

First of all, the system can measure the characteristic curve of low-power transistors, the output voltage range can be sent to + / -15v, and the current range can be up to 2A, but the power is still much smaller than that of traditional graphical instrument. In order to achieve the purpose of portability, the development of high-power and high-voltage direction will not be continued for the time being. Additional modules can be added for subsequent work, such as widening the output voltage range and increasing the signal output current intensity to measure more powerful transistors.

Secondly, this system only intuitively shows the characteristic curve of the transistor, and does not carry out other processing on the data, and cannot directly see the various parameters of the transistor and the amplification factor. The follow-up work can add some data processing in the upper computer, so as to display the characteristics of the tube more intuitively and comprehensively.

Finally, in the interest of time, this system USES the finished product, the data acquisition card without the function of circuit STM32 modulus conversion module, if want to further improve the system integration and portability, can consider to use STM32 data directly, but needs to be on the upper and lower position machine communication to make some improvements, in order to realize the data upload and display in real time.

Reference

[1] FangShang-xia.Virtual Transistor Diagram Based on LabVIEW and USB Interface.Chengdu.University of Electronic Science and Technology of China.2006.

[2] Liu Jun.Study on Transistor Characteristic Tester Based on Virtual Instrument [D]. Chongqing: Chongqing University, 2008.

[3] Zhao Zhongyi. Semiconductor tube characteristics of the principle of the instrument, maintenance, testing and application [M]. Beijing: Electronic Industry Press, 1994.

[4] YuanYuan,GuJun.VirtualInstrumentBasicTutorial[M].Chengdu.University of Electronic Science and Technology Press.2002.

[5] LiuJun.Study on Transistor Characteristic Intrument based on Virtual Instrument[D].Chongqing.Chongqing University.2008.

[6] HouGuo-ping,Ye Qi-xin.LabVIEW7.1.LabVIEW7.1 programming and virtual instrument design[M].Beijing.Tsinghua University Press.2003.

[7] Mukesh Kumar，Mansav Joshi，Sanjeev Sharma. Design and Implementation of Embedding Web Server for Real Time Data Acquisition and Logging System[J]. International Journal of Computer Applications,2012,42(11):13-16.

[8] National Instruments Corporation. LabVIEW User Manual. Reference Materials, 2003

[9] DAI Yi-song. Noise of Electronic System and Method of Low Noise Design [M]. Changchun: Jilin People Publishing House, 1984.

[10] Deshpande S G,Jenq-Neng H. A real-time interactive virtual classroom multimedia distance learning system[J]. Multimedia,IEEE Transactions on. 2001,3(4):432-444.

[11] National Instruments Corporation.Using NI-VISA 3.0 to Control USB Device.Reference Materials,2005.

[12] Liang Zhi-guo, ZHU Ji-jie. An Evaluation Method for the Dynamic Noise of Data Acquisition System [J]. Modern Measurement and Test,1999, (3): 23-26.

APPENDIX A BLOCK DIAGRAM OF UPPER COMPUTER PART

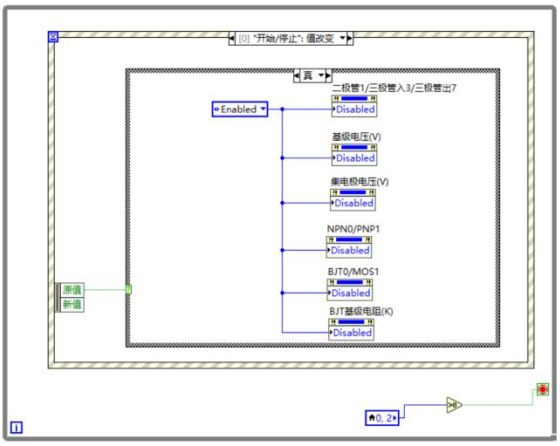

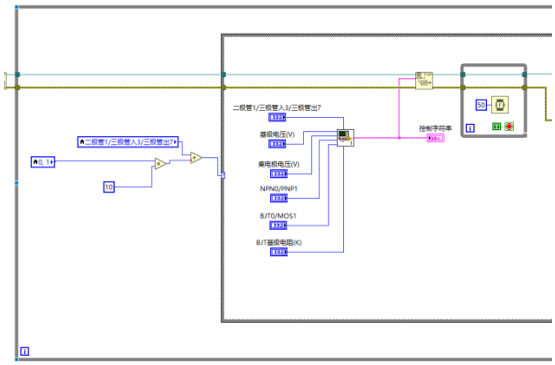

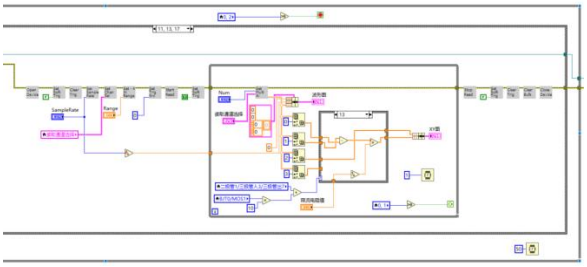

APPENDIX B LOWER COMPUTER CORE PROGRAM CODE

```
int main(void)
 {
    uint16_t len;
    u32 data=0;
    u32 i;
    int a=0;
    int b=0;
    int c=0;

    delay_init();
NVIC_PriorityGroupConfig(NVIC_PriorityGroup_2);

    Dac1_Init();        Dac2_Init();

RCC_APB2PeriphClockCmd(RCC_APB2Periph_GPI
OG, ENABLE);

      GPIO_InitStructure.GPIO_Pin =
GPIO_Pin_0|GPIO_Pin_1|GPIO_Pin_2|GPIO_Pin_3|G
PIO_Pin_4|GPIO_Pin_5|GPIO_Pin_6|GPIO_Pin_7|GP
IO_Pin_8|GPIO_Pin_9|GPIO_Pin_10;
      GPIO_InitStructure.GPIO_Mode =
GPIO_Mode_Out_PP;
      GPIO_InitStructure.GPIO_Speed =
GPIO_Speed_50MHz;
      GPIO_Init(GPIOG, &GPIO_InitStructure);



    initBSP();
    reg_wizchip_spi_cbfunc(0,0);
    reg_wizchip_spiburst_cbfunc(0,0);
    Reset_W5500();
    setNetwork();
    uart_init(9600);
    Dac2_Set_Vol(0);
    Dac1_Set_Vol(0);

    GPIO_SetBits(GPIOG,GPIO_Pin_10);

  while(1)
  {
     switch(getSn_SR(0))
     {
          case SOCK_INIT:
  listen(0);          break;
          case SOCK_ESTABLISHED:
        if(getSn_IR(0) & Sn_IR_CON)
                {
                  setSn_IR(0, Sn_IR_CON);
             }                    len=getSn_RX_RSR(0);
                                    if(len>0)
                {
                  recv(0,buffer,len);
  W5500_print("%d\r\n",data);
                  data=0;
                  for(i=0;i<len;i++)
                  {
                    data=data*10+(buffer[i]-48);
                  }

                   GPIOG->ODR&=0X0000;
                   GPIOG->ODR|=data;
        }
          break;
          case SOCK_CLOSE_WAIT:
    close(0);                    break;
          case SOCK_CLOSED:
  socket(0,Sn_MR_TCP,local_port,Sn_MR_ND);
    break;
      }


    switch((data>>11)&0x07)          {
      case 0:                Dac2_Set_Vol(0);
Dac1_Set_Vol(0);
      GPIO_SetBits(GPIOG,GPIO_Pin_10);
      break;
      case 1:                      Dac2_Set_Vol(0);
Dac1_Set_Vol(0);
          delay_us(150);
          for(b=0;b<3001;b=b+10)                {
              Dac1_Set_Vol(b);
           }
          for(b=3000;b>=0;b=b-10)
           {
              Dac1_Set_Vol(b);
           }
          delay_us(150);
      break;
      case 3:
          Dac1_Set_Vol(3000);
          Dac2_Set_Vol(0);
          delay_us(150);
          for(b=0;b<3001;b=b+10)
             {
                Dac2_Set_Vol(b);
             }
          for(b=3000;b>=0;b=b-10)
             {
                Dac2_Set_Vol(b);
             }
          Dac2_Set_Vol(0);
          delay_us(150);
      break;
      case 7:
for(a=0;a<11;a++)                    {
                  c=a*300;
                  Dac2_Set_Vol(c);
Dac1_Set_Vol(0);                    delay_us(150);
                  for(b=0;b<3001;b=b+20)
                     {
                        Dac1_Set_Vol(b);
                     }
                  for(b=3000;b>=0;b=b-20)
                     {
                        Dac1_Set_Vol(b);
                     }
```

```
                Dac1_Set_Vol(0);
                delay_us(150);
                  }
        break;
    }
  }
```